TRANSACTIONS
OF THE ASME
Series C

Journal of HEAT TRANSFER

November 1961

RADIATION • CONDUCTION • CONVECTION • COMPLEX SYSTEMS • PHASE CHANGES AND MIXTURES • TRANSIENT PHENOMENA • THERMOPHYSICAL PROPERTIES • EXPERIMENTAL TECHNIQUES • THERMOMETRY • ANALOG METHODS • ANALYTICAL AND NUMERICAL METHODS • APPLICATIONS • DESIGN TECHNIQUES • HEAT EXCHANGERS • INSULATION • ECONOMIC FACTORS BIOTECHNOLOGY • ASTRONAUTICS

Published Quarterly by
THE AMERICAN SOCIETY OF MECHANICAL ENGINEERS

TRANSACTIONS
OF THE ASME
Series C

Journal of HEAT TRANSFER

VOL. 83 • SERIES C • NO. 4

November 1961

CONTENTS

391 **Temperature Distribution in a Slab Moving From a Chamber at One Temperature to a Chamber at Another Temperature** (60—WA-197)
G. Horvay

403 **Thermal Conductivity of Some Commercial Iron-Nickel Alloys** (60—WA-47)
T. W. Watson and H. E. Robinson

409 **Transient Temperature in a Melting Solid** (60—WA-277)
J. E. Sunderland and R. J. Grosh

415 **Heat Transfer to Longitudinal Laminar Flow Between Cylinders** (60—WA-40)
E. M. Sparrow, A. L. Loeffler, Jr., and H. A. Hubbard

423 **Axial Temperature Distribution for a Nuclear Reactor With Sinusoidal Space and Exponential Time-Varying Power Generation** (60—WA-194)
W. O. Doggett and E. L. Arnold

432 **Unsteady Laminar Flow in a Duct With Unsteady Heat Addition** (60—WA-174)
Morris Perlmutter and Robert Siegel

441 **Fully Developed Pressure Drop in Triangular Shaped Ducts** (60—WA-100)
L. W. Carlson and T. F. Irvine, Jr.

445 **The Effect of a Longitudinal Magnetic Field on Pipe Flow of Mercury** (60—WA-192)
Samuel Globe

454 **An Exact Solution of the Compressible-Flow Characteristics in Constant-Area Passages With Simultaneous Friction and Constant Heat Flux** (60—WA-177)
R. N. Noyes

457 **Experimental Ablation Rates in a Turbulent Boundary Layer** (60—WA-208)
E. P. Bartlett and M. R. Denison

466 **On Some Laminar Forced-Convection Problems** (60—WA-188)
L. N. Tao

473 **Unsteady Laminar Free Convection** (60—WA-211)
P. M. Chung and A. D. Anderson

479 **Buoyancy Effects in Forced Laminar Convection Flow Over a Horizontal Flat Plate** (60—WA-220)
Yasuo Mori

483 **Local Mass Transfer From Circular Cylinders in Cross Flow** (60—WA-193)
H. H. Sogin and V. S. Subramanian

494 **Radiant Interchange Between Circular Disks Having Arbitrarily Different Temperatures** (60—WA-75)
E. M. Sparrow and J. L. Gregg

TECHNICAL BRIEFS

503 **Two-Phase Frictional Pressure Drop Prediction From Levy's Momentum Model**
J. F. Marchaterre

505 **Transient Temperature Measurement Errors in Heated Slabs for Thermocouples Located at the Insulated Surface**
D. R. Burnett

506 **Heat Conduction in a Series Composite Wall**
J. J. Brogan and P. J. Schneider

508 **Heat Conduction Through Walls During Fire**
Lie Tiam Tjoan

510 **Heat Conduction in an Eccentrically Hollow, Infinitely Long Cylinder With Internal Heat Generation**
M. R. El-Saden

(Contents continued on inside of back cover)

EDITORIAL DEPARTMENT

Editor, J. J. JAKLITSCH, JR.
Consulting Editor, LEO BLOOGETT
Production, JEAN NORTH
Production Asst., CARMEN L. CABRANES
Art Editor, HENRY BALFOUR

HEAT TRANSFER DIVISION

Chairman, W. ROHSENOW
Secretary, S. OSTRACH
Papers Review, T. F. IRVINE, JR.
Consulting Editor, S. P. KEZIOS

OFFICERS OF THE ASME

President, W. H. BYRNE
Secretary, O. B. SCHIER, II
Treasurer, E. J. KATES
Assistant Treasurer, H. J. BAUER

PUBLICATIONS COMMITTEE

Chairman, HENDLEY N. BLACKMON
MARTIN GOLAND
VITO L. SALERNO
F. J. HEINZE
R. E. DERBY
Junior Representatives
J. W. FOLLANSBEE
STEWART H. ROSS

REGIONAL ADVISORY BOARD

Region I, H. M. ROGERS, JR.
Region II, ROBERT E. ABBOTT
Region III, A. F. BOCHENEK
Region IV, FRANCIS C. SMITH
Region V, WM. J. TITZEL
Region VI, C. R. EARLE
Region VII, RALPH L. SCORAH
Region VIII, G. CORRY MCDONALD
Region IX, M. S. UMBENHAUER
Region X, CARL J. ECKHARDT

Published quarterly by The American Society of Mechanical Engineers. Publication office at 20th and Northampton Streets, Easton, Pa. The editorial department is located at the headquarters of the Society, 345 East Forty-Seventh Street, New York 17, N. Y. Cable address, "Mechaneer," New York. Price $3.00 a copy, $10.00 annually; to members, $1.50 a copy, $5.00 annually. Add 50 cents for postage to all countries outside the United States and Canada. Changes of address must be received at Society headquarters seven weeks before they are to be effective on the mailing list. Please send old as well as new address. . . . By-Law: The Society shall not be responsible for statements or opinions advanced in papers or . . . printed in its publications (B13, Par. 4). . . . Second-class mail privileges authorized at Easton, Penna. . . . This publication is authorized to be mailed at the special rates of postage prescribed by Section 132.122 . . . © Copyright, 1961, by The American Society of Mechanical Engineers. Reprints from this publication may be made on condition that full credit be given the TRANSACTIONS of the ASME, Series C—Journal of Heat Transfer, and the author, and that date of publication be stated.

TRANSACTIONS OF THE ASME is indexed by the Engineering Index, Inc.

Temperature Distribution in a Slab Moving From a Chamber at One Temperature to a Chamber at Another Temperature

G. HORVAY
Metallurgy and Ceramics Research Department,
General Electric Research Laboratory,
General Electric Company,
Schenectady, N. Y.
Mem. ASME

When an infinitely long slab travels from a chamber at one temperature to a chamber isolated from the first, at a higher temperature, heat will leak out along the slab from the second chamber to the first, whose amount decreases as the speed of the slab increases. An estimate of the heat lost is of interest in hot-rolling, in some nuclear processes, and in some continuous casting processes. The problem of determining the temperature distribution and the heat flow in the two chambers is formulated in the form of dual integral equations, and the solution is obtained by the method of Wiener-Hopf.

Introduction

THE HEAT lost by backward conduction along a moving slab, which travels from a chamber at one temperature (the ambient ϑ_a) to a chamber at a higher temperature (say, ϑ_f), is of interest in a number of processes, such as hot-rolling, continuous casting [1].[1] Its determination requires solution of the equation of heat conduction

$$\frac{V}{\kappa}\frac{\partial\vartheta}{\partial Z} = \frac{\partial^2\vartheta}{X^2\partial\xi^2} + \frac{\partial^2\vartheta}{\partial Z^2} \tag{1}$$

subject to the boundary conditions:

$$\begin{aligned} Z < 0\text{: } & h_-[\vartheta(1, Z) - \vartheta_a] = -k\partial\vartheta(1, Z)/\partial\xi \\ Z > 0\text{: } & h_+[\vartheta_f - \vartheta(1, Z)] = k\partial\vartheta(1, Z)/\partial\xi \end{aligned} \tag{2a}$$

$$-\infty < Z < \infty\text{: } \partial\vartheta(0, Z)/\partial\xi = 0 \tag{2b}$$

In the foregoing, X is the half width of the slab, ξ and Z are co-ordinates in a stationary co-ordinate system; the ξ-axis coincides with the edge of the plane separating the two chambers, and Z is the axis of symmetry, Fig. 1. (The slab is infinitely deep into the plane of the paper.) h_-, h_+ are surface heat-transfer coefficients in the lower and upper regions, respectively, ϑ is temperature, k conductivity, γ density, c specific heat, $\kappa = k/\gamma c$ diffusivity. V is the speed of slab travel.

[1] Numbers in brackets designate References at end of paper.

Contributed by the Heat Transfer Division and presented at the Winter Annual Meeting, New York, N. Y., November 27–December 2, 1960, of THE AMERICAN SOCIETY OF MECHANICAL ENGINEERS. Manuscript received at ASME Headquarters, August 22, 1960. Paper No. 60—WA-197.

We nondimensionalize the problem by introducing the nondimensional axial co-ordinate

$$z = Z/X \tag{3a}$$

the nondimensional temperature

$$U(\xi, z) = \frac{\vartheta - \vartheta_a}{\vartheta_f - \vartheta_a} \tag{3b}$$

the nondimensional time (Fourier number)

$$\tau = \kappa t/X^2 = z/p \qquad (t = Z/V) \tag{3c}$$

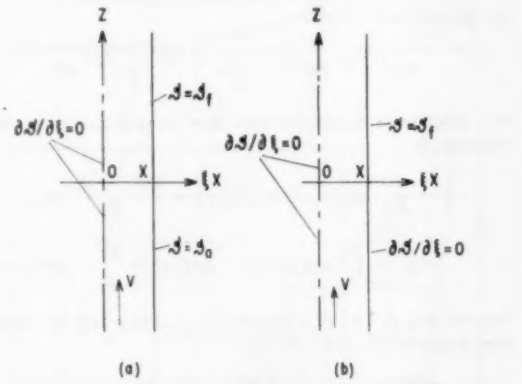

Fig. 1 Two-region heat-flow problem of a moving slab when its surface in space $Z > 0$, is maintained at temperature ϑ_f, and in the space $Z < 0$—(a) is maintained at temperature ϑ_a; (b) is insulated

Nomenclature

Dimensional Quantities

X = half width of slab
ξX, Z = transverse and axial co-ordinates, Fig. 1
t = time
V = velocity of slab motion
ϑ = temperature
k, γ, c = conductivity, specific weight, specific heat
$\kappa = k/\gamma c$ = diffusivity
h = heat-transfer coefficient, slab to surroundings
q = heat flux, equation (7)

Dimensionless Quantities

ξ, z = transverse and axial co-ordinates, equation (3)
τ = time (Fourier number)
p = velocity of slab motion (Peclet number)
U = temperature
$\mathbf{U}$ = function defined by (34)
β = heat-transfer coefficient (Biot number)
φ = flux function, equation (8)
σ_n, σ_n' = eigenvalue parameters, equations (13c), (17c)
$\Omega(\zeta)$ = function defined by (18a)
ψ, Ψ = see (20), (21)
μ = see (23)

the nondimensional velocity parameter (Peclet number)

$$p = XV/\kappa \tag{3d}$$

and the nondimensional heat-transfer coefficient (Biot number)

$$\beta_\pm = h_\pm X/k \tag{3e}$$

Problem (1), (2) may now be stated in the form. Solve

$$p\frac{\partial U}{\partial z} = \frac{\partial^2 U}{\partial \xi^2} + \frac{\partial^2 U}{\partial z^2} \tag{4}$$

subject to the conditions

$$\begin{aligned} z < 0: &\quad -\beta_- U(1, z) = \partial U(1, z)/\partial \xi \\ z > 0: &\quad \beta_+[1 - U(1, z)] = \partial U(1, z)/\partial \xi \end{aligned} \tag{5a}$$

$$-\infty < z < \infty: \quad \partial U(0, z)/\partial \xi = 0 \tag{5b}$$

We define mean temperature and mean downward conducted flux at any cross section z by

$$\bar{U}(z) \equiv \int_0^1 U(\xi, z)d\xi, \qquad \frac{d\bar{U}}{dz} \equiv \int_0^1 \frac{\partial U(\xi, z)}{\partial z}d\xi \tag{6}$$

Since ξ ranges from 0 to 1, mean flux is also total flux. The dimensionless $\partial U/\partial z$ is converted into dimensional flow $k\partial\vartheta/\partial Z$ per unit cross-sectional area by the formula

$$q_{\text{conduct}} = k\frac{\partial \vartheta}{\partial Z} = \frac{k(\vartheta_f - \vartheta_a)}{X}\frac{\partial U}{\partial z} \tag{7a}$$

In addition to the *downward conducted flux* there is, of course, also the *upward convected flux*

$$q_{\text{convect}} = \gamma c V(\vartheta - \vartheta_a) = \frac{k(\vartheta_f - \vartheta_a)}{X}pU \tag{7b}$$

The total axial downward heat flow passing any cross section therefore is

$$q = \int_0^1 [q_{\text{conduct}} - q_{\text{convect}}]d\xi = \frac{k(\vartheta_f - \vartheta_a)}{X}\bar{\varphi}(z) \tag{8a}$$

$$\bar{\varphi}(z) = \int_0^1 \varphi(\xi, z)d\xi, \qquad \varphi(\xi, z) = \frac{\partial U}{\partial z} - pU \tag{8b}$$

We call $\varphi(\xi, z)$ and $\bar{\varphi}(z)$ the *net flux function* and the *mean net flux*, respectively, and refer to

$$U_A \equiv -\frac{\bar{\varphi}(0)}{p} = \bar{U}(0) - \frac{d\bar{U}(0)}{pdz}, \qquad \vartheta_A = \vartheta_a + U_A(\vartheta_f - \vartheta_a) \tag{8c}$$

as the *apparent ambient temperature* of the slab (the "apparent entrance temperature to the upper chamber"). This terminology is further explained and exploited in [1]. We note that in our applications $\bar{\varphi}(0)$ (the heat lost from the upper chamber to the lower chamber) will turn out to be positive, i.e., U_A will be negative. Because of this heat loss, the apparent ambient ϑ_A is lower than the true ambient ϑ_a. We use the symbol

$$f \equiv \frac{\vartheta_f - \vartheta_A}{\vartheta_f - \vartheta_a} = 1 + \frac{\bar{\varphi}(0)}{p} \tag{8d}$$

to denote the "factor of apparent increase" in the temperature gap between the two chambers (the "effectiveness factor of the ambient temperature").

The two most important special cases of the boundary conditions (2*a*), (5*a*) are

(*a*) $$h_- = \infty, \qquad h_+ = \infty \tag{9a}$$

i.e.,

$$Z < 0: \ \vartheta(1, Z) = \vartheta_a, \quad Z > 0: \ \vartheta(1, Z) = \vartheta_f \tag{10a}$$

or, nondimensionally,

$$\beta_- = \infty, \quad \beta_+ = \infty \tag{9b}$$

$$z < 0: \ U(1, z) = 0, \qquad z > 0: \ U(1, z) = 1 \tag{10b}$$

and

(*b*) $$h_- = 0, \quad h_+ = \infty \tag{11a}$$

i.e.,

$$Z < 0: \ \partial\vartheta(1, Z)/\partial\xi = 0, \quad Z > 0: \ \vartheta(1, Z) = \vartheta_f \tag{12a}$$

or, nondimensionally

$$\beta_- = 0, \qquad \beta_+ = \infty \tag{11b}$$

$$z < 0: \ \partial U(1, z)/\partial\xi = 0, \quad z > 0: \ U(1, z) = 1 \tag{12b}$$

In the first case we assume that the temperatures ϑ_a, ϑ_f of the atmospheres in the two chambers are directly impressed on the surface of the moving slab (without an intervening boundary layer). This is the "usual" first approximation one makes in a heat-conduction problem. In the present problem this assumption will lead to infinite heat loss from the second chamber to the first chamber. In the second case we assume that ϑ_f is directly imposed on the slab surface in the second chamber, but the slab is insulated in the first chamber so as to minimize heat loss; heat can now escape the upper chamber only by being axially conducted to the heat sink at $z = -\infty$. In the present problem this assumption will be seen to lead to zero heat loss.

Evidently, therefore, the method of insulation vitally affects the amount of heat that leaks out along the slab, from the hot chamber to the cold chamber, and the loss may range between ∞ and 0, depending on whether there is no insulation or perfect insulation in the lower chamber.

In this paper the author shall work out the details of the solution for the two boundary conditions (9) (isothermal-isothermal, I-I) and (11) (adiabatic-isothermal, A-I), reserving the treatment of the general case for a later paper [2].

In the next section we present and discuss the results. In the following section we derive the solution (13) for the I-I boundary conditions, and in the final section we derive the solution (17) for the A-I boundary conditions.

Discussion of Results

It is shown in (28) that solution of (4) subject to the I-I boundary condition (10*b*) is

$$z < 0: \ U(\xi, z) = 2\sum_0^\infty (-1)^n \frac{(2n+1)\pi}{\sigma_n(p + \sigma_n)} e^{(p+\sigma_n)z/2} \times \cos(n + 1/2)\pi\xi$$

$$z > 0: \ U(\xi, z) = 1 + 2\sum_0^\infty (-1)^n \frac{(2n+1)\pi}{\sigma_n(p - \sigma_n)} e^{(p-\sigma_n)z/2} \times \cos(n + 1/2)\pi\xi \tag{13a, b}$$

$$\sigma_n^2 = p^2 + (2n+1)^2\pi^2 \tag{13c}$$

In Fig. 2 we plot level lines of the temperature in the slab for $p = 0, 0.1, 1, 10, \gg 1$. The case $p \gg 1$ (i.e., $p \simeq \infty$) is plotted for the values $\tau = 0, 0.1, 1, 10, \infty$ of the dimensionless time (3*c*).

The case $p = \infty$ corresponds to sudden immersion of a slab of

original temperature $U = 0$ into a medium at temperature $U = 1$. Thus one solves

$$\frac{\partial U(\xi, \tau)}{\partial \tau} = \frac{\partial^2 U(\xi, \tau)}{\partial \xi^2} \tag{14a}$$

subject to

$$U(\xi, 0) = 0 \tag{14b}$$

$$U(1, \tau) = 1, \quad \partial U(0, \tau)/\partial \xi = 0 \quad (\tau > 0) \tag{14c, d}$$

We quote the well-known solution:[2]

$$U = 1 - 4 \sum_0^\infty \frac{(-1)^n}{(2n + 1)\pi} e^{-(n+1/2)^2 \pi^2 \tau} \cos (n + 1/2)\pi\xi \tag{15}$$

One obtains this also from (13b) by making, for $p \gg 1$, the replacements

$$p - \sigma_n = p - p[1 + (2n + 1)^2\pi^2/p^2]^{1/2} = -(2n + 1)^2\pi^2/2p$$
$$\sigma_n = p, \qquad \tau = z/p \tag{16}$$

The case $p = 0$ illustrates the final equilibrium temperature established in a nonmoving slab on which the surface temperatures $U = 0$ and $U = 1$ are impressed in the two half spaces $z < 0$, $z > 0$.

When there is no motion then, of course, the temperature distribution is symmetric about $z = 0$, but when there is motion then, as the velocity is increased, more and more cold temperature is carried by the slab into the $z > 0$ region. It is seen that in the range $p > 10$ the approximation (14) holds, and axial temperature variations along slab sections of unit length are insignificant [if we disregard the vicinity of the singular point $(\xi, z) = (1, 0)$]. For $p > 10$ it is therefore justified to analyze the temperature flow in the upper chamber as if the slab were suddenly immersed into the warmer medium and only inward flow existed.

In Figs. 3(*a*, *b*) we plot the temperature distribution U and the axial conductive flux $\partial U/\partial z$ in the cross section $z = 0$ for various p. In Figs. 4(*a*, *b*, *c*), we plot the variation, with z and p, of the mean temperature $\bar{U}(z)$, of the mean conductive flux $d\bar{U}/dz$, and of the mean net flux $\bar{\varphi}(z) = d\bar{U}/dz - p\bar{U}$. We note that the mean temperature decreases at any given location as the speed of travel is increased.

From Fig. 3(*b*) it is seen that the axial conductive flux is $+\infty$ at $(\xi, z) = (1, 0)$. This is caused by the short circuit which exists between the hot chamber and the cold chamber in the vicinity of the point (1, 0). The infinity is so strong [it has the form $1/(1 - \xi)$] that, as seen from Fig. 4(*b*), even the mean flux over cross

[2] Reference [3], p. 100.

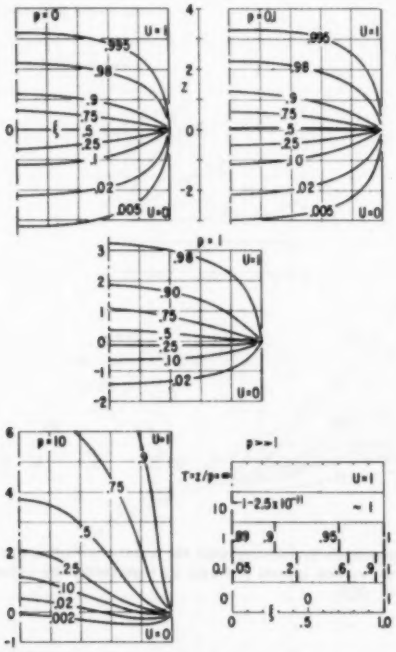

Fig. 2 Isothermals in moving slab for isothermal-isothermal boundary condition, at various speeds of travel as represented by value of Peclet number $p = VX/\kappa$

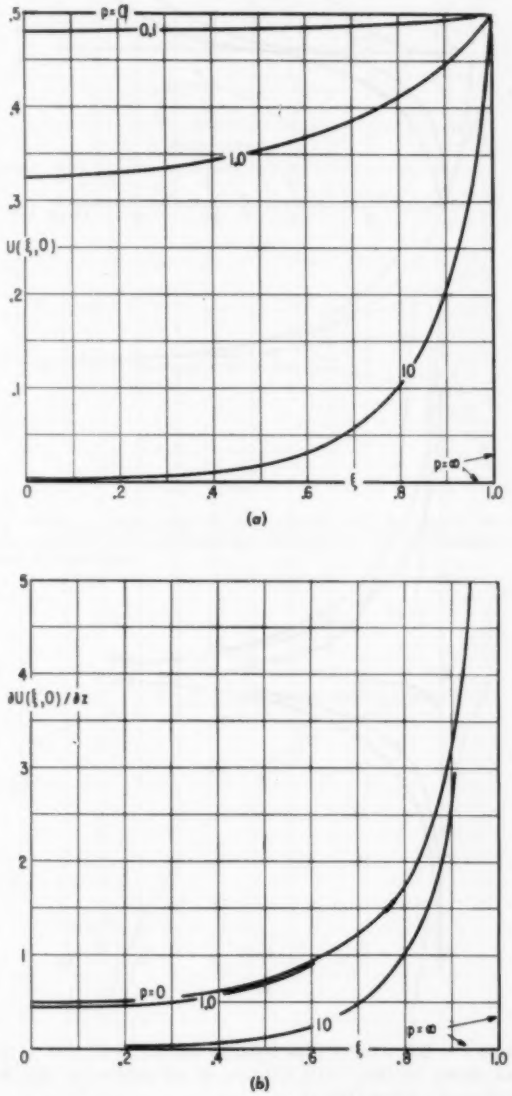

Fig. 3 Profiles of (*a*) temperature U; (*b*) conducted heat flux $\partial U/\partial x$ at cross section $x = 0$ for various speeds (I-I b.c.)

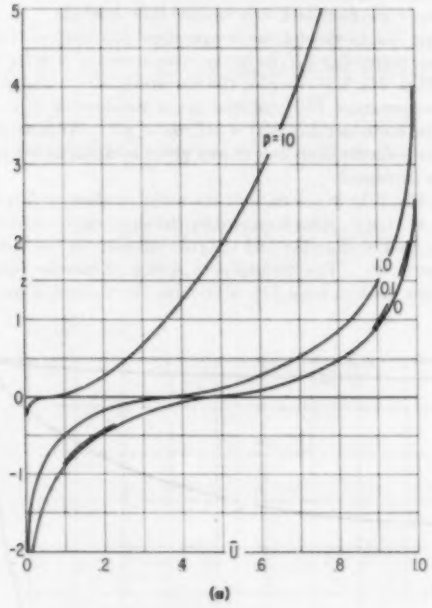

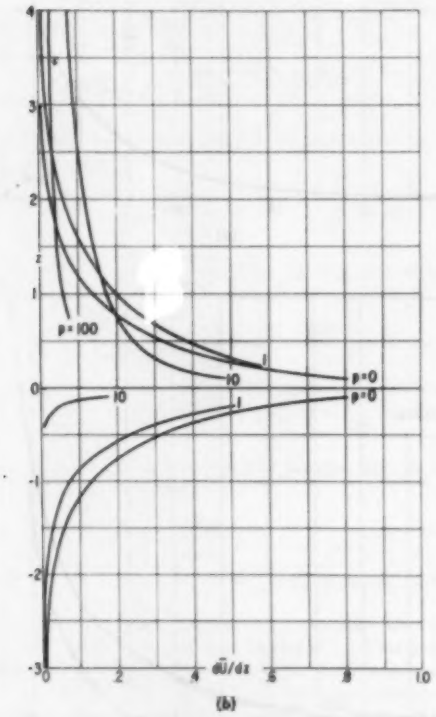

section $z = 0$ is infinite [this becomes infinite as $\ln 1/(1 - \xi)$].

As shown in (48), (51), solution of (4) subject to the A-I boundary condition (11*b*) is

$$z < 0:\ U = \frac{e^{pz}}{\Omega^2(p/2)} + \frac{2p}{\Omega(p/2)} \sum_1^\infty \frac{(-1)^n e^{(p+\sigma_n')z/2}}{\sigma_n'\Omega(\sigma_n'/2)} \times \cos n\pi\xi \quad (17a)$$

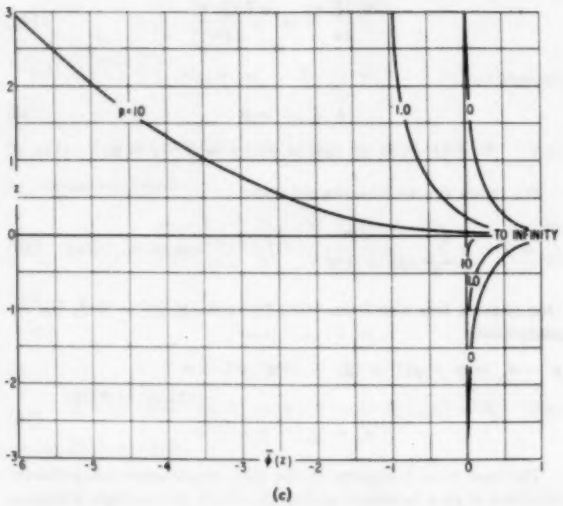

Fig. 4 Variation of (*a*) mean temperature $U(x)$; (*b*) mean conducted flux $d\bar{U}/dx$; (*c*) mean net flux $\bar{\varphi}(x) = d\bar{U}/dz - p\bar{U}$ with x and p (I-I b.c.)

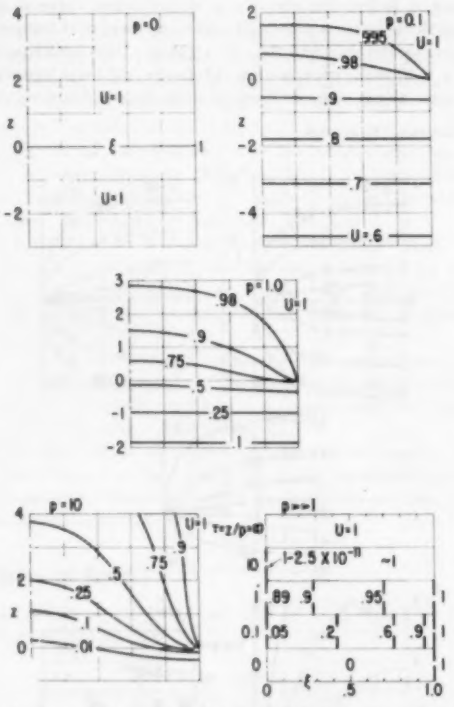

Fig. 5 Isothermals in moving slab for adiabatic-isothermal boundary condition, at various speeds of travel as represented by value of Peclet number $p = VX/\kappa$

$$z > 0:\ U = 1 - \frac{2p}{\Omega(p/2)} \sum_0^\infty \frac{(-1)^n \Omega(\sigma_n/2) e^{(p-\sigma_n)z/2}}{(n + 1/2)\pi\sigma_n} \times \cos(n + 1/2)\pi\xi \quad (17b)$$

$$\sigma_n' \equiv [p^2 + 4n^2\pi^2]^{1/2}, \qquad \sigma_n \equiv [p^2 + (2n+1)^2\pi^2]^{1/2} \quad (17c)$$

$$\Omega(\zeta) \equiv \prod_{k=1}^{\infty} \frac{\dfrac{\zeta}{(k-1/2)\pi} + \left[1 + \dfrac{p^2/4}{(k-1/2)^2\pi^2}\right]^{1/2}}{\dfrac{\zeta}{k\pi} + \left[1 + \dfrac{p^2/4}{k^2\pi^2}\right]^{1/2}} \tag{18a}$$

$$= \lim_{K\to\infty} \prod_{k=1}^{K} \frac{k}{k-1/2} \frac{\zeta + \sigma_{k-1}/2}{\zeta + \sigma_k'/2} \tag{18b}$$

In Fig. 5 we plot the level lines of the temperature in the slab for $p = 0$, 0.1, 1, 10, and $\gg 1$. On using (16) and noting that, as $p \to \infty$,

$$\Omega(\sigma_n/2) \to \Omega(p, 2) \tag{19}$$

the case $p \gg 1$ is seen to lead to (15).

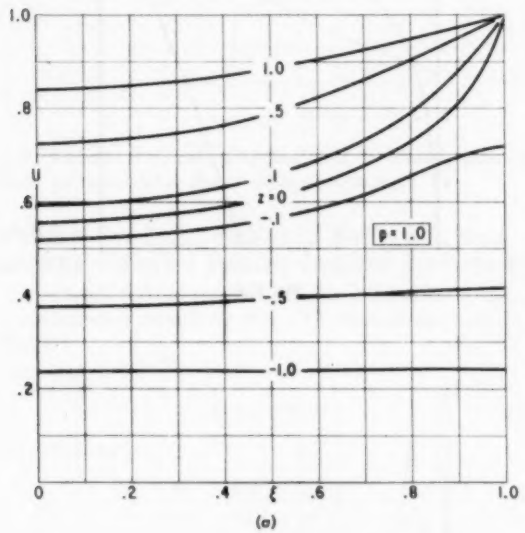

(a)

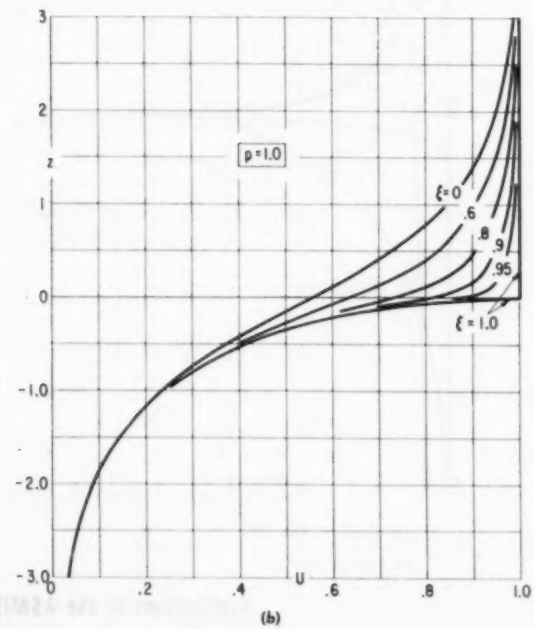

(b)

Some details of the determination in Fig. 5 are shown in Fig. 6(*a*), for $p = 1$. We determined the variation of U with ξ at given axial locations $z = 0, \pm 0.1, \pm 0.25, \ldots$, from formulas (17*a*, *b*); then obtained from the figure the cross plots of U versus z for various ξ as shown in Fig. 6(*b*); from the latter we finally determined the level curves shown in Fig. 5. In Fig. 6(*c*) we plot the slopes $\partial U/\partial z$ of the afore-mentioned cross plots. This figure explains the behavior of the conducted flux $\partial U/\partial z$ near the cross section $z = 0$. For $\xi = 1$ and $z > 0$ the flux is evidently zero; see equation 17(*b*). At the point $(\xi, z) = (1, 0)$ the flux jumps to infinity, see Appendix, but as seen from Fig. 9, the total flux through the cross section remains finite.

In Fig. 7 we plot the variation of the surface temperature $U(1,$

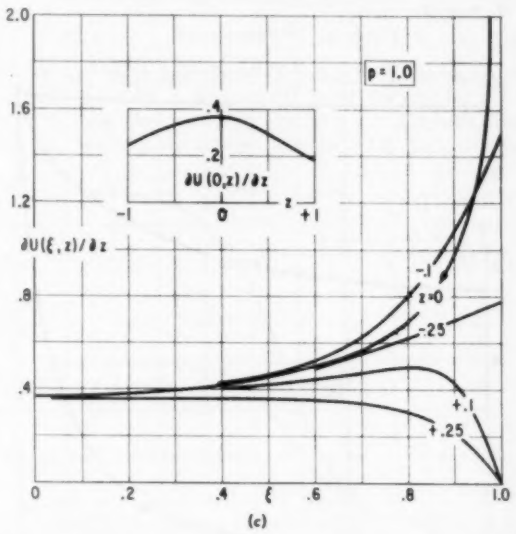

(c)

Fig. 6 Profiles of temperature U (*a*) at various cross sections z; (*b*) at various abscissas ξ; (*c*) conducted flux $\partial U/\partial z$, at various cross sections z all for $p = 1$, (A-I b.c.)

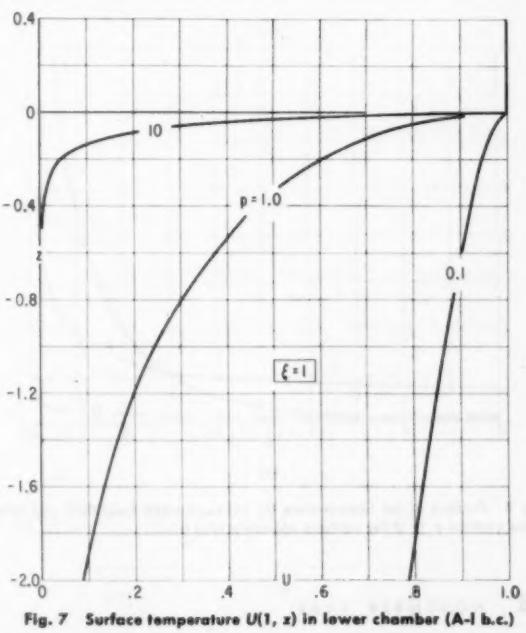

Fig. 7 Surface temperature $U(1, z)$ in lower chamber (A-I b.c.)

z) in the lower chamber for various values of p. The infinite slope of U for $\xi = 1$ at $z = 0$ is again noted.

In Figs. 8(a, b) we plot the temperature distribution U and axial conductive flux $\partial U/\partial z$ in the cross section $z = 0$ for various p; in Figs. 9(a, b, c) we plot the variation, with z and p, of $\bar{U}(z)$, $d\bar{U}/dz$, $\bar{\varphi}(z) = d\bar{U}/dz - p\bar{U}$. Figs. 5, 8, 9 are the counterparts of Figs. 2, 3, 4 for the new boundary conditions.

In Fig. 10 we plot the mean temperature at the entrance cross section to the upper chamber, $\bar{U}(0)$, versus p (on a logarithmic scale), for the two cases $\beta = \infty$, $\beta = 0$ treated in this paper.[3] The calculated points $p = 0.1, 1, 10$ are indicated by circles. The calculated two-cycle plot was extended to the indicated four-cycle plot by interpolating, in the Cartesian plot of $\bar{U}(0)$ versus $p^{1/2}$ and versus $p^{-1/2}$, for $p = 0.1, 100$.

[3] Curves of $\bar{U}(0)$, $d\bar{U}(0)/dz$, U_A versus p will be given for $\beta = 0, 0.1, 1, 10, \infty$ in [2].

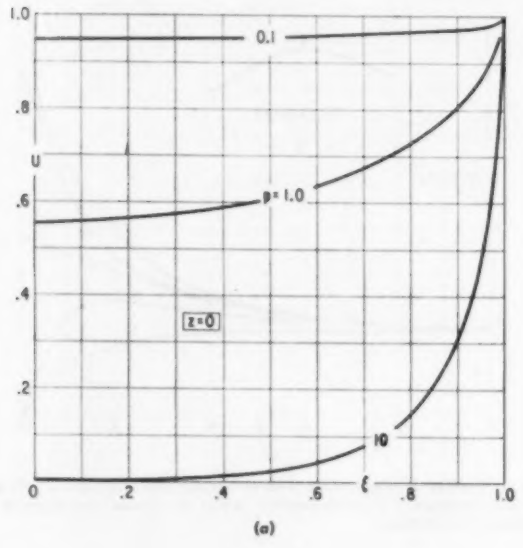

(a)

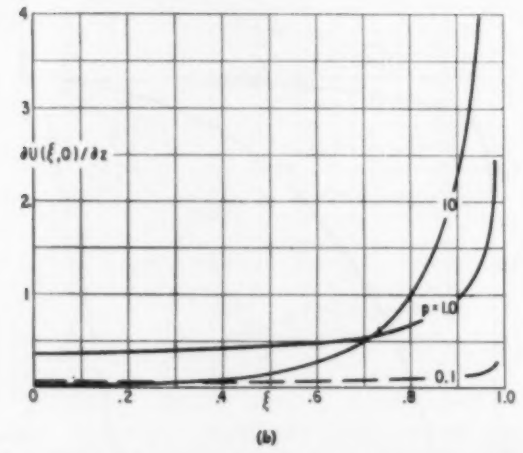

(b)

Fig. 8 Profiles of (a) temperature U; (b) conducted heat flux $\partial U/\partial x$ at cross section $z = 0$ for various speeds p (A-I b.c.)

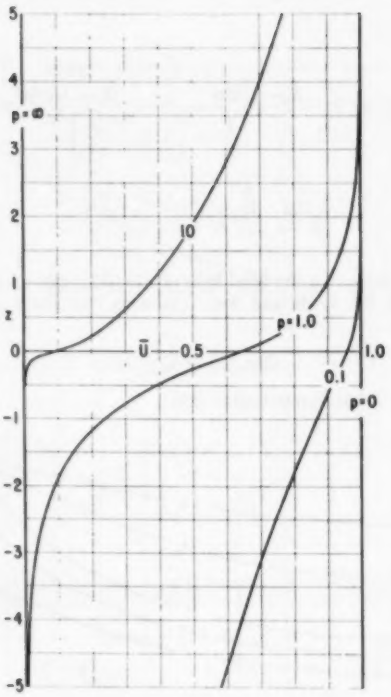

Fig. 9(a)

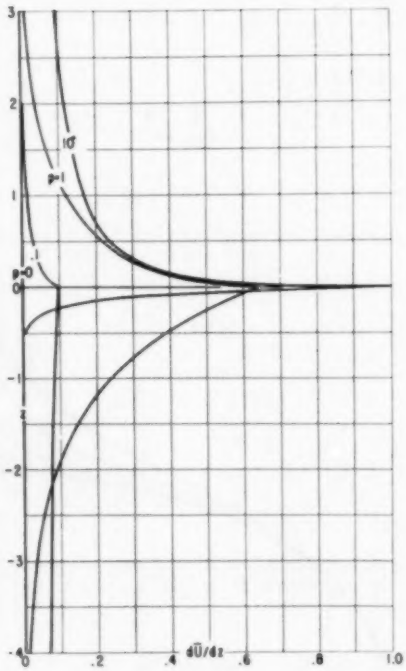

Fig. 9(b)

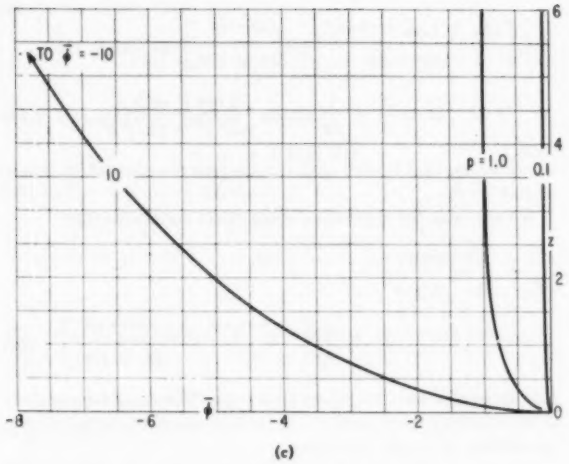

(c)

Fig. 9 Variation of (a) mean temperature $\bar{U}(z)$; (b) mean conducted flux $d\bar{U}/dz$; (c) mean net flux $\bar{\phi}(z) = d\bar{U}/dz - p\bar{U}$ (A-I b.c.)

Solution of Two-Region Problem for Moving Slab When Isothermal-Isothermal Boundary Conditions Are Prescribed[4]

In equation (13) we gave the solution of equation (4) subject to the boundary conditions (9*b*). We arrive at this solution as follows:

We write

$$\psi = e^{-pz/2}U \tag{20a}$$

Then (4) becomes

$$\frac{\partial^2\psi}{\partial\xi^2} + \frac{\partial^2\psi}{\partial z^2} - \frac{p^2}{4}\psi = 0 \tag{20b}$$

subject, in case (9*b*), to the boundary conditions

$$z < 0\colon\ \psi(1, z) = 0, \quad z > 0\colon\ \psi(1, z) = e^{-pz/2} \tag{21a}$$

$$-\infty < z < \infty\colon\ \partial\psi(0, z)/\partial\xi = 0 \tag{21b}$$

Introducing the Fourier transform of ψ,

$$\Psi(\xi) = \int_{-\infty}^{\infty} e^{i\alpha z}\psi(\xi, z)dz \tag{22}$$

and placing this into the transforms of (20*b*), (21), we are led to the differential equation

$$\frac{d^2\Psi}{d\xi^2} - \mu^2\Psi = 0, \quad \mu^2 \equiv \alpha^2 + p^2/4 \tag{23}$$

and the boundary conditions

$$\Psi(1) = \int_0^{\infty} e^{(i\alpha - p/2)z}\,dz = -\frac{1}{i}\,\frac{1}{\alpha + ip/2} \tag{24a}$$

$$d\Psi(0)/d\xi = 0 \tag{24b}$$

Solution of (23) subject to (24) gives

$$\Psi(\xi) = -\frac{1}{i}\,\frac{1}{\alpha + ip/2}\,\frac{\cosh\mu\xi}{\cosh\mu} \tag{25}$$

hence, by the inversion theorem

$$\psi(\xi, z) = -\frac{1}{2\pi i}\int_{-\infty}^{\infty}\frac{e^{-i\alpha z}}{\alpha + ip/2}\,\frac{\cosh\mu\xi}{\cosh\mu}\,d\alpha \tag{26}$$

The integrand has the pole

$$\alpha = -ip/2 \tag{27a}$$

and has simple poles also at the roots

$$\mu = (\alpha^2 + p^2/4)^{1/2} = (n + {}^1/_2)\pi i \tag{27b}$$

$$\alpha_n = -(\mu^2 - p^2/4)^{1/2} = -i\sigma_n/2 \tag{27c}$$

$$\hat{\alpha}_n = +(\mu^2 - p^2/4)^{1/2} = i\sigma_n/2 \tag{27d}$$

$$\sigma_n = [p^2 + (2n + 1)^2\pi^2]^{1/2}, \quad n = 0, 1, 2, \ldots \tag{27e}$$

(in lower and upper half planes) of $\cosh\mu = 0$. By closing the integration path by a semicircle II below the axis for $z > 0$, and by a semicircle I above the axis for $z < 0$ (the path should cross the imaginary axis between poles as in Fig. 11*a*), we assure

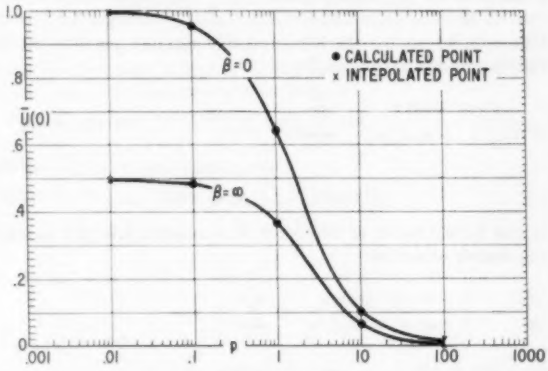

Fig. 10 Dependence of mean temperature $\bar{U}(0)$, at entrance cross section on speed of travel p for I-I ($\beta = \infty$), and A-I ($\beta = 0$) boundary conditions

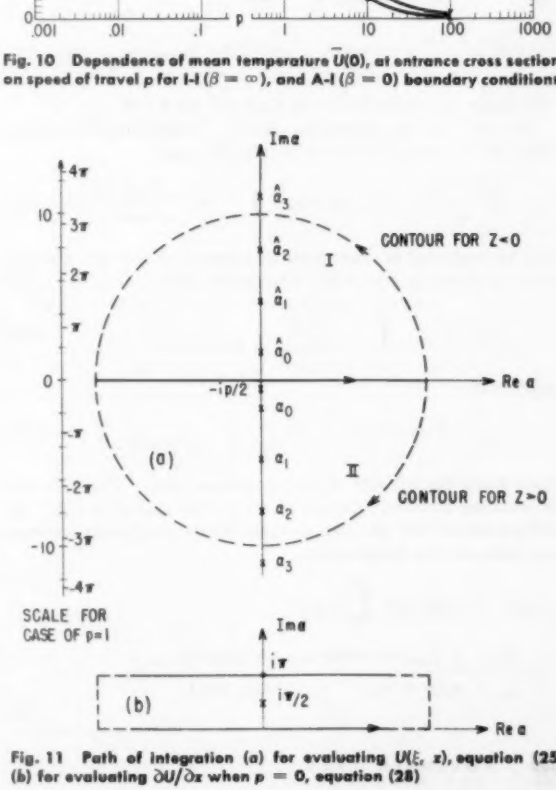

Fig. 11 Path of integration (a) for evaluating $U(\xi, z)$, equation (25); (b) for evaluating $\partial U/\partial x$ when $p = 0$, equation (28)

[4] The method of Rosenthal [4] is also suitable for dealing with this case.

that the semicircles do not contribute to the integral as their radii tend to infinity. Equation (26) then reduces to

$$z > 0:\ \psi = \sum_{\alpha = -ip/2,\ \alpha_0,\ \alpha_1,\ \ldots} \operatorname{Res} \frac{e^{-i\alpha z}}{\alpha + ip/2} \frac{\cosh \mu\xi}{\cosh \mu}$$

$$= e^{-pz/2} + \sum_{\alpha_0,\ \alpha_1,\ \ldots} \frac{\mu_k e^{-i\alpha_k z} \cosh \mu_k \xi}{\alpha_k(\alpha_k + ip/2) \sinh \mu_k}$$

$$= e^{-pz/2} + 2 \sum_0^\infty (-1)^n \frac{(2n+1)\pi}{\sigma_n(p - \sigma_n)} e^{-\sigma_n z/2} \cos (n + 1/2)\pi\xi \tag{28}$$

$$z < 0:\ \psi = -\sum_{\alpha_0,\ \alpha_1,\ \ldots} \operatorname{Res} \frac{e^{-i\alpha z}}{\alpha + ip/2} \frac{\cosh \mu\xi}{\cosh \mu}$$

$$= 2 \sum_0^\infty (-1)^n \frac{(2n+1)\pi}{\sigma_n(p + \sigma_n)} e^{\sigma_n z/2} \cos (n + 1/2)\pi\xi$$

By (20*a*) we may rewrite (28) in the form stated in (13).

Equal in importance to the temperature expression is the expression of the conducted flux $\partial U/\partial z$. The series which we obtain on term-by-term differentiation of (13) diverges for $z = 0$. However, by adding the left-hand side and the negative of the right-hand side of the identity

$$\frac{1}{2} \frac{\cos \xi' \cosh z'}{\cos^2 \xi' + \sinh^2 z'} \equiv \sum_0^\infty (-1)^n e^{-(2n+1)|z'|} \cos (2n+1)\xi' \tag{29a}$$

$$\xi' \equiv \pi\xi/2, \qquad z' \equiv \pi z/2 \tag{29b}$$

to the formal series of $\partial U/\partial z$, it is converted into the rapidly converging expansion

$$\frac{\partial U}{\partial z} = \frac{1}{2} \frac{\cos \xi' \cosh z'}{\cos^2 \xi' + \sinh^2 z'} + \sum_0^\infty (-1)^n$$

$$\times \left[\frac{(2n+1)\pi}{\sigma_n} e^{(p \mp \sigma_n)z/2} - e^{\mp(2n+1)z'} \right] \cos (2n+1)\xi' \tag{30}$$

The upper sign holds for $z > 0$, the lower for $z < 0$.

We arrive at the expression (29*a*) by considering the integral (23) for the special case $p = 0$. In this case

$$\frac{\partial(e^{pz/2}\psi)}{\partial z} \equiv F(\xi, z) = \frac{1}{2\pi} \int_{-\infty}^{\infty} e^{-i\alpha z} \frac{\cosh \alpha\xi}{\cosh \alpha} d\alpha \tag{31}$$

may be evaluated in closed form by integration over the alternate contour shown in Fig 11(*b*). One shows that

$$\int_{-\infty}^{\infty} \frac{e^{m\alpha}\, d\alpha}{\cosh \alpha} = \frac{\pi}{\cos m\pi/2} \tag{32a}$$

and hence

$$F(\xi, \pm z) = 1/2 \operatorname{Re} \frac{1}{\cos (\xi - i|z|)\pi/2} \tag{32b}$$

from which the left side of (29*a*) follows at once. The right side is obtained by differentiation of (13), after placing $p = 0$. By integration of (20), one now also obtains the excellently converging series for the temperature

$$z < 0:\ U = \mathbf{U} + 2 \sum_0^\infty (-1)^n$$

$$\times \left[\frac{(2n+1)\pi e^{(p+\sigma_n)z/2}}{\sigma_n(p + \sigma_n)} - \frac{e^{(2n+1)z'}}{(2n+1)\pi} \right] \cos (2n+1)\xi' \tag{33}$$

$$z > 0:\ U = \mathbf{U} + 2 \sum_0^\infty (-1)^n$$

$$\times \left[\frac{(2n+1)\pi e^{(p-\sigma_n)z/2}}{\sigma_n(p - \sigma_n)} + \frac{e^{(2n+1)z'}}{(2n+1)\pi} \right] \cos (2n+1)\xi'$$

$$\mathbf{U} \equiv \frac{1}{2} + \frac{1}{2\pi} \arctan \frac{2 \cos \xi' \sinh z'}{\cos^2 \xi' - \sinh^2 z'} \tag{34}$$

where we use that branch of the arctangent function which is zero when $z' = 0$.

We also note the expression of the mean conducted flux

$$\frac{d\bar{U}}{dz} = \frac{1}{2\pi} \ln \frac{\cosh z' + 1}{\cosh z' - 1}$$

$$+ 2 \sum_0^\infty \left[\frac{e^{(p \mp \sigma_n)z/2}}{\sigma_n} - \frac{e^{\mp(2n+1)z'}}{(2n+1)\pi} \right] \tag{35}$$

(use upper sign for $z > 0$, lower for $z < 0$). The mean temperature at an arbitrary cross section z is best obtained by term-by-term integration of series (13), since

$$\int_{-\infty}^{z} \ln (\cosh z \pm 1) dz$$

cannot be evaluated in closed form.

Solution of Two-Region Problem for Moving Slab When Adiabatic-Isothermal Boundary Conditions Are Prescribed

In contrast to the "pure" boundary-value problem of the preceding section (where the temperature was prescribed along the entire boundary $\xi = 1$), solution of the "mixed" boundary-value problem (where temperature is prescribed for $z > 0$, temperature gradient for $z < 0$) is intrinsically more difficult. However, the "Wiener-Hopf technique" is available for treating the latter problem, and we now proceed to its use.[5]

The expression

$$e^{-pz/2}U = \psi(\xi, z) = \frac{1}{2\pi} \int_{-\infty}^{\infty} A(\alpha) e^{-i\alpha z} \frac{\cosh \mu\xi}{\cosh \mu} d\alpha \tag{36}$$

is the starting point. We have seen, in establishing (26), that this expression satisfies the differential equation (20*b*) and the boundary condition (5*b*). The problem thus reduces to so determine the function $A(\alpha)$ that also the boundary conditions (12*b*); i.e.,

$$z > 0:\ \psi(1, z) = \frac{1}{2\pi} \int_{-\infty}^{\infty} A(\alpha) e^{-i\alpha z} d\alpha = e^{-pz/2}$$

$$z < 0:\ \frac{\partial \psi(1, z)}{\partial \xi} = \frac{1}{2\pi} \int_{-\infty}^{\infty} A(\alpha) e^{-i\alpha z} \mu \tanh \mu d\alpha = 0 \tag{37a, b}$$

be satisfied. Equations (37*a*, *b*) constitute *dual integral equations* for the unknown function $A(\alpha)$. Completing the integration path to a closed contour by adding an upper half circle for $z < 0$, a lower half circle for $z > 0$, as in Fig. 11(*a*), assuming that $A(\alpha)$ grows more slowly than exponentially as the radii of the half circles expand (this will be verified in (44) and the Appendix), so that the factor $\exp\{-|zIm(\alpha)|\}$ in the integrand of (37*a*, *b*) insures the vanishing of the integrals on the half circles, we conclude from (37*b*) that[6]

[5] The method was first used by J. Schwinger and by E. T. Copson around 1945. For excellent exposition of the method (as well as brief history) see Noble [5], and the résumés in [6, 7, 8].

[6] In our derivation we follow, as model, P. C. Clemmow's presentation [9], of the Sommerfeld diffraction problem. F S U H F ≡ free of singularities in upper half plane; F S L H F ≡ free of singularities in lower half plane.

$$A(\alpha)\ \mu\tanh\mu = \text{F S U H F} \tag{38a}$$

Next we conclude from (37*a*) that

$$A(\alpha) = -\frac{1}{i}\frac{\chi(\alpha)}{\chi(-ip/2)}\frac{1}{\alpha + ip/2} \tag{38b}$$

where the analytic function

$$\chi(\alpha) = \text{F S L H F} \tag{38c}$$

For, in this case (37*a*) becomes

$$-\frac{1}{2\pi i}\int_{-\infty}^{\infty}\frac{\chi(\alpha)}{\chi(-ip/2)}\frac{e^{-i\alpha z}}{\alpha + ip/2}\,d\alpha = \operatorname*{Res}_{-ip/2}\frac{e^{-i\alpha z}}{\alpha + ip/2} = e^{-pz/2} \tag{39}$$

The problem thus reduces to determining $A(\alpha)$ from (38*a*, *b*, *c*). Let

$$B(\alpha) = A(\alpha)\ \mu\tanh\mu, \quad \mu^2 = \alpha^2 + p^2/4 \tag{40}$$

then by (38*b*, *c*)

$$(\alpha + ip/2)A(\alpha) = \frac{\mu\coth\mu}{\alpha - ip/2}B(\alpha) = i\frac{\chi(\alpha)}{\chi(-ip/2)} = \text{F S L H F} \tag{41a}$$

$$B(\alpha) = \text{F S U H F} \tag{41b}$$

If we may write $\mu\coth\mu$ in the form[7]

$$\mu\coth\mu = K_+(\alpha)K_-(\alpha) \tag{42}$$

where K_+ *is free of singularities and zeros in the finite upper half plane,* K_- *is free of singularities and zeros in the finite lower half plane,* then we may conclude that

$$K_+(\alpha)B(\alpha) = \frac{\alpha - ip/2}{K_-(\alpha)}\frac{i\chi(\alpha)}{\chi(-ip/2)} \tag{43}$$

where the left side is free of singularities in the finite upper half plane, the right is free of singularities in the finite lower half plane.[8] Since the two sides are analytic on the common Re α-axis,[9] they are each other's analytic continuation, and define a regular function, say, $J(\alpha)$, in the entire finite α-plane. For large values of $|\alpha|$ in the lower half plane K_- grows as $|\alpha|^{1/2}$, hence the right side of (43) cannot increase faster than $|\alpha|^{1/2}$. This is demonstrated in Noble.[10] By the extended Liouville theorem it follows that the right side of (43) must be a polynomial of degree not exceeding 1/2, i.e., we obtain that J is a constant. By placing $\alpha = -ip/2$ into the right side of (43) we find that this constant is

$$J = \frac{p}{K_-(-ip/2)} \tag{44a}$$

and hence

$$B(\alpha) = \frac{p}{K_-(-ip/2)K_+(\alpha)} \tag{44b, c}$$

$$A(\alpha) = \frac{p\mu\coth\mu}{\mu^2K_-(-ip/2)K_+(\alpha)} = \frac{pK_-(\alpha)}{(\alpha^2 + p^2/4)K_-(-ip/2)}$$

Thus we obtain the result that solution of our problem is

$$U = e^{pz/2}\psi = \frac{pe^{pz/2}}{2\pi K_-(-ip/2)}\int_{-\infty}^{\infty}\frac{K_-(\alpha)e^{-i\alpha z}}{\alpha^2 + p^2/4}\frac{\cosh\mu\xi}{\cosh\mu}\,d\alpha \tag{45a}$$

The factorization (42) of $\mu\coth\mu$ may be found in [5][11] and in [10]. One obtains

$$K_+(-\alpha) = K_-(\alpha) = \Omega(i\alpha) \tag{46a}$$

$$\Omega(\zeta) \equiv \prod_{k=1}^{\infty}\frac{\left[1 + \dfrac{p^2/4}{(k - 1/2)^2\pi^2}\right]^{1/2} + \dfrac{\zeta}{(k - 1/2)\pi}}{\left[1 + \dfrac{p^2/4}{k^2\pi^2}\right]^{1/2} + \dfrac{\zeta}{k\pi}} \tag{46b}$$

and consequently

$$U = \frac{pe^{pz/2}}{2\pi\Omega(p/2)}\int_{-\infty}^{\infty}\frac{\Omega(i\alpha)e^{-i\alpha z}}{\alpha^2 + p^2/4}\frac{\cosh\mu\xi}{\cosh\mu}\,d\alpha \tag{45b}$$

In order to evaluate the integral (45*b*) we complete the contour by a lower semicircle for $z > 0$, and by an upper semicircle for $z < 0$. In the former case we have poles at

$$\alpha = -ip/2 \tag{47a}$$

and at the lower half plane roots

$$\mu = (\alpha^2 + p^2/4)^{1/2} = (n + 1/2)\pi i \tag{47b}$$

of $\cosh\mu = 0$, i.e., at

$$\alpha_n = (\mu^2 - p^2/4)^{1/2} = -i\sigma_n/2, \qquad \sigma_n^2 = p^2 + (2n + 1)^2\pi^2 \tag{47c}$$

Thus, for $z > 0$

$$e^{-pz/2}U = \psi = -\frac{p}{2\pi i}\int\left[\frac{-i\Omega(i\alpha)}{(\alpha^2 + p^2/4)\Omega(p/2)}e^{-i\alpha z}\frac{\cosh\mu\xi}{\cosh\mu}\right]\times d\alpha = p\sum_{-ip/2,\ \alpha_0,\ \alpha_1,\ \ldots}\operatorname{Res}[\ ]$$

$$= e^{-pz/2} + p\sum_{\alpha_0,\ \alpha_1,\ \ldots}\frac{-i\Omega(i\alpha_k)}{\mu_k\alpha_k\Omega(p/2)}e^{-i\alpha_k z}\frac{\cosh\mu_k\xi}{\sinh\mu_k} \tag{48}$$

which yields the result stated in (17*b*).

For $z < 0$ we rewrite (45) on the basis of (42) as

$$\psi = \frac{p}{2\pi K_-(-ip/2)}\int_{-\infty}^{\infty}\frac{e^{-i\alpha z}}{(\alpha^2 + p^2/4)K_+(\alpha)}\frac{\mu\cosh\mu\xi}{\sinh\mu}\,d\alpha \tag{49a}$$

$$= \frac{p}{2\pi i}\int\left[\frac{ie^{-i\alpha z}}{(\alpha^2 + p^2/4)\Omega(p/2)\Omega(-i\alpha)}\frac{\mu\cosh\mu\xi}{\sinh\mu}\right]d\alpha$$

$$= p\sum_{ip/2,\ \alpha_1',\ \alpha_2',\ \ldots}\operatorname{Res}[\ ] \tag{49b}$$

where

$$\alpha_n' = i\sigma_n'/2, \qquad \sigma_n' = (p^2 + 4n^2\pi^2)^{1/2}, \qquad n = 1, 2, \ldots \tag{50a}$$

are the nonzero upper half-plane roots of

$$\sinh\mu = 0,$$

[7] The factors K_+, K_- are given in (46).

[8] Finite half plane = inside of a semicircle (with the center at the origin), having arbitrarily large, but finite, radius R. In other words, we do not place restrictions on K_+, K_- at $R = \infty$, except that they must be there of at most algebraic (rather than exponential) growth; cf. Noble [5].

[9] In fact, they are analytic in the common strip between $\alpha = 0$ and the larger of $-ip/2$, α_0.

[10] Reference [5], p. 130. For convenience we repeat the argument in the first part of the Appendix. This will help explain the behavior of $\partial U/\partial z$ at $(\xi, z) = (1, 0)$, in the last section of the Appendix.

[11] See footnote 10

i.e., of

$$\mu = (\alpha^2 + p^2/4)^{1/2} = n\pi i \tag{50b}$$

We find

$$\psi = \frac{e^{pz/2}}{\Omega^2(p/2)} + \frac{p}{\Omega(p/2)} \sum_{\alpha_1', \ldots} \frac{ie^{-i\alpha z'z}}{\alpha_k'\Omega(-i\alpha_k')} \frac{\cosh \mu_k \xi}{\cosh \mu_k} \tag{51}$$

and the expression stated in (17*a*) follows at once.

Equating, at $z = 0$, the expressions (17*a*), (17*b*), their ξ-integrals (0 to 1), and their z-derivatives, we obtain some interesting nontrivial identities involving the Ω-functions.

Acknowledgment

The author is indebted to Miss M. DaCosta for checking the derivations, programming the calculations for the IBM 650 computer, and plotting the curves for the figures. Thanks also are due to F. VerSnyder for discussing the practical implications of the results.

The author is grateful to the referee for calling attention to the vast literature for Graetz's problem (see e.g., [12, 13, 14] and references therein) and for pointing out that the present solution coincides with the solution of the corresponding Graetz problem (the solid slab is replaced by a liquid slab) when there is slug flow. In view of this connection between the two problems it seems that it would have been preferable to refer to β as Nusselt number.

References

1 G. Horvay, "Some Problems of Continuous Casting," to be submitted shortly to a technical magazine.

2 G. Horvay, "The Effect of Discontinuous Biot Number on the Temperature Distribution in Moving Slabs," Proc. International Heat Transfer Conference, Boulder, Colo., 1961.

3 H. S. Carslaw and J. C. Jaeger, "Conduction of Heat in Solids," Oxford University Press, Oxford, England, 1959.

4 D. Rosenthal, "The Theory of Moving Sources of Heat and Its Application to Metal Treatments," TRANS. ASME, vol. 68, 1946, p. 849.

5 B. Noble, "Methods Based on the Wiener-Hopf Technique," Pergamon Press, New York, N. Y., 1958.

6 P. M. Morse and H. Feshbach, "Methods of Theoretical Physics I, II," McGraw-Hill Book Company, Inc., New York, N. Y., 1953.

7 S. N. Karp, "Wiener-Hopf Techniques and Mixed Boundary-Value Problems," *Communications on Pure and Applied Mathematics*, vol. 3, 1950, p. 411.

8 A. E. Heins, "The Scope and Limitations of the Method of Wiener and Hopf," *Communications on Pure and Applied Mathematics*, vol. 9, 1956, p. 447.

9 M. Born and E. Wolf, "Principles of Optics," Pergamon Press, New York, N. Y., 1959.

10 A. E. Heins, "Water Waves Over a Channel of Finite Depth With a Dock," *American Journal of Mathematics*, vol. 70, 1948, p. 730.

11 H. E. Saltzer, "Method of Summing Slowly Convergent Series," *Journal of Mathematics and Physics*, vol. 33, 1955, p. 356.

12 M. Jakob, "Heat Transfer," John Wiley & Sons, New York, N. Y., vol. 1, 1949, p. 451.

13 J. R. Sellars, M. Tribus, and J. S. Klein, "Heat Transfer to Laminar Flow in a Round Tube or Flat Conduit—The Graetz Problem Extended," TRANS. ASME, vol. 78, 1956, p. 441.

14 P. J. Schneider, "Effect of Axial Conduction on Heat Transfer in the Entrance Regions of Parallel Plates and Tubes," TRANS. ASME, vol. 79, 1957, p. 765.

APPENDIX

Calculation of $\Omega(\zeta)$

Noting the identity (Noble [5] p. 128)

$$\prod_{k=1}^{\infty} \left[1 + \frac{\zeta}{ak + b}\right] e^{-\zeta/ak} \equiv e^{-C\zeta/a} \frac{\Gamma(1 + b/a)}{\Gamma(1 + \{b + \zeta\}/a)} \tag{52}$$

C = Euler's constant = 0.5772 . . . .
we may write $\Omega(\zeta)$ of equation (18) in the form

$$\Omega(\zeta) = \Omega_0(\zeta)\omega(\zeta) \tag{53a}$$

$$\Omega_0(\zeta) = [\Omega(\zeta)]_{p=0} = \prod_1^{\infty} \frac{\left[1 + \dfrac{\zeta}{(k - 1/2)\pi}\right] e^{-\zeta/k\pi}}{\left[1 + \dfrac{\zeta}{k\pi}\right] e^{-\zeta/k\pi}} = \sqrt{\pi}\, \frac{\Gamma(1 + \zeta/\pi)}{\Gamma(1/2 + \zeta/\pi)} \tag{53b}$$

$$\omega(\zeta) = \lim_{K \to \infty} \omega_K(\zeta) \tag{53c}$$

$$\omega_K(\zeta) = \prod_{k=1}^{K} \frac{[p^2 + (2k - 1)^2\pi^2]^{1/2} + 2\zeta}{(2k - 1)\pi + 2\zeta} \cdot \frac{2k\pi + 2\zeta}{[p^2 + 4k^2\pi^2]^{1/2} + 2\zeta} \tag{53d}$$

Thus

$$\omega_K(\sigma_n/2) = \prod_{k=1}^{K} \frac{\sigma_{k-1} + \sigma_n}{(2k - 1)\pi + \sigma_n} \cdot \frac{2k\pi + \sigma_n}{\sigma_k' + \sigma_n}$$

$$\omega_K(\sigma_n'/2) = \prod_{k=1}^{K} \frac{\sigma_{k-1} + \sigma_n'}{(2k - 1)\pi + \sigma_n'} \cdot \frac{2k\pi + \sigma_n'}{\sigma_k' + \sigma_n'} \tag{54}$$

We also note

$$\Omega(p/2) = \Omega(\sigma_0'/2) \tag{55}$$

Since

$$\omega(\zeta) \to 1 \quad \text{as} \quad |\zeta| \to \infty \tag{56}$$

the asymptotic behavior of $\Omega(\zeta)$ for large $|\zeta|$ is governed by the behavior of $\Omega_0(\zeta)$. Using Stirling's formula

$$\Gamma(\zeta) \to (2\pi)^{1/2} e^{-\zeta} \zeta^{\zeta - 1/2} \left[1 + \frac{1}{12\zeta} + \ldots\right] \text{ as } |\zeta| \to \infty, \quad -\pi < \arg \zeta < \pi \tag{57}$$

we obtain

$$\Omega_0(\zeta) \to \sqrt{\pi}\, \frac{e^{-1+\zeta/\pi}}{e^{-1/2+\zeta/\pi}} \frac{(1 + \zeta/\pi)^{1/2+\zeta/\pi}}{(1/2 + \zeta/\pi)^{\zeta/\pi}} \approx \left(\frac{\zeta}{e}\right)^{1/2} \tag{58a}$$

provided

$$-\pi < \arg \zeta < \pi \tag{58b}$$

This proves the statement, after equation (43), about the behavior of $\Omega(i\alpha)$ for large $|\alpha|$, $-\pi \leqslant \arg \alpha = \arg \zeta - \pi/2 \leqslant 0$.

The factors Ω_0, ω of Ω were calculated by formulas (53), (54), on a souped-up model IBM 650, using, in the case of ω_K, $K = 10, 15, 30$ for $p = 10^{-1}, 10^0, 10^1$, respectively[12]; the values obtained were extrapolated to $K = \infty$ by Saltzer's method [11], as discussed in the next section of the Appendix. In Table 1 we tabulate σ_n, σ_n', $\omega(\sigma_n/2)$, $\omega(\sigma_n'/2)$, $\Omega(\sigma_n/2)$, $\Omega(\sigma_n'/2)$ for $p = 10^{-1}, 10^0, 10^1$.

Saltzer's Extrapolation Formula

Let $S_1, S_2, \ldots, S_K$ be partial sums of a converging sequence. Then

$$S_\infty \sim \frac{1}{D} [B_K S_K + B_{K-1} S_{K-1} + B_{K-2} S_{K-2} + B_{K-3} S_{K-3}] \tag{59a}$$

[12] Direct use of formula (18*b*) is unsuitable for calculation of Ω because of poor convergence.

Table 1 Values of σ_n, σ_n', $\omega(\sigma_n/2)$, $\omega(\sigma_n'/2)$, $\Omega(\sigma_n/2)$, $\Omega(\sigma_n'/2)$

(The last digit shown in ω, Ω is uncertain)

n	σ_n	σ_n'	$\omega(\sigma_n/2)$	$\omega(\sigma_n'/2)$	$\Omega(\sigma_n/2)$	$\Omega(\sigma_n'/2)$
			$p = 0.1$			
0	3.14318	0.10000	1.00020	1.00040	1.5714	1.1223
1	9.42531	6.28398	1.00009	1.00013	2.3565	2.0003
2	15.70828	12.56677	1.00006	1.00007	2.9456	2.6670
3	21.99138	18.84982	1.00004	1.00005	3.4361	3.2003
4	28.27451	25.13294	1.00004	1.00004	3.8656	3.6571
5	34.55767	31.41609	1.00003	1.00003	4.2522	4.0635
6	40.84083	37.69924	1.00002	1.00003	4.6066	4.4329
7	47.12400	43.98241	1.00002	1.00003	4.9356	4.7739
8	53.40717	50.26559	1.00002	1.00002	5.2441	5.0921
9	59.69035	56.54876	1.00002	1.00002	5.5354	5.3917
			$p = 1.0$			
0	3.29691	1.00000	1.01842	1.02973	1.6238	1.2411
1	9.47768	6.36227	1.00900	1.01215	2.3830	2.0340
2	15.73976	12.60610	1.00591	1.00714	2.9653	2.6893
3	22.01387	18.87606	1.00440	1.00504	3.4529	3.2180
4	28.29201	25.15263	1.00350	1.00390	3.8803	3.6728
5	34.57199	31.43184	1.00290	1.00317	4.2653	4.0774
6	40.85295	37.71237	1.00248	1.00268	4.6187	4.4457
7	47.13450	43.99367	1.00217	1.00231	4.9470	4.7855
8	53.41644	50.27543	1.00192	1.00204	5.2545	5.1028
9	59.69864	56.55751	1.00173	1.00182	5.5452	5.4018
10	65.98103	62.83981	1.00157	1.00165	5.8218	5.6849
11	72.26355	69.12228	1.00144	1.00150	6.0851	5.9550
12	78.54619	75.40486	1.00132	1.00138	6.3380	6.2132
13	84.82890	81.68753	1.00123	1.00128	6.5811	6.4610
14	91.11168	87.97028	1.00115	1.00119	6.8162	6.6996
			$p = 10$			
0	10.48187	10.00000	1.2982	1.3088	3.200	3.162
1	13.74141	11.81010	1.2419	1.2723	3.445	3.302
2	18.62096	16.05969	1.1887	1.2133	3.783	3.609
3	24.15804	21.33790	1.1511	1.1681	4.132	3.958
4	29.99063	27.04912	1.1249	1.1368	4.471	4.304
5	35.97530	32.96908	1.1060	1.1147	4.794	4.635
6	42.04716	39.00286	1.0919	1.0985	5.101	4.950
7	48.17324	45.10480	1.0811	1.0862	5.393	5.249
8	54.33522	51.25055	1.0724	1.0765	5.671	5.534
9	60.52213	57.42606	1.0655	1.0688	5.938	5.806
10	66.72703	63.62266	1.0597	1.0624	6.193	6.067
11	72.94533	69.83473	1.0548	1.0572	6.439	6.318
12	79.17388	76.05848	1.0507	1.0527	6.677	6.559
13	85.41043	82.29127	1.0472	1.0489	6.907	6.793
14	91.65336	88.53118	1.0441	1.0456	7.129	7.019
15	97.90143	94.77682	1.0414	1.0427	7.345	7.238
16	104.15374	101.02711	1.0390	1.0401	7.555	7.450
17	110.40954	107.28124	1.0368	1.0379	7.758	7.657
18	116.66829	113.53858	1.0349	1.0358	7.958	7.858
19	122.92954	119.79862	1.0332	1.0340	8.152	8.055
20	129.19290	126.06097	1.0316	1.0324	8.342	8.248
21	135.45811	132.32529	1.0302	1.0309	8.528	8.435
22	141.72491	138.59133	1.0289	1.0295	8.709	8.619
23	147.99310	144.85884	1.0277	1.0283	8.887	8.799
24	154.26251	151.12766	1.0266	1.0271	9.062	8.975
25	160.53300	157.39763	1.0256	1.0261	9.234	9.148
26	166.80444	163.66860	1.0246	1.0251	9.401	9.318
27	173.07673	169.94049	1.0237	1.0242	9.566	9.485
28	179.34978	176.21317	1.0229	1.0233	9.729	9.648
29	185.62353	182.48658	1.0222	1.0225	9.890	9.809

where

$$D = 6, \quad B_K = 125, B_{K-1} = -192, B_{K-2} = 81, B_{K-3} = -8 \tag{59b}$$

In preparing the entries for Table 1 we have used $m = 2$, and checked the calculated extrapolations by graphical extrapolation, plotting S_K versus $1/K$, and determining the value of S at the origin $1/K = 0$.

The Heat Flux at (1, 0)

From (49*a*) we obtain

$$\frac{\partial U}{\partial z} = \frac{p}{2\pi\Omega(p/2)} \int_{-\infty}^{\infty} \frac{e^{(-i\alpha+p/2)z}}{(i\alpha + p/2)\Omega(-i\alpha)} \frac{\mu \cosh \mu\xi}{\sinh \mu} d\alpha \tag{60a}$$

For $z = 0$ this reduces to

$$\left[\frac{\partial U}{\partial z}\right]_{z=0} = \frac{p}{2\pi\Omega(p/2)} \int_{-\infty}^{\infty} \frac{1}{(i\alpha + p/2)\Omega(-i\alpha)} \frac{\mu \cosh \mu\xi}{\sinh \mu} d\alpha \tag{60b}$$

From (58), (60) it is seen that when $z = 0$, $\xi \to 1$

$$|\partial U/\partial z| \to \infty \tag{61}$$

because for large α the integrand behaves as $\alpha^{-1/2}$, and

$$\int_{m}^{\alpha>>1} \alpha^{-1/2} d\alpha \sim \alpha^{1/2} \tag{62}$$

On the other hand, on integrating with respect to ξ we obtain a finite value for the total flux through the cross section $z = 0$:

$$\int_0^1 \left[\frac{\partial U}{\partial z}\right]_{z=0} d\xi = \text{finite} \tag{63}$$

because the ξ integration brings about an $\alpha^{-1/2}$ variation of the α-integrand at large α. The same conclusions are reached also by means of (45*b*). Nevertheless, from (17*b*) it follows that

$$[\partial U/\partial z]_{\xi=1,\, z=0+\epsilon} = 0 \quad (\epsilon > 0) \tag{64}$$

Thus we conclude that the temperature gradient $\partial U/\partial z$ jumps from 0 to ∞ as we pass along $\xi = 1$ from the positive z to the negative z-region. (However, the total flux through $z = 0$ remains finite, in contrast to the $\beta = \infty$ case.) As z is further decreased, $\partial U/\partial z$ drops off rapidly. This is illustrated in Fig. 6.

DISCUSSION

G. M. Dusinberre[13]

This paper is an interesting exercise in applied mathematics; unfortunately, it is also an example of a vast structure built on a less-than-vast foundation.

The boundary conditions, which the author states without any explanation or justification, are perfectly tenable—mathematically. But physically, what shall we think about two chambers separated by a wall of zero thickness but of infinite thermal resistance? In view of this, any question of accuracy of the results is largely academic.

Probably there are engineers concerned with this type of problem who would prefer physical accuracy to mathematical elegance. To these the writer would suggest finite-difference solutions, by methods available in the literature. Realistic boundary conditions can be introduced and the third dimension can be handled if necessary. It may be that a few dozen nodes will be needed to define the temperature field with sufficient precision. Then for the steady state one will need a computer program which will solve that number of simultaneous linear algebraic equations. Such programs exist for many computers.

The author might discuss the nature and magnitude of the errors involved in applying his results to any real situation with the physically necessary finite separation of the chambers. He might also, in his forthcoming papers, introduce more realistic boundary conditions.

Author's Closure

With the passing of Professor Dusinberre the heat-transfer field has lost one of its colorful, dedicated, and warmhearted champions, who strongly believed in calling a spade a spade (if to him it looked like a spade). The author hoped to answer the criticism (of which he was forewarned) in kind, but in the light of the events, he shall forego such answer.

[13] Department of Mechanical Engineering, Pennsylvania State University, University Park, Pa. Fellow ASME. Deceased, December 30, 1960.

Thermal Conductivity of Some Commercial Iron-Nickel Alloys

T. W. WATSON
Mechanical Engineer

H. E. ROBINSON
Chief, NBS Heat Transfer Section,
National Bureau of Standards,
U. S. Dept. of Commerce,
Washington, D. C.

Results of laboratory determinations of thermal conductivities in the temperature range −150 to 540 deg C are presented for 12 iron-nickel alloys. Six samples are of low nickel content, in the range from 1 to 9 per cent, and six others have nickel contents in the range from 35 to 80 per cent. A sample of AISI 1015 steel is included for comparative purposes.

The determinations were made on bar specimens about 2.54 cm in diameter and 37 cm long, by an absolute steady-state method with heat flowing longitudinally in the bar. Computation of results from observed data was effected by means of a digital computer.

Introduction

EXPERIMENTAL DATA concerning the thermal conductivity of iron-nickel alloys containing various percentages of nickel have not been comprehensively available in published literature. The information available on iron-nickel alloys is grouped generally in temperature ranges either above or below room temperature. Van Dusen and Shelton [1, 2][1] determined thermal conductivities using a comparative method over the range 100 to 600 deg C on alloys, including some nickels. Powell [3] published some results on nickel and other materials at temperatures from about 50 to 800 deg C. Others [4] have compiled results on many metals and a few nickel alloys for temperatures from a few degrees above absolute zero to about room temperature.

Recognizing the need for values of thermal conductivity embracing a wide band of temperature above and below room temperature, the National Bureau of Standards, in co-operation with the International Nickel Company, made determinations of the thermal conductivity of a number of commercial iron-nickel alloys.

In previous publications, thermal conductivity determinations were made either above or below room temperature with different specimens and by different methods. The measurements by which the data for this paper were obtained cover the entire temperature range from −150 to 540 deg C with the same specimen, using the same method.

This paper presents results of thermal conductivity determinations for 12 iron-nickel alloys in the temperature range −150 to 540 deg C. Six iron-base alloys had nickel contents ranging from 1 to 9 per cent, and six other alloys had nickel contents ranging from 35 to 80 per cent. Results for a sample of AISI 1015 steel are included for comparative purposes.

Samples

Thirteen samples were furnished by the International Nickel Company in the form of bars, from which the cylindrical specimens were machined to a diameter of about 2.54 cm and to the other dimensions given for the specimen in Fig. 1. The materials on which the thermal conductivity determinations were made, together with their principal chemical compositions and heat-treatments, are listed in Table 1. The chemical compositions of the specimens and heat-treatment histories were provided by the International Nickel Company.

Apparatus and Test Method

The test apparatus is shown schematically in Fig. 1. The specimen, a bar 37 cm long and of uniform external dimensions, is supported at the top end concentrically within a stainless-steel guard cylinder, which in turn is held concentrically within a cylindrical outer container. The space between the specimen and the guard cylinder is filled with diatomaceous earth powder insulation, which is also used to insulate the space surrounding the guard. An electrical heater is secured in the hole at the bottom (hot) end, and the supporting trivet at the top (coolant) end provides a liquid-tight connection for circulating a coolant in the top drill-hole.

Temperatures along the specimen were measured by eight thermocouples, as indicated. Thermocouples were similarly located in almost exactly corresponding positions on the guard cylinder. The thermocouples were made from 26-gage calibrated

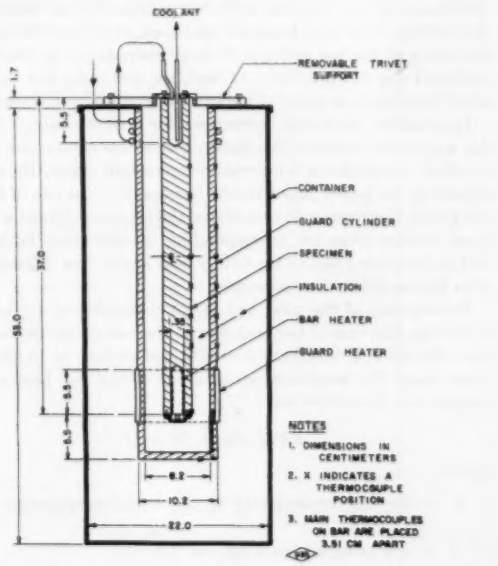

Fig. 1 Apparatus for measuring the thermal conductivity of metals

[1] Numbers in brackets designate References at end of paper.

Contributed by the Heat Transfer Division and presented at the Winter Annual Meeting, New York, N. Y., November 27–December 2, 1960, of THE AMERICAN SOCIETY OF MECHANICAL ENGINEERS. Manuscript received at ASME Headquarters, July 5, 1960. Paper No. 60—WA-47.

Table 1 Principal chemical composition and heat-treatment of materials (supplied by the International Nickel Company)

Specimen	Material	Principal chemical composition (% by weight) Fe %	Ni %	C %	Cr %	Mn %	Si %	Heat-treatment Normalized deg F	Oil quenched deg F	Tempered deg F
1	AISI 1015	99.1		0.15		0.55	0.15	1750		1100
2	1 per cent Ni	97.984	1.04	0.126		0.56	0.27	1700		1100
3	AISI 2315	95.483	3.46	0.16		0.54	0.32	1650		1100
4	AISI 4340(QT)[a]	95.747	1.87	0.40	0.74	0.68	0.28	1600	1500	1100
5	AISI 4340(NT)[a]	95.747	1.87	0.40	0.74	0.68	0.28	1600		1100
6	AISI 2515	94.076	4.91	0.14		0.52	0.33	1600		1100
7	9 per cent Ni	90.29	8.56	0.10		0.77	0.28	1650 + 1450		1050
8	High-perm-49	49.503	49.15	0.035	0.09	0.44	0.54	Packed in powder and annealed in hydrogen 5 hr at 1200 deg F, 5 hr at 2150 deg F, furnace cooled to 800 deg F, cooled in hydrogen		
9	HyMu-80[b]	15.283	79.24	0.049	0.08	0.71	0.19			
10	Low-exp-42	56.303	42.11	0.085	0.09	0.97	0.16	Annealed for 1/2 hr at 1500 deg F, furnace cooled		
11	Invar	63.97	35.41	0.06		0.40	0.13	1/2 hr at 1525 deg F, water quenched, 1 hr at 600 deg F, air cooled, 48 hr at 205 deg F, air cooled		
12	Free cut invar	62.233	35.84	0.08	0.12	0.81	0.34			
13	NI-Span-C[c]	49.332	41.95	0.03	5.31	0.42		After machining at NBS, age hardened for 6 hr in vacuum furnace at 1260 deg F, furnace cooled		

[a] Mo 0.25. [b] Mo 4.20. [c] Al 0.38, Ti 2.51.

chromel and alumel wires, with welded junctions peened into holes 0.11 cm in diameter and 0.17 cm deep.

For a given steady-state longitudinal flow of heat in the specimen, the mean temperatures of the six successive 3.51-cm spans between thermocouples on the specimen decrease from the hotter to the cooler end. The average conductivity of the specimen over each 3.51-cm span was determined from the observed data of a test, which thus yielded six values of thermal conductivity corresponding to six different mean temperatures. The temperature drop across a span ranged from 20 to 90 deg C in different tests.

In principle, if there were no heat exchange between the specimen and its surrounding guard and powder insulation, the six values of conductivity could be determined from the measured electrical power input to the bar heater and the average temperature gradient in each of the six spans along the specimen. In actuality, because of the outward heat losses from the guard and differences in the variation with temperature of the thermal conductivities of the guard and the specimen, exact matching of temperatures of the bar and guard at all corresponding longitudinal positions was not feasible. At best, the specimen was subject to small heat losses or gains at various parts of its convex surface.

In practice, to enable corrections for heat exchanges between bar and guard, a pair of steady-state tests was conducted, in both of which the specimen temperatures were kept closely the same by adjusting the power input to the bar heater. In one of the tests the guard thermocouple just above the heater was kept a few degrees warmer than the corresponding thermocouple on the bar, and in the second test of the pair, it was kept a few degrees cooler than the specimen thermocouple.

In each test of the pair, and at the mid-point of a given span of the bar, the sum of the heat flow in the bar at that point and of the total net heat loss from the bottom of the bar up to that point must equal the measured power input to the bar heater. This relation can be written as

$$kA\Delta t/\Delta x + fS = Q \qquad (1)$$

where

k = the bar conductivity at the mean temperature of the span;
A = the cross-sectional area of the bar;
Δt = the temperature drop from end to end of the span;
Δx = the length of the span;
fS represents the total net heat loss from the bar, from its bottom end to the mid-point of the given span, expressed as the product of S, which is a close approximation of the integral $\int_0^x (t_{bar} - t_{guard})dx$, and an average heat-transfer coefficient f for the thermal path from bar to guard;
Q = the measured power input to the bar heater.

The two tests of a pair differ moderately in the resulting values of Δt, S, and Q, and therefore two equations (1) can be written for each of the six spans of the bar, which can be solved simultaneously to determine k and f. For this to be strictly valid, k and f must have equal values in the two equations. Since the mean temperatures of the span in the two tests will in general differ slightly, and the conductivity of the bar may vary with temperature, a slight adjustment is made to the observed values of Δt so that k corresponds to the mean of the span mean temperatures in the two tests. The equality of f in the two tests is not so readily assured, but because the magnitude of fS in these tests was generally on the order of 5 per cent of Q, a moderate difference in the values of f in the two equations would affect the solved value of $Ak/\Delta x$ only slightly.

The computation of results directly from the observed data was effected by an IBM 704 digital computer suitably programmed to compute the thermal conductivity and the corresponding mean temperature for each of the six spans. The computer was used to fit a third-power equation to the thermal conductivity and temperature results, by the method of least squares.

Discussion of Results

The results of the thermal conductivity determinations are shown in Figs. 2 to 6, inclusive, and Table 2.

A typical example of data obtained in the complete testing of a specimen is shown in Fig. 2. The 30 individual values of thermal conductivity plotted represent five sets of tests, each with values for the six consecutive spans, as indicated by the different symbols. The solid line represents the trinomial fitting the data as determined by the computer. The triangles and circles represent the results from two sets of tests in the range −150 to 210 deg C, with different heat inputs to the specimen and using liquid nitrogen as the coolant. The squares (one light and one dark) and inverted triangles likewise show results from 100 to 540 deg C for three sets of tests, using different heat inputs with 40 deg C water as coolant. The five sets of tests overlap, with agreement of results within the limits of the scattering shown. The extreme departure of the data from the smooth curve is less than 1.5 per

Table 2 Results of thermal conductivity determinations of some commercial iron-nickel alloys

Material	Thermal conductivity w/cm deg C[a]								
	−150 deg C	−100 deg C	0 deg C	100 deg C	200 deg C	300 deg C	400 deg C	500 deg C	540 deg C
AISI 1015	0.467	0.493	0.520	0.519	0.499	0.466	0.430	0.396	0.386
1 per cent Ni	0.375	0.408	0.452	0.468	0.461	0.441	0.412	0.382	0.371
AISI 4340 NT	0.262	0.296	0.344	0.369	0.377	0.372	0.359	0.345	0.340
AISI 4340 QT	0.275	0.307	0.354	0.379	0.386	0.380	0.366	0.348	0.341
AISI 2315	0.271	0.307	0.360	0.388	0.397	0.392	0.378	0.359	0.351
AISI 2515	0.244	0.281	0.335	0.367	0.379	0.378	0.367	0.350	0.343
9 per cent Ni	0.196	0.231	0.284	0.319	0.336	0.341	0.336	0.324	0.318
Invar	0.093	0.109	0.134	0.154	0.171	0.186	0.201	0.216	0.223
Free cut invar	0.089	0.104	0.129	0.150	0.167	0.182	0.197	0.211	0.217
Low-exp-42	0.120	0.136	0.159	0.175	0.184	0.191	0.199	0.212	0.218
High-perm-49	0.158	0.173	0.194	0.205	0.210	0.211	0.213	0.218	0.222
NI-Span-C	0.076	0.091	0.116	0.137	0.154	0.170	0.184	0.198	0.204
HyMu-80	0.153	0.167	0.189	0.208	0.222	0.234	0.245	0.255	0.260

[a] $1 \frac{\text{watt}}{\text{cm deg C}} = 603.3 \frac{\text{Btu} - \text{in.}}{\text{hr ft}^2 \text{ deg F}} = 0.2390 \frac{\text{cal} - \text{cm}}{\text{sec cm}^2 \text{ deg C}}$

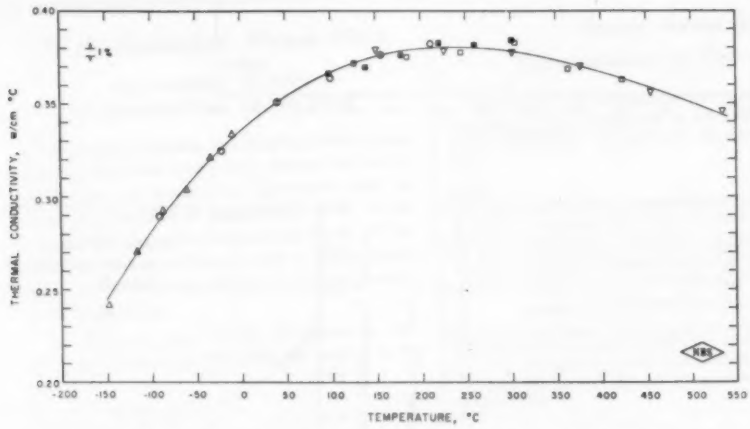

Fig. 2 A typical example of thermal conductivity determinations made on one bar specimen (AISI 2515). Symbols represent five sets of test, each with values for six consecutive spans.

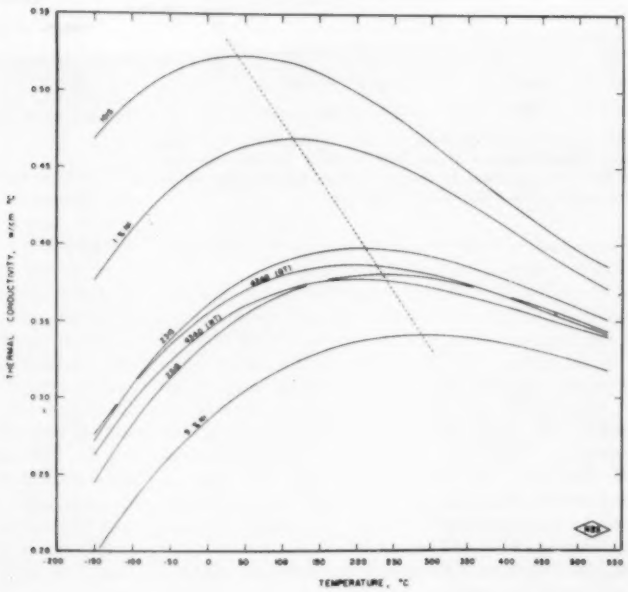

Fig. 3 Thermal conductivity of iron-nickel alloys and one steel

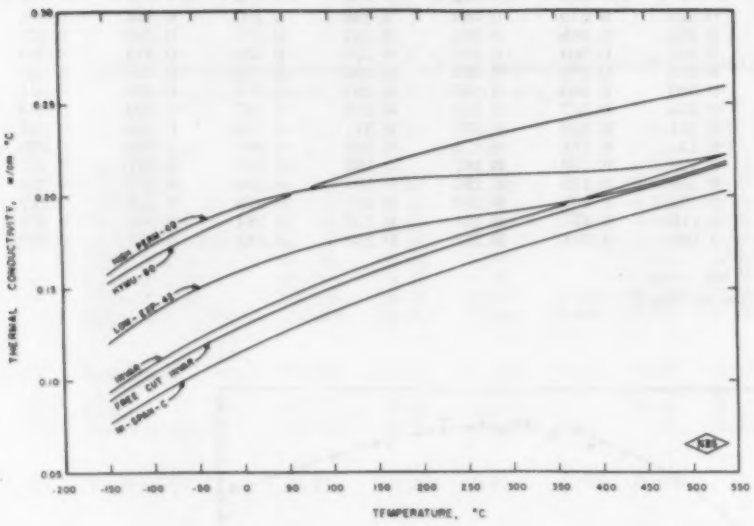

Fig. 4 Thermal conductivity of high-nickel alloys with nickel contents ranging from about 35 to 80 per cent

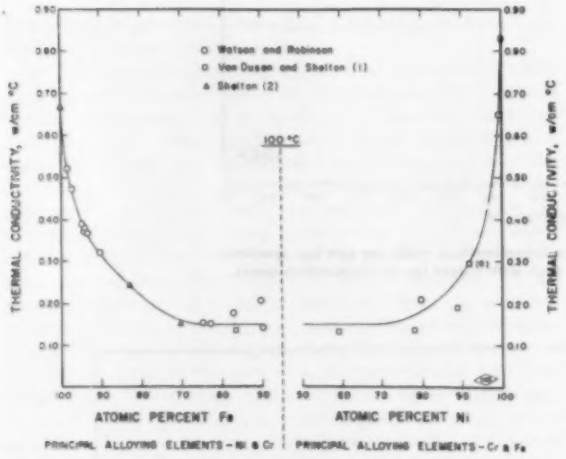
Watson and Robinson
Van Dusen and Shelton (1)
Shelton (2)
100 °C
THERMAL CONDUCTIVITY, w/cm °C
ATOMIC PERCENT Fe
ATOMIC PERCENT Ni
PRINCIPAL ALLOYING ELEMENTS - Ni & Cr
PRINCIPAL ALLOYING ELEMENTS - Cr & Fe

Fig. 5 Correlation of thermal conductivity data at 100 deg C, including some previous National Bureau of Standards results. (a) Does not contain Cr or Fe, but is included for information (nominal composition: Ni 95 per cent, Al 2 per cent, Mn 2 per cent, Si 1 per cent).

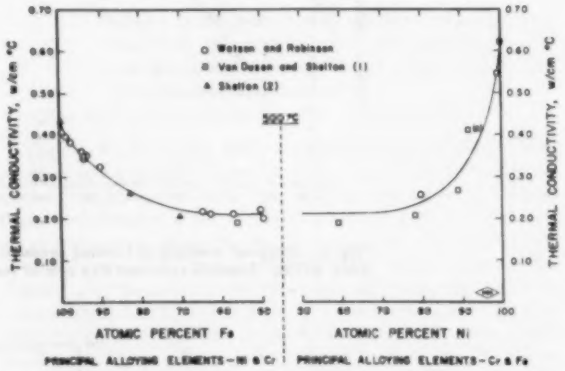
Watson and Robinson
Van Dusen and Shelton (1)
Shelton (2)
500 °C
THERMAL CONDUCTIVITY, w/cm °C
ATOMIC PERCENT Fe
ATOMIC PERCENT Ni
PRINCIPAL ALLOYING ELEMENTS - Ni & Cr
PRINCIPAL ALLOYING ELEMENTS - Cr & Fe

Fig. 6 Correlation of thermal conductivity data at 500 deg C, including some previous National Bureau of Standards results. (a) Does not contain Cr or Fe, but is included for information (nominal composition: Ni 95 per cent, Al 2 per cent, Mn 2 per cent, Si 1 per cent).

cent. The magnitude of 1 per cent departure at 0.38 w/cm deg C is indicated by arrows near the top left of the graph.

Fig. 3 shows the results of thermal conductivity determinations for seven specimens, as follows: One 1015 steel and six iron-nickel alloys with varying percentages of nickel up to approximately 9 per cent. In this range of nickel content, the thermal conductivity tends to decrease with the increase in nickel content. In this respect, the 4340 (QT) and (NT) specimens (1.87 per cent Ni) were exceptions. These specimens had 0.4 per cent carbon, 0.74 per cent chromium, and 0.25 per cent molybdenum, which influenced the thermal conductivity. In addition, the effect on thermal conductivity of oil-quenching the 4340 (QT) bar specimen is shown by its approximately 2.4 per cent greater conductivity than that of the 4340 (NT) specimen.

In general, the differences in thermal conductivity values of the seven bar specimens are greatest at low temperatures, with differences gradually becoming smaller as the temperature increases, and there is a trend that suggests possible convergence of the values within a small region at some higher temperature. The seven curves have positive slopes from −150 deg C up to a temperature at which a maximum value of thermal conductivity occurs and negative slopes from the point of maximum conductivity to 540 deg C. These trends were also indicated in work reported by other investigators [2, 3, 4]. The dotted line drawn across the curves shows that the maximum conductivities of these alloys are nearly linear with the temperatures at which they occur, except for the two 4340 specimens.

The thermal conductivities of the six high-nickel alloys in Fig. 4 differ from those of the iron-nickel alloys in that the conductivities increase with temperature over the entire range −150 to 540 deg C. The conductivities of the high-nickel alloys are markedly lower than those of the iron-nickel alloys shown in Fig. 3, but the trend suggests that they approach values similar to those for the iron-nickel alloys at a higher temperature, about 1000 deg C.

Figs. 5 and 6 show at 100 and 500 deg C, respectively, a correlation of these data determined by an absolute method with the results of Van Dusen and Shelton [1, 2] obtained by a comparative method. The scatter of some of the points is probably due to unknown minor elements present (Van Dusen and Shelton

for the most part reported only nominal compositions) and/or to the effects of heat-treatment on the lattice structure. Certain trends are evident. The thermal conductivities decrease as the atomic per cents of the base metals (iron or nickel) decrease to an atomic per cent of about 70. At this point, the thermal conductivity becomes relatively constant with a further decrease in atomic per cent. The minimum values of thermal conductivity at 100 and 500 deg C are approximately the same as those obtained recently on 316 and 347 stainless steels at the National Bureau of Standards with the same apparatus. The minimum value of thermal conductivity of the iron-base alloys at 100 deg C is about one fourth and at 500 deg C is about one half of the value for iron. In the case of the nickel-base alloys, the minimum value of thermal conductivity at 100 deg C is about one sixth and at 500 deg C is about one third of the value for nickel.

The results presented indicate that further research may be desirable, using specimens of known compositions with known and varied heat-treatment histories, and it is particularly desirable to extend the temperature range to 1000 deg C or higher. For more complete correlation, as predicted by the Wiedemann-Franz-Lorenz ratio, the electrical resistivity of the same specimens should also be measured over a wide temperature range.

References

1 M. S. Van Dusen and S. M. Shelton, "Apparatus for Measuring Thermal Conductivity of Metals up to 600 C," *J. Research NBS*, vol. 12, no. 4 (April, 1934) RP 668.

2 S. M. Shelton, "Thermal Conductivity of Some Irons and Steels Over the Temperature Range 100 to 500 C," *J. Research NBS*, vol. 12, no. 4 (April, 1934) RP 669.

3 R. W. Powell, "Thermal Conductivities of Solid Materials at High Temperatures," Research, Butterworth's Scientific Publications, London, England, vol. 7, no. 12 (1954).

4 R. L. Powell and W. A. Blanpied, "Thermal Conductivity of Metals and Alloys at Low Temperatures," NBS Circular 556 (1954).

DISCUSSION

D. L. McElroy[2]

Accurate experimental measurements of thermal conductivity over an extended temperature range by an absolute method are elusive to obtain, but are sorely needed in current heat-transfer engineering. This paper presents useful and precise information on practical engineering materials and has revealed a number of interesting trends among the alloys studied. This method shows promise as being simple and does yield high precision values. This reader believes that it is important that a statement regarding the accuracy of this equipment be made by the authors. The following four points should be expanded.

1 It is not too surprising that this absolute method, as do most other absolute methods, though seldom recognized by nonexperimentalists in thermal conductivity measurements, requires a correction for heat losses. The authors' attention to this appears to be quite acceptable in view of the resulting precision obtained. However, inclusion of examples of the moderate differences in the values of f obtained would aid in substantiating their analysis.

2 The difference in thermal conductivities for two heat-treatments of AISI 4340 certainly warrants inclusion of the microstructures of these two specimens. This would be worth while for all of the specimens since the variations in thermal history can change their microstructures, the phases present, and their distribution, all of which could affect the thermal conductivity values obtained. Because of the precision obtained in this work, it certainly will be referenced by future workers; and this inclusion would greatly assist meaningful intercomparisons.

[2] Oak Ridge National Laboratory, Oak Ridge, Tenn. (Operated by Union Carbide Nuclear Company for the U. S. Atomic Energy Commission.)

3 The inclusion of the tabulated temperature dependence of the thermal conductivity of the specimens is helpful. It would seem of equal importance to complete this table with the trinomial equations used in the figures.

4 It may be beyond the scope of the present paper, but further research is certainly desirable to obtain the cause-effect relations observed among these specimens, although such diagnostic studies might be more suited to simpler alloys. Some of the trends observed in these alloys are certainly more complex than simple compositional effects. For example, this reader fails to obtain a "nearly linear" relation between the maximum thermal conductivity values and nickel content for the iron-rich alloys, indicating that this is not a simple relation.

J. W. Sands[3]

The thermal conductivity data which Watson and Robinson have developed in such an exemplary manner will be most helpful in plugging some of the numerous voids in our information. This is particularly true with respect to what the authors call high nickel alloys, but which we refer to as iron-nickel alloys. We have been depending on values published by Ingersoll in 1920. For some time we have felt that these values were much too low, and here our suspicions are confirmed. We are very glad to be now in possession of reliable data.

The anomalous behavior of the 42 per cent and 49 per cent nickel alloys as indicated in the authors' Fig. 4 is undoubtedly associated with the magnetic transformation, or Curie point. In pure nickel the effect is so pronounced that the slope of the curve reverses sign at the Curie temperature. In the authors' Fig. 6, based on 500 C, the 42 per cent nickel alloy is back in line as this temperature is well above its Curie point. The 49 per cent nickel alloy is almost lined up, as its Curie temperature is just about 500 C.

Much thermal conductivity work has been carried out at the National Physical Laboratory in England. In Fig. 7 the writer has compared their results on two steels with those the authors have obtained on similar compositions. Considering that the steels were manufactured in two different countries, it would appear that the correlation is amazingly good. This should serve to impart confidence in the conductivity data of both the great national laboratories.

The authors suggest that the values for the two groups of alloys studied are tending to merge at a temperature estimated to be about 1000 C. The NPL work indicates that this is a fact. Their tests were made on eight carbon steels, eight low alloy steels, and six high alloy steels, including 18-8 stainless, straight

[3] Development and Research Division, The International Nickel Company, Inc., New York, N. Y.

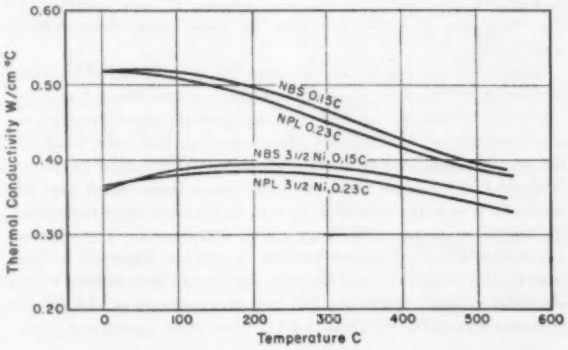

Fig. 7 Thermal conductivity determinations of steels at the National Bureau of Standards, and at the National Physical Laboratory, England

chromium stainless, 28 per cent nickel, Hadfield manganese, and even high-speed tool steel. At 1000 C they had all merged at a value of about 0.265 watt/cm deg C.

The authors have shown a 2.4 per cent greater conductivity for the quenched 4340 over the normalized 4340, both being tempered at 1100 F. R. W. Powell of the NPL has shown in two papers in the *Journal of the Iron and Steel Institute* that conductivity in the as-quenched condition is 20 to 50 per cent less than the value in the unhardened state. However, conductivity increases with tempering temperature. Maximum conductivity is achieved by tempering about 100 deg C below the critical.

Bibliography

5 "Physical Constants of Some Commercial Steels at Elevated Temperatures," edited by the British Iron and Steel Research Association, Butterworths, London, 1953.

6 R. W. Powell, "The Effect of Quenching on the Thermal Conductivities and Electrical Resistivities of Steel," *Journal of the Iron and Steel Institute*, vol. 184, 1956, p. 6.

7 R. W. Powell and R. P. Tye, "The Effect of Oil Quenching and Tempering on the Thermal Conductivities and Electrical Resistivities of Three Steels," *Journal of the Iron and Steel Institute*, vol. 184, 1956, p. 10.

8 L. H. Ingersoll, "Some Physical Properties of Nickel-Iron Alloys," *Physical Review*, series 2, vol. 16, 1920, p. 126.

Authors' Closure

The discussions by Messrs. McElroy and Sands are appreciated.

In regard to the accuracy of the results, the use of successive spans on the specimen largely compensated for random inaccuracies in specimen thermocouple position and calibration, since the data were reduced to a smoothed curve. Specimen heater power measurements were made with considerable exactness; agreement of results using different heaters indicated that the heater potential-drop connections were properly placed. The effect of heat conduction in thermocouple and other wires connected to the specimen was made as small as feasible by taking the wires radially from the specimen to near the guard and thence longitudinally to the top of the apparatus in close proximity to the inner diameter of the guard. The observed test data were accepted only for test periods in which no significant temperature in the system changed more than 0.1 deg C in an hour.

The method of simultaneous solution appears to compensate quite closely for radial interchanges of heat between the bar and the guard, as indicated by agreement of results for the cooler spans in one test with those for the hotter spans in other tests where the mean temperatures overlap. It is less certain that the method of simultaneous solution accounts for that fraction of the longitudinal flow of heat in the powder insulation surrounding the bar which originates from, or goes to, the specimen.

Efforts have been made to evaluate this effect, both experimentally and by mathematical analysis, which we plan to describe in a more detailed publication on the method. The evaluations indicated that this effect may cause the conductivities obtained to be high by from zero to 0.003 watt/cm deg C; our judgment is that they are probably not high by more than about 0.0015 watt/cm deg C.

Some confirmation of this estimate has been obtained by comparison of results with those obtained in a quite different apparatus of the (absolute) cut-bar type designed for measurements on small cylindrical specimens. Measurements had been made in the present apparatus on a metal of conductivity similar to that of Ni-Span-C; a sample from the same piece from which the bar specimen was taken was measured in the cut-bar apparatus over the common temperature range 120 to 600 deg C. The six conductivities obtained in the cut-bar apparatus departed by less than 0.0025 watt/cm deg C from the values of the smoothed curve obtained in this apparatus; the root-mean-square of the six departures was 0.001 watt/cm deg C. The close agreement of the results of the two absolute methods of measurement does not render impossible approximately equal systematic errors in both, but does give support to the estimate made in the foregoing.

Table 3 Coefficients of the equations[a] for thermal conductivity

$$k = A_0 + A_1\left(\frac{t}{1000}\right) + A_2\left(\frac{t}{1000}\right)^2 + A_3\left(\frac{t}{1000}\right)^3$$

Specimen	A_0	A_1	A_2	A_3
AISI 1015	0.5202	0.1174	−1.3796	1.2975
1 per cent Ni	0.4524	0.2827	−1.3958	1.0958
AISI 2315	0.3597	0.3973	−1.2130	0.8291
AISI 4340(QT)	0.3542	0.3572	−1.1459	0.8152
AISI 4340(NT)	0.3441	0.3577	−1.1467	0.8697
AISI 2515	0.3353	0.4203	−1.1545	0.7479
9 per cent Ni	0.2846	0.4343	−0.9880	0.5518
High-perm-49	0.1938	0.1543	−0.4928	0.5638
HyMu-80	0.1896	0.2044	−0.2412	0.1915
Low-exp-42	0.1598	0.1879	−0.4418	0.5487
Invar	0.1340	0.2256	−0.2450	0.2455
Free cut invar	0.1288	0.2268	−0.2161	0.1804
Ni-Span-C	0.1156	0.2278	−0.1979	0.1437

[a] k, w/cm deg C; $-150 < t < 540$, deg C.

In connection with the four points mentioned by Mr. McElroy in his discussion, the following may be of interest.

1 The simultaneous solution of the equations (1) yields, of course, only one (average) value of f for each span considered. The value of f for a given span was found to depend on the average insulation temperature up to that span, increasing with increasing temperature. For the whole series of tests (all spans and temperatures), the values of f obtained ranged between 0.0009 and 0.0036 watt/cm C. The effect of two moderately different values of f in the two tests of a pair, and their influence on the solved value of $Ak/\Delta x$, can be ascertained by trial solutions of the pair of equations (1). For two values of f, differing by 10 per cent from their average, the effect on $Ak/\Delta x$ is less than 0.5 per cent, if $f_{ave}S$ is not greater than about 5 per cent of Q, as was the case in these tests.

2 Measurements were made of the Rockwell C hardness of the AISI 4340 specimens after the tests, at the centers of the hottest and coolest test spans. For the NT specimen, the values were 27 and 28, respectively; for the QT specimen, 34 at both spans. Microstructure determinations have not yet been made, because the specimens are being kept intact for electrical conductivity measurements over the whole temperature range, which we are not in a position to make at this time. However, the electrical conductivity at 27 deg C was measured, with an accuracy estimated as within 0.5 per cent, yielding the values tabulated in the following.

Specimen	Temp (T) deg K	Th Cond (k) w/cm C	Elec Cond (σ) 1/ohm cm	Lorentz No. ($k/\sigma T$) (volt/deg K)^2
4340 NT	300	0.353	3.46×10^4	34.0×10^{-9}
4340 QT	300	0.363	3.62×10^4	33.4×10^{-9}

The hardness measurements indicate that there was no confusion of the specimens, while the electrical conductivity measurements support the finding of a greater thermal conductivity for the quenched specimen than for the normalized specimen at 27 C.

3 Table 3 gives the coefficients of the trinomial equations fitted to the test data points by the method of least squares, from which the smoothed values of conductivity in Table 2 were obtained.

4 Diagnostic examination of the thermal conductivity trends of these alloys is unquestionably of interest, as Mr. Sands has also pointed out in his discussion. It is hoped we will be able to pursue this matter further, for these and possibly other and simpler compositions. It is encouraging that these limited data may be useful also for possibly fruitful diagnostic inquiries.

Transient Temperature in a Melting Solid

J. E. SUNDERLAND[1]
Assistant Professor of Mechanical Engineering, Northwestern University, Evanston, Ill., Assoc. Mem. ASME

R. J. GROSH
Professor of Mechanical Engineering, Purdue University, Lafayette, Ind., Assoc. Mem. ASME

A method of analysis is given for determining the temperature distribution in a semi-infinite, homogeneous solid initially at a constant temperature and then suddenly heated by convection so that a phase change occurs and the new phase is removed upon formation. The method appears applicable to problems involving melting, freezing, or sublimation and to situations where the environment temperature and heat-transfer coefficient vary with time. It consists of calculating the temperature before the phase change occurs, during the transient process of phase change, and after steady-state conditions are obtained if such is possible. During the transient process, a numerical or graphical method of solution may be used which is an extension of the Binder [1][2] method. Numerical results obtained with a digital computer are given for the case where the environment temperature and coefficient of heat transfer are constant and provide a method for determining the velocity and position of the moving phase front.

Introduction

TRANSIENT heat-conduction problems involving phase changes are of considerable importance. They occur during the aerodynamic heating of high-speed vehicles, nuclear-reactor operation, welding, food processing, and boiling, to mention a few specific instances. Unfortunately, the problems are nonlinear and therefore are of considerable difficulty. General solutions, such as are known for problems without latent heat effects [2], are unknown.

Few investigations have been carried out concerning the problem of transient temperature distribution in a melting solid where the melt is removed upon formation. The temperature during the initial stages of heat transfer when no phase change occurs can be readily calculated, by comparison, from results of a fairly general nature [1, 2]. Landau [3] and Masters [4] have considered the problem after this initial stage when very large heat transfer occurs at the exposed surface. That is, for instance, when the environment temperature is much different from the surface temperature and the coefficient of heat transfer is nearly constant so that the surface heat flux is constant. The results of both Landau and Masters were obtained by the numerical solution of partial differential equations. Citron [5] developed a numerical solution for an infinitely wide slab insulated on one side and exposed to a varying heat input on the other side. Murray and Landis [6] made a study of numerical and machine solutions. Sutton [7] and Roberts [8] studied the effect of the viscous melt, continuously removed, on the melting rate of a solid. Otis [9] and Neel and Von Glahn [10, 11] have developed analog circuits for studying such problems, and Goodman [12] has developed an approximate technique, which is analogous to that used in boundary-layer theory, for determining the position of the melting front. A survey of other results can be found elsewhere [13].

[1] Formerly, Instructor, School of Mechanical Engineering, Purdue University, Lafayette, Ind.

[2] Numbers in brackets designate References at end of paper.

Contributed by the Heat Transfer Division and presented at the Winter Annual Meeting, New York, N. Y., November 27–December 2, 1960, of THE AMERICAN SOCIETY OF MECHANICAL ENGINEERS. Manuscript received at ASME Headquarters, September 9, 1960. Paper No. 60—WA-277.

Nomenclature

c = specific heat, Btu/lb deg F

$D/Dt = \frac{\partial}{\partial t} + u\frac{\partial}{\partial x} + v\frac{\partial}{\partial y} + w\frac{\partial}{\partial z}$, substantial derivative

$\mathrm{erf}(x) = \frac{2}{\pi^{1/2}}\int_0^x e^{-t^2}dt$, Gauss's error integral

$\mathrm{erfc}(x) = 1 - \mathrm{erf}(x)$, complement of error integral

$\exp(x) = e^x$

h = film coefficient of heat transfer, Btu/hr sq ft deg F

i = 1, 2, 3, . . . integer representing position

j = 1, 2, 3, . . . integer representing time

k = thermal conductivity, Btu/hr ft deg F

$K = \frac{T_e - T_m}{T_m - T_i}$, dimensionless temperature excess

L = latent heat, Btu/lb

$M = \frac{h(T_e - T_m)}{L\rho}\left(\frac{t_m}{\alpha}\right)^{1/2}$, dimensionless boundary condition

$N = h\left(\frac{t_m}{k\rho c}\right)^{1/2}$, dimensionless melting initiation time

q'' = heat input per unit area, Btu/hr sq ft

q''' = heat generation per unit volume, Btu/hr cu ft

t = time, hr

t_m = time for surface to reach melting temperature, hr

T = temperature, deg F

T_e = environment temperature, deg F

T_i = initial temperature of solid deg F

T_m = melting temperature of solid, deg F

u = velocity in x-direction, fph

v = velocity in y-direction, fph

w = velocity z-direction, fph

x, y, z = Cartesian co-ordinates, ft

α = thermal diffusivity, sq ft/hr

Δ = increment of independent variable

$\theta = \frac{T - T_i}{T_m - T_i}$, dimensionless temperature

$\mu = \frac{uL\rho}{h(T_e - T_m)}$, dimensionless velocity

μ_∞ = dimensionless steady-state velocity

$\xi = \frac{x}{(\alpha t_m)^{1/2}}$, dimensionless distance

ρ = density, lb pcf

$\tau = t/t_m$, dimensionless time after melting begins

In this paper, methods are described for calculating the temperature distribution in a semi-infinite, homogeneous solid initially at constant temperature. It was assumed that the solid was suddenly heated by convection so that eventually a phase change occurred and the new phase was removed upon formation. Thermal properties were assumed constant and, for the major part of the analysis, the environment temperature and heat-transfer coefficient were also considered constant; however, a method of solution is described for the case where the latter quantities vary with time. Only phase changes of the first order were considered. Second-order phase changes and changes that occur over a range of temperature, such as for instance in the case of alloys, were not considered.

Fundamental Equations

The partial differential equation for heat conduction in a moving isotropic solid with heat generation and variable thermal properties can be written as

$$\rho c \frac{DT}{Dt} = \nabla \cdot (k \nabla T) + q'''(x, y, z, t) \tag{1}$$

The co-ordinate system for this problem was assumed to be arranged so that the origin of the x-axis coincided with the phase front and the semi-infinite solid filled the positive half of the x-axis as shown in Fig. 1. It was further assumed in order to simplify the equation that: (a) The transient heat conduction was one dimensional; (b) the heat generation per unit volume was negligible; (c) the thermal properties were constant; (d) a first-order phase change occurred at the temperature T_m, (e) the solid was at a uniform initial temperature; and (f) convective heating (or cooling) with constant environment temperature and coefficient of heat transfer took place at the accessible face. Thus equation (1) could be written as

$$\frac{\partial T}{\partial t} + u(t) \frac{\partial T}{\partial x} = \alpha \frac{\partial^2 T}{\partial x^2} \tag{2}$$

and the initial and boundary conditions were

$$T(x, 0) = T_i \tag{3}$$

$$T(\infty, t) = T_i \tag{4}$$

$$-k \frac{\partial}{\partial x} T(0, t) = h[T_e - T(0, t)]; \; t < t_m \tag{5}$$

$$T(0, t) = T_m; \; t \geq t_m \tag{6}$$

where t_m was the time required for initiation of the phase change after the start of heating. An additional condition was required to obtain the speed with which the phase front moved; this was furnished by an energy balance at the phase front

$$-k \frac{\partial}{\partial x} T(0, t) + \rho L u(t) = h(T_e - T_m) \tag{7}$$

for $t \geq t_m$. After the phase change took place, equation (7) was used instead of the boundary condition expressed by equation (5). The speed with which the phase front moved when viewed from the solid was $u(t)$; for problems involving melting, $u(t)$ and the latent heat of transformation were negative.

A general solution of equations (2) through (7) could not be obtained and therefore numerical methods were used for part of the analysis. To facilitate the solution, the calculation of temperature was divided into three parts to obtain:

1 The temperature distribution before the phase change occurred.

2 The transient temperature distribution while the phase change occurred.

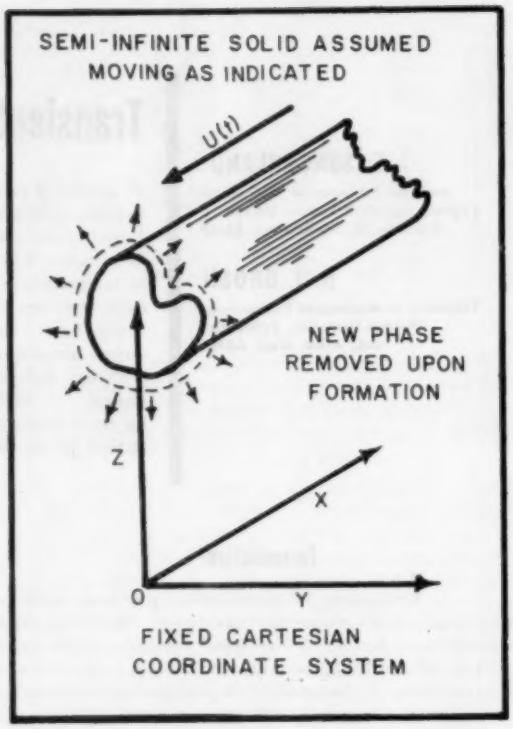

Fig. 1 Co-ordinate system

3 The steady-state temperature distribution with phase change if such were possible.

Temperature Before the Phase Change Occurs

This problem was one of finding the temperature distribution in a semi-infinite solid due to a sudden change in environment temperature. The solution is well known [14] and has been put into graphical form for easy reference [15]. The analytical solution is

$$\frac{T - T_i}{T_e - T_i} = \operatorname{erfc}\left[\frac{x}{2(\alpha t)^{1/2}}\right] - \exp\left[\frac{hx}{k} + \frac{h^2}{k^2} \alpha t\right] \operatorname{erfc}\left[\frac{x}{2(\alpha t)^{1/2}} + \frac{h}{k} (\alpha t)^{1/2}\right] \tag{8}$$

The temperature distribution at the instant the phase change first occurred was nondimensionalized as

$$\theta = (1 + k)\left[\operatorname{erfc}\left(\frac{\xi}{2}\right) - \exp(N\xi + N^2) \operatorname{erfc}\left(\frac{\xi}{2} + N\right)\right] \tag{9}$$

where K, ξ, and N were thought of as a dimensionless temperature excess, distance, and melting initiation time, respectively. Since θ was one for ξ equal to zero, the following relationship between K and N

$$\frac{K}{K + 1} = \exp N^2 \operatorname{erfc} N \tag{10}$$

was determined.

Equation (10) has been tabulated in reference [16] for values of the argument ranging from 0.00 to 3.00 in increments of 0.05 or

0.10. The values were reported with four significant figures. Radau [17] tabulated $(\pi/2)^{1/2} \exp x^2 \operatorname{erfc} x$ to twelve significant figures for integral values of x^2 from 3 to 16. The function $(\pi/2)^{1/2} \exp(x^2/2) \operatorname{erfc}(x/\sqrt{2})$ has been tabulated by Sheppard [18] to 24 places for values of x ranging from 0.00 to 10.0 in increments of 0.10 and to 12 places for values of x ranging from 0.00 to 10.0 in increments of 0.01, and by Mills [19] to five places for values of x ranging from 0.00 to 4.00 in increments of 0.01, 4.00 to 5.00 in increments of 0.05, and 5.00 to 10.0 in increments 0.10. The function $\exp x^2 \operatorname{erfc} x$ was tabulated in reference [13] for values of the argument x running from 0.10 to 7.00 in increments of 0.01. The values reported were given to four, five, or six significant figures with an error of plus or minus one in the last figure. For the values of the argument less than 0.10 or greater than 7.00, convenient expressions were given for the function.

Transient Temperature During Phase Change

The solution during transient phase change was obtained by numerical methods. It was convenient to nondimensionalize the equations and translate the time scale by letting time equal zero at the first instant of phase change. Thus equations (2), (3), (4), (6), and (7) became

$$\frac{\partial \theta}{\partial \tau} + \mu(\tau) M \frac{\partial \theta}{\partial \xi} = \frac{\partial^2 \theta}{\partial \xi^2} \tag{11}$$

$$\theta(\xi, 0) = (1 + k)\left[\operatorname{erfc}\left(\frac{\xi}{2}\right) - \exp(N\xi + N^2) \operatorname{erfc}\left(\frac{\xi}{2} + N\right)\right] \tag{12}$$

$$\theta(0, \tau) = 1 \tag{13}$$

$$\theta(\infty, \tau) = 0 \tag{14}$$

$$\mu(\tau) = 1 + \frac{1}{KN} \frac{\partial \theta}{\partial \xi}(0, \tau) \tag{15}$$

It should be noted that M is negative for melting.

In order to determine numerical solutions to equations (11) through (15), the derivatives in these equations were replaced by forward and central differences with

$$\xi = i\Delta\xi \tag{16}$$

$$\tau = j\Delta\tau \tag{17}$$

Then equation (11) became

$$\left[\frac{\Delta\tau}{\Delta\xi^2} - \frac{M\mu(j)\Delta\tau}{2\Delta\xi}\right]\theta(i+1, j) + \left[1 - \frac{2\Delta\tau}{\Delta\xi^2}\right]\theta(i, j) + \left[\frac{\Delta\tau}{\Delta\xi^2} + \frac{M\mu(j)\Delta\tau}{2\Delta\xi}\right]\theta(i-1, j) - \theta(i, j+1) = 0 \tag{18}$$

This equation related the temperature at a time corresponding to $(j + 1)$ to that at the time j. Therefore it was possible to determine the temperature at any time from knowledge of the initial temperature distribution.

Since the problem at hand was nonlinear, some concern was expressed in regard to round-off errors and convergence. For nonlinear equations there were no complete answers to the convergence of difference equations. By use of the digital computer and hand computations, it was shown, however, that the solution of equation (18) converged to the steady-state values of temperature with suitable choices for $\Delta\tau$ and $\Delta\xi$. For transient conditions, it was not possible to test the results. However, in the case of large K, greater than 50, it can be assumed that the heat input is constant and the numerical results thereby obtained agreed with those of Landau [3]. If round-off errors decrease as successive calculations are carried out, the difference equation is said to be stable. However, if the difference equation is unstable, the errors may oscillate with increasing amplitude as the solution is carried out. By using an analysis outlined in reference [20], it was found that the stability requirements are satisfied if $\Delta\xi \leq 2$ and $\Delta\tau/\Delta\xi \leq \frac{1}{2}$. The numerical integration of equation (18) was simplified if $\Delta\tau/\Delta\xi = \frac{1}{2}$. Under this condition equation (18) became

$$\theta(i, j+1) = \frac{1}{2}\left[1 - \frac{M\mu(j)}{2}\Delta\xi\right]\theta(i+1, j) + \frac{1}{2}\left[1 + \frac{M\mu(j)}{2}\Delta\xi\right]\theta(i-1, j) \tag{19}$$

and the stability was assured if $\Delta\xi \leq 2$.

Before solving equation (19), $\mu(j)$ was determined from the boundary condition equation (15). To find $\partial\theta/\partial\xi$ in equation (15), the following three-term forward difference was used:

$$\frac{\partial \theta}{\partial \xi} = -\frac{11}{6}\theta(0, j) + 3\theta(1, j) - \frac{3}{2}\theta(2, j) + \frac{1}{3}\theta(3, j) \tag{20}$$

Since $\theta(0, j) = 1$, equations (15) and (20) were combined to show that

$$\mu(j) = 1 + \frac{1}{KN} \cdot \frac{1}{\Delta\xi}\left[-\frac{11}{6} + 3\theta(1, j) - \frac{3}{2}\theta(2, j) + \frac{1}{3}\theta(3, j)\right] \tag{21}$$

Hence by using equation (21), $\mu(j)$ was determined from the temperature at the first three positions and then used in equation (19) to calculate $\theta(i, j + 1)$.

With the problem arranged in the nondimensional form, it was of interest to determine the range of the parameters M, N, and K that are encountered. A conservative estimate for the range of M based on an approximation for t_m taken from [3] along with data for 18 metals and a few nonmetals indicated that $-4.5 < M < 0$. For values of $K > 50$, the initial heat input was found to be at most 2 per cent greater than the heat input when melting takes place, and it would be reasonable to assume that the heat input is constant. The temperature distribution in the semi-infinite solid with constant heat input has been worked out in detail by Landau [3], hence values of K greater than 50 were not of interest. The minimum value of K studied was 0.1; at this value, the difference between $(T_s - T_i)$ and $(T_m - T_i)$ was only 10 per cent. It followed then that a suitable range for K was from 0.1 to 50.

To summarize, the solution for the transient temperature distribution was found by determining the initial temperature distribution from equation (9). The velocity $\mu(j)$ was calculated from equation (21), and for $\Delta\tau/\Delta\xi = 1/2$, the temperature at a later time was calculated from equation (19). For problems involving other boundary conditions, equation (12) would be different, but all the remaining equations would be the same. The temperature distribution was calculated in the manner described above with a Datatron 204 digital computer. The results have not been included in this paper because of the difficulty of portraying a large amount of numerical data.

Once the velocity of melting reached a constant value, the temperature distribution was independent of time. By solving equation (11) with the boundary conditions given in equations (13) and (14), the steady-state temperature distribution was found to be

$$\theta(\xi) = \exp(\mu_\infty M\xi) \tag{22}$$

where

$$\mu_\infty = KN/(KN - M) \tag{23}$$

as was determined by combining equations (15) and (22).

The Velocity of the Melting Front

The velocity of the melting front is of importance in determining the transient temperature distribution and the amount of material that has been melted. As a result, the system of equations was solved on a digital computer and curves for the velocity were determined for values of M equal to -0.5, -1, and -2; and K equal to 0.1, 0.5, 1.0, 10, and 50.

The ratio μ/μ_∞ is plotted as a function of the dimensionless time τ in Figs. 2 to 4. For a given problem one can determine K, N, and M from the boundary conditions and properties; calculate μ_∞; and then find the velocity at any given time.

Generally, the curves served as an indication as to how close the temperature distribution was to the steady-state condition since both velocity and temperature should approach steady-state conditions together. The curves can also be used in an aid for finding the transient temperatures from equation (19); instead of using equation (21) to determine $\mu(j)$ the curves can be used, thus saving computation time.

It was observed that the nondimensional velocity could be closely approximated by the relation

$$\mu/\mu_\infty = 1 - \exp(-\beta\tau^{1/2}) \tag{24}$$

where β depended on N, K, and M. This relation was examined

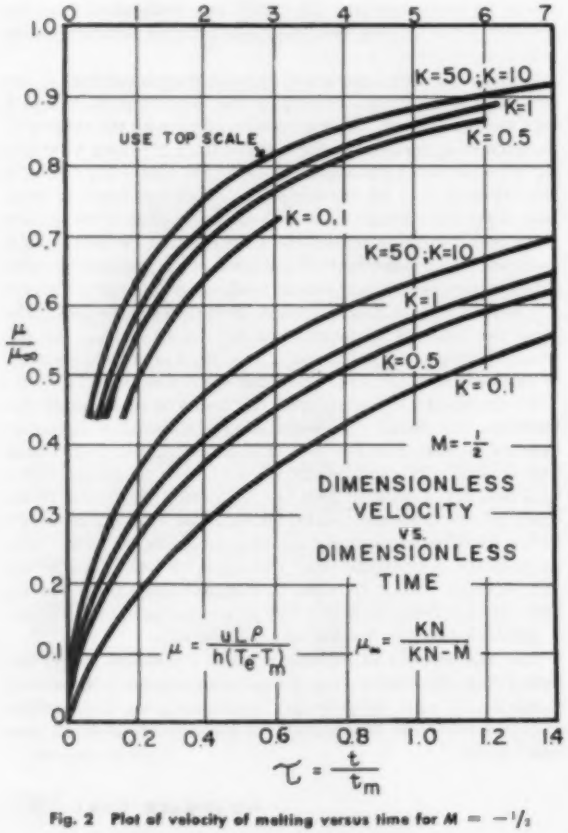

Fig. 2 Plot of velocity of melting versus time for $M = -1/2$

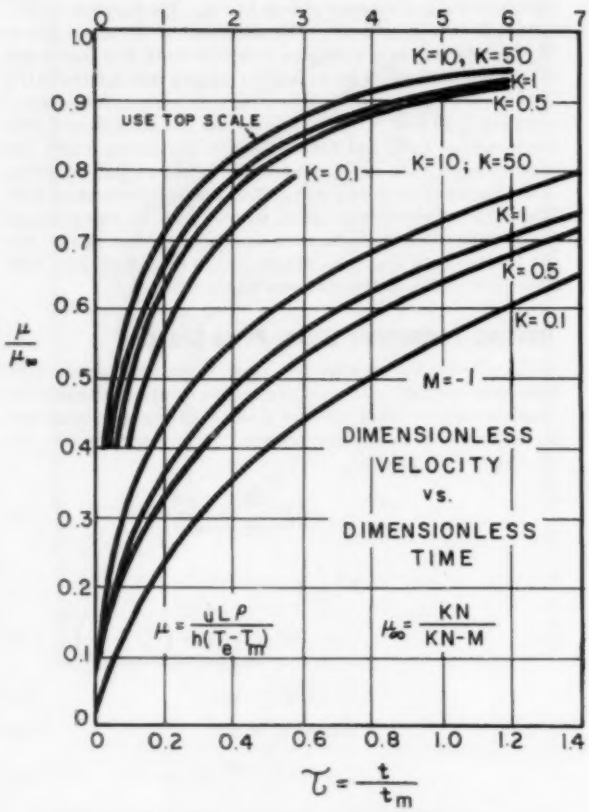

Fig. 3 Plot of velocity of melting versus time for $M = -1$

to see if it would satisfy the differential equation and boundary conditions; however, the results were negative. A careful study showed that it gives a good representation of the velocity for large K but for small values of K it did not produce good agreement with the computer results. Since Landau's work for a constant heat input was comparable to boundary conditions using large K, his results were briefly checked and found in most cases to be in good agreement with the relation. Equation (24) was not, however, verified as being a solution for Landau's problem.

Variable Environment Temperature and Heat-Transfer Coefficient

For melting problems where the melt was removed upon formation, and the environment temperature and coefficient of heat transfer varied with time, it was advantageous to write the difference equations in the form of physical quantities. Thus equations (19) and (21) became

$$T(i, j+1) = \mu(j)\frac{\Delta x}{4\alpha}[T(i+1, j) - T(i-1, j)] + \frac{1}{2}[T(i+1, j) + T(i-1, j)] \tag{25}$$

$$\mu(j) = \frac{h(j)}{L\rho}[T_e(j) - T_m] - \frac{K}{L\rho}\cdot\frac{1}{\Delta x}\left[-\frac{11}{6}T_m + 3T(1, j) - \frac{3}{2}T(2, j) + \frac{1}{3}T(3, j)\right] \tag{26}$$

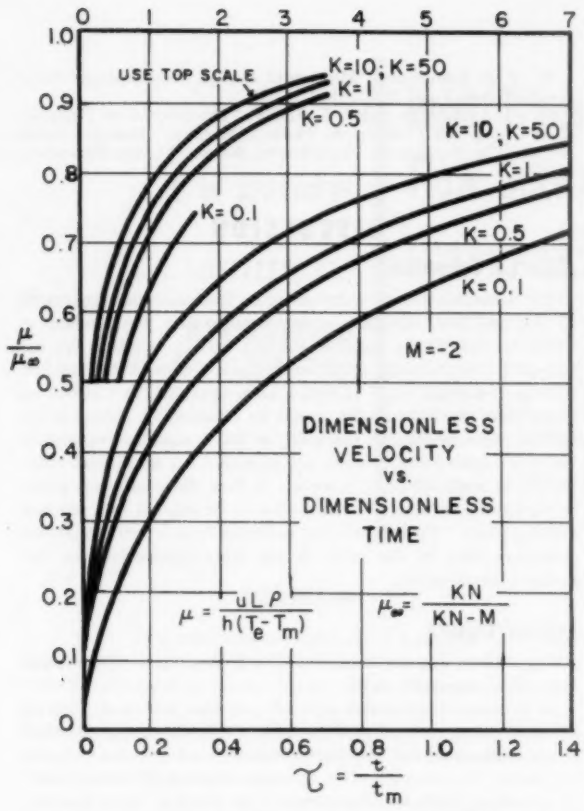

Fig. 4 Plot of velocity of melting versus time for $M = -2$

Once melting started, both equations were used regardless of the initial temperature distribution; equation (25) was also used prior to the time melting started.

Once the initial temperature distribution was determined, the subsequent temperatures were found by either a graphical or a numerical technique. The graphical techniques used for solving transient heat-conduction problems are clearly described by Hawkins and Agnew [21] and the numerical techniques are described in the foregoing.

When the graphical technique was used, the initial temperature distribution $T(i, 0)$ was first plotted. To find the temperature at the end of the first time increment, it was then noted that the velocity u is zero, and equation (25) reduces to

$$T(i, 1) = \frac{1}{2}[T(i + 1, 0) + T(i - 1, 0)] \qquad (27)$$

Hence the temperature at the end of the initial time increment was found by the simple graphical averaging process shown in Fig. 5. If ABCD . . . represented the initial distribution, then for $j = 1$, the temperatures were AEFG . . . To determine the transient distribution at time $j = 2$, points A and F were connected, thus giving position $i = 1$ an "average temperature" (point H) which was corrected as follows. The velocity was determined from equation (26) from the previous values of the temperature, and an amount equal to

$$\frac{\mu\Delta x}{4\alpha}[T(2, 1) - T(0, 1)] \qquad (28)$$

was subtracted from the "average temperature," thus giving point I as the final result. This last operation was conveniently carried out by using proportional dividers. The procedure was repeated, averaging, subtracting, and occasionally calculating μ until the temperature distribution desired was calculated.

Summary

A detailed analysis was made of the transient and steady-state temperature distribution in a semi-infinite solid. The solid, initially at a uniform temperature, was assumed to be heated by an environment at a temperature above the melting point and as the body melted, the melt was immediately removed. Expressions were obtained for the temperature distribution before melting started and after steady-state conditions developed. Finite-difference techniques were employed for finding the transient temperatures and velocities. A digital computer was used to solve the difference equations and obtain the transient temperature and the velocity of the melting front. A method was determined for solving problems with variable environment temperature and heat-transfer coefficient which is quite similar to the Binder technique often used in transient heat-conduction problems without melting.

Acknowledgments

The authors gratefully acknowledge the support from the Office of Ordnance Research, U. S. Army, and the use of a Datatron 204 digital computer made available by Purdue University.

References

1 M. Jakob, "Heat Transfer," vol. 1, John Wiley & Sons, Inc., New York, N. Y., 1949.

2 H. S. Carslaw and J. C. Jaeger, "Conduction of Heat in Solids," Oxford at the Clarendon Press, New York, N. Y., 1959, p. 282.

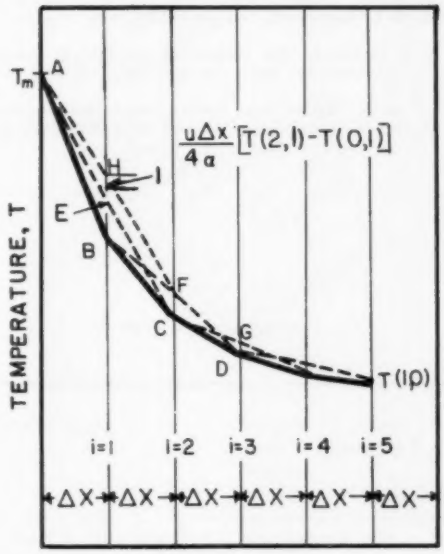

Fig. 5 Graphical solution for the transient temperature distribution with melting

3 H. G. Landau, "Heat Conduction in a Melting Solid," *Quarterly of Applied Mathematics*, vol. 8, 1950, pp. 81–94.

4 J. I. Masters, "Problem of Intense Surface Heating of a Slab Accompanied by Change of Phase," *Journal of Applied Physics*, vol. 27, May, 1956, pp. 477–484.

5 S. J. Citron, "Heat Conduction in a Melting Slab," Institute of the Aeronautical Sciences, Report No. 59-68, presented January, 1959.

6 W. D. Murray and F. Landis, "Numerical and Machine Solutions of Transient Heat-Conduction Problems Involving Melting or Freezing, Part I," JOURNAL OF HEAT TRANSFER, TRANS. ASME, Series C, vol. 81, 1959, pp. 106–112.

7 G. W. Sutton, "The Hydrodynamics and Heat Conduction of a Melting Surface," *Journal of the Aeronautical Sciences*, vol. 25, 1958, p. 29.

8 L. Roberts, "On the Melting of a Semi-Infinite Body of Ice Placed in a Hot Stream of Air," *Journal of Fluid Mechanics*, vol. 4, part 5, September, 1958, p. 505.

9 D. R. Otis, "Solving the Melting Problem Using the Electric Analogy of Heat Conduction," 1956 Heat Transfer and Fluid Mechanics Institute, Stanford University, p. 29.

10 C. B. Neel, Jr., "An Investigation Utilizing an Electric Analogue of Cyclic De-Icing of a Hollow Steel Propeller With an External Blade Shoe," NACA TN 2852, 1952.

11 V. H. Von Glahn, "The Icing Problem—Current Status of NACA Techniques and Research," AGARD, Papers Presented at the Seventh Meeting of the Wind Tunnel and Model Testing Panel, 1955, p. 293.

12 T. R. Goodman, "The Heat Balance Integral and Its Application to Problems Involving a Change of Phase," TRANS. ASME, vol. 80, 1958, p. 335.

13 J. E. Sunderland and R. J. Grosh, "The Transient Temperature Distribution in Semi-Infinite Solids With Melting," Final Technical Report, Office of Ordnance Research Contract No. DA-33-008 ORD-1219, Purdue University, August, 1958.

14 H. S. Carslaw and J. C. Jaeger, op. cit., p. 72.

15 M. P. Heisler, "Temperature Charts in Solids During Heating or Cooling," *Industrial and Engineering Chemistry*, vol. 34, 1942, p. 874.

16 H. S. Carslaw and J. C. Jaeger, op. cit., p. 485.

17 R. Radau, "Tables of the Integral $f(x) = \sqrt{\pi/2} \exp x^2 \operatorname{erfc} x$," Annals de L'Observatorie de Paris in 1885 Memoires, vol. 18, pp. B 1-25.

18 W. P. Sheppard, "The Probability Integral," British Association for the Advancement of Science, Mathematical Tables, vol. VII, 1939, pp. 1–22.

19 J. P. Mills, "Tables of the Ratio : Area to Bounding Ordinate, for and Portion of Normal Curve," *Biometrika*, vol. 18, 1926, pp. 395–400.

20 F. B. Hildebrand, "Methods of Applied Mathematics," Prentice Hall, New York, N. Y., 1952, p. 334.

21 G. A. Hawkins and J. T. Agnew, "The Solution of Transient Heat Conduction Problems by Finite Differences," Research Series No. 98, The Engineering Experimental Station, Purdue University.

DISCUSSION

Robert J. Schoenhals[3]

The authors are to be commended on their thorough treatment of this problem. As they correctly point out, the problem is nonlinear due to the variable velocity $u(t)$ in equation (2), although the nonlinearity arises not because u varies with time but because it depends on T as indicated in equation (7). It can be noted that the nonlinearity would be removed by taking a co-ordinate system fixed in the solid, in which case the convective term of equation (2) would not appear. An additional complexity is involved here, however, in that the conditions given by equations (6) and (7) would need to be applied to a moving melting front. This complexity indicates to this writer that the procedure used in this paper is the more appropriate for the problem investigated.

Authors' Closure

The authors wish to thank Professor Schoenhals for his interest and comments on this paper.

As Professor Schoenhals pointed out, the nonlinear term in equation (2) can be removed by using a co-ordinate system fixed in the solid; however, the problem remains complex because the boundary conditions given by equations (6) and (7) would apply to a moving surface. In solving this problem by numerical analysis, it is the opinion of the authors that the method described can be most easily employed. However, if thermal analog techniques are used, it is easier to consider the co-ordinate system to be fixed in the solid. A solution of this type is given in reference [13].

[3] Assistant Professor of Mechanical Engineering, Purdue University, Lafayette, Ind.

Heat Transfer to Longitudinal Laminar Flow Between Cylinders

E. M. SPARROW[1]
Assoc. Mem. ASME

A. L. LOEFFLER, JR.[2]

H. A. HUBBARD
Lewis Research Center NASA, Cleveland, Ohio

Consideration is given to the fully developed heat-transfer characteristics for longitudinal laminar flow between cylinders arranged in an equilateral triangular array. The analysis is carried out for the condition of uniform heat transfer per unit length. Solutions are obtained for the temperature distribution, and from these, Nusselt numbers are derived for a wide range of spacing-to-diameter ratios. It is found that as the spacing ratio increases, so also does the wall-to-bulk temperature difference for a fixed heat transfer per unit length. Corresponding to a uniform surface temperature around the circumference of a cylinder, the circumferential variation of the local heat flux is computed. For spacing ratios of 1.5 ~ 2.0 and greater, uniform peripheral wall temperature and uniform peripheral heat flux are simultaneously achieved. A simplified analysis which neglects circumferential variations is also carried out, and the results are compared with those from the more exact formulation.

Introduction

In a previous investigation (reference [1]),[3] consideration was given to the longitudinal laminar flow between cylinders arranged in regular array. Here, attention is directed to analyzing the heat-transfer characteristics of such a flow. This configuration has potential application in compact heat exchangers and has been frequently considered in connection with the cores of nuclear reactors.

A schematic diagram of the system under study is shown in Fig. 1. The cylindrical rods between which the fluid flows are arranged in equilateral triangular array, and the flow is laminar and fully developed. The thermal situation to be considered here is the condition of uniform heat transfer along the length of the passage. The goal of this analysis is to determine the fully developed heat-transfer characteristics of the problem, taking into account the circumferential variations of the temperature distribution which inevitably arise in the cross section of a noncircular passage. The existence of such peripheral variations is what makes the problem both interesting and challenging. The starting point of the study is the basic law of energy conservation appropriate to the three-dimensional situation. Solutions are found for a wide range of spacing to diameter ratios, and corresponding heat-transfer results are obtained. For large spacings, the flow about any given cylinder should be little influenced

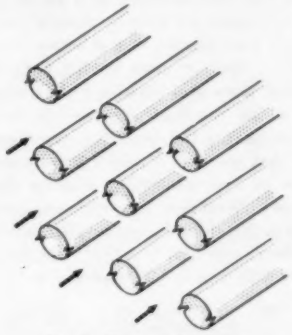

Fig. 1 Flow configuration

[1] At present, Professor of Mechanical Engineering, University of Minnesota, Minneapolis, Minn.

[2] At present, Research Engineer, Grumman Aircraft Engineering Corp., Bethpage, N. Y.

[3] Numbers in brackets designate References at end of paper.

Contributed by the Heat Transfer Division of The American Society of Mechanical Engineers and presented at the Winter Annual Meeting, New York, N. Y., November 27–December 2, 1960. Manuscript received at ASME Headquarters, June 6, 1960. Paper No. 60—WA-40.

Nomenclature

$A, B, \ldots, F$ = constants in the temperature solution
c_p = specific heat at constant pressure
d = cylinder diameter, $2r_0$
d_e = equivalent diameter, equation (27)
h = heat-transfer coefficient
j = summation index
k = thermal conductivity
M = mass flow parameter, $(w/12\rho)/s^2\left(-\frac{1}{\mu}\frac{dp}{dz}\right)$
m = summation index
N = normal direction
$\mathrm{Nu}_d, \mathrm{Nu}_{d_e}$ = Nusselt number, hd/k and hd_e/k, respectively
n = summation index
p = static pressure
Q = heat-transfer rate per unit length from one cylinder
q = local heat-transfer rate per unit area
$\bar{q}$ = circumferential average of q, $Q/2\pi r_0$
r = radial co-ordinate; r_0, cylinder radius; r^*, outer radius of equivalent annulus
s = half spacing between centers of cylinders
T = temperature; T_w, wall temperature; T_b, bulk temperature; T_0, entering fluid temperature
u = axial-velocity distribution
w = mass rate of flow associated with one cylinder
z = axial co-ordinate measuring distance from the entrance of the passage
δ_j = dimensionless coefficients in velocity solution
θ = angular co-ordinate
μ = absolute viscosity
ρ = density
ω_j = dimensionless coefficients in temperature solution

by the presence of neighboring cylinders. With this in mind, a simplified analysis has also been carried out neglecting circumferential variations, and the heat-transfer results thus obtained are compared with those from the more complete formulation.

Analysis

Mathematical Formulation. To predict the heat-transfer characteristics from first principles, we must begin with the fundamental physical law of energy conservation. The mathematical representation of this law appropriate to a fully developed flow may be written in cylindrical co-ordinates as follows

$$\rho c_p u \frac{\partial T}{\partial z} = k\left(\frac{\partial^2 T}{\partial r^2} + \frac{1}{r}\frac{\partial T}{\partial r} + \frac{1}{r^2}\frac{\partial^2 T}{\partial \theta^2} + \frac{\partial^2 T}{\partial z^2}\right) \quad (1)$$

where u, the axial velocity, depends on both cross section co-ordinates r and θ.

To facilitate applying equation (1) to the system under study, we refer to Fig. 2. The left-hand sketch is a cross-sectional view. From the symmetry of the situation, it is easy to see that consideration need be given only to the typical 30 deg element which is blackened in the sketch. Once the solution is known within this element, then it is known everywhere throughout the cross section. An enlarged view of the typical element is shown at the right, along with the boundary conditions and dimensional nomenclature. The condition that the normal derivative be zero is an expression of symmetry. On the inner boundary, $r = r_0$, the temperature is assigned a value T_w which is independent of angle. Physically speaking, this means that the surface temperature is uniform around the circumference in a given cross section, although it will vary along the length. Such a boundary condition could correspond, for example, to a situation of uniform internal heat generation in rods or tubes having high thermal conductivity. Of course, there still remains a circumferential temperature variation within the fluid and this will be included in the analysis. Before leaving the boundary conditions, it is interesting to observe that the case of uniform peripheral surface temperature is one of two interesting limiting conditions.[4] The other, uniform peripheral heat flux, still remains to be analyzed.

The first step in attacking equation (1) is to introduce the condition of fully developed heat transfer. For the case of uniform heat transfer per unit length, this condition is

$$\frac{\partial T}{\partial z} = \text{const} = \frac{Q}{wc_p} = \frac{(Q/12)}{(w/12)c_p} \quad (2)$$

where w and Q respectively represent the mass flow and the heat transfer per unit length associated with a single cylinder in the array; while $(w/12)$ and $Q/12$ are the quantities appropriate to the typical 30 deg element of Fig. 2.

Next, it is necessary to know the velocity distribution u. In reference [1], a very accurate, but approximate solution for the velocity has been derived in the form

$$\frac{u}{s^2\left(-\frac{1}{\mu}\frac{dp}{dz}\right)} = \frac{\sqrt{3}}{\pi}\ln\frac{r}{r_0} - \frac{1}{4}\left[\left(\frac{r}{s}\right)^2 - \left(\frac{r_0}{s}\right)^2\right] + \sum_{n=1}\frac{\delta_n}{6n}\left[\left(\frac{r}{s}\right)^{6n} - \frac{r_0^{12n}}{r^{6n}s^{6n}}\right]\cos 6n\theta \quad (3)$$

The coefficients δ_1 through δ_7 have been tabulated to four decimal places in the reference for a wide range of spacing ratios, and additional significant figures were available when needed in the heat-transfer analysis. Another piece of information which is needed from the velocity solution is the relation between the mass flow w and the pressure drop. For convenience, we define a dimensionless grouping M as[5]

$$M \equiv \frac{(w/12\rho)}{s^4\left(-\frac{1}{\mu}\frac{dp}{dz}\right)} \quad (4)$$

Numerical values of M may be obtained as a function of spacing ratio from Fig. 6 of reference [1].

Then the information contained in equations (2) through (4) may be introduced into the energy equation (1). After rearrangement, the governing equation for T is found to be

$$\frac{\partial^2 T}{\partial r^2} + \frac{1}{r}\frac{\partial T}{\partial r} + \frac{1}{r^2}\frac{\partial^2 T}{\partial \theta^2} = \frac{Q/12k}{Ms^2}\left\{\frac{\sqrt{3}}{\pi}\ln\frac{r}{r_0} - \frac{1}{4}\left[\left(\frac{r}{s}\right)^2 - \left(\frac{r_0}{s}\right)^2\right] + \sum_{n=1}^{l}\frac{\delta_n}{6n}\left(\frac{r}{s}\right)^{6n}\left[1 - \left(\frac{r_0}{r}\right)^{12n}\right]\cos 6n\theta\right\} \quad (5)$$

Solution of the Governing Equation. In approaching equation (5), we look for particular and homogeneous solutions. Thus the solution for T is expressed as the sum of these separate solutions as follows

$$T = T_p + T_h \quad (6)$$

For a particular solution, any function satisfying equation (5) will suffice. It is easily verified by direct substitution that the following expression is a satisfactory particular solution

$$T_p = \frac{(Q/12k)r^2}{Ms^2}\left\{-\frac{\sqrt{3}}{4\pi} + \frac{1}{16}\left(\frac{r_0}{s}\right)^2 - \frac{1}{64}\left(\frac{r}{s}\right)^2 + \frac{\sqrt{3}}{4\pi}\ln\frac{r}{r_0} + \sum_{n=1}\frac{\delta_n}{24n}\left(\frac{r}{s}\right)^{6n}\left[\frac{1}{6n+1} + \frac{(r_0/r)^{12n}}{6n-1}\right]\cos 6n\theta\right\} \quad (7)$$

To find the homogeneous equation, we set the right side of equation (5) equal to zero and get

[4] A thorough discussion of thermal boundary conditions in noncircular ducts is given in reference [2].

[5] In reference [1] the symbol Q is used to denote $w/12\rho$.

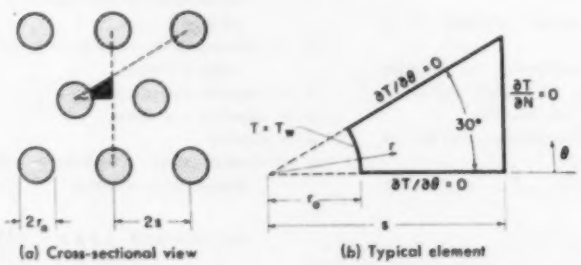

(a) Cross-sectional view (b) Typical element

Fig. 2 Diagram used in mathematical formulation

$$\frac{\partial^2 T_h}{\partial r^2} + \frac{1}{r}\frac{\partial T_h}{\partial r} + \frac{1}{r^2}\frac{\partial^2 T_h}{\partial \theta^2} = 0$$

This is the well-known Laplace equation, the solution to which may be found in various books on advanced calculus as

$$T_h = A + B \ln r + \sum_m (C_m r^m + D_m r^{-m})(E_m \cos m\theta + F_m \sin m\theta) \quad (8)$$

where m takes on integral values to insure that T is single valued, i.e., that $T(\theta) = T(\theta + 2\pi)$. The constants $A, B, \ldots, F$ remain to be determined from the boundary conditions.

So, the general solution of equation (5) is given by equation (6) in conjunction with T_p and T_h from (7) and (8). But, to complete the solution, there still remains the task of satisfying the boundary conditions. Starting with the most easily applied conditions, we first impose the symmetry requirement that $\partial T/\partial\theta = 0$ at $\theta = 0$ deg and at $\theta = 30$ deg, see Fig. 2(b). After differentiating equation (6) and substituting from (7) and (8), it is found that the condition at $\theta = 0$ deg yields

$$F_m \equiv 0 \quad (9)$$

while from the condition at $\theta = 30$ deg, it follows that

$$m = 6, 12, 18, \ldots \quad (10)$$

to insure that $\sin m\pi/6 = 0$. With this information, it is convenient to rephrase the temperature solution (6) as

$$T = T_p + A + B \ln r + \sum_{j=1} (C_j r^{6j} + D_j r^{-6j}) \cos 6j\theta \quad (11)$$

where T_p is still given by equation (7) and E_j has been set equal to unity without loss of generality.

Next, it is required that at the surface of the cylinder, $r = r_0$, the temperature take on the value T_w independent of angle. Applying this condition to equation (11), it is found that

$$A = T_w - B \ln r_0 - \frac{(Q/12k)r_0^2}{Ms^2}\left\{-\frac{\sqrt{3}}{4\pi} + \frac{3}{64}\left(\frac{r_0}{s}\right)^2\right\} \quad (12a)$$

$$D_j = -C_j r_0^{12j} - \frac{(Q/12k)}{Ms^2}\frac{\delta_n}{2(36n^2-1)}\frac{r_0^{12n+2}}{s^{6n}}, \quad n = j \quad (12b)$$

Further, to make certain that energy conservation is satisfied on an over-all basis for the typical element of Fig. 2(b), we equate the heat transfer per unit length, $Q/12$, to the heat conducted at the surface of the cylinder, i.e.,

$$Q/12 = \int_0^{\pi/6} -k\left(\frac{\partial T}{\partial r}\right)_{r_0} r_0 d\theta \quad (13)$$

This insures that there is no net energy transport across the other boundaries of the typical element. Of course, over-all energy would be automatically satisfied by an exact solution; but if an approximate solution is being contemplated, then it must be imposed as a separate requirement. Inserting equation (11) into the over-all conservation condition (13) gives

$$B = \frac{Q/12k}{Ms^2}\left[-\frac{6Ms^2}{\pi} + \frac{\sqrt{3}}{4\pi}r_0^2 - \frac{1}{16}\frac{r_0^4}{s^2}\right] \quad (14)$$

Before going ahead to the final boundary condition, it is useful to bring together the findings of the previous paragraph. Introducing equations (12) and (14) into the temperature solution (11) and substituting for T_p from equation (7) gives

$$T - T_w = \frac{Q/12k}{Ms^2}\left\{\left[\frac{\sqrt{3}}{4\pi}(r^2 + r_0^2) - \frac{1}{16}\frac{r_0^4}{s^2} - \frac{6Ms^2}{\pi}\right]\ln\frac{r}{r_0} - \frac{1}{64}\frac{(r^4 - r_0^4)}{s^2} + \left[-\frac{\sqrt{3}}{4\pi} + \frac{1}{16}\left(\frac{r_0}{s}\right)^2\right](r^2 - r_0^2)\right\} + \sum_{j=1} C_j r^{6j}\left[1 - \left(\frac{r_0}{r}\right)^{12j}\right]\cos 6j\theta + \frac{(Q/12k)r^2}{Ms^2}\sum_{n=1}\delta_n \cos 6n\theta\left\{\frac{(r/s)^{6n}}{24n}\left[\frac{1}{6n+1} + \frac{(r_0/r)^{12n}}{6n-1}\right] - \frac{(r_0/r)^2}{2(36n^2-1)}\frac{r_0^{12n}}{r^{6n}s^{6n}}\right\} \quad (15)$$

Remembering that δ_n and M are known numerical constants whose values depend upon s/r_0, it is seen that the temperature distribution will be completely determined as soon as the C_j are found. At our disposal is the condition that $\partial T/\partial N = 0$ on the right-hand boundary of the typical element, see Fig. 2(b), on which $r = s/\cos\theta$. In applying this condition, it is convenient to use the identity

$$\frac{\partial T}{\partial N} = \frac{\partial T}{\partial r}\cos\theta - \frac{\partial T}{\partial \theta}\frac{\sin\theta}{r} \quad (16)$$

Then, introducing the temperature distribution (15) and setting $\partial T/\partial N = 0$ for $r = s/\cos\theta$, there is obtained after considerable rearrangement

$$\sum_{j=1}\omega_j(\cos\theta)^{1-6j}\left[\cos(6j-1)\theta + \left(\frac{r_0\cos\theta}{s}\right)^{12j}\cos(6j+1)\theta\right] = -\sum_{n=1}\delta_n\left\{\frac{3n}{36n^2-1}\left(\frac{r_0}{s}\right)^{12n+2}(\cos\theta)^{6n+1}\cos(6n+1)\theta + \frac{\cos(6n-1)\theta + (1/3n)\cos\theta\cos 6n\theta}{4(6n+1)(\cos\theta)^{6n+1}} + \frac{(r_0/s)^{12n}(\cos\theta)^{6n-1}}{4(1-6n)}[\cos(6n+1)\theta - (1/3n)\cos\theta\cos 6n\theta]\right\} - \left[-\frac{6M}{\pi} + \frac{\sqrt{3}}{4\pi}\left(\frac{r_0}{s}\right)^2 - \frac{1}{16}\left(\frac{r_0}{s}\right)^4\right]\cos^2\theta - \frac{1}{8}\left(\frac{r_0}{s}\right)^2 - \frac{\sqrt{3}}{2\pi}\ln\left(\frac{s}{r_0\cos\theta}\right) + \frac{1}{16\cos^2\theta} + \frac{\sqrt{3}}{4\pi} \quad (17)$$

where

$$\omega_j = C_j\frac{6js^{6j}M}{(Q/12k)} \quad (17a)$$

The only unknowns appearing in equation (17) are the coefficients ω_j (i.e., C_j). In considering ways of solving for the ω_j, the first thought might be to use the Fourier series method. If workable, this procedure would provide an infinite number of ω_j values while satisfying equation (17) at all points along the boundary, 0 deg $\leq \theta \leq$ 30 deg. However, Fourier methods cannot be applied in the present problem and some other approach must be used. The procedure employed here is as follows: First, the summation involving the ω_j is truncated after i terms. Next, the condition (17) is applied successively at i values of θ in the range 0 deg $\leq \theta \leq$ 30 deg. This yields i linear equations, each of which contains i unknown values of ω_j. As soon as the s/r_0 ratio is specified, the right-hand side of each equation can be reduced to a numerical constant since the values of δ_n and M are available from reference [1]. So, there are i linear, inhomogeneous algebraic equations, the solution to which yields numerical values for

the ω_j. To check the accuracy of the results, the entire procedure may be reapplied using additional terms in the summation. From this, it is found that the additional terms do not significantly affect the numerical values of the first few coefficients. Another important fact is that the magnitudes of the ω_j decrease quite rapidly with increasing j, so that only the first few ω_j are really important. These favorable circumstances somewhat ease the task of finding a sufficient number of accurate ω_j values. The numerical results which have been obtained for the ω_j are listed in Table 1 as a function of the spacing ratio s/r_0.

With the ω_j values now known, then the coefficients C_j are also known through equation (17a). With these, we may return to the temperature distribution (15). For convenience, the summation involving the C_j may be rephrased as

$$\sum_{j=1} C_j r^{6j}\left[1-\left(\frac{r_0}{r}\right)^{12j}\right]\cos 6j\theta = \frac{Q/12k}{M}\sum_{j=1}\frac{\omega_j}{6j}\left(\frac{r}{s}\right)^{6j}\left[1-\left(\frac{r_0}{s}\right)^{12j}\right]\cos 6j\theta \quad (18)$$

Since δ_n and M are also known numerical constants (reference [1]), then it is clear that once the geometrical parameters r_0 and s have been specified, the temperature distribution within the typical elements is determined. So, we are now in a position to proceed with the determination of the heat-transfer results.

Heat-Transfer Characteristics

Wall-to-Bulk Temperature Difference and Nusselt Number. The solution which has just been presented gives the distribution of the temperature in a cross section relative to the wall temperature T_w at that cross section. So, to complete the solution, there still remains the task of finding T_w. Moreover, in practice, it is the wall temperature itself which is usually the quantity of greatest practical interest, for example, on a materials limit or a thermal stress basis.

Now, in a situation where the wall heat flux is prescribed, the bulk temperature is immediately determined according to the following relation

$$T_b = T_0 + \frac{Q}{wc_p}z \quad (19)$$

where T_0 is the temperature of the fluid at the entrance to the heated passage. Making use of this, the wall temperature may be written as

$$T_w \equiv T_b + (T_w - T_b) = T_0 + \frac{Q}{wc_p}z + (T_w - T_b) \quad (20)$$

From this, it is clear that the wall-to-bulk temperature difference $(T_w - T_b)$ is the key to the determination of the wall temperature. In addition, as soon as $T_w - T_b$ is known, then Nusselt number results can be obtained.

To compute the wall-to-bulk temperature difference, we start with the standard definition of the bulk temperature

$$T_b \equiv \frac{\iint_{\text{Area}} T\,\rho u r\,dr\,d\theta}{\iint_{\text{Area}} \rho u r\,dr\,d\theta} \quad (21)$$

The denominator is simply the mass flow. Specializing to the typical element of Fig. 2(b) and subtracting away the wall temperature, there is obtained

$$T_w - T_b = \frac{\rho\int_0^{30^\circ}\int_{r_0}^{s/\cos\theta}(T_w - T)ur\,dr\,d\theta}{w/12} \quad (22)$$

In evaluating the integrand, the velocity distribution is introduced from equation (3), while the temperature distribution is taken from equation (15) as modified by (18). After making these substitutions and rephrasing in terms of dimensionless variables, the following functional relation is revealed

$$\frac{T_w - T_b}{Q/12k} = f(s/r_0) \quad (23)$$

This is an interesting result in that the dependence on geometry enters only as the ratio s/r_0, rather than as s and r_0 separately. It is easy to see that multiplying out the temperature and velocity distributions in the integrand of equation (22) leads to an exceedingly lengthy expression which is made even longer when the double integration is carried out. To display only the end result of the integration would require considerable space. In the interest of a concise presentation, the details associated with the evaluation of equation (22) will be omitted and only a few general remarks will be made as follows: In organizing the computations, separate account was kept of the contribution due to the nonseries portion of u and $T - T_w$ and of the contribution due to the series terms. As expected, the relative importance of the series terms increased as the spacing decreased. The integrations which arose in connection with equation (22) were carried out analytically as far as possible; however, it was ultimately necessary to compute some specific integrals by numerical means and these are given in the Appendix with the hope that this information may be useful to others.

From the evaluation of equation (22), numerical results for the wall-to-bulk temperature difference have been obtained as a function of the spacing ratio s/r_0. These results will be reported in terms of the customary Nusselt number representation. First, a heat-transfer coefficient is defined as

$$h \equiv \frac{Q}{\pi d(T_w - T_b)} = \frac{Q/12}{(\pi d/12)(T_w - T_b)} \quad (24)$$

Then, using the cylinder diameter as characteristic dimension, the Nusselt number becomes

$$\mathrm{Nu}_d = \frac{hd}{k} = \left(\frac{12}{\pi}\right)\frac{Q/12k}{T_w - T_b} \quad (25)$$

It may be seen that the Nusselt number is essentially the reciprocal of the dimensionless bulk temperature parameter which has been displayed in equation (23). From this it follows that the Nusselt number depends only on the spacing ratio s/r_0. Utilizing the numerical values obtained from evaluating equation (22), a graph of Nu_d as a function of s/r_0 has been prepared and is presented as the solid curve of Fig. 3, left-hand ordinate. It is seen from the figure that Nu_d monotonically increases as s/r_0 decreases; and with this, it follows from equation (25) that the wall-to-bulk temperature difference is smaller at smaller spacings for a fixed heat input. This trend is in accord with physical reasoning.

Now, with the relation between heat transfer and temperature difference established by Fig. 3, we may return to the computation of the wall temperature variation as given by equation (20). Dividing through by Q/k and introducing equation (25), there is obtained

$$\frac{T_w - T_0}{Q/k} = \frac{z}{(w/\mu)\mathrm{Pr}} + \frac{1}{\pi \mathrm{Nu}_d} \quad (26)$$

At a fixed flow, the value of $(T_w - T_0)/(Q/k)$ at a particular z will diminish as the spacing diminishes. But, there will, of course, be a price in pressure drop to be paid to maintain the fixed flow. On the other hand, at a fixed pressure drop, w will diminish with

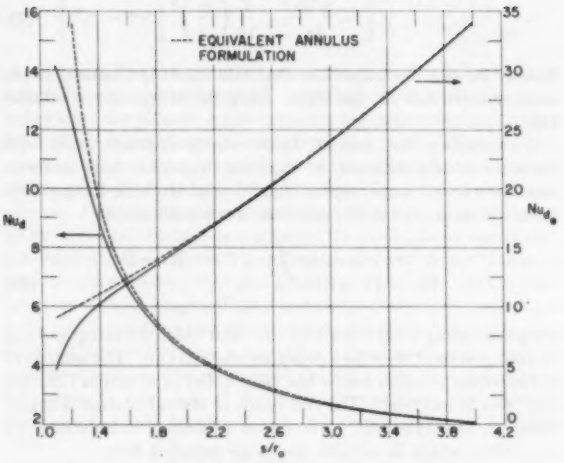

Fig. 3 Nusselt number results

decreasing spacing; and so, under this condition, the two terms of equation (26) vary in opposite directions. The dependence of the flow rate on spacing ratio is more acute (see Fig. 6, reference [1]) than is that of the Nusselt number. So, for z values sufficiently large to establish fully developed conditions, it would be expected that $(T_w - T_0)/(Q/k)$ would increase with decreasing spacing when the pressure drop is fixed.

Before leaving this section, it may be worth while to discuss briefly two other aspects of the results. First, it may be of interest to compare the heat-transfer performance with that for laminar flow inside a circular tube ($\mathrm{Nu}_d = 48/11$). If we ask for the same wall-to-bulk temperature difference at a given heat flux per unit length, then this is achieved at a spacing ratio of 2.03. The second topic relates to the equivalent diameter. It is reasonably well-accepted that for laminar flow, the use of the equivalent diameter as a characteristic dimension is not sufficient to remove the dependence of the heat-transfer results upon geometrical parameters. However, in the present problem, we are in a position to once again check on this point. From the defini ion

$$d_* = \frac{4(\text{cross-sectional area})}{\text{heated perimeter}} \tag{27a}$$

it is easy to show that

$$\frac{d_*}{d} = \frac{6(s/r_0)^2}{\sqrt{3}\,\pi} - 1 \tag{27b}$$

Then, since $\mathrm{Nu}_{d_*} = (\mathrm{Nu}_d)(d_*/d)$, we may find the dependence of Nu_{d_*} upon s/r_0 by using the results which have previously been presented. A curve derived in this way has been plotted as a solid line in Fig. 3, right-hand ordinate. It is seen that the geometrical factors involved in the equivalent diameter have given Nu_{d_*} a completely opposite trend to that of Nu_d. However, the variation in Nu_{d_*} is not less than that experienced by Nu_d.

Peripheral Variation of Local Heat Transfer. In the previous section, attention has been focused on over-all quantities such as the heat transfer per unit length, the bulk temperature, and the Nusselt number. Here, consideration is given to the local heat transfer at various positions around the periphery of a cylinder. Since the velocity distribution varies with angular position around a cylinder while the surface temperature is prescribed to be independent of angle, it is evident that there may be a circumferential variation of the local heat transfer.

To compute the local heat transfer, we use Fourier's law

Table 1 Listing of ω_j values

s/r_0	$\omega_1 \times 10^2$	$\omega_2 \times 10^3$	$\omega_3 \times 10^5$	$\omega_4 \times 10^7$
4.0	2.9649	0.39239	0.579	~0.3
2.0	1.2712	0.12031	0.136	~0.05
1.5	0.71081	0.014556	−0.195	~−1.5
1.2	0.37039	−0.1323	−1.20	~−6.0
1.1	0.25961	−0.2065	−1.12	~7.0

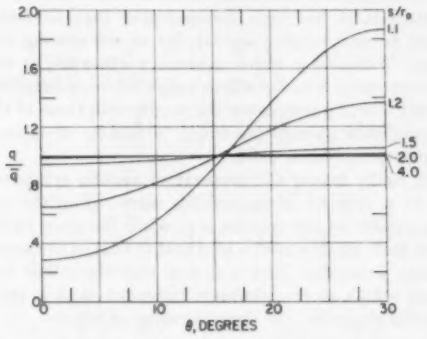

Fig. 4 Peripheral variation of wall heat transfer

$$q = -k\left(\frac{\partial T}{\partial r}\right)_{r_0} \tag{28}$$

where q represents the heat transfer per unit area. The temperature distribution is introduced from equation (15) as modified by (18) and after some rearrangement, it is found that

$$\frac{q}{\bar{q}} = 1 - \frac{\pi}{6M}\left\{\sum_{j=1} 2\omega_j \left(\frac{r_0}{s}\right)^{4j} \cos 6j\theta + \sum_{n=1} \frac{\delta_n (r_0/s)^{6n+2}}{2(6n-1)} \cos 6n\theta\right\} \tag{29}$$

where $\bar{q}$, the mean local heat transfer, is related to the heat transfer per unit length Q by

$$\bar{q} = \frac{Q}{2\pi r_0} \tag{29a}$$

Utilizing the tabulated values of ω_j from Table 1 with the δ_j and M from reference [1], the circumferential variation of q has been evaluated. The results are plotted in Fig. 4 as a function of θ for parametric values of the spacing ratio s/r_0. By the symmetry considerations already mentioned in connection with Figs. 2(a and b), the variation over the entire circumference is known once the results for a typical 30 deg section have been given.

From Fig. 4, it is seen that for close spacings (small s/r_0), there is a significant circumferential heat-transfer variation; while for open spacings (large s/r_0), the heat transfer is essentially uniform around the circumference. Clearly, for all spacing ratios of 2 or greater, there is essentially no distinction between the case of peripherally uniform wall temperature or peripherally uniform heat transfer. For many applications, this statement might be considered applicable even to spacing ratios as low as 1.5. The trend of decreasing peripheral variations with increasing spacing may be explained on physical grounds. For close spacings, a given cylinder is much influenced by the presence of its neighbors, with the result that the velocity distribution is circumferentially nonuniform and so is the heat transfer. As the spacing grows larger, the flow about a given cylinder is less distributed by its neighbors. The resulting trend of the velocity toward axial symmetry is accompanied by a trend toward a more uniform surface heat transfer.

It is interesting to note that the largest heat transfer occurs at $\theta = 30$ deg, the location of the largest open area for flow. On the other hand, the smallest heat transfer occurs at $\theta = 0$ deg, which is the location of the smallest open area for flow. From this, it may be inferred that if the heat transfer were prescribed to be circumferentially uniform while the surface temperature is permitted to vary, the hot spot would occur at $\theta = 0$ deg.

Simplified Analysis for Large Spacings

Both from physical reasoning and from the results of the foregoing analysis, it has been demonstrated that circumferential variations become smaller and smaller as the spacing ratio s/r_0 increases. With this in mind, it seems worth while to reanalyze the problem using a model which neglects circumferential variations; and then, by comparing the results with those of the complete formulation already presented, to find for what conditions the simplified analysis is valid.

A flow model having the property of angular symmetry with respect to a cylinder is an annulus surrounding the cylinder. The inner radius of the annulus is r_0, while the outer radius r^* is chosen so that the flow area is identical to that in the actual configuration. From Fig. 2(*a*), it is seen that the actual flow area associated with a given cylinder is composed of 12 of the blackened typical elements. So, equating areas as follows

$$\pi(r^{*2} - r_0^2) = 12\left[\frac{s^2}{2}\tan\frac{\pi}{6} - \pi\frac{r_0^2}{12}\right] \tag{30a}$$

there is obtained

$$r^* = \left(\frac{2\sqrt{3}}{\pi}\right)^{1/2} s \tag{30b}$$

The velocity problem for such an annulus is described by

$$\frac{\partial^2 u}{\partial r^2} + \frac{1}{r}\frac{\partial u}{\partial r} = \frac{1}{\mu}\frac{dp}{dz} \tag{31a}$$

$$u(r_0) = 0, \qquad \frac{\partial u}{\partial r}(r^*) = 0 \tag{31b}$$

It is easily verified by direct substitution that the solution for the velocity distribution is given by

$$\frac{u}{s^2\left(-\frac{1}{\mu}\frac{\partial p}{\partial z}\right)} = \frac{\sqrt{3}}{\pi}\ln\frac{r}{r_0} - \frac{1}{4}\left[\left(\frac{r}{s}\right)^2 - \left(\frac{r_0}{s}\right)^2\right] \tag{32}$$

which is identical to the nonseries part of the more complete velocity solution (3). From this, the flow parameter M which has been defined in equation (4) can be evaluated to be

$$M = \frac{1}{2\pi}\ln\frac{r^*}{r_0} - \frac{3}{8\pi} + \frac{\sqrt{3}}{12}\left(\frac{r_0}{s}\right)^2 - \frac{\pi}{96}\left(\frac{r_0}{s}\right)^4 \tag{33}$$

Next, by modifying the governing equation (5) to apply to the annulus, the temperature distribution problem may be formulated as

$$\frac{\partial^2 T}{\partial r^2} + \frac{1}{r}\frac{\partial T}{\partial r} = \frac{Q/12k}{Ms^2}\left\{\frac{\sqrt{3}}{\pi}\ln\frac{r}{r_0} - \frac{1}{4}\left[\left(\frac{r}{s}\right)^2 - \left(\frac{r_0}{s}\right)^2\right]\right\} \tag{34a}$$

$$T(r_0) = T_w, \qquad \frac{\partial T}{\partial r}(r^*) = 0 \tag{34b}$$

From this, the solution for the temperature is found to be

$$T - T_w = \frac{Q/12k}{Ms^2}\left\{\left[\frac{\sqrt{3}}{4\pi}(r^2 + r_0^2) - \frac{1}{16}\frac{r_0^4}{s^2} - \frac{6Ms^2}{\pi}\right]\ln\frac{r}{r_0} - \frac{1}{64}\frac{(r^4 - r_0^4)}{s^2} + \left[-\frac{\sqrt{3}}{4\pi} + \frac{1}{16}\left(\frac{r_0}{s}\right)^2\right](r^2 - r_0^2)\right\} \tag{35}$$

It may be seen by inspection that this result is identical to the nonseries portion of the more complete temperature solution (15).

To compare the over-all heat-transfer characteristics with those previously obtained, we compute the wall-to-bulk temperature difference. Applying the definition of the bulk temperature from equation (21) to the annulus, there is obtained,

$$T_w - T_b = \frac{2\pi\rho\int_{r_0}^{r^*}(T_w - T)ur\,dr}{w} \tag{36}$$

By substituting from equations (32) and (35), the integrand can be evaluated and then the integration carried out. The same type of functional relation which has been noted in equation (23) has also been found here. The end result of the calculation is reproduced in the Appendix to facilitate numerical calculations for s/r_0 values which lie outside the range reported here.

With the wall-to-bulk temperature difference at our disposal, the Nusselt number Nu_d can be evaluated from equation (25). The results thus obtained have been plotted as a dotted line on Fig. 3, left-hand ordinate. By comparing with the solid curve from the more exact calculation, it is seen that the neglect of circumferential variations leads to a smaller wall-to-bulk temperature difference at a fixed heat transfer per unit length. So, for a given bulk temperature at a cross section, the wall temperature prediction from the simplified calculation is low. If errors up to 5 per cent in the Nusselt number prediction can be tolerated, then from Fig. 3 it is found that the results based on the neglect of circumferential variations may be used for spacing ratios as low as 1.5. As the spacing becomes progressively smaller, the deviations become increasingly larger. The same comments apply to the Nu_{d_e} curves associated with the right-hand ordinate

An analysis using the equivalent annulus approximation has been carried out in reference [3] for turbulent flow for spacings down to 1.375. If the flow is fully turbulent, then the effects of circumferential variations will likely be smaller than in a laminar flow. On this basis, we may conclude that the use of the equivalent annulus model appears justifiable in the turbulent case for the spacings considered in reference [3].

Concluding Remarks

The analysis presented here is for the condition of fully developed heat transfer. It is therefore of interest to inquire about the heated length required to achieve fully developed conditions. Unfortunately, there appears to be no information available about the thermal entrance region for the specific geometry under consideration here; and, in general, there is very little known about the thermal entrance region in noncircular ducts. An indication of the complexity of the entrance region problem may be found from the experiments of Eckert and Irvine [4] who studied turbulent heat transfer in an electrically heated isosceles triangular duct having an apex angle of 11.5 deg. They found that the entrance length was markedly longer than in a circular tube and, further, that the fully developed condition was not achieved simultaneously at all points around the periphery of the cross section. These findings serve to generally discourage the application of circular tube results to noncircular ducts.

The boundary conditions considered in this paper were a longitudinally uniform heat flux and a circumferentially uniform surface temperature. It may be useful to discuss qualitatively the heat-transfer results which might be expected for other boundary

conditions. For the situation where the heat flux is both longitudinally and circumferentially uniform, it has already been noted that the Nusselt number results are essentially unchanged from those found here provided that $s/r_0 > 1.5$. For progressively smaller spacings, significant circumferential nonuniformities in surface temperature can develop. If a heat-transfer coefficient for this situation were defined based on a circumferentially averaged surface temperature, it would be expected that the corresponding Nusselt numbers would fall below[6] those of Fig. 3 (solid lines). For the situation where the surface temperature is both longitudinally and circumferentially uniform, a fully developed heat-transfer condition also exists. For this case, it would be expected that a Nusselt number based on the wall-to-bulk temperature difference would also fall below that found here. Of course, for the case of longitudinally uniform surface temperature, the bulk temperature is no longer given by equation (19).

For situations where fully developed heat-transfer conditions do not exist, there is often a temptation to locally apply the fully developed results. For laminar flows, such a procedure may lead to inaccuracies even in circular geometries, and for noncircular ducts, it is additionally risky.

[6] Such trends were also reported in reference [5] for a circular sector duct.

APPENDIX

(a) Integral Table.

All integrals are over the range 0 to $\pi/6$

$$\int \theta \tan\theta \, d\theta = 0.05069781$$

$$\int (\ln\cos\theta)\cos 6\theta \, d\theta = 0.0150977$$

$$\int \frac{(\ln\cos\theta)\cos 6\theta \, d\theta}{(\cos\theta)^{8}} = 0.0370858$$

$$\int \frac{(\ln\cos\theta)\cos 12\theta \, d\theta}{(\cos\theta)^{14}} = -0.0434739$$

$$\int \frac{(\ln\cos\theta)\cos 6\theta \, d\theta}{(\cos\theta)^{10}} = 0.04655214$$

$$\int \frac{(\ln\cos\theta)\cos 12\theta \, d\theta}{(\cos\theta)^{16}} = -0.0577564$$

$$\int \frac{(\ln\cos\theta)\cos 6\theta \, d\theta}{(\cos\theta)^{-4}} = 0.00966175$$

$$\int \frac{(\ln\cos\theta)\cos 12\theta \, d\theta}{(\cos\theta)^{-10}} = 0.000874072$$

$$\int \frac{(\ln\cos\theta)\cos 6\theta \, d\theta}{(\cos\theta)^{-2}} = 0.01207813$$

$$\int \frac{(\ln\cos\theta)\cos 12\theta \, d\theta}{(\cos\theta)^{-8}} = 0.000413828$$

$$\int \frac{\cos 6\theta \, d\theta}{(\cos\theta)^{8}} = -0.195504853059$$

$$\int \frac{\cos 12\theta \, d\theta}{(\cos\theta)^{14}} = 0.24953325973$$

$$\int \frac{\cos 6\theta \, d\theta}{(\cos\theta)^{-4}} = 0.0487139289629$$

$$\int \frac{\cos 12\theta \, d\theta}{(\cos\theta)^{-10}} = 0.00934144946$$

$$\int \frac{\cos 6\theta \, d\theta}{(\cos\theta)^{10}} = -0.278775438621$$

$$\int \frac{\cos 12\theta \, d\theta}{(\cos\theta)^{16}} = 0.35013873273$$

$$\int \frac{\cos 6\theta \, d\theta}{(\cos\theta)^{-2}} = 0.0270632938683$$

$$\int \frac{\cos 12\theta \, d\theta}{(\cos\theta)^{-8}} = -0.01065617196$$

$$\int \frac{\cos 6\theta \, d\theta}{(\cos\theta)^{12}} = -0.3833738263351$$

$$\int \frac{\cos 12\theta \, d\theta}{(\cos\theta)^{18}} = 0.4834095306$$

$$\int \frac{\cos 12\theta \, d\theta}{(\cos\theta)^{-6}} = -0.01087364485$$

$$\int \frac{\cos 12\theta \, d\theta}{(\cos\theta)^{2}} = 0.00993262699$$

$$\int \frac{\cos 12\theta \, d\theta}{(\cos\theta)^{4}} = 0.02483882327$$

$$\int (\cos\theta)^{6} d\theta = 0.37912963362$$

$$\int (\cos\theta)^{10} \, d\theta = 0.354917462776$$

$$\int (\cos\theta)^{-14} \, d\theta = 1.2290323215$$

$$\int (\cos\theta)^{-18} \, d\theta = 1.43544637803$$

(b) Wall-to-Bulk Temperature Difference for Equivalent Annulus.

Let

$$\alpha = r_0/s, \qquad \beta = \left[\frac{2\sqrt{3}}{\pi}\right]^{1/2}$$

Then

$$\begin{aligned}\frac{T_b - T_w}{(Q/12k)(\pi/6M^2)} = \frac{3}{4\pi^2}\Bigg[&\frac{\beta^4}{4}\left(\ln\frac{\beta}{\alpha}\right)^2 - \frac{1}{8}\beta^4\left(\ln\frac{\beta}{\alpha}\right) + \frac{1}{32}\beta^4 - \frac{1}{32}\alpha^4\Bigg] \\ &+ \frac{\sqrt{3}}{\pi}\left[-\frac{6M}{\pi} + \frac{\sqrt{3}}{4\pi}\alpha^2 - \frac{1}{16}\alpha^4\right] \\ &\left[\frac{\beta^2}{2}\left(\ln\frac{\beta}{\alpha}\right)^2 - \frac{\beta^2}{2}\left(\ln\frac{\beta}{\alpha}\right) + \frac{\beta^2}{4} - \frac{\alpha^2}{4}\right] \\ &- \frac{5\sqrt{3}}{64\pi}\left[\frac{\beta^6}{6}\left(\ln\frac{\beta}{\alpha}\right) - \frac{\beta^6}{36} + \frac{\alpha^6}{36}\right] + \frac{1}{2048}[\beta^8 - \alpha^8] \\ &+ \left\{\left[-\frac{3}{4\pi^2} + \frac{\sqrt{3}}{16\pi}\alpha^2 + \frac{3M}{2\pi} + \frac{\alpha^4}{64}\right]\right. \\ &\left.\left[\frac{\beta^4}{4}\left(\ln\frac{\beta}{\alpha}\right) - \frac{\beta^4}{16} + \frac{\alpha^4}{16}\right]\right\} \\ &+ \left[\frac{3}{4\pi^2}\alpha^2 + \frac{\sqrt{3}}{64\pi}\alpha^4 - \frac{3M}{2\pi}\alpha^2 - \frac{1}{64}\alpha^6\right]\end{aligned}$$

$$\left[\frac{\beta^2}{2}\left(\ln\frac{\beta}{\alpha}\right)-\frac{\beta^2}{4}+\frac{\alpha^2}{4}\right]+\left[\frac{\sqrt{3}}{16\pi}-\frac{5}{256}\alpha^2\right]\frac{(\beta^6-\alpha^6)}{6}$$
$$+\left(-\frac{\sqrt{3}}{8\pi}\alpha^2+\frac{7}{256}\alpha^4\right)\frac{(\beta^4-\alpha^4)}{4}$$
$$+\left[\frac{\sqrt{3}}{16\pi}\alpha^4-\frac{3}{256}\alpha^6\right]\frac{(\beta^2-\alpha^2)}{2}$$

References

1 E. M. Sparrow and A. L. Loeffler, Jr., "Longitudinal Laminar Flow Between Cylinders Arranged in Regular Array," *AIChE Journal*, vol. 5, 1959, pp. 325–329.

2 James P. Hartnett and Thomas F. Irvine, Jr., "Nusselt Values for Estimating Turbulent Liquid Metal Heat Transfer in Noncircular Ducts," *AIChE Journal*, vol. 3, 1957, pp. 313–317.

3 O. E. Dwyer and P. S. Tu, "Heat Transfer Rates for Parallel Flow of Liquid Metals Through Tube Bundles—I," AIChE Paper No. 119, Third National Heat Transfer Conference, Storrs, Conn., 1959.

4 E. R. G. Eckert and T. F. Irvine, Jr., "Pressure Drop and Heat Transfer in a Duct With Triangular Cross Section," JOURNAL OF HEAT TRANSFER, TRANS. ASME, Series C, vol. 82, 1960, pp. 125–138.

5 E. R. G. Eckert, T. F. Irvine, Jr., and J. T. Yen, "Local Laminar Heat Transfer in Wedge-Shaped Passages," TRANS. ASME, vol. 80, 1958, pp. 1433–1438.

DISCUSSION

John Happel[7]

It is interesting to note that the equivalent annulus formulation shown in Fig. 3 gives results which are close to the exact treatment for s/r_0 spacing ratios down to 1.5. The writer had the opportunity to review the senior authors' paper, reference [1], which was concerned with the hydrodynamic problem of longitudinal laminar flow between cylinders and mentioned that the annulus model now used by them for their simplified heat-transfer formulation gave the leading term in their fluid flow treatment [equations (3) and (32) in the present paper]. An extension of this simplified hydrodynamic model, designated as the "free-surface model," is also useful in more complicated problems such as flow perpendicular to arrays of cylinders (J. Happel, *AIChE Journal*, vol. 5, 1959, p. 174) and through beds of spheres (J. Happel, *AIChE Journal*, vol. 4, 1958, p. 197) at low velocities. It was also suggested that it might be useful to apply it not only to the case of longitudinal flow heat transfer as the present authors have done. For flow perpendicular to cylinders or around spheres it is, of course, apparent that the heat-transfer problem will be more complicated since convective contributions will appear, resulting in a peripheral variation of wall heat transfer even at large spacings. However, the success of the model in predicting hydrodynamic behavior in such systems leads me to believe that extension to heat transfer may be successful at least in a limited range and perhaps lead to useful methods of data correlation.

[7] Professor and Chairman, Dept. of Chemical Engineering, New York University, College of Engineering, New York, N. Y.

Authors' Closure

The authors thank Professor Happel for his interest and for his illuminating remarks. The problems to which he has reference in the latter part of his discussion are exceedingly difficult, and some approximate approach seems very much in order. The "free surface model" suggested by Professor Happel appears to be a good starting point for analysis.

Axial Temperature Distribution for a Nuclear Reactor With Sinusoidal Space and Exponential Time-Varying Power Generation

W. O. DOGGETT
Associate Professor, Department of Physics, North Carolina State College, Raleigh, N. C.

E. L. ARNOLD
Assistant Professor, Department of Electrical Engineering, U. S. Military Academy, West Point, N. Y.

Analytic temperature distributions are obtained for the fuel and coolant regions of a heterogeneous, convection-cooled reactor with axial power variation $e^{\omega t} \sin(\pi z/H)$. The fundamental assumption in the governing differential equations is that the temperature distribution in the fuel region does not vary in the direction transverse to the coolant flow. The solutions involve two and three-parameter integrals encountered and numerically evaluated previously which are integrated herein and arranged in a form suitable for desk calculations. Closed-form expressions are developed for the final steady-state axial distributions which are applicable at times long in comparison with the characteristic temperature-response times.

Introduction

The equations governing heat conduction and transfer in a convection-cooled, heterogeneous core have been presented by several authors [1, 2].[1] The rigorous formulation takes into account the time variation of both the axial and transverse temperature distribution in the fuel and coolant regions. Solutions have been obtained for special conditions such as step power change with constant coolant temperature [3], zero velocity coolant [4], and insulated fuel elements [5]. In general, these special cases lead to nonclosed-form solutions which require numerical evaluation for each point of interest. An integral formulation has been used to obtain an approximation for the shutdown transient temperature of a reactor core [6]. For cases with turbulent flow in which the fuel plates are sufficiently thin, the transverse variation can be suppressed in the time-dependent equations. Then the effect of heat absorption and the attendant temperature rise of the fuel are adequately described by a bulk model based on a heat-capacity concept. The resulting heat-balance equations have been solved for general time-dependent but space-independent power variation [7]. The solutions contained nonclosed-form functions, some of which had been tabulated in earlier work [8]. Agreement between these solu-

[1] Numbers in brackets designate References at end of paper.

Contributed by the Heat Transfer Division and presented at the Winter Annual Meeting, New York, N. Y., November 27–December 2, 1960, of The American Society of Mechanical Engineers. Manuscript received at ASME Headquarters, August 22, 1960. Paper No. 60—WA-194.

Nomenclature

a = $RcM = v\tau_c = H\tau_c/\tau_s$ characteristic distance that coolant flows during coolant response time τ_c, ft
a_i, i = 0, 1, 2, 3, = defined in equation (37)
A = area of coolant channel in a plane transverse to axial-flow direction, sq ft
A_f = area of fuel plate in a plane transverse to direction of coolant flow, sq ft
$b(s)$ = defined in equation (30)
b_i, i = 1, 2, 3, = defined in equation (32)
B^2 = $(\pi/H)^2$, axial buckling of reactor, ft^{-2}
c = specific heat of coolant, Btu/lb$_M$-deg F
c_f = specific heat of fuel region, Btu/lb$_M$-deg F
c_i, i = 1, 2, . . ., 6, = coefficients of time functions, equations (10), (41), and (44)
d_i, i = 2, 3, . . ., 6, = coefficients of time functions, equations (10), (40), and (44)
d = reactor power density extrapolation distance, ft
$f(s)$ = defined in equation (36)
$F(z, t)$ = general function of z and t
$\bar{F}(z, s)$ = general function Laplace transformed with respect to t
$\bar{\bar{F}}(p, s)$ = general function Laplace transformed with respect to t and z
$g_i(s), i$ = 1, 2, . . ., 8, = Laplace transform functions defined in Table 1
$G_i(t), i$ = 1, 2, . . ., 8, = functions of time defined in Table 1
$G_i(t)*G_j(t)$ = convolution integral of $G_i(t)$ and $G_j(t)$, equation (43)
H = axial core height, ft
i = summing index
$I_n(x)$ = modified Bessel function of first kind and nth order
k = summing index
K = $\dfrac{c_4 - c_3\alpha}{c_3\beta}$ = dimensionless constant introduced in the Appendix (section, "Evaluation of the ψ_Γ-Functions")
L_t = Laplace transform operator with respect to time, sec
L_z = Laplace transform operator with respect to distance, ft
L_z^{-1} = inverse Laplace transform operator, ft^{-1}
M = ρAv = coolant mass-flow rate, lb$_M$/sec^{-1}
p = complex variable used in Laplace transform with respect to distance, ft^{-1}

(*Continued on next page*)

tions and experimental measurements was good. In the present paper we solve the heat-balance equations for the axial power variation $e^{wt} \sin (\pi z/H)$. The Nomenclature in this paper generally conforms with that used in reactor calculations [9].

The solution developed herein is exact and rigorously complete. It is recognized that excellent approximate numerical methods have been developed which may be applied to this problem. However, the usefulness of exact analytic solutions for checking convergence of approximate methods and for parameter studies is well known. A discussion of the relative merits of exact versus approximate numerical techniques may be found in the Discussion and Authors' Closure in reference [7].

Formulation of the Problem

Consider the bare cell in Fig. 1. The axial power density in the fuel in Btu/sec-ft is

$$\begin{aligned} P(z, t) &= P_0 \sin (\pi z/H), \qquad t \leq 0 \\ P(z, t) &= P_0 e^{wt} \sin (\pi z/H), \qquad t \geq 0 \end{aligned} \tag{1}$$

where w is the reciprocal period and H is the axial length of the fuel plate. Generalization of this power to the case of a reflected core is straightforward although not presented here.

The following assumptions are imposed:

1 No power is produced in the coolant.

2 Axial enthalpy transfer in the cell is due to coolant flow only.

3 The coolant temperature and velocity are constant across the flow cross section.

4 The fuel temperature distribution does not vary in the transverse direction (valid for sufficiently thin plates).

5 The following quantities are constant and uniform throughout:

Coolant flow area, entering coolant temperature, heat-transfer coefficient, coolant velocity, and fuel and coolant properties.

The heat-conservation equations based on the first law of thermodynamics for an element of fuel and incompressible coolant at z of thickness dz are

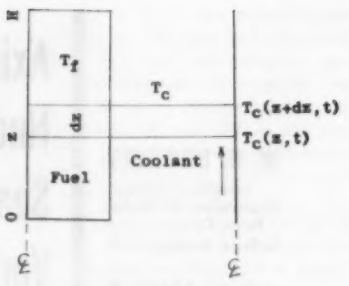

Fig. 1 Fuel-coolant half cell

$$P(z, t)dz = A_f \rho_f c_f dz \frac{\partial T_f(z, t)}{\partial t} + \frac{dz}{R} [T_f(z, t) - T_c(z, t)] \tag{2}$$

$$A\rho c dz \frac{\partial T_c(z, t)}{\partial t} = \frac{dz}{R} [T_f(z, t) - T_c(z, t)] - cM[T_c(z + dz, t) - T_c(z, t)] \tag{3}$$

in which T_f is the local fuel-plate temperature, deg F, and T_c is the bulk coolant temperature, deg F. Other symbols are defined in the Nomenclature. Equation (2) states that a fraction of the power generated in the fuel channel stays there and increases its temperature, while the remainder is transferred to the coolant. Equation (3) states that the temperature of the element of the coolant is increased by the heat transferred from the fuel less the heat removed by coolant flow. Equations (2) and (3) are based on the frequently used "thin-fuel-element" approximation in which the local fuel-region temperature is equal to the local surface temperature. Cylindrical and other geometries may be represented by these equations provided the film resistance R

Nomenclature

$P(z, t)dz$ = axial power density, Btu/sec-ft

$P_n(z, t) = RP(z, t)$ = normalized axial power density, deg F

$\bar{P}_n(z, s)$ = Laplace transform with respect to time of normalized power density, deg F-sec

$\bar{P}_n'(p, s)$ = double Laplace transform with respect to t and z of normalized axial power density, deg F-sec-ft

P_0 = axial peak power density, Btu/sec-ft

$q = t^*\left(\frac{1}{t_f} - \alpha\right)$ = dimensionless shifted time, equation (47)

$q' = t^*/\tau_f$, dimensionless shifted time, equation (45)

$q'' = t^*(w + 1/\tau_f)$ = dimensionless shifted time, equation (46)

$r = \frac{\beta}{(1/\tau_f) - \alpha}$ dimensionless "frequency," equation (47)

R = film resistance for heat flow from fuel region to coolant, sec-ft-deg F/Btu

s = complex variable used in Laplace transform with respect to time except in equation (47) and Appendix (section, "Evaluation of the $\frac{\psi}{\phi}_{\Gamma}$-Functions"), sec^{-1}

$s = \frac{z}{a\tau_f\left(\frac{1}{\tau_f} - \alpha\right)}$ = dimensionless distance in equation (47) and Appendix (section as above)

$s' = z/a$ dimensionless distance, equation (45)

$s'' = \frac{z}{a\tau_f(w + 1/\tau_f)}$ = dimensionless distance, equation (46)

$s_{3,4}, s_{5,6}$ = roots of denominator of $f(s)$, equation (37)

$S(t^*)$ = unit step function, $S(t^*) = 0$ for $t^* < 0$ and $S(t^*) = 1$ for $t^* > 0$, dimensionless

t = time, sec

$t^* = t - \tau_c z/H$ = shifted time, sec

$T_c(z, t)$ = local coolant temperature, deg F

$T_c(z, 0)$ = initial local coolant temperature, deg F

$T_c(0) = T_c(0, 0)$ = constant entering coolant temperature, deg F

$\bar{T}_c(z, s)$ = Laplace transform with respect to t of coolant temperature distribution, deg F-sec

$\bar{T}_c'(p, s)$ = double Laplace transform with respect to t and z of coolant temperature, deg F-sec-ft

$T_c^{\circ\prime}(p, t = 0)$ = Laplace transform with respect to z of initial coolant temperature distribution, deg F-ft

(Continued on next page)

(assumed constant) is suitably specified.[2] In solving equations (2) and (3), the following characteristic times and distance will appear naturally:

$$\tau_f = RA_fc_f\rho_f, \text{ sec} \qquad \tau_v = H/v, \text{ sec}$$
$$\tau_c = RAc\rho, \text{ sec} \qquad a = RcM = v\tau_c = H\tau_c/\tau_v, \text{ ft}$$

With these definitions, equations (2) and (3) become

$$\tau_f \frac{\partial T_f}{\partial t} = P_n(z, t) - [T_f(z, t) - T_c(z, t)] \tag{4}$$

$$\tau_c \frac{\partial T_c}{\partial t} = [T_f(z, t) - T_c(z, t)] - a \frac{\partial T_c}{\partial z} \tag{5}$$

in which

$$\frac{\partial T_c}{\partial z} dz = T_c(z + dz, t) - T_c(z, t)$$
$$P_n(z, t) = RP(z, t) \tag{6}$$

These equations are frequently averaged over the core and employed in analog studies [11, 12, 13]. Solutions have been obtained for periodic power behavior [10, 14]. If the power rise is slow compared to the characteristic time τ_f associated with the heat capacity of the fuel; i.e., $w\tau_f \ll 1$, the energy retained by the fuel is negligible in comparison to that transferred to the coolant. Then the term $\tau_f(\partial T_f/\partial t)$ is negligible in comparison with either P_n or $T_f - T_c$ in equation (4), and τ_f may be set equal to zero with negligible error. The resulting equation,

$$\tau_c \frac{\partial T_c}{\partial t} = P_n - a \frac{\partial T_c}{\partial z} \tag{7}$$

is that which would be obtained if it were initially assumed that the generated power appeared instantaneously in the coolant with no time lag. Closed-form solutions to equation (7) have been developed [15] for the reflected core with the chopped-sine power density

$$P_0e^{wt} \sin [\pi(z + d)/H]$$

[2] See footnote 4 of reference [7], regarding comments by T. Irvine on the variation of the film coefficient.

Solution of Equations

Equations (4) and (5) can be solved by use of Laplace transforms. The initial conditions are taken as the steady-state distributions for power density $P_0 \sin (\pi z/H)$ with total channel power $2P_0H/\pi$ and constant entering temperature $T_c(0) = T(0, 0)$,

$$T_c(z, 0) = T_c(0) + \frac{P_0H}{\pi cM}\left(1 - \cos \frac{\pi z}{H}\right) \tag{8}$$

$$T_f(z, 0) = RP_0 \sin \frac{\pi z}{H} + T_c(z, 0) \tag{9}$$

The details of the transform solution are given in the Appendix. The result for the coolant is[3]

$$T_c(z, t) = T_c(0) + \frac{P_0H}{\pi cM}\left[\left(1 - \cos \frac{\pi z}{H}\right)\right.$$
$$+ \frac{\pi^2 w}{\tau_v^2} e^{-z/a}[1 + G_7(t)^*] \sum_{i=1}^{6} c_i[G_i(t^*)S(t^*)]$$
$$- \frac{\pi^2 w}{\tau_v^2} \sum_{i=1}^{6} c_iG_i(t) \cos \frac{\pi z}{H}$$
$$\left. + \frac{\pi w}{\tau_v\tau_c}[\tau_c + G_8(t)^*] \sum_{i=2}^{6} d_iG_i(t) \sin \frac{\pi z}{H}\right] \tag{10}$$

in which $t^* = t - \tau_c z/H$. The time functions $G_i(t)$ are listed in Table 1. The constants c_i and d_i depend on the characteristic values and the reciprocal period. $S(t^*)$ is the unit step function and $G_i(t)^*G_j(t)$ is the convolution integral defined by equation (43) in the Appendix. The convolutions are written explicitly in the first section of the Appendix. The solution for the fuel temperature is closely related to equation (10) and is described in the second section of the Appendix.

The variation of the axial temperature distributions approaches a constant shape at a time long compared with the characteristic times. The asymptotic coolant temperature reduces to the simple closed form (fourth section of the Appendix)

[3] Note that $G_7(t)$ contains z as parameter.

Nomenclature

$\bar{T}_c^{\circ}(z = 0, s)$ = Laplace transform with respect to t of entering coolant temperature, deg F-sec
$T_f(z, t)$ = local fuel plate temperature, deg F
$T_f(z, 0)$ = initial local fuel temperature, deg F
$\bar{T}_f(z, s)$ = Laplace transform with respect to time of fuel temperature, deg F-sec
$\bar{T}_f'(p, s)$ = double Laplace transform with respect to t and z of fuel temperature, deg F-sec-ft
$T_f^{\circ\prime}(p, t = 0)$ = Laplace transform with respect to z of initial fuel temperature distribution, deg F-sec
v = coolant velocity, fps
w = reciprocal period, sec^{-1}
x = dummy variable except in Figs. 3, 4, and 5
x = real part of s in Figs. 3, 4, and 5, sec^{-1}
X = defined after equation (39), sec^{-2}
y = dummy variable except in Figs. 3, 4, and 5
y = imaginary part of s in Figs. 3, 4, and 5, sec^{-1}
Y = defined after equation (39), sec^{-2}
z = axial distance, ft
Z = defined after equation (39), sec^{-2}
α, γ = negative real part of roots $-s_{3,4}$ and $-s_{5,6}$, sec^{-1}
β, δ = imaginary part of roots $s_{3,4}$ and $s_{5,6}$, sec^{-1}
$\eta = 1 + \dfrac{\tau_f/\tau_c}{1 + w\tau_f}$ = factor appearing in equation (11), dimensionless
θ_w = $\tan^{-1}(w/\lambda)$ = phase shift associated with relative magnitude of reactor period and characteristic coolant flow time, radians
λ = $\pi v/H = \pi/\tau_v$ = characteristic reciprocal time for coolant flow, sec^{-1}
ρ = density of coolant, lb$_M$/ft^3
ρ_f = density of fuel region, lb$_M$/ft^3
τ_c = $RAc\rho$ = characteristic coolant response time, sec
τ_f = $RA_fc_f\rho_f$ = characteristic fuel response time, sec
τ_v = H/v = time required for an element of coolant to pass through core, sec
$\psi_2(s', q')$, $\psi_2(s'', q'')$ = special functions of time and distance, equations (45) and (46), dimensionless
$\psi_7(s, q, r)$, $\psi_8(s, q, r)$, $\psi_9(s, q, r)$, $\psi_{10}(s, q, r)$ = special functions of time and distance, dimensionless

$$T_c(z, t) = T_c(0) + \frac{P_0 H}{\pi c M} \frac{e^{wt}}{(1 + w\tau_f)\left[1 + \left(\frac{w\tau_v \eta}{\pi}\right)^2\right]} \tag{11}$$

$$\times \left\{ e^{-w\tau_v \eta z/H} - \left[1 + \left(\frac{w\tau_v \eta}{\pi}\right)^2\right]^{1/2} \cos\left(\frac{\pi z}{H} + \tan^{-1}\frac{w\tau_v \eta}{\pi}\right)\right\}$$

in which

$$\eta = 1 + \frac{\tau_f/\tau_c}{1 + w\tau_f}$$

Similarly, the asymptotic fuel temperature is

$$T_f(z, t) = T_c(0) + \frac{1}{1 + w\tau_f}\left[RP_0 e^{wt} \sin\frac{\pi z}{H} + T_c(z, t) - T_c(0)\right] \tag{12}$$

where $T_c(z, t) - T_c(0)$ is given by equation (11). These forms reduce to previously obtained closed-form solutions [15] for the limiting case $\tau_f = 0$ for which $\eta = 1$:

$$T_c(z, t) = T_c(0) + \frac{P_0 H}{\pi c M} \frac{e^{wt}}{\left[1 + \left(\frac{w\tau_c}{\pi}\right)^2\right]}$$

$$\times \left\{ e^{-w\tau_v z/H} - \left[1 + \left(\frac{w\tau_c}{\pi}\right)^2\right]^{1/2} \cos\left(\frac{\pi z}{H} + \tan^{-1}\frac{w\tau_v}{\pi}\right)\right\}$$

$$t \geq \tau_v z/H \tag{13}$$

$$T_f(z, t) = T_c(0) + \left[RP_0 e^{wt} \sin\frac{\pi z}{H} + T_c(z, t) - T_c(0)\right]$$

$$t \geq \tau_v z/H \tag{14}$$

Thus at long times after the onset of the transient, the effect of the lag time associated with nonzero fuel heat capacity ($\tau_f \neq 0$) is seen (a) to increase effectively the characteristic coolant flow time τ_v by the factor η, which is dependent on the relative magnitude of τ_f to τ_c and the reactor period $1/w$, and (b) to decrease the temperature rise by the factor $(1 + w\tau_f)^{-1}$.

Numerical Comparison With Closed-Form Solutions

Numerical calculations were made for a typical heterogeneous reactor with metal fuel plates and water coolant. Characteristic constants are $\tau_f = 0.1$ sec and $\tau_c = \tau_v = 0.5$ sec. Coolant temperature distributions were computed for three reciprocal periods, equal to $2.5/\tau_v$, $1/\tau_v$, and $0.1/\tau_v$, at time 0.25 sec following the onset of the transient. All terms in equation (10) contributed to the calculated distributions in the lower half of the core for which $t \geq \tau_v z/H$, whereas the step function in the first sum in equation (10) made this sum vanish for the upper half of the core for which $t \leq \tau_v z/H$. These results are shown in Fig. 2, along with distributions obtained in the limiting case, $\tau_f = 0$. The latter curves are given by the following closed-form expressions [15]:

$$T_c(z, t) = T_c(0) + \frac{P_0 H}{\pi c M}\left\{1 - \cos\left(\lambda t - \frac{\pi z}{H}\right) + \frac{\lambda}{(w^2 + \lambda^2)^{1/2}}\left[\cos\left(\lambda t - \frac{\pi z}{H} - \theta_w\right) - e^{wt}\cos\left(\frac{\pi z}{H} + \theta_w\right)\right]\right\}, \quad t \leq \tau_v z/H \tag{15}$$

and

$$T_c(z, t) = T_c(0) + \frac{P_0 H}{\pi c M}\frac{\lambda}{(w^2 + \lambda^2)^{1/2}} e^{wt}\left[\frac{\lambda}{(w^2 + \lambda^2)^{1/2}} e^{-w\tau_v z/H} - \cos\left(\frac{\pi z}{H} + \theta_w\right)\right], \quad t \geq \tau_v z/H \tag{16}$$

in which $\theta_w = \tan^{-1}(w/\lambda)$ and $\lambda = \pi v/H = \pi/\tau_v$.

For slow variations, $w \leq 0.1/\tau_v = 0.2$ sec^{-1}, the closed-form solutions accurately predict the distribution. Thus for normal reactor operation with periods greater than 5 sec, the limiting forms for $\tau_f = 0$ can be used. It is interesting to note that the peak coolant temperature is no longer at the exit of the reactor for fast periods, but shifts toward the center.

Another series of calculations was performed to compare the asymptotic solution equation (11) with the exact solution equation (10) for the coolant distribution. The same characteristic constants were used with $t = 4$ sec for $w = 0.2$ and 5 sec^{-1}. The results agreed to three significant figures.

Acknowledgments

The authors are indebted to Dr. Raymond L. Murray for early discussions which led to undertaking this work. The authors also gratefully acknowledge the careful review of the paper by Dr. Thomas F. Irvine, Jr., and wish to express their appreciation to Prof. John A. Clark for bringing to their attention his evaluation of the functions ψ_7 and ψ_8 prior to publication, to Mr. Susumu Terayama and Mr. Makio Amano for their diligent calculational efforts, and to Dr. J. W. Carr III for providing operational time on the UNIVAC 1105 digital computer at the Computational Center of the University of North Carolina.

References

1 J. P. Silvers and J. R. Dietrich, "The Reactor Handbook," vol. 2, Engineering USAEC, 1955, p. 156.

2 R. P. Stein, "Transient Heat Transfer in Reactor Coolant Channels," AECU 3600, USAEC, 1957.

3 L. G. Epel, "Transient Temperatures in Infinite Plates, Infinite Cylinders, and Spheres Following a Simultaneous Step Change in Internal Heat Generation Rate, Coolant Temperature, and Heat-Transfer Coefficient," ORNL 2597, USAEC, 1958.

4 H. L. McMurray, "Temperature Distribution in a Fuel Plate With Exponentially Rising Power," IDO 16214, USAEC, 1955.

5 Francis Narin and David Langford, "Analytic Solutions for Transient Temperature Distributions in Two-Region Nuclear Reactor Fuel Elements," *Nuclear Science and Engineering*, vol. 6, 1959, p. 386.

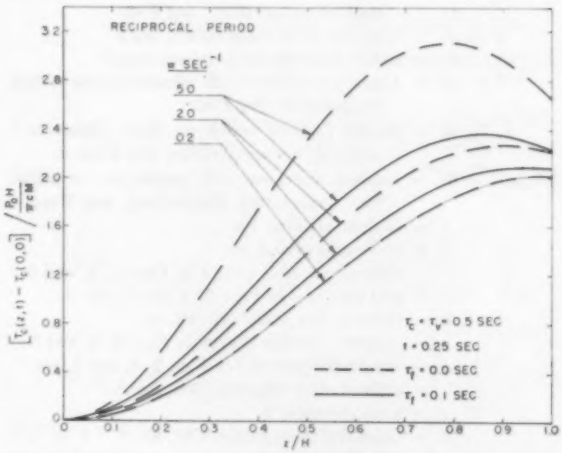

Fig. 2 Dimensionless coolant temperature spatial distribution

6 W. C. Reynolds and T. A. Dolton, "The Use of Integral Methods in Transient Heat Transfer Analysis," ASME Paper No. 58—A-248.

7 V. S. Arpaci and J. A. Clark, "Dynamic Response of Heat Exchangers Having Internal Heat Sources—Part III," JOURNAL OF HEAT TRANSFER, TRANS. ASME, Series C, vol. 81, 1959, pp. 253–266.

8 J. A. Clark, V. S. Arpaci, and K. M. Treadwell, "Response of Nuclear Reactor Coolant to Power Transients," TID 7529, vol. 1, USAEC, 1957, p. 79.

9 R. L. Murray, "Nuclear Reactor Physics," Prentice-Hall, Inc., Englewood Cliffs, N. J., 1957.

10 W. J. Yang, J. A. Clark, and V. S. Arpaci, "Dynamic Response of Heat Exchangers Having Internal Heat Sources—Part IV," JOURNAL OF HEAT TRANSFER, TRANS. ASME, Series C, vol. 83, 1961, p. 321.

11 R. P. Rose and S. O. Johnson, "A Method of Evaluating Heat Transfer Simulation in Pressurized Water Reactors," Report WAPD-T-542, Westinghouse Electric Corporation, Atomic Power Division, Bettis Field, Pa., 1956.

12 T. P. Bump and H. O. Monson, "Predicted Dynamic Behavior of EBR-II," Second International Conference on the Peaceful Uses of Atomic Energy, Geneva, Switzerland, 1958, paper 458.

13 E. P. Gyftopoulos and H. B. Smets, "Transfer Functions of Distributed Parameter Nuclear Reactor Systems," *Nuclear Sciences and Engineering*, vol. 5, 1959, p. 405.

14 Fred Storrer, "Temperature Response to Power Oscillations in a Solid Fuel Reactor," Paper No. 12-7, *Transactions of The American Nuclear Society*, 1959 Annual Meeting, Gatlinburg, Tenn., June, 1959.

15 W. O. Doggett, E. L. Arnold, and R. L. Murray, "Axial Temperature Distributions for a Heterogeneous Reactor During Slow Exponential Power Variation," to appear in *Nuclear Science and Engineering*.

16 R. V. Churchill, "Introduction to Complex Variables and Applications," McGraw-Hill Book Company, Inc., New York, N. Y., 1948.

17 J. W. Rizika, "Thermal Lags in Flowing Systems Containing Heat Capacitors," TRANS. ASME, vol. 76, 1954, p. 411; see also TRANS. ASME, vol. 78, 1956, p. 1407.

18 W. G. Bickley, et al., "Bessel Functions—Part II, Functions of Positive Integer Order," Mathematical Tables, vol. 10, British Association of the Advancement of Science, University Press, Cambridge, England, 1952, table 7.

APPENDIX

Coolant Temperature Distribution

Define the Laplace transform with respect to t as

$$L_t[F(z, t)] = \bar{F}(z, s) \tag{17}$$

and the subsequent Laplace transform with respect to z as

$$L_z[\bar{F}(z, s)] = \bar{F}'(p, s) \tag{18}$$

Also define the transforms of the initial and boundary conditions

$$\begin{aligned} L_z[T_c(z, t = 0)] &= T_c^{\circ\prime}(p, t = 0) \\ L_z[T_f(z, t = 0)] &= T_f^{\circ\prime}(p, t = 0) \\ L_t[T_c(z = 0, t)] &= \bar{T}_c^{\circ}(z = 0, s) \end{aligned} \tag{19}$$

The Laplace transforms of equations (4) and (5) are

$$\tau_f[s\bar{T}_f'(p, s) - T_f^{\circ\prime}(p, 0)] = \bar{P}_n'(p, s) - [\bar{T}_f'(p, s) - \bar{T}_c'(p, s)] \tag{20}$$

$$\tau_c[s\bar{T}_c'(p, s) - T_c^{\circ\prime}(p, 0)] = [\bar{T}_f'(p, s) - \bar{T}_c'(p, s)] - a[p\bar{T}_c'(p, s) - \bar{T}_c^{\circ}(0, s)] \tag{21}$$

Solving for $\bar{T}_f'(p, s)$ in equation (20), we get

$$\bar{T}_f'(p, s) = \frac{\bar{T}_c'(p, s) + \tau_f T_f^{\circ\prime}(p, 0) + \bar{P}_n'(p, s)}{1 + \tau_f s} \tag{22}$$

Next, solving for $\bar{T}_c'(p, s)$ in equation (21), we obtain

$$\bar{T}_c'(p, s) = \frac{\tau_c T_c^{\circ\prime}(p, 0) + a\bar{T}_c^{\circ}(0, s) + \left[\dfrac{\tau_f T_f^{\circ\prime}(p, 0) + \bar{P}_n'(p, s)}{1 + \tau_f s}\right]}{ap + 1 + \tau_c s - \dfrac{1}{1 + \tau_f s}} \tag{23}$$

in which $\bar{T}_f'(p, s)$ was replaced by equation (22).

The transformed initial and boundary conditions are

$$T_c^{\circ\prime}(p, 0) = \frac{T_c(0)}{p} + \frac{P_0 H}{\pi c M}\left\{\frac{(\pi/H)^2}{p[p^2 + (\pi/H)^2]}\right\} \tag{24}$$

$$T_f^{\circ\prime}(p, 0) = RP_0\left[\frac{\pi/H}{p^2 + (\pi/H)^2}\right] + T_c^{\circ\prime}(p, 0) \tag{25}$$

$$\bar{T}_c^{\circ}(0, s) = T_c(0)/s \tag{26}$$

In obtaining the Laplace transformation with respect to z in equations (24) and (25) and in the following derivation, it is assumed that the trigonometric functions extend to $z = \infty$. No error is incurred if we restrict the solutions to $z \leq H$.

With exponential power rise we have

$$P_n(z, t) = RP_0 e^{wt} \sin \frac{\pi z}{H} \tag{27}$$

which transforms into

$$\bar{P}_n'(p, s) = RP_0\left[\frac{1}{s - w}\right]\left[\frac{\pi/H}{p^2 + (\pi/H)^2}\right] \tag{28}$$

After substitution of the conditions (24), (25), (26), and (28) and rearrangement, the transformed coolant temperature, equation (23), becomes

$$\bar{T}_c'(p, s) = \frac{T_c(0)}{ps} + \frac{P_0 H}{\pi c M s}\frac{B^2}{p(p^2 + B^2)} + \frac{P_0\pi}{HcM}\frac{w}{s(s - w)(\tau_f s + 1)}\left\{\frac{1}{[p + b(s)](p^2 + B^2)}\right\} \tag{29}$$

in which $B = \pi/H$.

The explicit functional dependence of $b(s)$ is

$$b(s) = \frac{1}{a}\left(\frac{\tau_f s}{1 + \tau_f s} + \tau_c s\right) = \frac{1}{a}\left(1 - \frac{1}{1 + \tau_f s} + \tau_c s\right) \tag{30}$$

In order to invert into the spatial domain we note

$$\frac{1}{[p + b(s)](p^2 + B^2)} = \frac{b_1}{p + b(s)} + \frac{b_2 p + b_3}{p^2 + B^2} \tag{31}$$

in which

$$b_1 = -b_2 = b_3/b(s) = \frac{1}{[b(s)]^2 + B^2} \tag{32}$$

Substituting equations (31) and (32) into equation (29) and inverting with respect to p give

$$\bar{T}_c(z, s) = \frac{T_c(0)}{s} + \frac{P_0 H}{\pi c M s}\left(1 - \cos\frac{\pi z}{H}\right) + \frac{P_0\pi}{HcM}\left\{\frac{1}{[b(s)]^2 + B^2}\right\}\left[\frac{w}{s(s - w)(\tau_f s + 1)}\right]\left[e^{-b(s)z} - \cos\frac{\pi z}{H} + \frac{Hb(s)}{\pi}\sin\frac{\pi z}{H}\right] \tag{33}$$

Introduce the definition of $b(s)$, equation (30), into the exponential in equation (33) to obtain

$$e^{-b(s)z} = e^{-z/a}\, e^{\frac{s}{a\tau_f}\left(\frac{1}{s+1/\tau_f}\right)} e^{-s\tau_c z/a} \tag{34}$$

For convenience define $f(s)$ such that the coefficient of $(P_0 w/cM)$ $\sin(\pi z/H)$ in equation (33) is equal to

$$\frac{a}{\tau_v}\left(1 + \frac{1/\tau_c}{s + 1/\tau_f}\right) f(s) \tag{35}$$

Explicitly we may write

$$f(s) = \frac{(\tau_f s + 1)/\tau_f^2}{(s - w)(s^4 + a_3 s^3 + a_2 s^2 + a_1 s + a_0)} \tag{36}$$

in which

$$\begin{aligned} a_0 &= \frac{\pi^2}{\tau_f^2 \tau_v^2} & a_2 &= \left(\frac{1}{\tau_f} + \frac{1}{\tau_c}\right)^2 + \frac{\pi^2}{\tau_v^2} \\ a_1 &= \frac{2\pi^2}{\tau_f \tau_v^2} & a_3 &= 2\left(\frac{1}{\tau_f} + \frac{1}{\tau_c}\right) \end{aligned} \tag{37}$$

With these definitions, equation (33) becomes

$$\begin{aligned} \bar{T}_c(z, s) = {} & \frac{T_c(0)}{s} + \frac{P_0 H}{\pi c M s}\left(1 - \cos\frac{\pi z}{H}\right) \\ & + \frac{P_0 \pi w a^2}{HcM\tau_v^2}\left\{ e^{-z/a}\left[e^{-s\tau_c z/a}\, e^{\frac{s}{a\tau_f}\left(\frac{1}{s+1/\tau_f}\right)} \frac{f(s)}{s}\right]\right. \\ & \left. - \frac{f(s)}{s}\cos\frac{\pi z}{H} + \frac{H}{\pi a} f(s)\left(\tau_c + \frac{1}{s + 1/\tau_f}\right)\sin\frac{\pi z}{H}\right\} \end{aligned} \tag{38}$$

The temperature distribution in the time domain is obtained by inverting equation (38). The usual procedure requires separating $f(s)$ into partial fractions. The poles of the fourth-order part of $f(s)$ depend on reactor constants, and for finite nonzero characteristic times, they are found to be complex conjugates with negative real components of the form

$$\begin{aligned} s_{3,4} &= -\alpha \pm i\beta \\ s_{5,6} &= -\gamma \pm i\delta \end{aligned} \tag{39}$$

where α, β, γ, and δ are real, positive, nonzero numbers. These numbers are given by

$$\begin{Bmatrix} \alpha \\ \gamma \end{Bmatrix} = +\tfrac{1}{2}\left(\frac{1}{\tau_c} + \frac{1}{\tau_f}\right) \pm (\text{sign of } Y)\left[\frac{Z + X}{2}\right]^{1/2}$$

$$\begin{Bmatrix} \beta \\ \delta \end{Bmatrix} = \frac{\pi}{2\tau_v} \pm \left[\frac{Z - X}{2}\right]^{1/2}$$

in which

$$X = \tfrac{1}{4}\left(\frac{1}{\tau_c} + \frac{1}{\tau_f}\right)^2 - \frac{\pi^2}{4\tau_v^2}$$

$$Y = \frac{\pi}{2\tau_v}\left(\frac{1}{\tau_c} - \frac{1}{\tau_f}\right)$$

$$Z = +(X^2 + Y^2)^{1/2}$$

If three terms are computed with precision, the fourth can be obtained from the relation

$$\alpha\gamma = \beta\delta$$

and checked with the equation

$$\beta\gamma + \alpha\delta = \frac{\pi}{\tau_v \tau_f}$$

The behavior of $s_{3,4}$ and $s_{5,6}$ as functions of τ_v, τ_f, and τ_c is shown in Figs. 3, 4, and 5, respectively, in which root loci in the second quadrant of the complex s-plane ($s = x + iy$) are presented. In Fig. 3 the variation of $-\alpha + i\beta$ and $-\gamma + i\delta$ with τ_v is shown with τ_f and τ_c held constant at 0.1 and 0.5 sec, respectively. The roots begin at $-1/\tau_c + i\infty$ and $-1/\tau_f + i0$ for $\tau_v = 0$ and move along the loci to the origin and to $-1/\tau_f - 1/\tau_c + i0$ as $\tau_v \to \infty$. The location and values of $-\alpha + i\beta$ and $-\gamma + i\delta$ for $\tau_v = 0.5$ sec are indicated in the figure. Similar plots are shown in Figs. 4 and 5 with τ_f and τ_c as the varying parameters. In Fig. 4 one root terminates at $-1/\tau_c + i\pi/\tau_v$ for infinite τ_f. In case τ_c is less than τ_f, the semicircular type locus in Fig. 3 proceeds from $-1/\tau_f + i0$ to the origin and the other locus goes to $-1/\tau_f - 1/\tau_c + i0$ from $-1/\tau_c + i\infty$. The roots are distinct except in the rare case for which $\tau_c = \tau_f$ and $\pi/\tau_v = 1/\tau_c + 1/\tau_f$.

For distinct roots, equation (36) can be written

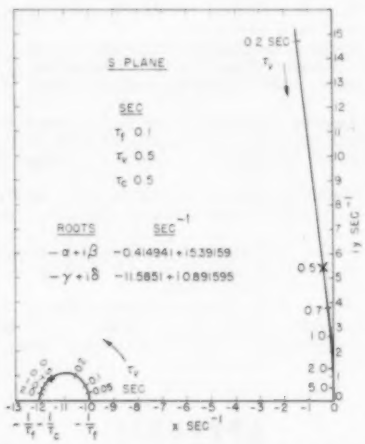

Fig. 3 Variation of the $f(s)$-poles $-\alpha + i\beta$ and $-\gamma + i\delta$ with τ_c for fixed τ_f and τ_v

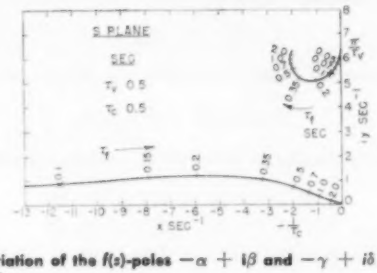

Fig. 4 Variation of the $f(s)$-poles $-\alpha + i\beta$ and $-\gamma + i\delta$ with τ_f for fixed τ_v and τ_c

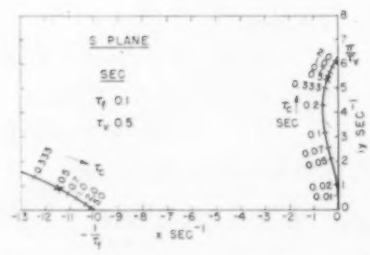

Fig. 5 Variation of the $f(s)$-poles $-\alpha + i\beta$ and $-\gamma + i\delta$ with τ_c for fixed τ_v and τ_f

$$f(s) = \frac{(\tau_f s + 1)/\tau_f^2}{(s - w)[(s + \alpha)^2 + \beta^2][(s + \gamma)^2 + \delta^2]} = \frac{d_1}{s - w} + \frac{d_2 s + d_3}{(s + \alpha)^2 + \beta^2} + \frac{d_4 s + d_5}{(s + \gamma)^2 + \delta^2} \quad (40)$$

Separating the $f(s)/s$ term in equation (38) into partial fractions, we obtain

$$\frac{f(s)}{s} = \frac{c_1}{s} + \frac{c_2}{s - w} + \frac{c_3 s + c_4}{(s + \alpha)^2 + \beta^2} + \frac{c_5 s + c_6}{(s + \gamma)^2 + \delta^2} \quad (41)$$

The d_i and c_i ($i = 1, \ldots, 6$) can be obtained in the usual manner [16]. These coefficients depend on the reactor parameters and the reciprocal period w. Expressing equation (38) in terms of $g_i(s)$ defined in Table 1, we obtain

$$\bar{T}_c(z, s) = \frac{T_c(0)}{s} + \frac{P_0 H}{\pi c M s}\left(1 - \cos\frac{\pi z}{H}\right) + \frac{P_0 H \pi^2 w}{\pi c M \tau_v^2}\left\{ e^{-z/ae - s\tau_v z/H}[1 + g_7(s)] \sum_{i=1}^{6} c_i g_i(s) - \sum_{i=1}^{6} c_i g_i(s) \cos\frac{\pi z}{H} + \frac{\tau_v}{\pi}\left[1 + \frac{g_8(s)}{\tau_c}\right] \sum_{i=2}^{6} d_i g_i(s) \sin\frac{\pi z}{H}\right\} \quad (42)$$

The exponential term with s in the exponent introduces the shifted unit step function $S(t - \tau_v z/H)$. The inversions of $g_i(s)$ defined as

$$G_i(t) = L_i^{-1}[g_i(s)], \quad (i = 1, 2, \ldots, 8)$$

are shown in Table 1. The inversion of the product $g_i(s)g_j(s)$ is the convolution integral

$$G_i(t) * G_j(t) = \int_0^t G_i(t')G_j(t - t')dt' = \int_0^t G_i(t - t')G_j(t')dt' \quad (43)$$

The inversion of $g_7(s)$ involves the modified Bessel function of the first order and kind. It may be obtained readily by applying basic theorems to the standard form $e^{1/s}$.

In symbolic form the inverted coolant temperature distribution is

$$T_c(z, t) = T_c(0) + \frac{P_0 H}{\pi c M}\left\{\left(1 - \cos\frac{\pi z}{H}\right) + \frac{\pi^2 w}{\tau_v^2} e^{-z/a}[1 + G_7(t^*)] \sum_{i=1}^{6} c_i[G_i(t^*)S(t^*)] - \frac{\pi^2 w}{\tau_v^2} \sum_{i=1}^{6} c_i G_i(t) \cos\frac{\pi z}{H} + \frac{\pi w}{\tau_v \tau_c}[\tau_c + G_8(t^*)] \sum_{i=2}^{6} d_i G_i(t) \sin\frac{\pi z}{H}\right\} \quad (44)$$

in which $t^* = t - \tau_v z/H$.

The integrals required in the convolutions are next evaluated. Those involving $G_7(t)$ do not appear to be integrable in closed form. The first two convolutions have been encountered in previous work [17] and were numerically evaluated for several values of the parameters. The numerical procedure consisted of expanding the Bessel function in $G_7(t)$.

$$I_1(x) = \sum_{k=0}^{\infty} \frac{x^{2k+1}}{2^{2k+1} k!(k + 1)!}$$

With this the first convolution becomes

$$[G_1(t^*)S(t^*)] * G_7(t) = \sum_{k=0}^{\infty} \frac{(s')^{k+1}}{k!(k + 1)!} \int_0^{q'} y^k e^{-y} dy \equiv \psi_2(s', q') \quad (45)$$

in which $s' = z/a$, $q' = t^*/\tau_f$. For brevity the step function $S(t^*)$ is omitted from the right side of equation (45) and from the following equations in which $S(t^*)$ appears on the left side. It is understood that these functions contribute only when $t^* > 0$. The function ψ_2 has been computed by Rizika [17] and is shown graphically in references [2 and 8]. A form more suitable for hand calculations is presented in the third section of the Appendix. Similarly

$$[G_2(t^*)S(t^*)] * G_7(t) = e^{wt^*}\psi_2(s'', q'') \quad (46)$$

in which

$$s'' = \frac{z}{a\tau_f(w + 1/\tau_f)}; \quad q'' = t^*(w + 1/\tau_f)$$

The next two terms can be evaluated in terms of the following new functions:[4]

[4] The s in these two equations is not related to the complex variable used earlier.

Table 1 Laplace transforms

$g(s)$	$G(t)$	Time restriction
$g_1(s) = \frac{1}{s}$	$G_1(t) = 1$	$t \geq 0$
$g_2(s) = \frac{1}{s - w}$	$G_2(t) = e^{wt}$	$t \geq 0$
$g_3(s) = \frac{s}{(s + \alpha)^2 + \beta^2}$	$G_3(t) = \frac{e^{-\alpha t}}{\beta}(\beta \cos \beta t - \alpha \sin \beta t)$	$t \geq 0$
$g_4(s) = \frac{1}{(s + \alpha)^2 + \beta^2}$	$G_4(t) = \frac{e^{-\alpha t}}{\beta} \sin \beta t$	$t \geq 0$
$g_5(s) = \frac{s}{(s + \gamma)^2 + \delta^2}$	$G_5(t) = \frac{e^{-\gamma t}}{\delta}(\delta \cos \delta t - \gamma \sin \delta t)$	$t \geq 0$
$g_6(s) = \frac{1}{(s + \gamma)^2 + \delta^2}$	$G_6(t) = \frac{e^{-\gamma t}}{\delta} \sin \delta t$	$t \geq 0$
$g_7(s) = e^{\frac{z}{a\tau_f(s + 1/\tau_f)}} - 1$	$G_7(t) = \left(\frac{z}{a\tau_f t}\right)^{1/2} (e^{-t/\tau_f}) I_1\left[2\left(\frac{zt}{a\tau_f}\right)^{1/2}\right]$	$t \geq 0$
$g_8(s) = \frac{1}{s + 1/\tau_f}$	$G_8(t) = e^{-t/\tau_f}$	$t \geq 0$
$g_i(s)e^{-s\tau_v z/H}$	$G_i(t - \tau_v z/H)S(t - \tau_v z/H)$	$t > \tau_v z/H$

$$\psi_9(s, q, r) = \sum_{k=0}^{\infty} \frac{s^{k+1}}{k!(k+1)!} \int_0^q e^{-y} y^k \cos ry \, dy$$

$$\psi_{10}(s, q, r) = \sum_{k=0}^{\infty} \frac{s^{k+1}}{k!(k+1)!} \int_0^q e^{-y} y^k \sin ry \, dy \tag{47}$$

in which

$$s = \frac{z}{a\tau_f\left(\frac{1}{\tau_f} - \alpha\right)}; \quad q = t^*\left(\frac{1}{\tau_f} - \alpha\right); \quad r = \frac{\beta}{\frac{1}{\tau_f} - \alpha}$$

With these definitions we get

$$c_2[G_2(t^*)S(t^*)]^*G_7(t) + c_4[G_4(t^*)S(t^*)]^*G_7(t)$$
$$= e^{-\alpha t^*}\left[\left(c_2\psi_{10} + \frac{c_4 - c_2\alpha}{\beta}\psi_9\right)\sin \beta t^* + \left(c_2\psi_9 + \frac{c_2\alpha - c_4}{\beta}\psi_{10}\right)\cos \beta t^*\right] \tag{48}$$

The ψ_9 and ψ_{10}-functions do not appear to be integrable in closed form and have not been numerically tabulated. They are peculiar to this work and are so designated to distinguish them from other ψ_i-functions introduced in references [7 and 10]. The ψ_9 and ψ_{10}-functions are also presented in a form suitable for hand calculations in the third section of the Appendix. In a similar manner we obtain

$$c_3[G_3(t^*)S(t^*)]^*G_7(t) + c_5[G_5(t^*)S(t^*)]^*G_7(t)$$
$$= e^{-\gamma t^*}\left[\left(c_3\psi_{10} + \frac{c_5 - c_3\gamma}{\delta}\psi_9\right)\sin \delta t^* + \left(c_3\psi_9 + \frac{c_3\gamma - c_5}{\delta}\psi_{10}\right)\cos \delta t^*\right]$$

in which γ and δ are to be used in ψ_9 and ψ_{10} instead of α and β. It is noted that $r(\alpha, \beta) = -r(\gamma, \delta)$. The remaining convolutions are

$$G_2(t)^*G_8(t) = \frac{e^{wt} - e^{-t/\tau_f}}{w + 1/\tau_f}; \tag{49}$$

$$d_3G_3(t)^*G_8(t) + d_4G_4(t)^*G_8(t)$$
$$= \frac{e^{-\alpha t}}{\left(\frac{1}{\tau_f} - \alpha\right)^2 + \beta^2}\left\{\left[\beta d_3 + \left(\frac{1}{\tau_f} - \alpha\right)\left(\frac{d_4 - d_3\alpha}{\beta}\right)\right]\sin \beta t + \left(\frac{d_3}{\tau_f} - d_4\right)\left[\cos \beta t - e^{-\left(\frac{1}{\tau_f} - \alpha\right)t}\right]\right\} \tag{50}$$

Similarly, $d_5G_5(t)^*G_8(t) + d_6G_6(t)^*G_8(t)$ can be obtained from equation (50) by replacing α, β, d_3, and d_4 by γ, δ, d_5, and d_6, respectively.

Fuel Temperature Distribution

The transformed temperature for the fuel region is obtained from equation (22)

$$T_f(z, s) = \frac{T_c(z, s) + \tau_f T_f(z, 0) + P_n(z, s)}{1 + \tau_f s} \tag{51}$$

The second and third terms in the numerator can be inverted immediately.

$$L_t^{-1}\left[\frac{\tau_f T_f(z, 0)}{1 + \tau_f s}\right] = T_f(z, 0)e^{-t/\tau_f}$$

$$L_t^{-1}\left[\frac{\bar{P}_n(z, s)}{1 + \tau_f s}\right] = \frac{RP_0}{\tau_f} G_2(t)^*G_9(t) \sin \frac{\pi z}{H} \tag{52}$$

Consider next the coolant temperature term [refer to equation (38)]. Inversion of the first two terms gives

$$\left[T_c(0) + \frac{P_0 H}{\pi c M}\left(1 - \cos \frac{\pi z}{H}\right)\right](1 - e^{-t/\tau_f}) \tag{53}$$

These terms may be combined with the foregoing $T_f(z, 0)$-term through the use of equations (8) and (9). The remaining terms in $\bar{T}_c(z, s)$ have the common factor $f(s)$ which contains $1 + \tau_f s$ in the numerator. This zero at $-1/\tau_f$ is removed by division by $1 + \tau_f s$ as required in equation (51). Hence the functions developed for these terms in $T_c(z, t)$ can be used directly in $T_f(z, t)$ provided the coefficients d_i and c_i are evaluated without the $1 + \tau_f s$-factor in the numerator of $f(s)$.

Evaluation of the ψ_i-Functions

The ψ_i-functions appearing in the solution are defined as follows (with primes omitted on s and q):

$$\psi_3(s, q) = \int_0^q \left(\frac{s}{y}\right)^{1/2} e^{-y} I_1[2(sy)^{1/2}]dy = \sum_{k=0}^{\infty} \frac{s^{k+1}}{k!(k+1)!} \int_0^q e^{-y} y^k dy \tag{54}$$

$$\left\{\begin{matrix}\psi_9(s, q, r)\\ \psi_{10}(s, q, r)\end{matrix}\right\} = \int_0^q \left(\frac{s}{y}\right)^{1/2} e^{-y} I_1[2(sy)^{1/2}] \left\{\begin{matrix}\cos ry\\ \sin ry\end{matrix}\right\} dy = \sum_{k=0}^{\infty} \frac{s^{k+1}}{k!(k+1)!} \int_0^q e^{-y} y^k \left\{\begin{matrix}\cos ry\\ \sin ry\end{matrix}\right\} dy \tag{55}$$

Integration gives

$$\psi_3(s, q) = -1 + e^q - e^{-q} \sum_{n=1}^{\infty} \left(\frac{s}{q}\right)^{n/2} I_n[2(sq)^{1/2}] \tag{56}$$

$$\left\{\begin{matrix}\psi_9(s, q, r)\\ \psi_{10}(s, q, r)\end{matrix}\right\} = \left\{\begin{matrix}-1\\ 0\end{matrix}\right\} + \left[e^{\frac{s}{1+r^2}} \left\{\begin{matrix}\cos\\ \sin\end{matrix}\right\}\left(\frac{sr}{1 + r^2}\right)\right] - e^{-q} \sum_{n=1}^{\infty} \left(\frac{s}{q(1 + r^2)}\right)^{n/2} I_n[2(sq)^{1/2}] \left\{\begin{matrix}\cos\\ \sin\end{matrix}\right\} (rq + n \tan^{-1} r) \tag{57}$$

Values of the higher order Bessel functions I_n are given in reference [18]. Other functions related to ψ_9 and ψ_{10} are

$$\left\{\begin{matrix}\psi_7(s, q, r)\\ \psi_8(s, q, r)\end{matrix}\right\} = \sum_{k=0}^{\infty} \frac{s^k}{(k!)^2} \int_0^q y^k e^{-y} \left\{\begin{matrix}\cos ry\\ \sin ry\end{matrix}\right\} dy \tag{58}$$

which have been evaluated numerically by Yang, Clark, and Arpaci [10]. ψ_7 and ψ_8 are connected to ψ_9 and ψ_{10} by the relations

$$\psi_9 = \psi_7 + r\psi_8 - 1 + e^{-q} I_0[2(sq)^{1/2}] \cos rq$$

$$\psi_{10} = \psi_8 - r\psi_7 + \frac{\sqrt{2}\, r}{(1 + r^2)^{1/4}} e^{-q} I_0[2(sq)^{1/2}] \sin\left(rq - \frac{\pi}{4} + \tan^{-1} r\right) \tag{59}$$

The following special properties are listed:

$$\left\{\begin{matrix}\psi_7\\ \psi_8\end{matrix}\right\} = \frac{d}{ds}\left\{\begin{matrix}\psi_9\\ \psi_{10}\end{matrix}\right\}$$

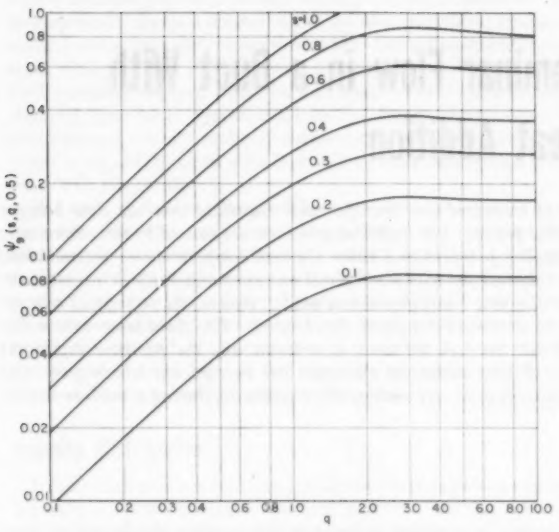

Fig. 6 Variation of the $\psi_9(s, q, r)$-function with $r = 0.5$

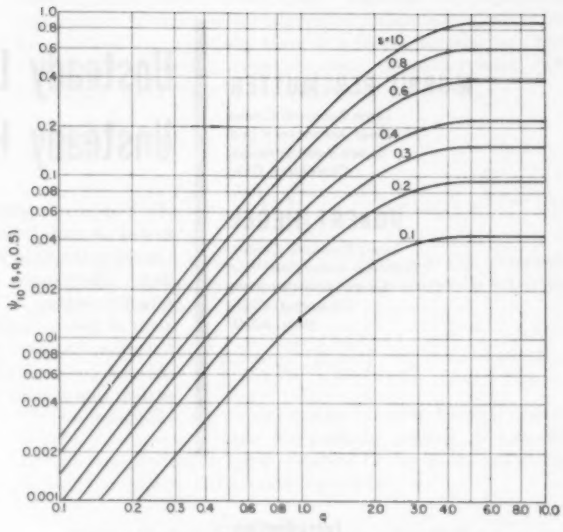

Fig. 7 Variation of the $\psi_{10}(s, q, r)$-function with $r = 0.5$

$$\begin{gathered}\psi_9(s, q, 0) = \psi_3(s, q)\\ \psi_{10}(s, q, 0) = 0\\ \psi_3(s, 0) = \psi_9(s, 0, r) = \psi_{10}(s, 0, r) = 0\\ \psi_3(0, q) = \psi_9(0, q, r) = \psi_{10}(0, q, r) = 0\\ \psi_3(s, +\infty) = -1 + e^{s}\end{gathered} \tag{60}$$

$$\begin{Bmatrix}\psi_9(s, +\infty, r)\\ \psi_{10}(s, +\infty, r)\end{Bmatrix} = \begin{Bmatrix}-1\\ 0\end{Bmatrix} + e^{\frac{s}{1+r^2}} \begin{Bmatrix}\cos\\ \sin\end{Bmatrix}\left(\frac{sr}{1+r^2}\right)$$

Typical graphs of ψ_9 and ψ_{10} are shown in Figs. 6 and 7 for positive values of the arguments such as were encountered for the $-\alpha \pm i\beta$-roots in the numerical example. For computational purposes, the following form is convenient:

$$\begin{aligned}&c_3[G_3(t^*)S(t^*)]^*G_7(t) + c_4[G_4(t^*)S(t^*)]^*G_7(t)\\ &= c_3(1 + K^2)^{1/2}\left\{-e^{-\alpha t^*}\cos(\tan^{-1}K - \beta t^*)\right.\\ &+ e^{\frac{s}{1+r^2}-\alpha t^*}\cos\left(\frac{sr}{1+r^2} + \tan^{-1}K - \beta t^*\right)\\ &- e^{-t^*/\tau_f}\sum_{n=1}^{\infty}\left(\frac{s}{q(1+r^2)}\right)^{n/2} I_n[2(sq)^{1/2}]\\ &\left.\cos(n\tan^{-1}r + \tan^{-1}K)\right\}\end{aligned}$$

in which

$$K = \frac{c_4 - c_3\alpha}{c_3\beta}$$

A similar expression may be written for the other convolution involving γ, δ, c_5, and c_6.

Asymptotic Behavior of Temperature Distributions

At long times after the beginning of the transient, the nonnegligible terms in the coolant temperature distribution equation (10) are

$$\begin{aligned}G_1(t) &= 1\\ G_2(t) &= e^{wt}\\ G_1(t^*) &= 1\\ G_2(t^*) &= e^{wt^*}\\ [G_1(t^*)S(t^*)]^*G_7(t) &= -1 + e^{s\tau_v/H\tau_c}\\ [G_2(t^*)S(t^*)]^*G_7(t) &= e^{wt^*}\left[-1 + e^{\frac{s\tau_v/H\tau_c}{1+w\tau_f}}\right]\\ G_2(t)^*G_8(t) &= \frac{e^{wt}}{w + 1/\tau_f}\end{aligned} \tag{61}$$

All other functions approach zero exponentially with time. The constants required for these remaining terms are

$$c_1 = -\tau_v^2/\pi^2 w$$

and

$$d_2 = wc_2 = \frac{(1 + \tau_f)/\tau_f^2}{w^4 + a_3w^3 + a_2w^2 + a_1w + a_0} \tag{62}$$

After algebraic manipulation, equations (10), (61), and (62) can be brought into the form presented in equation (11). In a similar manner, the asymptotic fuel temperature distribution can be expressed as shown in equation (12).

MORRIS PERLMUTTER
Lewis Research Center
National Aeronautics and
Space Administration,
Cleveland, Ohio

ROBERT SIEGEL
Lewis Research Center,
National Aeronautics and
Space Administration,
Cleveland, Ohio.
Mem. ASME

Unsteady Laminar Flow in a Duct With Unsteady Heat Addition

An analysis is made of transient heat transfer with transient laminar flow between heated (or cooled) parallel plates. The transient processes are caused by simultaneously changing the fluid pumping pressure and either the wall temperature or the wall heat flux. The solution is obtained for both the thermal entrance and fully developed heat-transfer regions. The slug-flow simplification is made; that is, the velocity at any instant of time is taken as uniform throughout the channel. The fluid temperature distribution, however, depends on both the axial co-ordinate and the position within the channel cross section. A few numerical examples are carried out which give some insight into various transient processes such as those occurring during a nuclear-reactor shutdown.

Introduction

An understanding of the dynamic behavior of heat-transfer devices has recently become of greater importance in connection with the control of modern high-performance, heat-transfer devices. This has led to a number of papers that have been concerned with unsteady heat-transfer processes in tubes and ducts. A few of these are listed in references [1 to 7].[1] In these references the flow velocity has generally been assumed steady, and various transient heat-transfer conditions have been applied at the walls, such as a time-varying surface temperature or heat flux. However, in many instances a time variation in velocity will also be present. For example, when a rocket engine first begins to fire, a simultaneous transient in stream velocity and wall heating will occur. In the case of flow in the cooling channels of a nuclear reactor, if a pump failure occurs, the control system will simultaneously shut down the power. Hence the coast down in flow will be accompanied by a transient in the heat being transferred at the channel walls.

The purpose of this paper is to obtain an understanding of the transient heat-transfer phenomena that occur in channel flows when there are simultaneous changes in pumping pressure and wall-heating conditions. The geometry selected for analysis is shown in Fig. 1. It consists of two parallel planes with incompressible laminar flow between them. A hydrodynamic entrance length is provided before the flow reaches the heated section. This means that within the heated section the velocity, although time-dependent, does not vary with axial position along the channel. In addition, the slug-flow simplification is applied to the velocity distribution. In this simplification the velocity distribution does not depend upon the co-ordinate across the channel. Hence at any instant of time the velocity is a constant throughout the flow passage and equal to the correct mean velocity at that instant. It has been demonstrated by [6, 7] that the slug-flow problem does reveal the essential physical behavior of the system, although the numerical magnitudes in the results are somewhat in error. The advantage of using this simplification is that exact mathematical solutions can be obtained for various boundary conditions, and hence the influence of the boundary conditions can be demonstrated. Even with this simplification, the solutions become fairly involved.

Two types of wall heat-transfer boundary conditions will be treated here. In the first group of problems, the wall temperature is step-changed from some initial to some final value, while in a second group the wall heat flux is step-changed from some initial to some final value. In the most general problem treated here, there can be a step change in wall temperature or heat flux

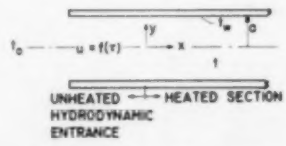

Fig. 1 Parallel-plate channel

[1] Numbers in brackets designate References at end of paper.

Contributed by the Heat Transfer Division and presented at the Winter Annual Meeting, New York, N. Y., November 27–December 2, 1960, of The American Society of Mechanical Engineers. Manuscript received at ASME Headquarters, August 5, 1960. Paper No. 60—WA-174.

Nomenclature

- a = half width of spacing between parallel plates
- c_p = specific heat at constant pressure
- E_n = eigenvalue, $(n + 1/2)\pi$; $E_m = (m + 1/2)\pi$
- F_n = function in problem where both pressure gradient and wall-temperature change, equation (9)
- G_n = function in problem where pressure gradient changes and wall temperature remains constant, equation (21)
- H_n = function in problem where both pressure gradient and wall heat flux change, equation (30)
- k = thermal conductivity of fluid
- L_n = function in problem where pressure gradient changes and wall heat flux remains constant, equation (38)
- M = function defined by equation (19a)
- Pr = Prandtl number of fluid, $c_p\mu/k = \nu/\alpha$
- p = static pressure
- q = local heat addition per unit area at channel walls; q_1, specified wall heat flux before transient; q_2, specified wall heat flux during transient
- Re = Reynolds number, $\bar{u}4a/\nu$
- T = dimensionless temperature, $(t - t_0)/(t_w - t_0)$
- T^* = dimensionless temperature, $(t - t_0)k/qa$

(Continued on next page)

with a simultaneous step change in the pumping pressure of the flowing fluid. As special cases of this solution, situations are considered where the wall temperature or heat flux is maintained constant while the flow velocity changes. Situations where the velocity remains constant while the wall temperature or heat flux is changed have been treated in [4 to 7]. Some information on simultaneous velocity and wall-temperature transients has been given in [8], which deals with flow in a circular tube with a uniform wall temperature.

The most general results given here are obtained by superposing more elementary solutions. These elementary solutions are obtained by solving the governing energy equation by using the method of characteristics. In the following description of the method, the transient velocity distribution will first be obtained. Then the elementary heat-transfer solutions will be found, and finally the method of superposition for solving more involved situations will be shown. A few numerical examples are carried out that illustrate the heat-transfer processes.

Velocity Distribution

In this paper we are concerned with transient velocities resulting from a sudden change in pressure gradient. In the velocity part of the problem, the entrance length at the beginning of the channel, where the velocity distribution changes with length, is not taken into account. Hence the velocity distribution can at most be a function of time and the transverse co-ordinate y in the channel. After this distribution is found, the dependence on y is removed by making the slug-flow approximation.

The equation of motion for incompressible laminar flow in the fully developed region between parallel plates is

$$\frac{\partial u}{\partial \tau} = -\frac{1}{\rho}\frac{\partial p}{\partial x} + \nu\frac{\partial^2 u}{\partial y^2} \tag{1}$$

where $\partial p/\partial x$ is a function of time only. This is of exactly the same form as the heat-conduction equation for the unsteady temperature distribution within a slab having time-varying internal heat generation.[2] The variable pressure gradient is analogous to the variable internal heat generation in the transient heat-conduction problem. The boundary condition of zero velocity at the walls of the channel corresponds to constant boundary temperatures in the heat-conduction solution. In reference [9],[3] the solution is given for the transient temperature distribution in a plane slab when the temperature is initially uniform and then a step in internal heat generation is introduced with the boundaries maintained at the initial temperature. This result immediately yields the solution for fully developed laminar flow in a parallel-plate channel where initially the velocity is zero and then a pressure gradient is suddenly imposed. By superposing this solution with a steady-state velocity distribution, we obtain the solution where initially there is a steady velocity and then the pressure gradient is abruptly changed to another value. The resulting transient velocity distribution is

$$\frac{u}{\bar{u}_2} = \frac{3}{2}(1 - Y^2) - 6\left(1 - \frac{\bar{u}_1}{\bar{u}_2}\right)\sum_{m=0}^{\infty}\frac{(-1)^m}{E_m^3}\cos(E_m Y)e^{-E_m^2\Theta} \tag{2}$$

where the dimensionless variables are defined in the Nomenclature. Note that the pressure gradient in the channel is taken into account by the steady-state relation

$$\bar{u}_2 = \frac{-a^2}{3\mu}\left(\frac{\partial p}{\partial x}\right)_2$$

Equation (2) will apply for all cases except when the final velocity is zero, which occurs when the pumping pressure is removed. In this case, by multiplying equation (2) by $\bar{u}_2/\bar{u}_1$ and letting $\bar{u}_2 = 0$, the velocity distribution is given by

$$\frac{u}{\bar{u}_1} = 6\sum_{m=0}^{\infty}\frac{(-1)^m}{E_m^3}\cos(E_m Y)e^{-E_m^2\Theta} \tag{2a}$$

For the slug-flow approximation, the velocity is defined as

$$\bar{u} = \int_0^1 u\,dY$$

Integrating equation (2) yields

$$\frac{\bar{u}}{\bar{u}_2} = 1 + 6\left(\frac{\bar{u}_1}{\bar{u}_2} - 1\right)\sum_{m=0}^{\infty}\frac{1}{E_m^4}e^{-E_m^2\Theta} \tag{3}$$

This can also be written in the convenient form

$$\frac{\bar{u} - \bar{u}_2}{\bar{u}_1 - \bar{u}_2} = 6\sum_{m=0}^{\infty}\frac{1}{E_m^4}e^{-E_m^2\Theta} \tag{4}$$

For the special case when $\bar{u}_2 = 0$, this is also the integrated form of equation (2a).

From this relation we can gain an idea of the length of time required for the transient velocity change to occur. A steady-state time is defined as the time required for 95 per cent of a given transient to take place. Hence we say that

$$\frac{\bar{u} - \bar{u}_2}{\bar{u}_1 - \bar{u}_2} = 0.05 = 6\sum_{m=0}^{\infty}\frac{1}{E_m^4}e^{-E_m^2\Theta_s}$$

and then solve for Θ_s. This yields $\Theta_s = \tau\nu/a^2 = 1.21$. For water at room temperature in a channel $^1/_4$ in. wide this gives a time of

[2] Reference [9], p. 10.
[3] Ibid., p. 130.

Nomenclature

t = temperature; t_0, temperature of fluid entering channel (a constant); t_w, wall temperature; $t_{w,1}$, specified wall temperature before transient; $t_{w,2}$, specified wall temperature during transient; $(t_w - t_0)_{max}$, maximum temperature difference during transient; $(t_w - t_0)_s$, steady-state temperature difference

u = fluid velocity; $\bar{u}$, mean fluid velocity; $\bar{u}_1$, mean velocity before transient; $\bar{u}_2$, final mean velocity after transient

X = dimensionless co-ordinate, $(4x/a)/\mathrm{Re\,Pr}$; X_0, value of X at $\Theta = 0$ at beginning of a characteristic line

x = axial distance from entrance of heated section of channel

Y = dimensionless co-ordinate, y/a

y = transverse co-ordinate measured from center line of channel

α = thermal diffusivity, $k/\rho c_p$

Θ = dimensionless time, $\tau\nu/a^2\mathrm{Pr}$; Θ_0, value of Θ at $X = 0$ at beginning of a characteristic line

θ = dimencionless time, $\tau\nu/a^2$; θ_s, steady-state value of θ

μ = absolute viscosity

ν = kinematic viscosity

ρ = fluid density

τ = time

about 12 sec. For air under the same conditions, since the kinematic viscosity is about 15 times larger than for water, the time will be 1/15 as long.

Uniform Wall Temperature

In this section a series of transient problems will be considered in which the wall temperature, which is uniform along the channel length, is step-changed from some initial to some final value. First, two basic solutions will be obtained. Then a superposition procedure will be discussed that will provide a means for using these solutions to build results for more involved situations.

Step Change in Both Wall Temperature and Pressure Gradient From an Unheated Initial Condition. The parallel-plate configuration treated here is illustrated in Fig. 1. For this solution, initially the walls are unheated and at the entering fluid temperature t_0. The flow velocity has a value $\bar{u}_1$, or it can be zero as a special case. Hence we have an unheated channel filled with flowing or stationary fluid, and the whole configuration is isothermal at temperature t_0. Then the pressure gradient is suddenly changed, and the fluid velocity within the channel begins to adjust toward a new final value. At the same instant, the wall temperature of the heated section is suddenly stepped to a new value $t_{w,2}$.

The time-dependent energy equation that governs the heat-transfer process for slug flow in the channel can be written as

$$\frac{\partial t}{\partial \tau} + \bar{u}\,\frac{\partial t}{\partial x} = \alpha\,\frac{\partial^2 t}{\partial y^2} \tag{5}$$

To obtain the equation in this form, constant properties are assumed and viscous dissipation and axial heat conduction are neglected compared with heat conduction in the y-direction. For convenience, the equation is first rewritten in terms of the dimensionless variables:

$$\Theta = \frac{\tau\nu}{a^2\mathrm{Pr}}, \qquad X = \frac{4x/a}{\mathrm{Re\ Pr}}, \qquad Y = \frac{y}{a}, \qquad T = \frac{t - t_0}{t_{w,2} - t_0}$$

where $\mathrm{Re} = \bar{u}_2 4a/\nu$. If $\bar{u}_2$ is zero as a special case, then $\bar{u}_1$ would be used in the Reynolds number. The slug-flow velocity expression from equation (3) is then inserted into the energy equation to obtain

$$\frac{\partial T}{\partial \Theta} + \left[1 + 6\left(\frac{\bar{u}_1}{\bar{u}_2} - 1\right)\sum_{m=0}^{\infty}\frac{1}{E_m^4}\,e^{-E_m^2\mathrm{Pr}\,\Theta}\right]\frac{\partial T}{\partial X} = \frac{\partial^2 T}{\partial Y^2} \tag{6}$$

This must be solved subject to the following boundary conditions:

$$T = 0 \text{ at } X = 0 \text{ for all } Y \text{ and } \Theta, \quad \text{entrance condition} \tag{7a}$$

$$T = 0 \text{ at } \Theta = 0 \text{ for all } Y \text{ and } X, \quad \text{initial condition} \tag{7b}$$

$$\frac{\partial T}{\partial Y} = 0 \text{ at } Y = 0, \quad \text{symmetry} \tag{7c}$$

$$T = 1 \text{ at } Y = \pm 1 \text{ for all } X \text{ and for } \Theta > 0, \quad \text{specified wall temperature} \tag{7d}$$

To form a transient solution we shall try a series solution of the same general form as the steady-state solution. For large times the steady-state solution will then be achieved. From [6] the steady-state solution for laminar slug flow in a parallel-plate channel is

$$T = 1 - 2\sum_{n=0}^{\infty}\frac{(-1)^n}{E_n}\,e^{-E_n^2 X}\cos E_n Y \tag{8}$$

For a transient solution we then try the similar form

$$T = 1 - 2\sum_{n=0}^{\infty}\frac{(-1)^n}{E_n}\,F_n(\Theta, X)\cos E_n Y \tag{9}$$

where $F_n(\Theta, X)$ must now be determined. For large times, F_n must converge to the steady-state result $e^{-E_n^2 X}$. The form of equation (9) automatically satisfies boundary conditions (7c) and (7d).

The trial solution is then substituted into the energy equation (6) with the result that each F_n must satisfy the relation

$$\frac{\partial F_n}{\partial \Theta} + \left[1 + 6\left(\frac{\bar{u}_1}{\bar{u}_2} - 1\right)\sum_{m=0}^{\infty}\frac{1}{E_m^4}\,e^{-E_m^2\mathrm{Pr}\,\Theta}\right]\frac{\partial F_n}{\partial X} = -E_n^2 F_n \tag{10}$$

This type of partial differential equation can be treated by using the method of characteristics.[4] In this approach the solution is obtained by considering a set of auxiliary ordinary differential equations obtained from the terms in equation (10):

$$d\Theta = \frac{dX}{1 + 6\left(\frac{\bar{u}_1}{\bar{u}_2} - 1\right)\sum_{m=0}^{\infty}\frac{1}{E_m^4}\,e^{-E_m^2\mathrm{Pr}\,\Theta}} = \frac{dF_n}{-E_n^2 F_n} \tag{10a}$$

By equating the first two of these terms we have an equation that can be integrated to yield the characteristic lines on the X-Θ-plane. In Fig. 2 the X-Θ-plane has been divided into two regions by the characteristic line originating at the origin. In region I the characteristics all originate from the X-axis, while in region II they originate from the Θ-axis. By equating the last term in equation (10a) with either of the other two terms, an equation for F_n along the characteristic lines is obtained.

In region I the function F_n is simply obtained by equating the first and last terms in equation (10a) and integrating:

$$\int_1^{F_n}\frac{dF_n}{F_n} = -E_n^2\int_0^{\Theta} d\Theta \tag{11}$$

The condition $F_n = 1$ at $\Theta = 0$ fulfills the boundary condition (7b). Integrating gives

$$F_n = e^{-E_n^2\Theta} \tag{12}$$

which is the equation for F_n in region I.

Now consider region II. From the first two terms of equation (10a) we have the equation for the characteristic lines,

$$\int_0^X dX = \int_{\Theta_0}^{\Theta}\left[1 + 6\left(\frac{\bar{u}_1}{\bar{u}_2} - 1\right)\sum_{m=0}^{\infty}\frac{1}{E_m^4}\,e^{-E_m^2\mathrm{Pr}\,\Theta}\right]d\Theta \tag{13}$$

where any characteristic in region II originates at a point $\Theta = \Theta_0$, $X = 0$. Integrating yields the equation for the characteristic line

[4] For example, reference [10], p. 371.

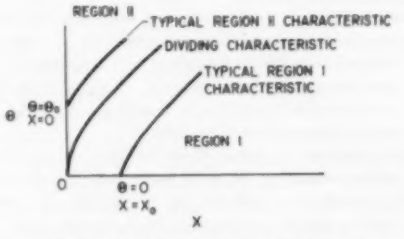

Fig. 2 Characteristic lines on X-Θ-plane

$$X = \Theta - \Theta_0 - \frac{6}{\mathrm{Pr}}\left(\frac{\bar{u}_1}{\bar{u}_2} - 1\right) \sum_{m=0}^{\infty} \frac{1}{E_m^4}\left(e^{-E_m^2 \mathrm{Pr}\,\Theta} - e^{-E_m^2 \mathrm{Pr}\,\Theta_0}\right) \quad (14)$$

From the first and third terms in equation (10*a*) we have the equation for F_n along a characteristic line in region II:

$$\int_1^{F_n} \frac{dF_n}{F_n} = -E_n^2 \int_{\Theta_0}^{\Theta} d\Theta \quad (15)$$

The boundary condition $F_n = 1$ at $X = 0$ (along the Θ-axis) insures that the condition (7*a*) will be satisfied. Integrating gives the function F_n in region II:

$$F_n = e^{-E_n^2(\Theta - \Theta_0)} \quad (16)$$

This equation is then solved for Θ_0, and the result is substituted into equation (14) to yield

$$X = -\frac{1}{E_n^2}\log_e F_n - \frac{6}{\mathrm{Pr}}\left(\frac{\bar{u}_1}{\bar{u}_2} - 1\right) \sum_{m=0}^{\infty} \frac{1}{E_m^4}\left(1 - e^{\frac{-E_m^2 \mathrm{Pr}}{E_n^2}\log_e F_n}\right) e^{-E_m^2 \mathrm{Pr}\,\Theta} \quad (17)$$

This is an implicit equation for F_n in region II.

The dividing line between the two regions is the characteristic line through the origin of the X-Θ-plane. This is given by equation (14) with Θ_0 set equal to zero:

$$X = \Theta - \frac{6}{\mathrm{Pr}}\left(\frac{\bar{u}_1}{\bar{u}_2} - 1\right) \sum_{m=0}^{\infty} \frac{1}{E_m^4}\left(e^{-E_m^2 \mathrm{Pr}\,\Theta} - 1\right) \quad (18)$$

We can now summarize the solution. Equation (18) divides the X-Θ-plane into two regions. For early times, so that we are in region I below the dividing line, equation (12) is used for F_n. For later times, so that we are in region II above the dividing line, we use equation (17) for F_n. The F_n are then summed according to equation (9) to yield the transient temperature distribution. Within the limitations of the assumed physical model, this provides an exact solution to the problem.

The evaluation of the F_n from equation (17) is a fairly involved computational task. Because similar expressions are encountered in the cases that are treated later, the method of evaluation will be discussed briefly. The computations were carried out on an IBM 704 digital computer. Equation (17) is first simplified by letting

$$M = -\frac{1}{E_n^2}\log_e F_n \quad (19a)$$

so that the equation becomes

$$X = M - \frac{6}{\mathrm{Pr}}\left(\frac{\bar{u}_1}{\bar{u}_2} - 1\right) \sum_{m=0}^{\infty} \frac{1}{E_m^4}\left(1 - e^{E_m^2 \mathrm{Pr}\,M}\right) e^{-E_m^2 \mathrm{Pr}\,\Theta} \quad (19b)$$

Thus we have to determine only one M, and all the F_n in region II are then found from the equivalent form of equation (19*a*)

$$F_n = e^{-E_n^2 M} \quad (19c)$$

Since the wall temperature is specified, what we would like to know is how the fluid temperature or the wall heat transfer varies as a function of time for different axial locations along the channel. To do this a value of Θ is first fixed in equation (19*b*) and then various values of M are substituted to yield corresponding X-values. M is then plotted as a function of X for the Θ-value chosen. By doing this for several Θ-values, a cross plot of M as a function of Θ for fixed X-values is obtained. Once M is known, the F_n can be found and the remainder of the solution carried out in a straightforward fashion.

The heat transferred from the wall to the fluid is obtained from Fourier's law:

$$q = k\left(\frac{\partial t}{\partial y}\right)_{y=0}$$

From equation (9) this yields

$$\frac{qa}{k(t_{w,2} - t_0)} = 2\sum_{n=0}^{\infty} F_n(\Theta, X) \quad (20)$$

This expression has been plotted in Fig. 3 for the case when $\bar{u}_1 = 0$; that is, when the pressure gradient is stepped from zero to a finite value. This is the most severe pressure change that can take place and hence reveals the maximum influence of the velocity transient. The evaluation has been carried out for $\mathrm{Pr} = 0.7$. The curves show that at each location the heat transfer goes through a minimum and then rises to the final steady value. This type of behavior was noted in [11], which considered the transient development of the free-convection boundary layer. In both of these instances the velocity distribution was developing with time during the heat-transfer process.

There is some physical interpretation that can be given to the characteristic solution. The dividing characteristic given by equation (18) gives the position as a function of time of a fluid particle that was at the entrance of the heated section when the transient was initiated. This is because this characteristic is a time integral of the slug-flow velocity. The characteristic curves in region I give the paths of fluid particles that were at some point X_0 when the transient started. In region II, each characteristic curve gives the position of a fluid particle that reaches the entrance of the heated section at some time Θ_0 after the transient has been initiated. To understand the transient process that takes place in region I, consider the fluid that is at the entrance of the heated section at the time the transient is initiated. At some later time the fluid will have traveled a certain distance

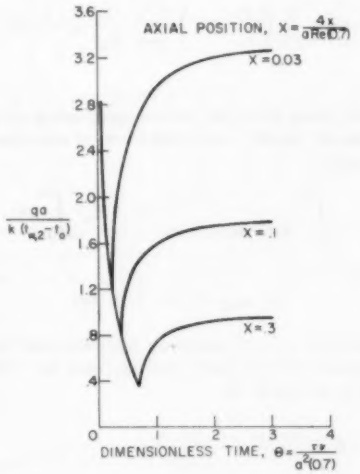

Fig. 3 Wall heat-flux response after a step in pressure gradient and wall temperature. $\mathrm{Pr} = 0.7$; initially: $\bar{u} = \bar{u}_1 = 0$, $t = t_{w,1} = t_0$; finally: $\bar{u} = \bar{u}_2$, $t_w = t_{w,2}$.

down the channel as given by the dividing characteristic. For larger distances downstream than this, there has not been any penetration, during the heating process, of fluid that was originally outside the tube. Hence there is no variation in heat transfer with X in this region, and the energy equation for region I reduces to that for transient heat conduction. The solution in this region is then the same as that for suddenly raising the temperature at the surfaces of a solid slab. Thus in Fig. 3 the curve going downward at the left is the result for one-dimensional conduction. When the fluid that was initially outside the channel reaches any given location, then the heat transfer at this position begins to increase toward the steady-state value.

Step Change in Pressure Gradient With Wall Temperature Kept Constant. Now consider another type of transient where initially the channel walls are at a uniform temperature and steady-state heat transfer is occurring. Then the pressure gradient in the channel is suddenly changed so that the flow velocity begins to adjust toward a new steady-state condition. Throughout this velocity transient the wall temperature remains unchanged.

The analysis follows in exactly the same fashion as in the preceding section. For this type of transient we shall again try a solution of the form used in equation (9):

$$T = 1 - 2\sum_{n=0}^{\infty} \frac{(-1)^n}{E_n} G_n(\Theta, X) \cos E_n Y \tag{21}$$

The only change from the previous section is in the initial boundary condition, so that equation (7*b*) no longer applies. Initially in this case steady-state heat transfer is taking place, so from equation (8) we have the initial condition for G_n at $\Theta = 0$

$$G_n = e^{-E_n^2 X \frac{\bar{u}_2}{\bar{u}_1}} \tag{22}$$

The ratio $\bar{u}_2/\bar{u}_1$ appears because X is nondimensionalized on the basis of $\bar{u}_2$, whereas at time zero in this problem the velocity is $\bar{u}_1$.

For a characteristic line in region I we equate the first two terms in equation (10*a*) and integrate:

$$\int_{X_0}^{X} dX = \int_0^{\Theta} \left[1 + 6\left(\frac{\bar{u}_1}{\bar{u}_2} - 1\right) \sum_{m=0}^{\infty} \frac{1}{E_m^4} e^{-E_m^2 \mathrm{Pr}\,\Theta}\right] d\Theta \tag{23a}$$

This gives

$$X - X_0 = \Theta - \frac{6}{\mathrm{Pr}}\left(\frac{\bar{u}_1}{\bar{u}_2} - 1\right) \sum_{m=0}^{\infty} \frac{1}{E_m^6} (e^{-E_m^2 \mathrm{Pr}\,\Theta} - 1) \tag{23b}$$

To obtain G_n along this characteristic originating at $X = X_0$ and $\Theta = 0$, integrate the first and third terms of equation (10*a*) with G_n replacing F_n:

$$\int_{e^{-E_n^2 X_0(\bar{u}_2/\bar{u}_1)}}^{G_n} \frac{dG_n}{G_n} = -E_n^2 \int_0^{\Theta} d\Theta \tag{24a}$$

which yields

$$G_n = e^{-E_n^2[\Theta + X_0(\bar{u}_2/\bar{u}_1)]} \tag{24b}$$

This is solved for X_0, and the result is substituted into equation (23*b*) to eliminate the arbitrary starting point X_0. The resulting relation for G_n in region I is

$$\log_e G_n = -E_n^2 \frac{\bar{u}_2}{\bar{u}_1} X + \left(\frac{\bar{u}_2}{\bar{u}_1} - 1\right) E_n^2 \left[\Theta + \frac{6}{\mathrm{Pr}} \sum_{m=0}^{\infty} \frac{1}{E_m^6} (e^{-E_m^2 \mathrm{Pr}\,\Theta} - 1)\right] \tag{25}$$

The dividing characteristic and results for G_n in region II are the same as for F_n in region II in the preceding section, since the only change in the present problem was confined to the initial condition in time. Hence the dividing characteristic is given by equation (18), and G_n in region II is found from equation (19*c*) as

$$G_n = e^{-E_n^2 M} \tag{26}$$

where M is obtained from equation (19*b*).

In Fig. 4, a particular example of this type of solution has been evaluated for Pr = 0.7. For this example the pressure gradient was given a step increase from an initial zero value. Initially then, there is no flow and the fluid in the heated section of the channel is all at the wall temperature with no heat being transferred. When the flow begins, there is a transient period during which the old fluid at temperature t_w is being swept out of the channel by the entering fluid at temperature t_0. During this period, which occupies region I, there is no wall heat transfer. This can be seen from equation (24*b*), where $G_n = 0$ if $\bar{u}_1$ is zero. After this initial transient period, heat transfer begins and the values rise toward the steady-state results. Because of the similarity of the two problems, the results of Fig. 4 were obtained for this special case from the calculations in the preceding section by merely letting the F_n in region I be zero.

Step Change in Both Pressure Gradient and Wall Temperature With Initial Steady Heating. In this section a more general case is considered. Initially there is both flow and steady-state heat transfer. Then both the pressure gradient and wall temperature are changed abruptly to new values. The resulting transient can be computed by a superposition of the two more elementary solutions found in the preceding sections. The superposition is illustrated in Fig. 5. The first part of the superposition is the case treated in the first section, and the solution from equation (9) is

$$t = (t_{w,2} - t_{w,1})\left[1 - 2\sum_{n=0}^{\infty} \frac{(-1)^n}{E_n} F_n(\Theta, X) \cos E_n Y\right] = (t_{w,2} - t_{w,1})[F_n \text{ solution}] \tag{27a}$$

The second part of the superposition in Fig. 5 was treated in the last section, and the solution from equation (21) is

$$t = (t_{w,1} - t_0)\left[1 - 2\sum_{n=0}^{\infty} \frac{(-1)^n}{E_n} G_n(\Theta, X) \cos E_n Y\right] + t_0 = (t_{w,1} - t_0)[G_n \text{ solution}] + t_0 \tag{27b}$$

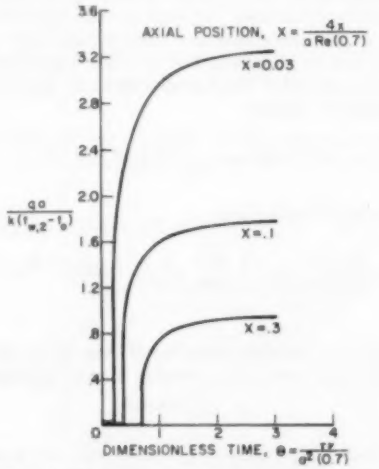

Fig. 4 Wall heat-flux response after a step in pressure gradient with wall temperature kept constant ($t_{w,2} = t_{w,1}$), Pr = 0.7; initially: $\bar{u} = \bar{u}_1 = 0$; finally: $\bar{u} = \bar{u}_2$

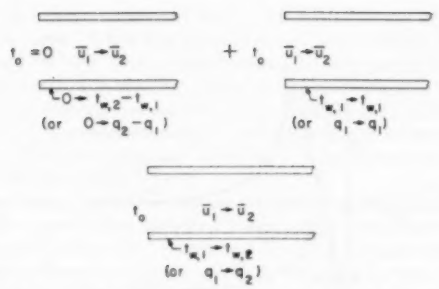
$t_0 = 0 \quad \bar{u}_1 \to \bar{u}_2$
$t_0 \quad \bar{u}_1 \to \bar{u}_2$
$=$
$t_0 - t_{w,2} - t_{w,1}$
(or $0 \to q_2 - q_1$)
$t_{w,1} \to t_{w,1}$
(or $q_1 \to q_1$)
$t_0 \quad \bar{u}_1 \to \bar{u}_2$
$t_{w,1} \to t_{w,2}$
(or $q_1 \to q_2$)

Fig. 5 Superposition of solutions for changing both pressure gradient and wall temperature (or wall heat flux)

Adding solutions, we then have the final result for the most general case treated here:

$$\frac{t - t_0}{t_{w,2} - t_0} = T = \left(\frac{t_{w,2} - t_{w,1}}{t_{w,2} - t_0}\right) [F_n \text{ solution}] + \left(\frac{t_{w,1} - t_0}{t_{w,2} - t_0}\right) [G_n \text{ solution}] \quad (27c)$$

Uniform Wall Heat Flux

A series of problems are now considered in which the wall heat flux is specified rather than the wall temperature. This type of problem is encountered, for example, in transients associated with nuclear-reactor operation. As in the foregoing analysis, two basic situations will be considered first, and then a more general case will be treated by superposition.

Step Change in Both Pressure Gradient and Wall Heat Flux From an Initially Unheated Condition. For this solution the walls of the channel are initially unheated and at the entering fluid temperature t_0. The flow velocity is steady at the value of $\bar{u}_1$. Then an abrupt change in pressure gradient is made and at the same instant a uniform wall heat flux q_2 is applied.

The energy equation that governs the ensuing transient process is the same as that given in equation (6), except that the dependent variable will now be called T^*, which has the dimensionless form

$$T^* = \frac{t - t_0}{q_2 a/k}$$

The boundary conditions are the same as in equations (7) except for condition (7*d*), which now becomes

$$\left(\frac{\partial T^*}{\partial Y}\right) = \pm 1 \text{ at } Y = \pm 1, \text{ for all } X \text{ and for } \Theta > 0 \quad (28)$$

The steady-state solution for laminar slug flow with uniform wall heat flux is given in [6] as

$$T^* = X + \frac{3Y^2 - 1}{6} - 2\sum_{n=1}^{\infty} \frac{(-1)^n}{(n\pi)^2} e^{-(n\pi)^2 X} \cos n\pi Y \quad (29)$$

For the transient solution, try the similar form,

$$T^* = H_0(\Theta, X) + \frac{3Y^2 - 1}{6} - 2\sum_{n=1}^{\infty} \frac{(-1)^n}{(n\pi)^2} H_n(\Theta, X) \cos n\pi Y \quad (30)$$

Substituting into the energy equation (6), the function H_0 must satisfy the relation

$$\frac{\partial H_0}{\partial \Theta} + \left[1 + 6\left(\frac{\bar{u}_1}{\bar{u}_2} - 1\right)\sum_{m=0}^{\infty} \frac{1}{E_m^4} e^{-E_m^2 \mathrm{Pr}\,\Theta}\right] \frac{\partial H_0}{\partial X} = 1 \quad (31a)$$

where the one on the right-side results from the second derivative of the $(3Y^2 - 1)/6$ term. The H_n are found from

$$\frac{\partial H_n}{\partial \Theta} + \left[1 + 6\left(\frac{\bar{u}_1}{\bar{u}_2} - 1\right)\sum_{m=0}^{\infty} \frac{1}{E_m^4} e^{-E_m^2 \mathrm{Pr}\,\Theta}\right] \frac{\partial H_n}{\partial X} = -(n\pi)^2 H_n \quad (31b)$$

Each of equations (31) will now be solved by using the method of characteristics.

The ordinary differential equations associated with equation (31*a*) are

$$d\Theta = \frac{dX}{1 + 6\left(\frac{\bar{u}_1}{\bar{u}_2} - 1\right)\sum_{m=0}^{\infty} \frac{1}{E_m^4} e^{-E_m^2 \mathrm{Pr}\,\Theta}} = dH_0 \quad (32)$$

From the initial condition of unheated fluid in the channel, H_0 must be zero at $\Theta = 0$. Hence in region I by integrating the first and last terms in equation (32) we obtain,

$$H_0 = \Theta \quad (33)$$

In region II, H_0 must be zero at $X = 0$ in order to maintain the entering temperature at t_0. In region II we obtain by integrating along a characteristic starting at Θ_0

$$H_0 = \Theta - \Theta_0 \quad (34a)$$

The characteristic line in region II is found by integrating the first and second terms in equation (32) subject to the initial condition that at $X = 0$, $\Theta = \Theta_0$,

$$X = \Theta - \Theta_0 - \frac{6}{\mathrm{Pr}}\left(\frac{\bar{u}_1}{\bar{u}_2} - 1\right) \sum_{m=0}^{\infty} \frac{1}{E_m^6} (e^{-E_m^2 \mathrm{Pr}\,\Theta} - e^{-E_m^2 \mathrm{Pr}\,\Theta_0}) \quad (34b)$$

Eliminating Θ_0 from equations (34*a*) and (34*b*) yields the implicit relation for H_0 in region II:

$$X = H_0 - \frac{6}{\mathrm{Pr}}\left(\frac{\bar{u}_1}{\bar{u}_2} - 1\right) \sum_{m=0}^{\infty} \frac{1}{E_m^6} e^{-E_m^2 \mathrm{Pr}\,\Theta} (1 - e^{E_m^2 \mathrm{Pr} H_0}) \quad (34c)$$

The dividing characteristic for the H_0-function is obtained from equation (34*b*) by letting $\Theta_0 = 0$:

$$X = \Theta - \frac{6}{\mathrm{Pr}}\left(\frac{\bar{u}_1}{\bar{u}_2} - 1\right) \sum_{m=0}^{\infty} \frac{1}{E_m^6} (e^{-E_m^2 \mathrm{Pr}\,\Theta} - 1) \quad (35)$$

Equation (31*b*) is treated in exactly the same way as (31*a*). The boundary conditions are that H_n is unity for $\Theta = 0$ in region I, and unity for $X = 0$ in region II. The final results are as follows:

Region I

$$H_n = e^{-(n\pi)^2 \Theta} \quad (36a)$$

Region II

$$X = -\frac{1}{(n\pi)^2} \log_e H_n - \frac{6}{\mathrm{Pr}}\left(\frac{\bar{u}_1}{\bar{u}_2} - 1\right) \cdot \sum_{m=0}^{\infty} \frac{1}{E_m^6} e^{-E_m^2 \mathrm{Pr}\,\Theta} \left(1 - e^{-\frac{E_m^2 \mathrm{Pr}}{(n\pi)^2} \log_e H_n}\right) \quad (36b)$$

Dividing characteristic

$$X = \Theta - \frac{6}{\mathrm{Pr}}\left(\frac{\bar{u}_1}{\bar{u}_2} - 1\right)\sum_{m=0}^{\infty}\frac{1}{E_m^4}\left(e^{-E_m^2 \mathrm{Pr}\,\Theta} - 1\right) \quad (36c)$$

It is noted that some of these equations are the same as those found for the uniform-wall-temperature case; for example, equations (18) and (19b) are the same as equations (35) and (34c). If we let N equal

$$-\frac{1}{(n\pi)^4}\log_e H_n$$

in equation (36b), then the resulting equation for N is the same as that for H_0 in equation (34c). Because of these duplications the computational effort is greatly reduced.

For a case where the wall heat flux is specified, we would like to compute the wall-temperature behavior. From equation (30) the wall temperature is given by

$$\frac{t_w - t_0}{q_2 a/k} = H_0(\Theta, X) + \frac{1}{3} - 2\sum_{n=1}^{\infty}\frac{1}{(n\pi)^4}H_n(\Theta, X) \quad (37)$$

As an example, this expression has been evaluated for the case where $\bar{u}_1 = 0$; that is, initially there is no flow. Then a pressure gradient is applied, and the wall heat flux is stepped from 0 to q_2. Two Prandtl numbers have been used, 0.7 and 0.01, which are typical of gases and liquid metals. The results are given in Figs. 6(a) and (b) and they illustrate how the wall temperature varies with time for a few axial locations. It is seen that the wall temperature increases to a maximum during the initial period of pure one-dimensional conduction, and then decreases to the steady-state value as the velocity accelerates to its final value. This overheating may be of some concern in practical situations. Of course, in practice the heat capacity of the walls will tend to smooth out the temperature behavior. In Fig. 6(b) the Prandtl number was left out of the dimensionless axial position and time. This keeps the numerical magnitudes in the same range as in Fig. 6(a) where the Prandtl number is of order unity. The ordinates in Fig. 6(b) are quite large compared with those in 6(a). However, because of the large values of thermal conductivity for liquid metals as compared with gases, the actual wall temperatures for similar heating rates will generally be smaller for the liquid metals.

The maximum wall temperature at a given position occurs when the fluid that was at the entrance of the heated section when the transient began reaches that position. For any X-location, this time can be found from the equation of the dividing characteristic. The time can be used in the equations for region I to solve for the peak in wall temperature. The peak value is then divided by the final steady wall temperature for that X-location, and this ratio is plotted in Fig. 7 for various Prandtl numbers. For very large X-values, the time for the fluid to reach a given location is large compared with the time for the velocity transient to occur. Hence, for large X, the velocity transient becomes unimportant, and the system behaves as if a steady velocity $\bar{u}_2$ were always present. The curves in Fig. 7 thus move toward a limit of unity for large X, since for the steady-velocity case there is no peak in wall temperature [6].

To understand the behavior of the curve at small X-values, fix attention on a fluid element extending across the channel width and of length dx. The particular element of interest is located at the entrance of the heated section at the instant the pressure gradient is applied. The peak wall temperature at any X-location occurs at the time that this fluid element passes that position. As it travels downstream it receives an amount of heat equal to $2q\,dx$ per unit time. Thus the longer it takes for this fluid ele-

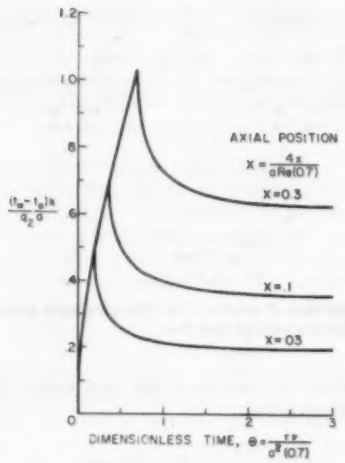

Fig. 6(a) Wall temperature response after a step in pressure gradient and wall heat flux. Initially: $\bar{u} = \bar{u}_1 = 0$, $q = q_1 = 0$; finally: $\bar{u} = \bar{u}_2$ $q = q_2$; Pr = 0.7.

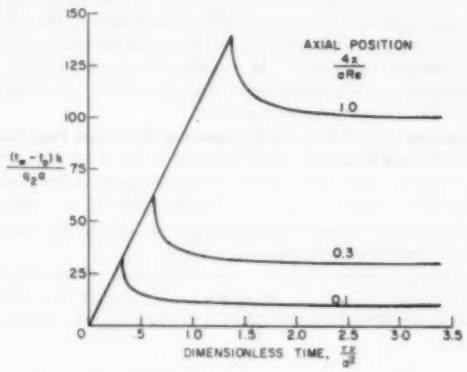

Fig. 6(b) Wall temperature response after a step in pressure gradient and wall heat flux. Initially: $\bar{u} = \bar{u}_1 = 0$, $q = q_1 = 0$; finally: $\bar{u} = \bar{u}_2$, $q = q_2$; Pr = 0.01.

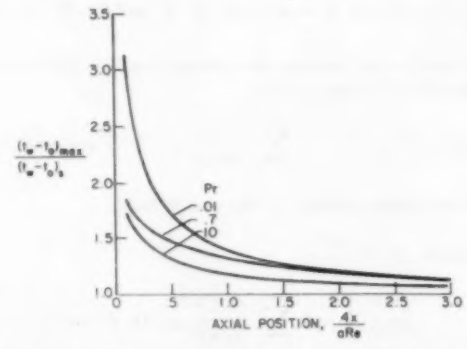

Fig. 7 Ratio of peak to steady-state wall temperature after a step in pressure gradient and wall heat flux. Initially: $\bar{u} = \bar{u}_1 = 0$, $q = q_1 = 0$; finally: $\bar{u} = \bar{u}_2$, $q = q_2$.

ment to travel to a given location, the hotter it will be when it reaches there. While this element is traveling to small X-values, the fluid velocity is very small because the flow has not had time to accelerate appreciably. Thus compared with steady state, where the velocity has accelerated to its final value, the fluid element will be much hotter when reaching locations at small values of X. This causes the curves in Fig. 7 to be increasingly higher as the X-value is decreased.

Step Change in Pressure Gradient With Wall Heat Flux Kept Constant. For this case there is initially a steady-state heat transfer taking place with uniform wall heat flux. Then the pressure gradient is abruptly changed so that the velocity undergoes a transient to a new steady value. Throughout this velocity transient the wall heat flux is kept constant at the initial value. For this case we again try a solution of the form given in equation (30):

$$T^* = L_0(\Theta, X) + \frac{3Y^2 - 1}{6} - 2\sum_{n=1}^{\infty} \frac{(-1)^n}{(n\pi)^2} L_n(\Theta, X) \cos n\pi Y \quad (38)$$

In region II the boundary conditions at $X = 0$ are the same for this problem as in the preceding case. Hence for region II the values for L_0 and L_n are equal to those for H_0 and H_n. The only thing new to consider is in region I. The initial temperature distribution can be obtained from equation (29) as: at $\Theta = 0$,

$$T^* = \frac{\bar{u}_2}{\bar{u}_1} X + \frac{3Y^2 - 1}{6} - 2\sum_{n=1}^{\infty} \frac{(-1)^n}{(n\pi)^2} e^{-(n\pi)^2(\bar{u}_2/\bar{u}_1)X} \cos n\pi Y \quad (39)$$

The initial condition on L_0 is then $L_0 = (\bar{u}_2/\bar{u}_1)X_0$ for a characteristic line starting at $\Theta = 0$ and $X = X_0$. The characteristic equations are the same as those given in equation (32), so the behavior of L_0 along a characteristic line in region I is given by

$$\int_{(\bar{u}_2/\bar{u}_1)X_0}^{L_0} dL_0 = \int_0^{\Theta} d\Theta$$

or

$$L_0 = \Theta + \frac{\bar{u}_2}{\bar{u}_1} X_0 \quad (40)$$

The characteristic line in region I is found by integrating the first two terms in equation (32) with the initial conditions $X = X_0$ at $\Theta = 0$:

$$X - X_0 = \Theta - \frac{6}{\mathrm{Pr}}\left(\frac{\bar{u}_1}{\bar{u}_2} - 1\right) \sum_{m=0}^{\infty} \frac{1}{E_m^4}\left(e^{-E_m^2 \mathrm{Pr}\,\Theta} - 1\right) \quad (41)$$

Eliminating X_0 from equations (40) and (41) results in an expression for L_0 in region I:

$$L_0 = \Theta + \frac{\bar{u}_2}{\bar{u}_1}\left[X - \Theta + \frac{6}{\mathrm{Pr}}\left(\frac{\bar{u}_1}{\bar{u}_2} - 1\right) \sum_{m=0}^{\infty} \frac{1}{E_m^4}\left(e^{-E_m^2 \mathrm{Pr}\,\Theta} - 1\right)\right] \quad (42)$$

The expressions for L_n are found in the same way, except that at $\Theta = 0$, $L_n = e^{-(n\pi)^2(\bar{u}_2/\bar{u}_1)X_0}$ for a characteristic originating at X_0. This yields for region I

$$\log_e L_n = -(n\pi)^2 \left\{\Theta + \frac{\bar{u}_2}{\bar{u}_1}\left[X - \Theta + \frac{6}{\mathrm{Pr}}\left(\frac{\bar{u}_1}{\bar{u}_2} - 1\right) \sum_{m=0}^{\infty} \frac{1}{E_m^4}\left(e^{-E_m^2 \mathrm{Pr}\,\Theta} - 1\right)\right]\right\} \quad (43)$$

With these equations we have L_0 and L_n in regions I and II, and the solution as given by equation (38) can be carried out. A numerical example will be discussed in the next section.

Step Change in Both Pressure Gradient and Wall Heat Flux With Initial Steady Heating. Now a more general case can be solved by superposing the two preceding solutions. Initially there is a steady-state heat transfer with a flow velocity $\bar{u}_1$ and a wall heat flux q_1. Then the pressure gradient is changed abruptly and the wall heat flux is also changed. A transient process ensues, and a steady state is eventually achieved with the velocity $\bar{u}_2$ and the wall heat flux q_2.

The superposition proceeds in the same manner as that given for the uniform-wall-temperature case. The procedure is illustrated in Fig. 5.

The first part of the superposition is the case treated by equation (30). This yields the temperature distribution

$$t = (q_2 - q_1)\frac{a}{k}\left[H_0(\Theta, X) + \frac{3Y^2 - 1}{6} - 2\sum_{n=1}^{\infty} \frac{(-1)^n}{(n\pi)^2} H_n(\Theta, X) \cos n\pi Y\right]$$

$$= (q_2 - q_1)\frac{a}{k}\,[H_n \text{ solution}] \quad (44a)$$

The second solution to be superposed is obtained from equation (38):

$$t = q_1 \frac{a}{k}\left[L_0(\Theta, X) + \frac{3Y^2 - 1}{6} - 2\sum_{n=1}^{\infty} \frac{(-1)^n}{(n\pi)^2} L_n(\Theta, X) \cos n\pi Y\right] + t_0$$

$$= q_1 \frac{a}{k}\,[L_n \text{ solution}] + t_0 \quad (44b)$$

Adding yields the desired general result,

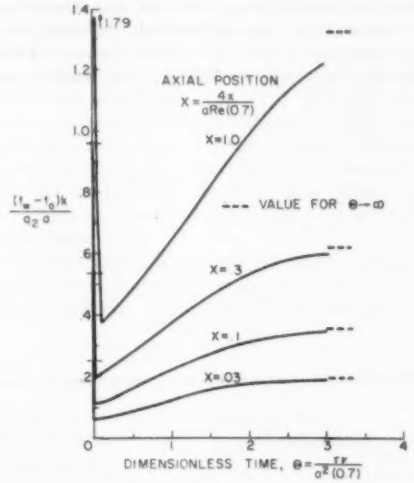

Fig. 8 Wall-temperature response after a step change in pressure gradient and wall heat flux. $\mathrm{Pr} = 0.7$; $q_1/q_2 = 5$; $\bar{u}_1/\bar{u}_2 = 10$.

$$\frac{t - t_0}{q_2 a/k} = \left(1 - \frac{q_1}{q_2}\right) [H_a \text{ solution}] + \frac{q_1}{q_2} [L_a \text{ solution}] \quad (44c)$$

A numerical example has been computed from this relation and is given in Fig. 8. Here there is initially a steady-state flow and wall heat transfer. Then the pressure gradient is abruptly decreased so that the velocity coasts down to one tenth of its original value. Simultaneously, the wall heat flux is dropped by a factor of 5. When the heat flux is abruptly reduced, there is a rapid decrease in wall temperature, since the velocity is still at a high value. This closely follows the process that would be obtained if the fluid flow were held steady while the heat flux was changed [6]. Then as the velocity gradually slows down, the wall temperature rises to the final steady-state distribution. This is the type of transient that might be encountered in a nuclear-reactor coolant passage when the power is suddenly reduced as the result of a primary cooling-pump failure.

Discussion

A method has been presented for evaluating transient heat-transfer effects during unsteady flow conditions. The numerical examples illustrate how heat-transfer overshoots can occur in situations where the velocity is changing with time. Two of the assumptions made here should be discussed further. (*a*) The slug-flow restriction; and (*b*) the assumption of negligible wall heat capacity.

The simplification provided by the slug-flow assumption has made it possible to obtain exact mathematical solutions to the governing energy equation. From these it is possible to gain a physical interpretation of the transient processes for different thermal boundary conditions. The numerical values are of course somewhat in error compared to the true situation with a two-dimensional velocity distribution. The authors are currently extending the analysis to account at least partially for the velocity distribution across the channel. By comparing [6 and 7], it is seen that the slug-flow approximation does yield a good indication of the physical behavior for the transients considered there.

Wall heat capacity will be expected to moderate, to some extent, the time response in the heat-transfer behavior. The results given here are the extreme cases when the wall heat capacity is negligible compared to that of the fluid. If a wall of finite capacity is placed between the heat source and the fluid, it will delay the heat flowing to the fluid, and this will enable the velocity transient to proceed partially. Hence the velocity transient would have a lesser role in this instance. For a wall of very large heat capacity, the velocity may reach a new steady state before the heating within the channel starts. Then the velocity transient would not have to be considered in the analysis, and the information in [4 to 7] could be utilized.

In closing, it should be mentioned that this type of analysis is not restricted to abrupt pressure-gradient changes, but can also be solved for other timewise pressure variations. The work is currently being extended to the case where a pulsating pressure gradient is present. By additional superposition, more complicated wall boundary conditions could be treated. For example, the specified wall temperature or heat flux could vary in the axial direction. The parallel-plate channel could be treated with one wall heated and one wall insulated. The analysis could also be carried out for other geometries such as the circular tube.

Acknowledgment

The authors would like to acknowledge the work of Miss Frances J. Schubert, who carried out the machine computations for the examples presented herein.

References

1 J. A. Clark, V. S. Arpaci, and K. M. Treadwell, "Dynamic Response of Heat Exchangers Having Internal Heat Sources—Part I," TRANS. ASME, vol. 80, 1958, pp. 612–624.

2 V. S. Arpaci and J. A. Clark, "Dynamic Response of Heat Exchangers Having Internal Heat Sources—Part II," TRANS. ASME, vol. 80, 1958, pp. 625–634.

3 V. S. Arpaci and J. A. Clark, "Dynamic Response of Heat Exchangers Having Internal Heat Sources—Part III," JOURNAL OF HEAT TRANSFER, TRANS. ASME, Series C, vol. 81, 1959, pp. 253–266.

4 E. M. Sparrow and R. Siegel, "Thermal Entrance Region of a Circular Tube Under Transient Heating Conditions," Proceedings of The Third U. S. National Congress for Applied Mechanics, Brown University, Providence, R. I., June, 1958.

5 R. Siegel and E. M. Sparrow, "Transient Heat Transfer for Laminar Forced Convection in the Thermal Entrance Region of Flat Ducts," JOURNAL OF HEAT TRANSFER, TRANS. ASME, Series C, vol. 81, 1959, pp. 29–36.

6 R. Siegel, "Transient Heat Transfer for Laminar Slug Flow in Ducts," *Journal of Applied Mechanics*, vol. 26, TRANS. ASME, Series E, vol. 81, 1959, pp. 140–142.

7 R. Siegel, "Heat Transfer for Laminar Flow in Ducts With Arbitrary Time Variations in Wall Temperature," *Journal of Applied Mechanics*, vol. 27, TRANS. ASME, Series E, vol. 82, June, 1960, pp. 241–249.

8 K. Millsaps and K. Pohlhausen, "Heat Transfer to Hagen-Poiseuille Flows," Proceedings, Conference on Differential Equations, University of Maryland, March, 1955.

9 H. S. Carslaw and J. C. Jaeger, "Conduction of Heat in Solids," Clarendon Press, Oxford, England, second edition, 1959.

10 F. B. Hildebrand, "Advanced Calculus for Engineers," Prentice-Hall, Inc., New York, N. Y., 1949.

11 R. Siegel, "Transient Free Convection From a Vertical Flat Plate," TRANS. ASME, vol. 80, 1958, pp. 347–359.

L. W. CARLSON
Research Engineer, Rocketdyne, Canoga Park, Calif.

T. F. IRVINE, JR.
Professor and Dean of Engineering, State University of New York, Oyster Bay, N. Y.
Mem. ASME

Fully Developed Pressure Drop in Triangular Shaped Ducts

Introduction

THE PREDICTIONS of fully developed turbulent pressure drops in noncircular ducts are presently based mainly on empericism. It has been found by Nikuradse [1][1] and others, that for a wide variety of duct shapes, the pressure drop correlations which are valid for circular tubes may be applied to noncircular ducts if the hydraulic diameter $\frac{(4 \times \text{cross-sectional area})}{\text{perimeter}}$ is substituted for the characteristic dimension in the friction factor and the Reynolds number. A large number of such investigations which relate to this hydraulic diameter concept have been summarized by Claiborne [2] and Eckert and Irvine [3].

Although the above procedure appears to work for a wide variety of cross sections, there is little rational justification for its use and it throws no light on the basic mechanisms involved in noncircular duct flow. In addition, there is no guarantee that the hydraulic diameter rule will continue to apply to as yet uninvestigated shapes.

Recently, Deissler and Taylor [4] have attempted to construct a model of turbulent noncircular duct flow from which calculations of the velocity field and pressure drop may be made. Essentially, their procedure consists of the specification that on lines normal to the duct walls the velocity distribution may be characterized by the universal velocity profile which has been established for circular tubes. This specification, if the point of maximum velocity is known, is sufficient to define an iterative calculation technique to determine the velocity field. Using this approach they have calculated the fully developed turbulent velocity field for a square and an equilateral triangle.

The analysis of Deissler and Taylor does not take into account secondary flows and the presence of exaggerated laminar sublayers in corner regions. The former have been observed in a number of experiments, for example in [1], and the latter have been investigated for narrow triangular shapes by Eckert and Irvine [5]. Nevertheless, for the square and equilateral triangular shape, the agreement between their calculations and experiments is satisfactory.

The purpose of the investigation reported here was to obtain pressure drop data for duct shapes which were more extreme than those investigated by Deissler and Taylor and which thus presented a more critical test of their analysis technique. These measurements were made on ducts with narrow isosceles triangular cross sections. It was also suspected from the nature of the flow in narrow corner regions [5] that large deviations might be expected from the use of the hydraulic diameter rule for such shapes. Such deviations had been observed previously on similar ducts and reported in [6].

Friction factors were measured therefore for isothermal, fully developed, laminar and turbulent flow in smooth isosceles triangular ducts having apex angles that varied from 4 to 39 degrees. Comparisons were made between the measurements and the values predicted by Deissler and Taylor for apex angles of 12 and 22.3 degrees. The calculations predicted that the friction data should fall below the circular tube line which agreed with experiment, although the quantitative comparison was not good. The hydraulic diameter rule was in error by 4 per cent for the apex angle of 38.8 degrees and by 20 per cent for the 4 degree apex angle.

Apparatus

The experimental apparatus used to obtain pressure drop data was similar to that described in [3] with the exception of the duct cross section and the entrance shape. In the setup used, air was drawn through the duct by a blower located downstream, after passing through a dust filter and cloth screen to reduce large scale inlet disturbances. The air then flowed past an abrupt entrance and into the hydrodynamic entrance section where it became fully developed. It then entered the section where the pressure drop readings were made, which consisted of four identical test sections in series. These multiple sections served to check on the reproducibility of the measurements and to insure that the flow was fully developed. The pertinent dimensions of the duct are listed in Table 1 for the various apex angles investigated.

After leaving the test section, the air passed through a transition section which changed the cross section to a circular shape by abrupt expansion. It then flowed through a flow measuring

[1] Numbers in brackets designate References at end of paper.

Contributed by the Heat Transfer Division and presented at the Winter Annual Meeting, New York, N. Y., November 27–December 2, 1960, of THE AMERICAN SOCIETY OF MECHANICAL ENGINEERS. Manuscript received at ASME Headquarters, July 28, 1960. Paper No. 60—WA-100.

Nomenclature

"C" = constant in equation (3)
D = hydraulic diameter
f = friction factor, equation (1)
P = pressure
Re = Reynolds number, equation (2)
$\bar{w}$ = average velocity in flow direction
Z = co-ordinate distance in flow direction
α = half angle of triangle apex
ρ = mass density
μ = dynamic viscosity

Superscripts

* refers to circular tube (See Fig. 10)

device, a throttling valve, and back to the room through the blower.

Table 1 Dimensions of experimental ducts

Apex angle, deg	Hydraulic diam, in.	Hydrodynamic entrance length, hydraulic diam	Individual test section length, hydraulic diam
4.01	0.1516 ± 0.0004	475	123
7.96	0.2895 ± 0.0006	248	58.6
12.0	0.4227 ± 0.0009	170	40.2
22.3	0.7122 ± 0.0010	101	23.9
38.8	1.0526 ± 0.0014	68	16.1

A sketch of the cross section of the duct is shown in Fig. 1. Each of the five ducts has identical parts except for their respective base plates which specify the apex angle. It may be noted in the figure that each pressure measuring station has two wall pressure taps at different transverse locations. This was for the purpose of checking for pressure differences normal to the flow directions. Such pressure differences were found to be negligibly small. All pressure taps consisted of a wall hole 0.018 in. diameter and, following the specifications of Rayle [7], had a countersink depth to hole diameter ratio of one half.

The possibility of air leakage into the duct exists where the side plates are pressed against the base plate. In operation, this seam was taped and painted after which leakage rates were measured by sealing off the entrance. The influence of leakage on the results is discussed in the section on errors.

Fig. 2 shows a sketch of the flow circuit including the physical dimensions of the hydrodynamic entrance section and the pressure measuring stations.

Depending on the magnitude of the pressure drops, different manometer schemes were used. For pressure differences greater than 0.01 in. of H_2O, a commercial manometer (Meriam Tupe A-750) was used which had an estimated accuracy of ±0.0005 in. of water. For smaller pressure differences the special micromanometer described in [8] was utilized. The latter can measure pressure differences of 0.001 in. of H_2O with an accuracy of one per cent.

Mass flow rates were determined either with Fischer Porter "Flowrators" or standard ASME flange tap orifices. The accuracy of each orifice is specified as 0.5 per cent and in their overlapping flow ranges, the orifices agreed to within 0.4 per cent. The accuracy of the Flowrators is estimated as one per cent.

Inlet air temperature was read from a calibrated mercury-in-glass thermometer positioned at the duct entrance. This temperature was used to evaluate physical properties and to calculate the density at the pressure and flow measurement stations. The accuracy of the thermometer was within 0.2 deg F for normal room temperature and this uncertainty had a negligible effect on any results. Barometric pressure was obtained from a Fortin type 2-380 barometer which is accurate to within 0.03 per cent.

As shown in the following section, the experimental data are presented in the form of friction factor against Reynolds number. These two quantities are defined by the following equations. The section on Nomenclature should be consulted for the meaning of the symbols.

$$\frac{\Delta P}{\Delta Z} = \frac{\rho \bar{v}^2}{2} \frac{f}{D} \tag{1}$$

and

$$\mathrm{Re} = \frac{\rho w D}{\mu} \tag{2}$$

A careful error analysis was made of the effect of instrument errors, geometric uncertainties, and duct leakage on the friction factor and Reynolds number. It was concluded that the maximum systematic error was 2.5 per cent in the friction factor and 2.12 per cent in the Reynolds number. These figures may be taken as the accuracies of the final results. The details of the error analysis are given in [9].

Presentation of Results

For each duct angle, friction factors were measured in the laminar, transitional, and turbulent regimes. The laminar data when compared against available theoretical solutions served as a check on the operation of the apparatus and added confidence to the turbulent flow results.

Figs. 3, 4, 5, 6, and 7 show the experimental friction factors for apex angles of 4.01, 7.96, 12.0, 22.3, and 38.8 degrees, respectively. Also shown in the figures as solid lines are the laminar solutions and the Blasius solution for the circular tube

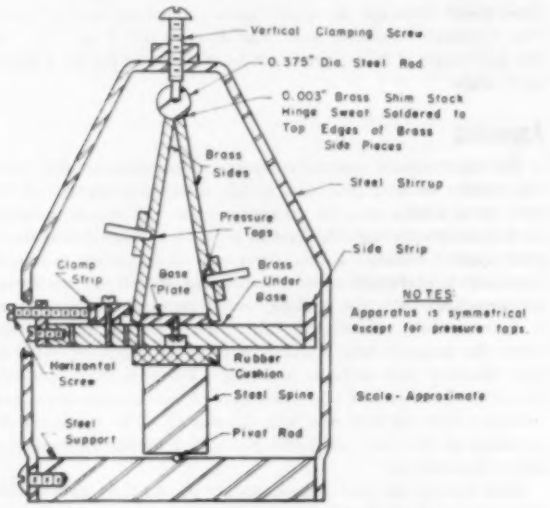

Fig. 1 Construction details of variable angle duct

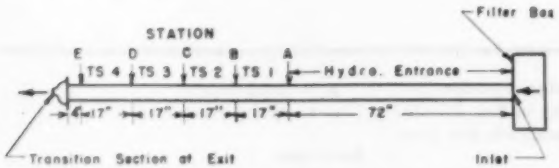

Fig. 2 Sketch of flow circuit showing test sections (TS)

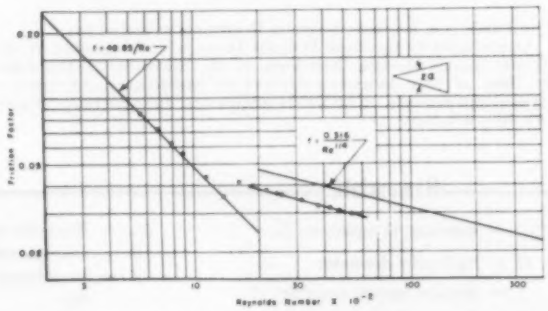

Fig. 3 Friction factor versus Reynolds number 2α = 4.01 deg

in turbulent fully developed flow. For the four smallest angles the laminar solutions used were those of Yen's [10] for a circular sector having the same apex angle. For the 38.8 deg angle the solution of Nuttall [11] for an isosceles triangle was used. The solid points in Figs. 5 and 6 are calculated points and will be discussed later.

Fig. 8 shows a comparison of the laminar results with the calculated lines. The open circles which are averages of all laminar points for each duct angle are values of the product friction factor against Reynolds number which has a unique value depending upon the cross-sectional shape for laminar flow. The solid lines in the figure are the theoretical solutions discussed above. It will be noted that the measurements differ from the calculated line by about 2 per cent in the worst case. This is in good agreement with the predictions of the error analysis.

Discussion of Results

Comparison of Figs. 3 through 7 shows that as the apex angle is made smaller the friction factor falls a greater amount below the circular tube line. This is seen more clearly in Fig. 9 where all of the data are shown on a single graph. The lines identified by the apex angles in this figure represent the best fit of the experimental data. The two curves for 22.3 and 38.8 degrees are dashed at the lower Reynolds numbers because the flow appears to be still in transition in these regions.

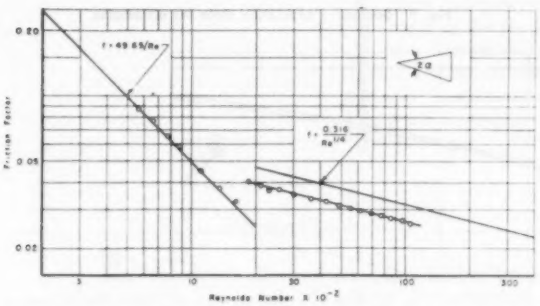

Fig. 4 Friction factor versus Reynolds number $2\alpha = 7.96$ deg

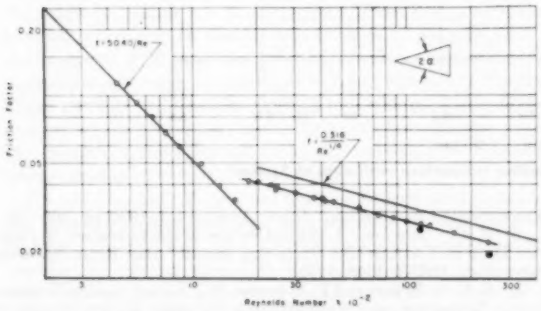

Fig. 5 Friction factor versus Reynolds number $2\alpha = 12.0$ deg

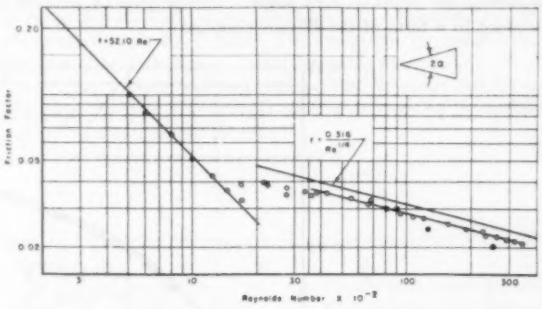

Fig. 6 Friction factor versus Reynolds number $2\alpha = 22.3$ deg

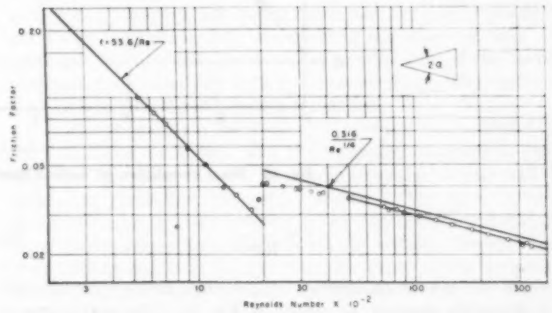

Fig. 7 Friction factor versus Reynolds number $2\alpha = 38.8$ deg

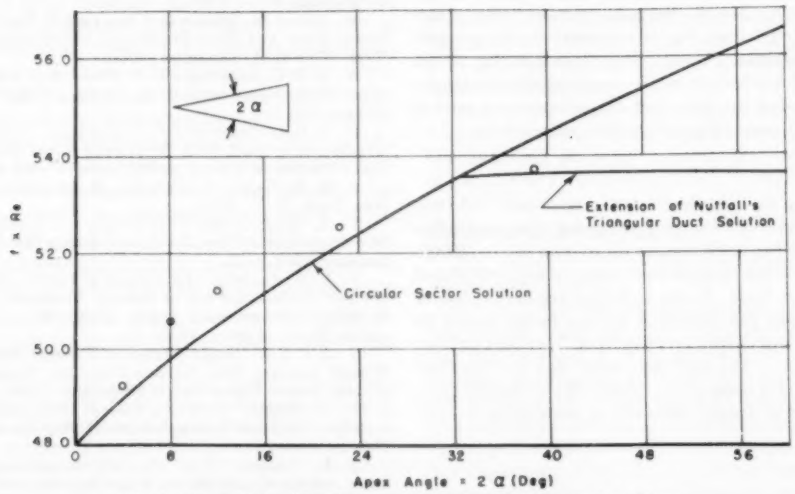

Fig. 8 Comparison of laminar measurements with theoretical solutions

Fig. 9 illustrates that the hydraulic diameter rule does not hold for the cross sections investigated and that the deviation is greatest for the small angles. Figs. 5 and 6 which contain the solid points calculated by the method of Deissler and Taylor show that for the 12 and 22.3 degree ducts their calculation method underestimates the friction factor by almost as much as the hydraulic diameter rule overestimates it, although the trend is in the right direction. It would appear that the considerable difficulty involved in the Deissler and Taylor calculation procedure is not justified for the types of cross sections considered here.

Fig. 10 is presented as a correlation of the experimental data to include the effect of apex angle. This is done by defining a constant in a form of the Blasius equation:

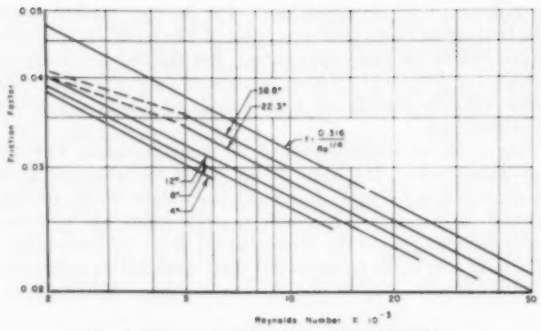

Fig. 9 Summary of friction data for all angles

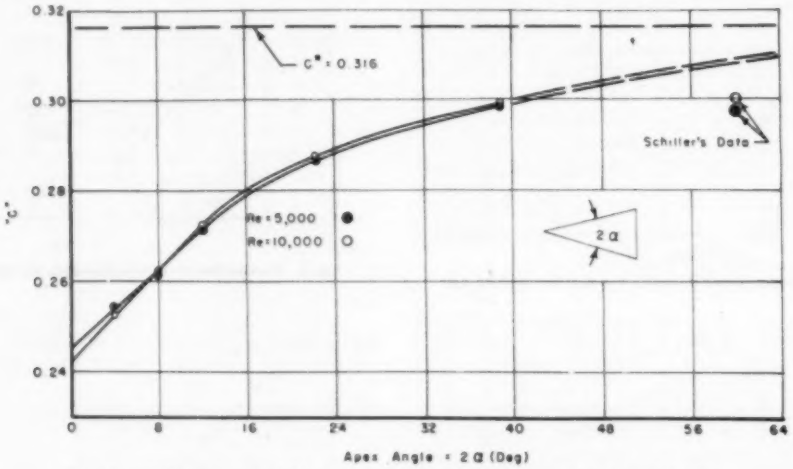

Fig. 10 Final correlation of friction data including comparison with data of Schiller

$$f = \frac{"C"}{Re^{0.25}} \qquad (3)$$

where "C" is a strong function of apex angle and a weak function of Reynolds number as shown in Fig. 9. The correlation is shown for two representative Reynolds numbers. The horizontal dashed line represents the constant for a circular tube and is identified as C^*. For the Reynolds number range of this study, the values of "C" from Fig. 10 represent the data within the limits of the experimental error. Also shown in Fig. 10 are the measurements of Schiller [12] made on an equilateral triangle. The agreement between his data and the extension of ours is within the combined error limits of the two experiments.

Summary

The friction factor for fully developed laminar and turbulent flow in smooth wall isosceles triangles of varying apex angles has been measured in the Reynolds number range from 500 to 30,000. In the laminar regime the measurements agreed with calculated values within two per cent. In the turbulent regime the use of the hydraulic diameter rule predicted friction factor values 20 per cent high for the four degree apex angle and 5 per cent high for the 38.8 degree angle. The turbulent data may be described within two per cent of a mean curve, $5000 < Re < 30{,}000$, using the apex angle and hydraulic diameter as correlating parameters.

References

1 J. Nikuradse, "Investigation of Turbulent Flow in Tubes of Non-Circular Cross Section," *Ingen. Arch.*, vol. 1, 1930, pp. 306–332.

2 H. C. Claiborne, "A Critical Survey of the Literature on Pressure Drop in Non-Circular Ducts and Annuli," Oak Ridge National Laboratory, ORNL 1248, 1952.

3 E. R. G. Eckert and T. F. Irvine, Jr., "Incompressible Friction Factor, Transition, and Hydrodynamic Entrance Length Studies of Ducts With Triangular and Rectangular Cross Sections," Proceedings of the Fifth Midwestern Conference on Fluid Mechanics, University of Michigan Press, 1957.

4 Robert G. Deissler and Maynard F. Taylor, "Analysis of Turbulent Flow and Heat Transfer in Non-Circular Passages," NACA Tech. Note 4384, September, 1958.

5 E. R. G. Eckert and T. F. Irvine, Jr., "Flow in Corners of Passages With Noncircular Cross Sections," TRANS. ASME, vol. 78, 1956, p. 709.

6 E. R. G. Eckert and T. F. Irvine, Jr., "Pressure Drop and Heat Transfer in a Duct With Triangular Cross Section," JOURNAL OF HEAT TRANSFER, TRANS. ASME, Series C, vol. 82, May, 1960, p. 125.

7 R. C. Dean, *Aerodynamic Measurements*, Eagle Enterprises, New York, N. Y., 1953.

8 R. Eichhorn and T. F. Irvine, Jr., "Description of a Sensitive Micromanometer," *The Review of Scientific Instruments*, vol. 29, no. 1, January, 1958, p. 23.

9 L. W. Carlson, "Experimental Friction Factors for Fully Developed Turbulent Flow in Smooth Triangular Ducts," MS thesis, Mechanical Engineering Dept., University of Minnesota, Minneapolis, Minn., August, 1959.

10 J. T. Yen, "Exact Solution of Laminar Heat Transfer in Wedge Shaped Passages With Various Boundary Conditions," WADC TR 57-224, Wright-Patterson Air Force Base, Ohio, 1957, p. 6.

11 H. Nuttal, "Flow of a Viscous Incompressible Fluid, Expression for a Uniform Triangular Duct," *Engineering*, vol. 178, 1954, p. 298.

12 L. Schiller, "Uber den Stromungswiderstand von Rohren verschiedenen Querschitts und Rauhigkeitsgrades," *Zeit. Ang. Math. und Mech.*, 1923, p. 2.

The Effect of a Longitudinal Magnetic Field on Pipe Flow of Mercury[1]

SAMUEL GLOBE
Harvard University and
Research and Development Division,
AVCO Corporation,
Wilmington, Mass.

An experimental investigation has been made of the effect of an axial magnetic field on transition from laminar to turbulent flow and on the turbulent friction factor for pipe flow of mercury. Magnetic-flux densities up to 5700 gauss were obtained with a water-cooled solenoid. Pipes of glass and aluminum were used of approximately 0.1 to 0.2 in. diam. The maximum Hartmann number, with the hydraulic radius (half the actual radius) taken as the characteristic length, was about 20. Measurements were made of the pressure gradient and velocity of flow. The transition Reynolds number was determined from the curve of friction factor against Reynolds number.

The results show an increasing value of minimum transition Reynolds number with Hartmann number. The magnetic field also brought about a decrease in the turbulent friction factor and corresponding shear force at the wall.

Introduction

When an electrically conducting fluid flowing through a pipe is subjected to a magnetic field parallel to the direction of the flow, there will be no interaction between the fluid and the magnetic field as long as the flow is laminar, because the flow and the magnetic vectors are then parallel. If the flow is turbulent, however, there will be components of velocity perpendicular to the magnetic field, and an interaction can be expected. The interaction will result in generated emf and currents in the fluid. These currents will in turn interact with the magnetic field to produce a ponderomotive force. By Lenz's law, the direction of this ponderomotive force will be such as to oppose the transverse motion that gave rise to the interaction.

We are thus led to speculate that a magnetic field parallel to the direction of flow in a pipe may represent an additional stabilizing influence, and may thereby delay the transition from laminar to turbulent flow. We may also speculate that a magnetic field might actually suppress turbulence in a conducting fluid, and re-establish laminar flow at Reynolds numbers above transition.

The instability of plane Poiseuille flow of a conducting fluid, under the influence of a magnetic field parallel to the flow, was first examined theoretically by Stuart [1],[2] who found that such a field does in fact increase the critical Reynolds number. It is difficult to apply Stuart's results directly to an experiment, because it is known that stability theory is not completely successful in predicting the onset of turbulence in pipe flow. For example, for plane Poiseuille flow, theory predicts a critical Reynolds number $(4v\delta/\nu)$ where v is the average velocity, δ is the half separation of the planes, and ν the kinematic viscosity of about 14,000, reference [2]; however, transition to turbulence occurs, if entry conditions are sufficiently disturbed, at Reynolds numbers between 2000 and 3000, reference [3]. For axisymmetric Poiseuille flow, infinitesimal disturbance theory predicts the fully developed flow to be completely stable [4], although in fact transition to turbulence occurs at a Reynolds number of about 2000, reference [3].

In view of the failure of stability theory to account quantitatively for transition of Poiseuille flow in ordinary hydrodynamics, it is hardly to be expected that Stuart's analysis should yield quantitatively correct results in magnetohydrodynamic pipe flow. However, one might hope that the theory would in some way predict correctly the effect of the magnetic field. It turns out, in fact, that an empirical modification of the theory does agree quantitatively with the experimental results, so far as the effect of the magnetic field is concerned.

In order to maintain the distinction between the instability (if any) predicted by theory, and the transition observed in practice, the Reynolds number at which transition occurs will be called the "transition Reynolds number." The term "critical Reynolds number" will be reserved for the minimum Reynolds number of neutral stability as predicted by stability theory. Now it is well known that in pipe flow the value of the transition Reynolds number is not unique, but depends on conditions at the entry to the pipe [5]. If the entry is kept smooth, transition will occur at much higher Reynolds numbers than the value of 2000 usually cited. However, there is a minimum value of the transition Reynolds number, which is observed when the entry conditions are sufficiently disturbed. It is this value that was obtained in the present experiment, by having the fluid enter the pipe over a sharp lip.

The primary object of this experiment may then be stated as follows: To measure the effect of a longitudinal magnetic field on the minimum Reynolds number of transition. A secondary object was to determine the effect of this field on turbulent flow.

Experimental Arrangements

The general experimental arrangements are shown schematically in Fig. 1.

The magnetic field was provided by a water-cooled solenoid, wound with copper tubing of $^1/_4$-in. OD and 0.031-in. wall, which was first ovalized in cross section. Cooling water was passed through the interior of the tubing. The main winding of the solenoid consisted of 20 layers of 58 turns each layer; to improve the uniformity of the field, a corrector winding, consisting of 16 layers of 6 turns per layer, was placed outside each end of the main winding. The position of the corrector windings was adjusted axially to give best uniformity of the longitudinal field along the axis. The solenoid had an ID of $1^1/_2$ in. and a length

[1] The material in this paper forms part of a PhD thesis submitted under the guidance of Prof. R. W. P. King to Harvard University.

[2] Numbers in brackets designate References at end of paper.

Contributed by the Heat Transfer Division and presented at the Winter Annual Meeting, New York, N. Y., November 27–December 2, 1960, of The American Society of Mechanical Engineers. Manuscript received at ASME Headquarters, April 12, 1960. Paper No. 60—WA-192.

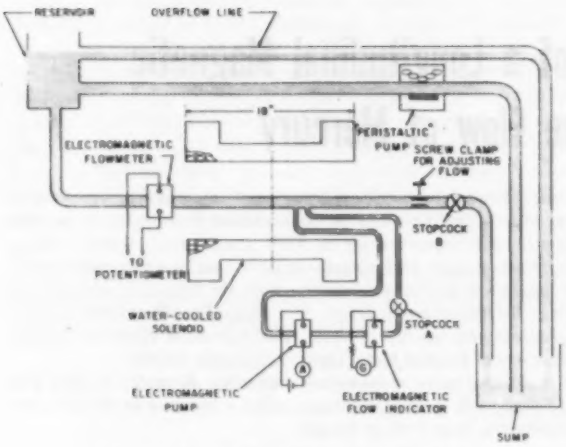

Fig. 1 General experimental arrangements

Mercury is pumped from sump to reservoir by means of peristatic pump. Overflow line helps to maintain a constant level in reservoir, and to smooth out fluctuations of pump. Mercury then passes through flowmeter, through test section within solenoid, and back to sump. Pressure drop between taps is measured by means of electromagnetic pump and electromagnetic flow indicator, as described in text.

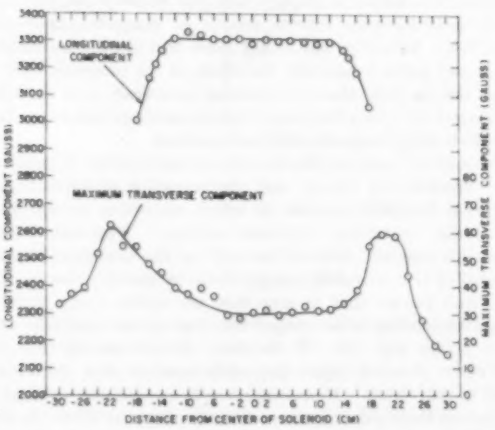

Fig. 2 Flux density on the axis of the solenoid (for a current of 100 amp)

of 18 in. of which the central 12 in. was the working length.

Within the central 12 in. the longitudinal component was uniform within about $\pm 1^1/_2$ per cent and the maximum transverse component was less than 1 per cent of the longitudinal component. A few measurements about $^1/_2$ in. off the axis showed the components of magnetic field there to be uniform within the same limits. The longitudinal and transverse components of the field are plotted in Fig. 2. The longitudinal flux density was measured with a fluxmeter manufactured by the Sensitive Instrument Research Company, and the transverse flux density with a Rawson Type 402 rotating-coil gaussmeter. The highest flux density in the experiment was 5700 gauss.

The fluid used in the experiment was mercury. The mercury was lifted from the sump, Fig. 1, to the reservoir by means of a "peristaltic" pump manufactured by Sigmamotor, Inc. Such a pump produced a fluctuating output, which was smoothed out by the volume of the reservoir as well as by the overflow line from the reservoir to the sump. The overflow line also served to provide a constant head of mercury, nearly independent of the rate of flow through the mercury circuit.

From the reservoir the mercury flowed through an electromagnetic flowmeter, then through the test section located within the solenoid, and back to the sump. The rate of flow was controlled by throttling the line with a screw clamp just upstream of the sump.

The test sections themselves were glass or aluminum tubes. The entrance of each test section had a sharp lip to provide a disturbance to the flow and promote transition to turbulence at the minimum transition Reynolds number. Pressure ports of $^1/_{16}$ in. diam were drilled through the wall of the tubes, and a glass half-round which itself had a blown "L" connection, was cemented over each pressure port. Tygon tubing was attached to the L, and at its other end, connected to the pressure-measuring apparatus. Connections between sections of the main mercury circuit were also made with Tygon tubing.

The volume velocity of the mercury was determined by means of an electromagnetic flowmeter, which was calibrated by weighing the amount of mercury passing through it in measured intervals of time. The electrical output of the flowmeter was measured with a potentiometer. The flowmeter gave a precision of about $^1/_2$ per cent. The magnetic field for the flowmeter, 3300 oersteds, was provided by a permanent magnet. The flowmeter element itself had a bore of $^1/_4$ in., and was made of Kel-F plastic. The electrodes in the flowmeter were stainless-steel screws. Pieces of glass tubing, 7 mm ID and 25 in. long, were connected to the flowmeter element on both sides by means of short stubs of Tygon tubing. These entrance and exit sections were fixed in orientation with respect to the flowmeter element. The possible change in sensitivity that may occur from changes in the flow profile through the flowmeter [6, 7], arising from changes in the orientation of the entrance and exit sections, was thereby avoided.

Apart from the electrodes in the flowmeter, the electrodes in the pressure-measuring apparatus, described later, and the aluminum test sections, when they were used, all parts of the mercury circuit were made of glass, Tygon tubing, or other plastic. All glass portions of the system were scrupulously cleaned before the system was filled with mercury, and Tygon tubing was never reused. Under these conditions, the apparatus could be run for a period of 4 or 5 weeks before the mercury began to show appreciable discoloration, and even at the end of this time, there was no change detectable in the operation of the system which could be attributed to the contamination of the mercury. On dismantling the system, one could see a film of discoloration adhering to the Tygon tubing, and to any glass that was struck by mercury in a free stream, as in the sump. These surfaces apparently acted as a filter for contaminants, while the glass test sections appeared superficially to be as clean on removal as they were on insertion.

The contact resistance between the stainless-steel electrodes and the mercury was found to be negligibly small unless the electrodes were exposed to the air after they had once been in contact with mercury. Under such circumstances the resistance between the terminals of the flowmeter increased to a fluctuating value of tens or hundreds of ohms. Careful cleaning of the surfaces of the electrodes after every exposure to air remedied this difficulty.

Measurement of the radius of the test section needs to be made with precision, because for a given rate of volume flow, the friction factor in a circular pipe is proportional to the fifth power of the radius. With the glass tubes, the average radius was determined by weighing the amount of mercury it took to fill a measured length of the test section between the pressure taps, the length being determined with a cathetometer. This observation was estimated to be precise within $^1/_4$ per cent or better. With the aluminum test section the measurement of the radius had to

be made mechanically, with a Starrett "small hole gage." This determination was estimated to be correct within 0.001 in. in 0.196 in. or about $^1/_2$ per cent.

The greatest problem associated with filling the system was the elimination of air bubbles. To assist in this process, vents, consisting of vertical glass tubes, were added at several of the junctions between sections of the circuit. Even so it was an arduous and delicate task to remove the bubbles. It was necessary to leave enough slack in the hoses connected to the test sections so that the test section could be removed completely from the solenoid, while the mercury circuit remained intact, in order that bubbles might be removed from the test section, the pressure ports, and the connecting sections.

The temperature of the mercury was taken during every run or calibration, and the viscosity and density of mercury needed for the calculations were taken from the Liquid Metals Handbook [8], for that temperature. However, the properties of mercury needed in calculating the Hartmann number were all taken at 25 deg C.

Measurement of Pressure Difference

The experimental observations consisted of a series of measurements of pressure gradient for different velocities at a given strength of magnetic field. The measurement of the pressure gradient presented a problem because the pressure drop between the ports was in most instances too small to be read on ordinary manometers. In addition, the observations were made under conditions of severe vibrations that precluded the use of optical observations.

To accomplish the measurement of pressure difference, a system was devised which is the hydraulic analog of a potentiometer. The method may be understood with the aid of Fig. 1. The two pressure ports, between which it is desired to measure the pressure difference, are joined to form a branch circuit. Flow of mercury would ordinarily occur in this branch circuit, but a d-c electromagnetic pump in the branch circuit generates a pressure head in a direction to oppose the flow. In principle, the current to the electromagnetic pump is adjusted until there is no flow in the branch circuit, at which point the current is a measure of the pressure difference between the two pressure ports. This null condition is indicated by the "electromagnetic flow indicator," which is an electromagnetic flowmeter element connected directly to a galvanometer.

At null, one should in theory be able to open or close stopcock A in the branch circuit, Fig. 1, without observing any deflection of the galvanometer. In practice, however, this procedure would ignore an important source of error; namely, the small pressure heads caused by thermal gradients in the mercury circuit. These pressure heads may produce a flow in the branch circuit even when there is no flow in the main circuit, as when stopcock B, Fig. 1, is closed. Accordingly, the procedure in making an observation was to adjust the current to the electromagnetic pump until opening stopcock A produced a deflection of the galvanometer equal to the deflection obtained with no flow in the main circuit. The thermal-pressure heads varied from zero, at best, to a pressure difference roughly equal to the minimum that was observed in the experiment, about 0.015 mm of Hg, at worst.

The success of this method of measuring the pressure difference depends upon the calibration of the electromagnetic pump. Calibration was achieved by connecting the pump to a pair of manometers, and observing the difference in height of the mercury columns for a given current to the pump. Since the pressure difference in calibration was about 5 mm Hg, while the smallest pressure difference measured in the experiment was about 0.015 mm Hg, it was important to be sure of the linearity of the relationship between current and generated head. Such linearity does not necessarily exist, even though one is using the pump to generate a static head. As is shown in the Appendix, however, this linearity can be assured by a certain way of constructing the pump.

The random error of a pressure-difference measurement varied from about 15 per cent at the smallest pressure difference to about 1 per cent at pressure differences of 0.25 mm Hg and above. In addition, there was a systematic error of between 1 and 2 per cent associated with the calibration of the electromagnetic pump.

Entry-Zone Effects

A fluid entering a pipe must traverse a certain length of entry zone before the flow is fully developed. For ordinary laminar flow, there exist calculations and some measurements of the flow characteristics in the entry zone [9]. Calculations of entry-zone effects for laminar magnetohydrodynamic flow have been made by Shercliff. In this experiment, however, we are concerned with the entry-zone effect for flow that enters turbulent, but may become laminar sufficiently far downstream of the entrance. The available experimental evidence is that, under such conditions, an entry length of 130 diameters is sufficient for a pipe of circular cross section and that 54 times the depth is sufficient for a rectangular channel of large aspect ratio [10]. In the present experiment the minimum distance between the upstream end of the pipe and the first pressure tap was 130 diameters, except for the trials where the spacing between taps was 6 in.; in these the distance was 110 diameters. Longer test sections could not be used because they raised practical difficulties in assembling, filling, and removing air bubbles from the mercury circuit. In order to increase the effective length of the entry zone, a separate 24-in. length of tubing, of the same ID as the test section, was inserted immediately upstream of the test section, and joined to it by a short stub of Tygon hose. In any event, the pressure-gradient observations indicated that the entry zone was long enough in the absence of a magnetic field to give fully developed flow between the pressure taps.

With the magnetic field applied, a second entry effect needs to be considered; namely, the settling of the flow after it enters the magnetic field. At all but the lowest Reynolds numbers, the flow enters the magnetic field in a turbulent condition. To determine whether or not a given intensity of magnetic field will succeed in rendering such a flow laminar, it is necessary to provide a sufficiently long entry zone within the magnetic field. For the purpose of estimating the length of the magnetic entry zone, we assume that the field is zero everywhere except in the middle 12 in. of the solenoids. In order to get the maximum length of magnetic entry zone, the test sections were always located so that the downstream tap was near the edge of the 12-in. length. On this basis, the magnetic entry zone was 44 diameters for the pipe of largest diameters, when the pressure taps were 2 in. apart, and 25 diameters when the taps were 6 in. apart.

The magnetic entry length was fixed by the design compromise imposed on the solenoid, and could therefore not be increased. The results of the experiment indicate that although it was sufficient for the pipe of smaller diameter, or for the smaller values of field, it was not long enough to produce fully developed laminar flow for the larger diameters and the strongest fields.

Increase in Transition Reynolds Number

To determine the value of the transition Reynolds number, the experimental results are plotted in dimensionless form in terms of the friction factor f and Reynolds number R. These are defined, respectively, by

$$= \left|\frac{\Delta p}{\Delta z}\right| \frac{r_h}{\frac{1}{2}\rho v^2} \qquad (1)$$

$$R = \frac{4vr_h}{\nu}$$

where $\Delta p/\Delta z$ is the pressure gradient, ρ is the density, v the average velocity, ν the kinematic viscosity, and r_h the hydraulic radius, defined as the wetted area of the cross section divided by the wetted perimeter. The magnetic field is characterized by the Hartmann number

$$M_h = B_0 r_h (\sigma/\eta)^{1/2}$$

where B_0 is the flux density of the applied field, and σ and η are the electrical conductivity and the viscosity of the fluid, respectively.

From the graphical relation between friction factor and Reynolds number, the transition Reynolds number is determined by noting where f reaches a minimum. In practice, this determination is made difficult by the random and systematic errors of the experiment, including the shortness of the magnetic entry zone. On the other hand, the phenomenon now to be described turned out to be helpful in determining the transition Reynolds number.

Between the regimes of laminar and turbulent flow, there is a transition region in which the friction factor increases with increasing Reynolds number. This transition region is associated with the "turbulent flashes" which, it is now generally agreed, mark the transition from laminar to turbulent flow [11, 12]. In the present experiment, readings taken in the transition region were marked by a fluctuation of the pressure drop. The fluctuation was observable as an instability in the position of the galvanometer spot at balance. The best visual average was taken of the galvanometer null position for such readings. Although this effect produced a much poorer precision in the determination of f in the transition region, it had the fortunate aspect that it permitted a better determination of the transition Reynolds number. The appearance of this fluctuation was used to confirm the determination of transition Reynolds number, and gave consistent results, even in those cases where the value of f was, because of the shortness of the magnetic entry zone, noticeably higher, below transition, than the theoretical laminar values. Observations in which the pressure-drop readings were observed to fluctuate are noted in the figures with a vertical line.

A series of measurements without magnetic field is shown in Fig. 3. The agreement between the observations on the one hand, and the theoretical line $f = 16/R$ in laminar flow and the Blasius relationship $f = 0.079R^{-1/4}$ for turbulent flow on the other, serves as an over-all calibration of the experiment.

Another set of observations, showing the effect of a magnetic field, is shown in Fig. 4. The pressure taps in these runs were located 2 in. apart, and the magnetic entry zone was 44 diameters long. Three things are notable in these results:

1 The increasing value of transition Reynolds number with increasing magnetic field.

2 The increase, above the laminar value, of f, just below transition, in the presence of a magnetic field.

3 The decrease in f, in turbulent flow under a magnetic field.

A similar series of runs with pipe of approximately the same diameter, but with a shorter magnetic entry zone, gave the results shown in Fig. 5. In these runs the pressure taps were 6 in. apart, and the magnetic entry zone was only 25 diameters long. The purpose of these runs was to see whether the increased friction factor below transition was properly ascribable to the shortness of the magnetic entry zone. A comparison between the two sets of runs which focuses on the effect of magnetic entry zone is shown in Fig. 6. This figure shows, for each of the two larger values of magnetic field, a direct comparison between the friction factor obtained with the 44-diameter entry zone and that obtained with the 25-diameter entry zone. The Reynolds number at transition is about the same for both lengths of entry zone, but, for the Reynolds numbers just below transition, the friction factors are seen to be higher for the shorter entry zone.

Runs were also made with a glass tube of diameter approximately half of those just discussed, and the results are shown in Fig. 7. The magnetic entry zone for this case was 84 diameters long. The friction factor is seen to follow the theoretical laminar line to transition. In addition, the effect on the transition Reynolds number of reducing the diameter by a factor of 2 is seen to be the same as that of reducing the intensity of magnetic field by a factor of 2, as one would expect from dimensional considerations.

Another set of runs was made with an aluminum tube. The

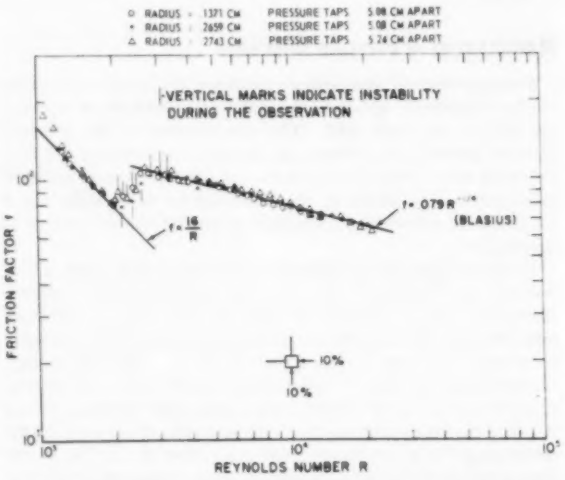
RADIUS = 1371 CM PRESSURE TAPS 5.08 CM APART
RADIUS = 2659 CM PRESSURE TAPS 5.08 CM APART
RADIUS = 2743 CM PRESSURE TAPS 5.74 CM APART
VERTICAL MARKS INDICATE INSTABILITY DURING THE OBSERVATION
f = 0.079R^-1/4 (BLASIUS)
f = 16/R
10%
10%
FRICTION FACTOR f
REYNOLDS NUMBER R

Fig. 3 Flow of mercury in glass tubes of circular cross section (no magnetic field). These observations, taken without a magnetic field, served as an over-all calibration of the experiment.

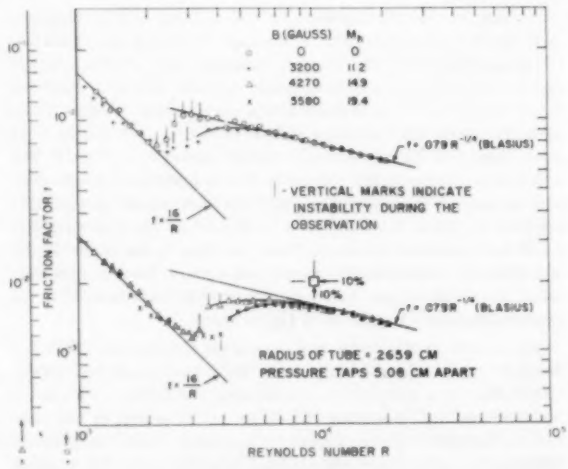

Fig. 4 Flow of mercury in a glass tube in presence of a longitudinal magnetic field. Note increase in transition Reynolds number and decrease in turbulent friction factor with increased magnetic field.

results of these are shown in Fig. 8, from which it is clear that, within the limit of error of the experiment, the magnetic field produces the same effects as with the glass tubes.

Correlation With Stuart's Theory

Stuart's analysis calculates the effect of a longitudinal magnetic field on the critical Reynolds number, i.e., the Reynolds number for neutral stability of the least stable mode of disturbance, for plane Poiseuille flow. The difference between instability as predicted by theory and transition as observed in practice has been mentioned previously. Any correspondence between Stuart's theory and this experiment must therefore be regarded as semi-empirical at best. Nevertheless, it turns out that an empirical modification of Stuart's theory can be made to correlate with the effect of a magnetic field on transition as observed in this experiment.

The results of Stuart's analysis are shown as the curve in Fig. 9.[3] Instead of plotting as the ordinate the critical Reynolds number itself, as Stuart does, Fig. 9 shows as the ordinate the ratio of the critical (or transition) Reynolds number to the critical (or transition) Reynolds number with no magnetic field.

The actual transition Reynolds numbers observed in the various runs are given in Table 1. Transition was taken to be the point where the friction factor was judged to begin increasing

[3] A similar analysis has also been done by Rossow (V. J. Rossow, "Boundary-Layer Stability Diagrams for Electrically Conducting Fluids in the Presence of a Magnetic Field," NACA TN 4282, Aug., 1958). Rossow's results generally confirm Stuart's, although Rossow finds a somewhat greater stabilizing influence from the magnetic field. The difference between Rossow's and Stuart's results increases with increasing Hartmann numbers. Since each of them calculates the critical Reynolds number for only a few points, and one must rely greatly on graphical interpolation, it is difficult to say exactly how much they differ. At the highest value of Hartmann number for which they calculate, the difference is about 20 per cent; at the highest value of Hartmann number used in this experiment the difference is 5 per cent or less. This experiment cannot be said to favor either analysis.

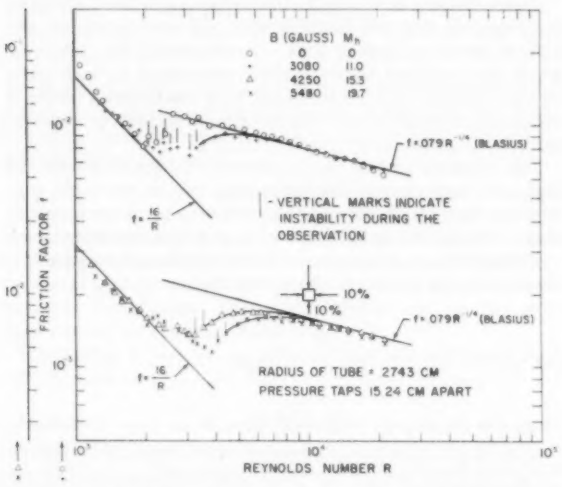

Fig. 5 Flow of mercury in a glass tube in presence of a longitudinal magnetic field. These are similar to results shown in Fig. 4, except that separation between pressure taps was 6 in. rather than the 2 in. of Fig. 4.

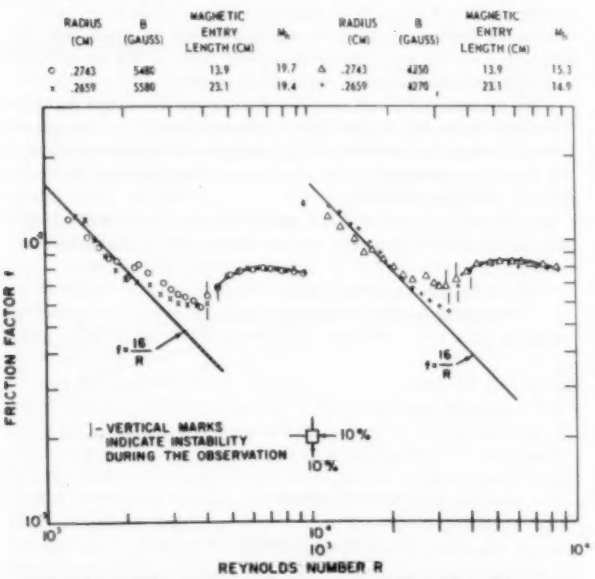
RADIUS (CM) | B (GAUSS) | MAGNETIC ENTRY LENGTH (CM) | M_h
○ .2743 | 5480 | 13.9 | 19.7
× .2659 | 5580 | 23.1 | 19.4
△ .2743 | 4250 | 13.9 | 15.3
+ .2659 | 4270 | 23.1 | 14.9
$f = \frac{16}{R}$
- VERTICAL MARKS INDICATE INSTABILITY DURING THE OBSERVATION
10%
10%
FRICTION FACTOR f
REYNOLDS NUMBER R

Fig. 6 Effect of magnetic entry length on friction factor in laminar flow. Each pair of graphs is for approximately the same conditions, except for the magnetic entry length. Pressure gradient below transition is seen to be higher for shorter magnetic entry lengths.

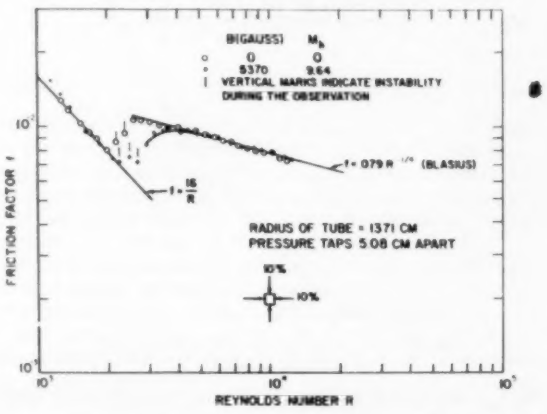

Fig. 7 Flow of mercury in a glass tube in presence of a longitudinal magnetic field. This is similar to Fig. 4, except that diameter of tube was about half that of Fig. 4.

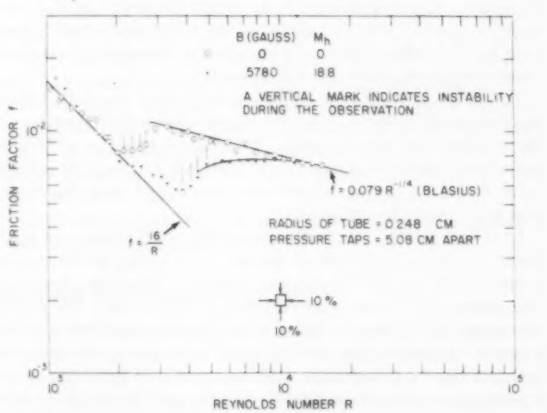

Fig. 8 Flow of mercury in an aluminum tube in presence of a longitudinal magnetic field

Table 1 Transition Reynolds number and other data of the experiment

Test section Radius, cm	Material	Magnetic flux density, gauss	R_t	R_t/R_0	M_h
0.2659....	glass	0	2100	1.00	0
		3200	2450	1.18	11.2
		4270	3100	1.48	14.9
		5580	3800	1.81	19.4
0.1371....	glass	0	2050	1.00	0
		5370	2300	1.12	9.64
0.2743....	glass	0	2050	1.00	0
		3080	2350	1.15	11.0
		4250	3200	1.56	15.3
		5480	3900	1.90	19.7
0.2708....	glass	0	2250	1.00	0
		5620	4000	1.78	19.5
0.249.....	aluminum	0	2230	1.00	0
		5600	3400	1.52	18.3
		5590	3550	1.59	18.2
0.248.....	aluminum	0	2100	1.00	0
		5780	3700	1.76	18.8

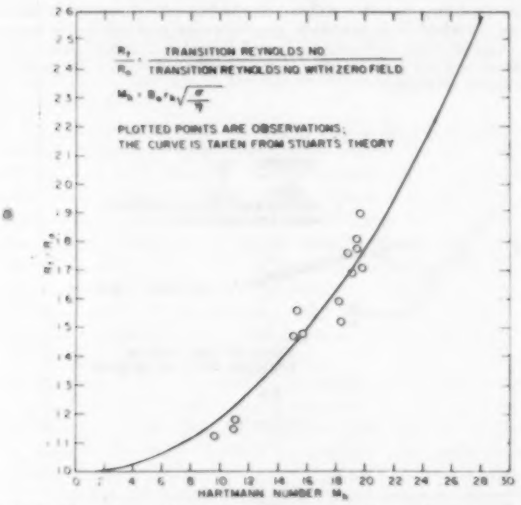
R_t / R_0 TRANSITION REYNOLDS NO / TRANSITION REYNOLDS NO WITH ZERO FIELD
$M_h = B_0 r_h \sqrt{\frac{\sigma}{\eta}}$
PLOTTED POINTS ARE OBSERVATIONS; THE CURVE IS TAKEN FROM STUARTS THEORY
HARTMANN NUMBER M_h

Fig. 9 Dependence of transition Reynolds number on Hartmann number

with increasing Reynolds number. The results of a few runs not shown in the preceding figures are also included. In this table R_t is the transition Reynolds number and R_0 the transition Reynolds number with zero field. Since the measured R_0 varied slightly with different test sections, the value of R_0 used to compute R_t/R_0 is the one that was observed in the particular series of measurements in which R_t was measured.

The value of R_t/R_0 and M_h given in Table 1 are shown as the plotted points in Fig. 9. In view of the degree of arbitrariness in the definition of the transition Reynolds number, and the experimental error of determining it (about 5 per cent for a single determination), the agreement between theory and experiment is as good as can be expected.

It is noteworthy that the agreement with theory is made possible in part by the use of the hydraulic radius as the characteristic length in the Hartmann number. Since the hydraulic radius for a pipe of circular cross section is just half the radius, this might be regarded as just a trick to introduce a factor of 2 or 4 into the Hartmann number. On the other hand, the hydraulic radius is known to correlate other quantities in hydrodynamics. For example, the turbulent friction factor and Reynolds number can be correlated for arbitrary shape of cross section if the hydraulic radius is used as the characteristic length. Furthermore, the hydraulic radius for a channel between infinite planes is the half-separation of the planes, and this is the characteristic length used by Stuart in his stability analysis.

Effect of Magnetic Field on Turbulent Friction Factor

The graphs of friction factor against Reynolds number show that the magnetic field produces not only an increase in the transition Reynolds number, but also a decrease in the turbulent friction factor. In order to place this effect more clearly in evidence, the turbulent results are cross plotted in Fig. 10, which shows the ratio of turbulent friction factor to turbulent friction factor at zero field, as a function of Hartmann number, for four different values of Reynolds number.

The decrease in turbulent friction factor can be rationalized on the argument that the magnetic field will tend to inhibit any motion across the lines of force. Consequently, the motion by which the turbulent eddies transfer momentum to each other will be reduced. The result should be a less flattened profile of velocity, and therefore a smaller pressure drop for a given average velocity of flow.

The turbulent friction factors derived from the runs with the aluminum pipe are especially interesting because one might suppose that they permit distinguishing viscous from electromagnetic drag. The friction factor was measured in this experiment from a pressure drop, in accordance with the definition of equation (1). However, it can be defined also by the relation

$$f = \frac{\tau}{\frac{1}{2}\rho v^2} \tag{2}$$

where τ is the average tangential stress at the wall. Definitions (1) and (2) are completely equivalent for ordinary hydrodynamic flow, since the pressure gradient is balanced only by the shear on the wall. With magnetohydrodynamic flow, this is no longer true, since electromagnetic body forces may be exerted on the fluid. It may be shown, however, that when the applied field is parallel to the flow, there will be no average electromagnetic drag opposing the flow if the pipe is circular, and is a perfect conductor. Aluminum has an electrical conductivity some 35 times that of mercury, and we may therefore expect that in the aluminum tube the drag on the mercury is entirely viscous.

Now consulting Fig. 10, we find that the friction factor for the aluminum tube falls below the results estimated for the glass tubes by about 2.5 per cent on the average. Is this a real effect; i.e., was there measurable electromagnetic drag opposing the flow through the glass tubes?

Actually 2.5 per cent is just about the limit of error with which the turbulent friction factor can be determined. Furthermore,

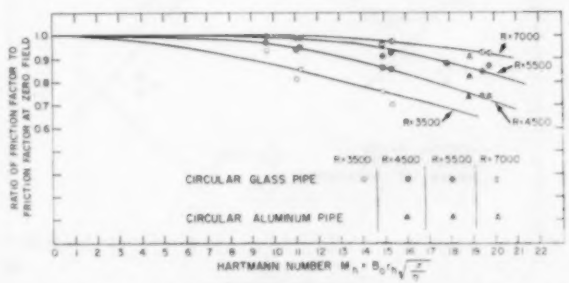

Fig. 10 Effect of longitudinal magnetic field on friction factor in turbulent pipe flow

(These curves are gotten by cross plotting the results of Figs. 4, 5, 7, and 8 in the turbulent regime.)

the following order-of-magnitude calculation shows that the effect should be negligible.

Suppose that v is the rms value of the velocity fluctuations. Then we may expect fluctuations of current density of magnitude $\sigma v B_0$. These will in turn give rise to magnetic induction components of order-of-magnitude $\pi a \sigma v B_0 \mu$ where a is the radius of the tube, and μ the permeability. The fluctuations in the three co-ordinate directions are about the same in magnitude, and are correlated in time, as shown by the measurements of Laufer [13]. Hence we may expect an electromagnetic drag of $\pi a \mu (\sigma v B_0)^2$ per unit volume, or $\pi^2 a^3 \mu (\sigma v B_0)^2$ per unit length of tube. On the other hand, the viscous force per unit length is $2\pi a \tau$, where τ is the shear stress at the wall. Hence the ratio between the electromagnetic drag and the viscous drag is given by

$$\alpha \sim \frac{\pi \mu a^2 (\sigma v B_0)^2}{2\tau} \tag{3}$$

Now v may be estimated either from the mixing-length theory of turbulence and the logarithmic profile for turbulent flow [14], or directly from the measurements by Laufer [13]. By either method, the estimate is

$$v \sim (\tau/\rho)^{1/2} \tag{4}$$

Of course this estimate is based on the assumption that the velocity fluctuations are undisturbed by the magnetic field. However, the magnetic field will, if anything, reduce the fluctuations as estimated by equation (4), and therefore use of (4) will over-estimate the electromagnetic drag.

Eliminating v between equation (3) and (4), and regrouping various quantities, we find that

$$\alpha \sim 2\pi M_A^2 (\mu \sigma \nu)$$

Here $\mu\sigma\nu$ is the ratio of the kinematic to the magnetic viscosity. Its value for mercury is about 10^{-7}. The highest value for M_A in this experiment is about 20, from which we find that α is about 0.025 per cent, or too small to have been measured.

It is clear, then, that the electromagnetic drag in this experiment was negligible.

Effect of Transverse Field

It is known that a transverse magnetic field has a very great effect on the profile and stability of pipe flow. One may ask then whether any of the observed effects—the delay in transition, the increase in friction factor above the laminar value below transition, and the decrease in turbulent friction factor—is caused or substantially modified by the transverse field of the solenoid. Fig. 2 shows that over the middle portion of the solenoid the transverse field on the axis is about 1 per cent of the longitudinal field. Outside the working length of the solenoid the transverse field increases; at about $8^1/_2$ in. from the center it reaches a maximum of 2 per cent of the longitudinal field at the center. In order to make an upper estimate of its effect, we shall use this value of 2 per cent.

In so far as the delay in transition is concerned, we may gain a first insight by considering the stability analysis, performed by Lock [15], for flow between infinite planes in the presence of a transverse field. The largest Hartmann number for the longitudinal field in this experiment was about 20. Consequently, the largest Hartmann number for the transverse field is about 0.4. From the curve that Lock gives, it is difficult to estimate what the increase in critical Reynolds number would be for an M_A as low as 0.4; interpolating linearly between $M_A = 0$ and $M_A = 1$ gives a value of R_c/R_0, where R_c is the critical Reynolds number, of about 1.3. In this experiment the observed value of R_c/R_0 was about 1.8, Fig. 10. Moreover, Lock's analysis is known, from the experimental work of Hartmann and Lazarus [16], and Murgatroyd [17], to overestimate very considerably the increase in transition Reynolds number. In particular, from the work of Hartmann and Lazarus a direct numerical estimate may be made. In a run with a pipe of circular cross section in which M_A was about 1.2, they found R_t/R_0 to be 1.03; for $M_A = 1.7$ they found R_t/R_0 to be 1.12. A curve fitted to all their observations on circular pipes, and rectangular pipes with field parallel to the short dimension, provides an estimate of $1.01 < R_t/R_0 < 1.02$ for $M_A = 0.4$. Since the maximum transverse M_A in this experiment was certainly less than 0.4, it appears that the transverse field had a negligible effect on the transition Reynolds number.

With respect to the increase in friction factor below transition, we may again look first to the theory of laminar flow between infinite planes in the presence of a transverse field. The average velocity across a channel of half-separation δ may be written as follows [18]:

$$v = \frac{\frac{-\partial p}{\partial z}\delta^2}{\eta} \frac{M_A \coth M_A - 1}{M_A^2} \tag{5}$$

When equation (5) is expanded for small values of M_A, one obtains

$$v = -\frac{1}{3}\frac{\partial p}{\partial z}\frac{\delta^2}{\eta}\left(1 - \frac{M_A^2}{15} + \ldots\right) \tag{6}$$

The term $-\frac{1}{3}\frac{\partial p}{\partial z}\frac{\delta^2}{\eta}$ in (6) is just the average velocity in plane Poiseuille flow. Hence an M_A of 0.4 would decrease the average flow, for the same pressure gradient, only about 1 per cent. Furthermore, it is to be noted that equation (6) predicts that the same fractional decrease in average velocity will occur for all pressure gradients, while the increase in friction factor in the experiment occurred only for the higher Reynolds numbers.

Hartmann and Lazarus give an empirical formula, derived from their experiments, for determining the pressure drop in magnetohydrodynamic flow in a circular pipe under a transverse field. It is indeed interesting that their formula involves the use of the theoretical equation for magnetohydrodynamic flow between infinite planes, with half the radius (the actual number they recommend is $0.51a$) substituted for the half-separation of the planes. This is exactly what has been done in the foregoing calculations in using the hydraulic radius for estimating the effect of the transverse field.

Finally, so far as the turbulent friction factor is concerned, we may note that the transverse field would be expected to increase it rather than to decrease it. The physical reason for this is that the transverse field will tend to inhibit motion across the lines of force. Again, from an empirical formula given by Hartmann and Lazarus, one may calculate that in the present experiment the transverse field could not have increased the turbulent pressure gradient by more than about 1 per cent within the range of Reynolds numbers where the longitudinal field reduces the friction factor.

It therefore appears that the transverse field cannot account for the results of this experiment.

Comparison With Another Experiment

During the course of this experiment a report [19] appeared of an experiment with similar objectives, conducted at NACA. The report of the NACA experiment says that the "application of the magnetic field produced very little change in Reynolds number of transition when large initial disturbances were introduced at the entrance to the flow tube." In the terminology

of our experiment, the NACA experimenters report little or no increase in the minimum Reynolds number of transition.

The conditions of the NACA experiment were such that M_h was 6.7 for all the runs with magnetic field. Under such conditions the expected increase in the minimum Reynolds number of transition, according to Fig. 9, is about 8 per cent. Observations in the NACA experiment were made at rather widely separated values of velocity. Furthermore, the pressure-drop measurements were made over a long length of tube, and included ordinary entrance-zone effects, and magnetic-entrance-zone effects. Under such circumstances an 8 per cent increase in the transition Reynolds number can easily be overlooked. The NACA experiment does not appear to be in conflict with the results reported here.

Conclusions

The following conclusions may be stated for this experiment:

(*a*) An axial magnetic field will increase the minimum Reynolds number of a transition in pipe flow of a conducting fluid.

(*b*) The transition Reynolds number can be correlated with Stuart's theory of instability for flow between infinite planes, if one uses the hydraulic radius as the characteristic length in the dimensionless variables.

(*c*) The friction factor for turbulent pipe flow is decreased by an axial magnetic field, but the decrease in friction factor becomes smaller and ultimately vanishes as the Reynolds number increases.

Acknowledgments

The author acknowledges helpful discussions with and suggestions from Profs. R. W. P. King, G. F. Carrier, T. Wu, and Dr. F. K. Willenbrock of Harvard University, Prof. L. M. Trefethen of Tufts University, and Dr. M. E. Malin of the Avco Corporation.

This work was supported by the U. S. Air Force.

References

1 J. T. Stuart, "On the Stability of Viscous Flow Between Parallel Planes in the Pressure of a Co-Planar Magnetic Field," *Proceedings of The Royal Society*, series A, vol. 221, 1954, pp. 189–206.

2 C. C. Lin, "The Theory of Hydrodynamic Stability," Cambridge University Press, Cambridge, England, 1955, p. 29.

3 S. Goldstein, "Modern Development in Fluid Dynamics," Clarendon Press, Oxford, England, 1952, p. 319.

4 See reference [2], p. 98.

5 O. G. Tietjens, "Applied Hydro- and Aeromechanics," Dover Publications, Inc., New York, N. Y., 1957, p. 33 ff.

6 J. A. Shercliff, "Relation Between the Velocity Profile and the Sensitivity of Electromagnetic Flowmeters," *Journal of Applied Physics*, vol. 25, 1954, pp. 817–818.

7 J. A. Shercliff, "Experiments on the Dependence of Sensitivity on Velocity Profile in Electromagnetic Flowmeters," *Journal of Scientific Instruments*, vol. 32, 1955, p. 441.

8 R. W. Lyon, editor-in-chief, "Liquid Metals Handbook," second edition, U. S. Government Printing Office, Washington, D. C., June, 1952.

9 See reference [3], pp. 229–310.

10 See reference [3], pp. 320–321.

11 E. R. Lindgren, "The Transition Process and Other Phenomena in Viscous Flow," *Arkiv for Fysik*, vol. 12, 1957, pp. 1–169.

12 M. V. Morkovin, "Transition From Laminar to Turbulent Shear Flow—A Review of Some Recent Advances in Its Understanding," TRANS. ASME, vol. 80, 1958, pp. 1121–1128.

13 John Laufer, "The Structure of Turbulence in Fully Developed Pipe Flow," NACA Report 1174, 1954, pp. 417–434.

14 S. I. Pai, "Viscous Flow Theory, II—Turbulent Flow," D. Van Nostrand Company, Inc., New York, N. Y., 1957, pp. 46–47.

15 R. C. Lock, "The Stability of the Flow of an Electrically Conducting Fluid Between Parallel Planes Under a Transverse Magnetic Field," *Proceedings of The Royal Society*, series A, vol. 233, 1954, p. 105.

16 J. Hartmann and F. Lazarus, Det Kgl. Danske Videnskaberne Selskab, *Math-fys. Meddelelser*, vol. 15, 1937, p. 1.

17 W. Murgatroyd, "Experiments on Magneto-Hydrodynamic Channel Flow," *Philosophical Magazine*, vol. 44, 1953, pp. 1348–1354.

18 T. G. Cowling, "Magnetohydrodynamics," Interscience Publishers, Inc., New York, N. Y., 1957, p. 15.

19 Michael Bader and W. C. A. Carlson, "Measurement of the Effect of an Axial Magnetic Field on the Reynolds Number of Transition in Mercury Flowing Through a Glass Tube," NACA TN 4274, May, 1958.

20 See reference [18], p. 2 ff.

APPENDIX

Linearity of an Electromagnetic Pump

Suppose that a d-c electromagnetic pump is used to generate a static pressure head Δp, as in a pair of mercury manometers. Under what conditions will the pump produce a linear relationship between Δp and I, the current fed to the pump?

It is clear that $\int\int \mathbf{V}\cdot d\mathbf{A}$ is zero where A is any surface bounded by the containing pipe and $\mathbf{V}$ is the velocity of the fluid. However, unless $\mathbf{V}$ is everywhere zero, there will be closed streamlines in the liquid which will give rise to pressure losses and will prevent Δp from being proportional to I.

Let us start with the steady-state form of the equation of motion for incompressible magnetohydrodynamic flow. This may be written as [20]

$$\rho(\mathbf{V}\cdot\Delta\mathbf{V}) = \mathbf{j}\times\mathbf{B} - \nabla p + \eta\nabla^2\mathbf{V} \tag{7}$$

where ρ is the density, $\mathbf{j}$ the current density, and η the viscosity. Substitute for $(\mathbf{V}\cdot\nabla)\mathbf{V}$ according to the vector identity

$$\mathbf{C}\times(\nabla\times\mathbf{C}) = \frac{1}{2}\nabla|\mathbf{C}|^2 - (\mathbf{C}\cdot\nabla)\mathbf{C}$$

Then equation (7) becomes

$$\frac{1}{2}\nabla|\mathbf{V}|^2 - \mathbf{V}\times(\nabla\times\mathbf{V}) = \mathbf{j}\times\mathbf{B} - \nabla p + \eta\nabla^2\mathbf{V} \tag{8}$$

Now suppose that closed streamlines exist, and integrate (8) around any such streamline. All terms drop out except those involving $\mathbf{j}\times\mathbf{B}$ and $\nabla^2\mathbf{V}$ and the integration reduces to

$$-\oint \mathbf{j}\times\mathbf{B}\cdot d\mathbf{l} = \eta\oint(\nabla^2\mathbf{V})\cdot d\mathbf{l} = \eta\nabla^2\oint\mathbf{V}\cdot d\mathbf{l} \tag{9}$$

It follows that a necessary and sufficient condition for $\mathbf{V}$ to be zero everywhere is that

$$\oint \mathbf{j}\times\mathbf{B}\cdot d\mathbf{l} = 0$$

for any closed path in the liquid. By Stokes's theorem the last condition can be written

$$\int\int[\nabla\times(\mathbf{j}\times\mathbf{B})]\cdot d\mathbf{A} = 0 \tag{10}$$

where A is any surface in the liquid. For (10) to be true for any surface in the liquid, the integrand itself must vanish:

$$\nabla\times(\mathbf{j}\times\mathbf{B}) = 0 \tag{11}$$

Now expand (11) according to the vector identity

$$\nabla\times(\mathbf{C}_1\times\mathbf{C}_2) = (\nabla\cdot\mathbf{C}_2)\mathbf{C}_1 - (\nabla\cdot\mathbf{C}_1)\mathbf{C}_2 + (\mathbf{C}_2\cdot\nabla)\mathbf{C}_1 - (\mathbf{C}_1\cdot\nabla)\mathbf{C}_2$$

and apply the divergence conditions

$$\nabla\cdot\mathbf{B} = 0$$

and

$$\nabla\cdot\mathbf{j} = 0$$

Then equation (11) reduces to

$$(\mathbf{j}\cdot\nabla)\mathbf{B} = (\mathbf{B}\cdot\nabla)\mathbf{j} \tag{12}$$

Suppose that **B**, of magnitude B_0, has a component in the x-direction only, and has a constant value wherever **j** has any sensible magnitude. This requirement can be met by having closely spaced pole-pieces and electrodes, with the pole-pieces covering a considerably larger area than the electrodes. Under these conditions (12) reduces to

$$\frac{\partial j_x}{\partial x} = \frac{\partial j_y}{\partial x} = \frac{\partial j_z}{\partial x} \tag{13}$$

Let the pressure head Δp be generated in the z-direction and the electrodes be normal to the y-direction. Suppose also that the walls bounding the rectangular channel in the x-direction are electrical insulators, so that current edge effects in the x-direction are negligible. Then j_x, $\partial j_y/\partial x$, and $\partial j_z/\partial x$ vanish, and (13) is satisfied.

An Exact Solution of the Compressible-Flow Characteristics in Constant-Area Passages With Simultaneous Friction and Constant Heat Flux

R. N. NOYES
Principal Engineer,
General Electric Company,
Aircraft Nuclear Propulsion Department
Cincinnati, Ohio. At present,
Senior Engineer,
Research Laboratory,
General Motors Corporation,
Warren, Mich., Mem. ASME

An exact solution is presented for the flow of a compressible fluid in a constant-area passage in which wall friction is present and the total temperature of the fluid rises linearly with distance through the passage. For fluid properties that are invariant with temperature, this is specifically the case of constant heat flux. From this exact solution, an approximate simplified form is derived that should be applicable to predicting flow performance for most types of operation of constant-area heat exchangers.

Introduction

THE various equations describing the flow characteristics of a compressible fluid under the simultaneous influence of friction and arbitrary heat addition (see p. 231 of reference [1][1]) are not exact and, as of present, no generalized integrating factor has been found that will permit closed-form integration for any fluid-temperature variation.

In reference [2] a completely integrated solution was obtained for the special case of total fluid temperature varying exponentially with distance through the flow passage.

When the flow-passage wall temperature is constant, Reynolds analogy may be used to determine the variation of total temperature with passage length. Reference [3] indicates a method for determining the flow characteristics for this type of boundary condition that is noniterative but does require numerical integration.

In the present paper a completely integrated solution is presented for the case in which the total fluid temperature varies linearly with distance through a constant flow area passage. For invariant fluid properties, this solution constitutes flow at constant heat flux.

Method of Analysis

The one-dimensional steady-state momentum equation for a compressible fluid may be written as (see equation (8.21) of reference [1])

$$\frac{\rho u du}{g} + dp + \left(\frac{\rho u^2}{2g}\right)\frac{4fdx}{D} = 0 \tag{1}$$

where the symbols in equation (1) and elsewhere in this report are defined in the list of symbols. Using the equation of state for an ideal gas

$$p = \rho R t \tag{2}$$

the pressure in equation (1) may be eliminated so as to yield

$$du^2 + 2gR\left(dt + t\frac{d\rho}{\rho}\right) + u^2\left(\frac{4fdx}{D}\right) = 0 \tag{3}$$

If U and $\bar{x}$ are defined as

$$U \equiv \frac{u}{\sqrt{gRT_0}} \tag{4}$$

$$\bar{x} \equiv \frac{4}{D}\int_0^x f dx = \frac{4\bar{f}x}{D} \tag{5}$$

then equation (3) becomes

$$dU^2 + 2\left(\frac{dt}{T_0} + \frac{t}{T_0}\frac{d\rho}{\rho}\right) + U^2 d\bar{x} = 0 \tag{6}$$

Logarithmic differentiation of the continuity equation for constant flow area yields

$$\frac{d\rho}{\rho} = -\frac{du}{u} = -\frac{dU}{U} \tag{7}$$

[1] Numbers in brackets designate References at end of paper.

Contributed by the Heat Transfer Division and presented at the Winter Annual Meeting, New York, N. Y., November 27–December 2, 1960, of THE AMERICAN SOCIETY OF MECHANICAL ENGINEERS. Manuscript received at ASME Headquarters, May 27, 1960. Paper No. 60—WA-177.

Nomenclature

A = cross-sectional flow area
D = equivalent hydraulic diameter
f = local friction factor
g = mass conversion constant
m = heat-flux parameter defined by equation (11)
p = static pressure at x
p_0 = static pressure at $x = 0$
P = total pressure at x
P_0 = total pressure at $x = 0$
R = gas constant
t = static temperature at x
T = total temperature at x
$\bar{T}$ = defined in equation (9) as T/T_0
T_0 = total temperature at $x = 0$
u = axial velocity in flow passage
x = axial distance through flow passage
w = weight flow rate of fluid
γ = ratio of specific heats
ρ = density

Dimensionless Parameters

$\mathbf{M}$ = Mach number
$\bar{x}$ = friction-distance parameter $(4\bar{f}x/D) = \int_0^x \frac{4fx}{D}$
U = $\left(u/\sqrt{gRT_0}\right)$
U_0 = value of U at $x = 0$

Elimination of the density between equations (6) and (7) results in

$$dU^2 + 2\left(\frac{dt}{T_0} - \frac{t}{T_0}\frac{dU}{U}\right) + U^2 d\bar{x} = 0 \tag{8}$$

From the energy equation

$$\frac{t}{T_0} = \frac{T}{T_0} - \frac{\gamma - 1}{2\gamma} U^2 = \bar{T} - \frac{\gamma - 1}{2\gamma} U^2 \tag{9}$$

A combination of equations (8) and (9) will then yield

$$\left(U^2 + 2\frac{d\bar{T}}{d\bar{x}}\right) d\bar{x} = \left(\frac{\bar{T}}{U^2} - \frac{\gamma + 1}{2\gamma}\right) dU^2 \tag{10}$$

For a linear variation of total temperature with friction-distance parameter, then

$$\bar{T} = 1 + m\bar{x} \tag{11}$$

where m is a constant proportional to the heat flux for constant-fluid properties. Substitution of equation (11) into equation (10) results in

$$d\bar{x} - \frac{m\bar{x}}{U^2(U^2 + 2m)} dU^2 = \left(\frac{1 - \frac{\gamma + 1}{2\gamma} U^2}{U^2 + 2m}\right) \frac{dU^2}{U^2} \tag{12}$$

Equation (12) is linear in $\bar{x}$ and may be integrated to yield

$$m\bar{x} = \sqrt{\frac{1 + \frac{2m}{U_0^2}}{1 + \frac{2m}{U^2}}} - 1 - \frac{\left(\frac{\gamma + 1}{2\gamma}\right) m}{\sqrt{1 + \frac{2m}{U^2}}} \ln \left\{ \frac{U^2}{U_0^2} \left[\frac{1 + \frac{m}{U^2} + \sqrt{1 + \frac{2m}{U^2}}}{1 + \frac{m}{U_0^2} + \sqrt{1 + \frac{2m}{U_0^2}}} \right] \right\} \tag{13}$$

wherein at $\bar{x} = 0$, $U = U_0$. Equation (13) thus relates (implicitly) U to $\bar{x}$ for any initial U_0 and m. As $m \to 0$, equation (13) reduces to

$$\bar{x} = \left(\frac{1}{U_0^2} - \frac{1}{U^2}\right) - \left(\frac{\gamma + 1}{2\gamma}\right) \ln \frac{U^2}{U_0^2} \tag{14}$$

Since it is easily shown that

$$U^2 = \frac{\gamma M^2 \left(\frac{T}{T_0}\right)}{1 + \frac{\gamma - 1}{2} M^2} = \frac{\gamma M^2 (1 + m\bar{x})}{1 + \frac{\gamma - 1}{2} M^2} \tag{15}$$

then substitution of equation (15) into (14), with $m = 0$, results in

$$\bar{x} = \frac{1}{\gamma}\left(\frac{1}{M_0^2} - \frac{1}{M^2}\right) - \left(\frac{\gamma + 1}{2\gamma}\right) \ln \left\{ \frac{M^2}{M_0^2} \left[\frac{1 + \frac{\gamma - 1}{2} M_0^2}{1 + \frac{\gamma - 1}{2} M^2} \right] \right\} \tag{16}$$

which is the same form as a combination of equations (6.20) and (6.21) given in reference [1] for isothermal flow with friction.

Useful relations in addition to that given by equation (15) are

$$\frac{w\sqrt{gRT}}{PAg} = \frac{U}{\sqrt{\bar{T}}} \left(1 - \frac{\gamma - 1}{2\gamma} \frac{U^2}{\bar{T}}\right)^{\frac{1}{\gamma - 1}} \tag{17}$$

$$\frac{pAg}{w\sqrt{gRT}} = \frac{\sqrt{\bar{T}}}{U} \left(1 - \frac{\gamma - 1}{2\gamma} \frac{U^2}{\bar{T}}\right) \tag{18}$$

Thus from equations (17) and (18) it follows that

$$\frac{P}{P_0} = \bar{T} \left(\frac{U_0}{U}\right) \left[\frac{1 - \frac{\gamma - 1}{2\gamma} U_0^2}{1 - \frac{\gamma - 1}{2\gamma} \frac{U^2}{\bar{T}}} \right]^{\frac{1}{\gamma - 1}} \tag{19}$$

$$\frac{p}{p_0} = \bar{T} \left(\frac{U_0}{U}\right) \left[\frac{1 - \frac{\gamma - 1}{2\gamma} \frac{U^2}{\bar{T}}}{1 - \frac{\gamma - 1}{2\gamma} U_0^2} \right] \tag{20}$$

An approximate explicit expression for U may be obtained by use of a Maclaurin expansion of the logarithmic quantity that appears in equation (13) in terms of $\left[\left(1 + \frac{2m}{U_0^2}\right) \Big/ \left(1 + \frac{2m}{U^2}\right)\right]^{1/2} - 1$. Using the first two terms of such an expansion eventually leads to the result

$$\frac{U^2}{U_0^2} = \frac{\bar{T}^2}{1 - U_0^2 \left(\frac{\bar{T} - 1}{2m}\right) \left[\frac{5}{6}\left(\frac{\gamma + 1}{\gamma}\right)(4U_0^2 + 3m) + \bar{T} + 1\right]} \tag{21}$$

Discussion

From equations (13) and (15), the variation of Mach number M with friction-distance parameter $\bar{x}$ can be determined as a function of heat-flux parameter m and U_0. Fig. 1 shows this variation for various values of m and a value of U_0 corresponding to an arbitrary initial value of M = 0.15. The curve for $m = 0$ was calculated using equation (16).

Fig. 2 shows the error in Mach number introduced by using the approximate explicit form for U, equation (21). Two sets of curves are shown in Fig. 2, both of which are for a $\gamma = 1.4$. These sets are for arbitrary initial Mach numbers of 0.15 and 0.25. At the lower inlet Mach number, the error in M is fairly insensitive

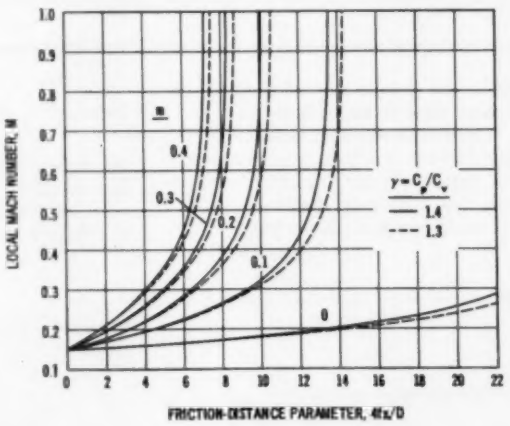

Fig. 1

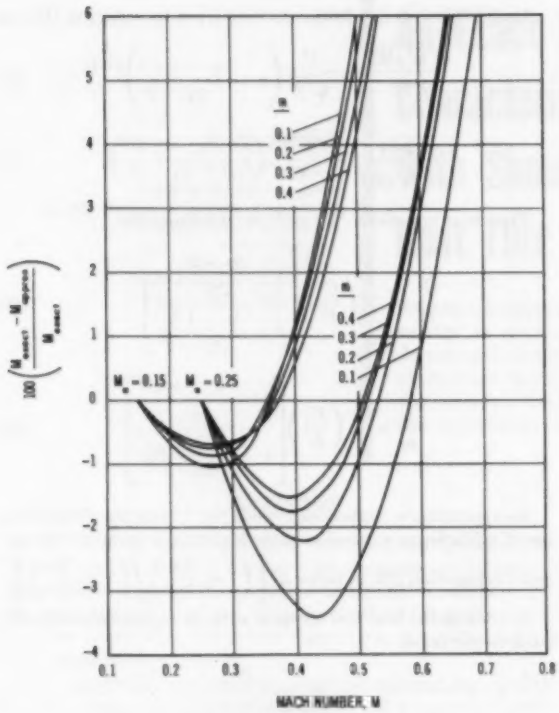

Fig. 2

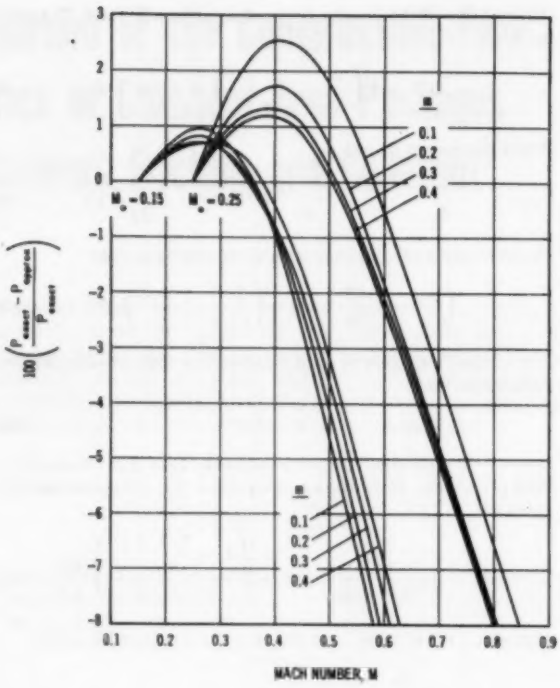

Fig. 3

to the heat-flux parameter m. As the inlet Mach number increases this sensitivity also increases. Fig. 2 shows that for an inlet Mach number of 0.15, equation (21) predicts the value of U, and hence $\mathbf{M}$ from equation (15), with an accuracy of ± 1 per cent up to an exit Mach number of 0.4 for all heat-flux rates of practical interest. For an inlet Mach number of 0.25 an accuracy of approximately ± 3 per cent is maintained up to an exit Mach number of 0.6. Although not shown, the error in $\mathbf{M}$ is practically insensitive to a decrease in γ from 1.4 to 1.3.

It should be pointed out that the approximate formula for U, equation (21), was tailored to apply to m values between 0.1 and 0.4 As a consequence, equation (21) is not valid as $m \to 0$.

In Fig. 3 the error in total pressure is shown when computed from equations (19) and (21). As in Fig. 2, two initial Mach numbers and four heat-flux parameters m have been assumed. Fig. 3 shows that the error in total pressure is slightly less than the error in Mach number when both are computed using a value of U given by equation (21).

References

1 A. H. Shapiro, "The Dynamics and Thermodynamics of Compressible Flow," vol. I, Ronald Press, New York, N. Y., 1953.

2 M. Sibulkin and W. K. Koffel, "Chart for Simplifying Calculations of Pressure Drop of a High-Speed Compressible Fluid Under Simultaneous Action of Friction and Heat-Transfer Application to Combustion-Chamber Cooling Passages," NACA TN 2067, March, 1950.

3 M. F. Valerino, "Generalized Charts for Determination of Pressure Drop of a High Speed Compressible Fluid in Heat Exchanger Passages," *Journal Aero Sciences*, vol. 16, no. 5, May, 1949.

E. P. BARTLETT
Senior Engineer, Aeronutronic, Division of Ford Motor Company, Newport Beach, Calif.

M. R. DENISON
Manager, Fluid Dynamics and Propulsion, Aeronutronic, Division of Ford Motor Company, Newport Beach, Calif. At present, Principal Scientist Electro Optical Systems Inc., Pasadena, Calif.

Experimental Ablation Rates in a Turbulent Boundary Layer

An exploratory experimental program on the ablation of graphite, a combustible sublimator, is reported which verifies an analysis of turbulent ablation rates previously developed. A blowdown system was employed using a mixture of oxygen and nitrogen as the working gas. The use of a high percentage of oxygen enabled the simulation of re-entry ablation conditions. Ablation rates were predicted within 30 per cent with no adjustment of empirical constants derived from incompressible turbulent skin-friction experiments. The predictions were consistently high. Temperature of the reacting surface, determined by means of a radiamatic pyrometer, was predicted within 10 per cent. The analysis can be applied to a wide variety of ablation materials including those which go through a liquid phase, provided proper account is taken of the chemistry, and provided the simplifying assumptions are valid.

Introduction

An effective means of absorbing the high heat fluxes of re-entry is through the mechanism of ablation; i.e., melting and vaporization or sublimation of the surface of the thermal shield. Therefore considerable interest has been shown in the mechanism of ablation of late as indicated by a survey article by Adams [1].[1] Most of the theoretical work which has been done is concerned with the laminar boundary layer [2, 3] as turbulent phenomena are imperfectly understood. Furthermore, the majority of the experimental work which has been accomplished is limited to the laminar boundary layer. The test facility primarily used in ablation studies is the air-stabilized arc-jet [4]. The power required to develop sufficiently large Reynolds numbers so as to attain turbulent flow is extremely large [5].

Unfortunately a turbulent boundary layer is prevalent in high-speed re-entry. In this paper experiments on the combustion of graphite under turbulent-flow conditions are described. Re-entry ablation conditions, i.e., heat and mass fluxes and temperatures, are simulated by compensating for a lack of kinetic energy in the gas stream by increasing the heat of combustion with excess oxygen. Analysis of the degree of simulation is beyond the scope of this paper. The experimental results are correlated with an analysis of Denison [6] for heat and mass transfer with chemical reaction under turbulent-flow conditions. Although the experiments were confined to the combustion of graphite, the analysis can be extended to other materials including those which melt and vaporize, with little modification of the method by which the reactions in the gas phase are considered.

[1] Numbers in brackets designate References at end of paper.

Contributed by the Heat Transfer Division and presented at the Winter Annual Meeting, New York, N. Y., November 27–December 2, 1960, of The American Society of Mechanical Engineers. Manuscript received at ASME Headquarters, August 22, 1960. Paper No. 60—WA-208.

Experimental Facility

An experimental investigation of the combustion of graphite under simulated re-entry conditions was studied by means of a blowdown system with a controlled mixture of oxygen and nitrogen as the flowing gas. A blowdown system supplied a dense, low-speed flow of a cold gas for durations up to several minutes. The graphite model, in the shape of a hollow cylinder, was heated to approximately 3000 deg F prior to a run by means of an induction heater. The flow of an oxidizing gas over the hot graphite caused ignition and further heating (due to the heat of combustion) to some equilibrium temperature. Thus the combustion sustained itself until the oxygen pressure was reduced.

The blowdown system employed is shown schematically in Fig.

Nomenclature

B = ratio of mass injection to skin friction, equation (1)
B^* = value of B with reactants in stoichiometric proportion
c_{f_e} = skin-friction coefficient based on local free-stream conditions
c_p = specific heat
h_{c_w} = enthalpy of solid graphite at surface conditions
h_i^0 = heat of formation of chemical species i
h_s = total enthalpy
k_i = mass fraction of chemical species i
l = mixing length
$\dot{m}_w$ = net flux of surface material
P = pressure
q_w = heat flux conducted into or radiated from surface
$\widetilde{\mathrm{Re}}_{wt}$ = effective Reynolds number for turbulent flow based on wall conditions, equation (3)
r_0 = distance from axis of symmetry to body surface
t = time
T = temperature
u = velocity in streamwise direction
x = tangential distance from stagnation point along body surface
y = distance normal to body surface
β = exponent used to trace influence of mixing length assumption
Γ_{0_e} = mass fraction of oxygen at outer edge of boundary layer regardless of molecular structure
κ = exponent used in blunt-body coordinate system; unity for bodies of revolution and zero for two-dimensional bodies
μ = viscosity
ρ = density
ϕ = integral defined by equation (3)

Subscripts

c = graphite
e = edge of boundary-layer conditions
i = ith chemical species
w = body-surface conditions

Table 1 Characteristics of blowdown system

Maximum gas flow rate, lb/sec	50
Oxygen concentration, per cent	0 to 100
Test-section Mach number	0.41
Plenum-chamber pressure, psig	50 to 350
Plenum-chamber temperature	Ambient
Reynolds number per ft	1.5×10^7 to 10^8

1. Oxygen and nitrogen were bled into the blowdown tanks in the desired mixture ratio and mixed by means of a circulation pump. The mixed gas flowed through a plenum chamber containing screens and baffles to insure a smooth flow into the graphite test body. The flow then passed through the graphite specimen inducing burning of the inner surface of the cylinder, and then exited to the atmosphere through a converging-diverging nozzle. Nitrogen was used to purge the chamber prior to a run and to maintain a balance pressure on the outside of the graphite body. The test section, partially disassembled, is shown in Fig. 2. The rear bulkhead, containing the nozzle assembly, has been removed to make visible the induction-heating coil. The graphite cylinder is placed inside this coil.

The blowdown tank system has a capacity of 600 cu ft and is capable of operation at 2000 psi. During the operation of a test, the pressure was reduced by automatic pressure regulation to the desired pressure in the test-chamber plenum. Pertinent information concerning the blowdown system and the range of operating conditions is listed in Table 1.

The induction-heating unit is rated at 100 kw at a frequency of 10,000 cycles per sec (cps). This unit was sufficient to heat a specimen from room temperature to 3000 F in approximately one minute. The induction coil was chromeplated and therefore served as a radiation shield to keep heat losses from the specimen low. The coil was water-cooled requiring a flow of 30 gpm.

During heating the front end of the graphite cylinder was cantilevered inside the induction-heating coil to minimize critical heat losses and thus sustain high temperature at the entry. When the heating was accomplished and the run was ready to proceed, the specimen was pushed forward into position by means of a hydraulic actuator. This assembly is shown schematically in Fig. 3. The exhaust nozzle also shown in Fig. 3 was water film-cooled both inside and outside. In spite of this precaution several nozzles were damaged during the course of the tests due to the intense heat.

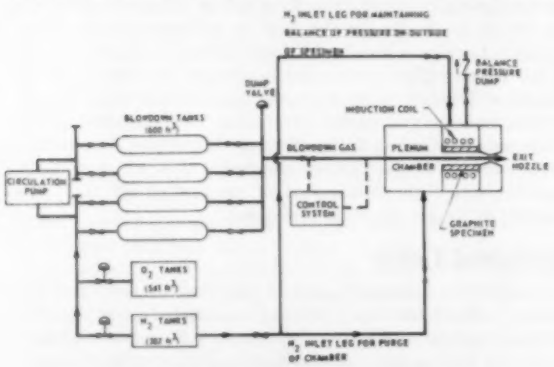

Fig. 1 Schematic of blowdown system

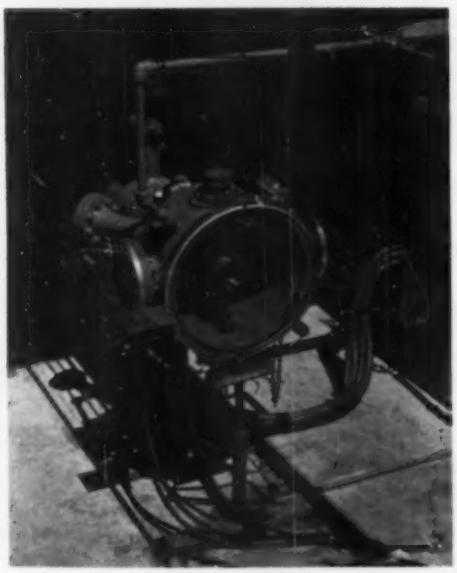

Fig. 2 Test chamber

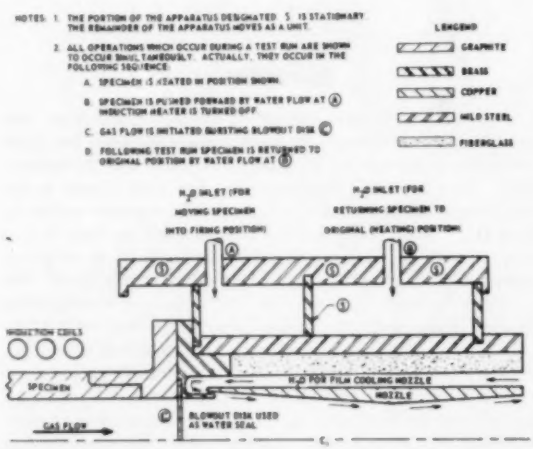

Fig. 3 Schematic of hydraulic actuator and nozzle assembly in heating position

Specimen Geometry

The specimen geometry is shown in Fig. 4. In checkout of the system several other entrance designs were used but proved to be unsatisfactory as the boundary layer was well established at the point of ignition. As burning proceeded a groove would then form causing the boundary layer to separate. By analogy with the heat-transfer experiments of Seban [7], it is supposed that subsequent reattachment of the boundary layer caused local high heat flux and hence mass flux at the point of reattachment, thereby increasing the depth of the groove, an unstable condition. With the design shown in Fig. 4, the boundary layer effectively started near the ignition point so that the problem was greatly reduced. A shallow groove still persisted, especially with low oxygen concentration, but fortunately the groove did not seem to have a large effect on the correlation of mass loss downstream from the groove.

Instrumentation

The instrumentation for these exploratory experiments was kept to a minimum. Graphite surface temperatures and instantaneous burning rates were measured at a single location

during each run and the over-all decrease in thickness was obtained by comparing dimensions before and after each run.

A radiamatic pyrometer was employed to measure the temperature of the burning graphite surface. The temperature was recorded on a continuous-record strip-chart recorder. The inside of the specimen was viewed through a quartz window built into the plenum chamber upstream from the test section. The line of sight passed through the entrance of the specimen at an angle of 30 deg from the specimen wall. The radiamatic pyrometer was factory calibrated for black-body conditions. In this application no correction for nonblack body was necessary as the graphite cylindrical body serves as an enclosure. The factory calibration was checked periodically against an optical pyrometer.

Instantaneous burning rates were obtained by the use of an x-ray system. The change in attenuation of an x-ray beam passing through the graphite specimen indicated a change in specimen thickness and hence instantaneous burning rates. This, of course, gave the average of the local burning rates at two points diametrically opposed. It will be shown that in several runs the surface was not smooth. The meaning of the x-ray data in these runs is questionable. A rather refined x-ray system consisting of a scintillation detector, pulse-height analyzer, EPUT (events per unit time) counter, and digital recorder was found to be necessary, Fig. 5. The x-ray beam struck a scintillation crystal whose light pulses were converted to electrical pulses and amplified in the detector. They were further amplified in the analyzer and certain pulses which were sensitive to small graphite thickness changes were selected. These selected pulses were then counted over 1-sec intervals and printed every 2 sec. Hollow tubes were inserted in the test section to accommodate the x-ray beam in order to minimize the length of the high-pressure path. These tubes increased the sensitivity of the measurement and decreased the adverse effect of pressure fluctuations. With the system shown in Fig. 5 consistent x-ray data were obtained in several runs.

The decrease in specimen thickness was measured at the completion of the run, at several points along the length of the graphite specimen by the use of a micrometer. At each station, measurements were made at several points around the circumference, these being averaged to give an average decrease in thickness as a function of distance measured along the direction of flow.

In addition to the data measurements mentioned, several system measurements were made. These included plenum-chamber pressure, oxygen concentration, and certain critical temperatures. The plenum-chamber pressure was measured using a strain-gage transducer and a direct-print oscillograph. An oxygen analyzer was employed to monitor the oxygen concentration. Chromel-alumel thermocouples were used to measure specimen heating in the initial phases of a test and the temperature of various parts of the test apparatus.

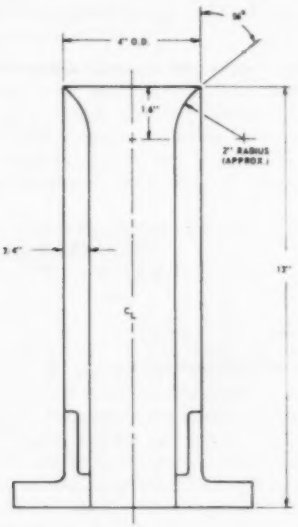

Fig. 4 Specimen geometry

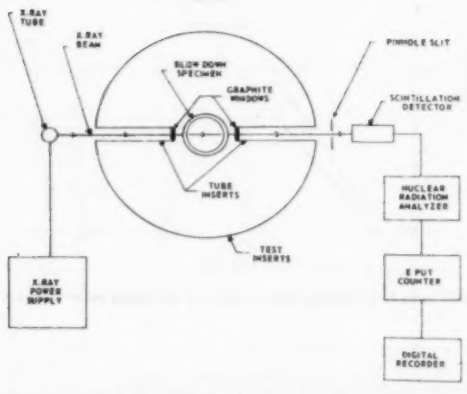

Fig. 5 Schematic of x-ray thickness-measuring instrumentation

Experimental Results

A total of 15 data-gathering runs were made during the course of the experimental investigation. The results of these runs are summarized in Tables 2 and 3. Before discussing these results, detailed results are presented for a typical run, designated in Table 2 as Run no. 14. The grade of graphite used in this run was CS 3-12 supplied by National Carbon Company. The run was at 100 per cent oxygen with a plenum-chamber pressure of 165 psia. The oscillograph trace of plenum-chamber pressure is reproduced in Fig. 6. This clearly shows the pressure transients

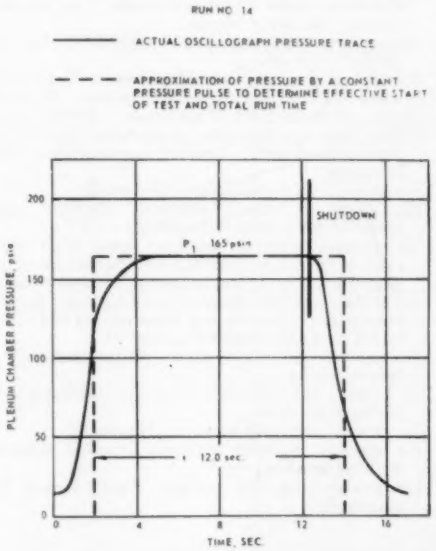

Fig. 6 Pressure-time history in a typical run. Run no. 14, National Carbon Company CS 3-12 at 6 in. from lip; 100 per cent oxygen; 165 psia.

Table 2 Summary of experimental results

Run no.	Per cent oxygen by weight, Γ_{O_2}	Plenum-chamber pressure, P_1, psia	Run duration, t, sec	Graphite[a] grade	Density, ρ_{s_0} pcf	Total decrease in thickness 6 in. from lip of specimen, in.	Average surface regression rate 6 in. from lip of specimen (in/sec) $\times 10^3$	Average ablation rate 6 in. from lip of specimen, $\dot{m}_w$ (lb/sec-ft^2) $\times 10^2$	Graphite surface equilibrium temp, deg R
1	41	327	14.6	Speer 3474D (L)	98	0.112	0.77	6.3	...
2	42	305	9.9	3474D (L)	98	0.076	0.77	6.3	...
3	41	305	10.3	3474D (L)	98	0.087	0.84	6.9	...
4	28	171	60.0	3474D (L)	98	0.337	0.56 (0.26)	4.6 (2.1)	3300
5	53	180	20.4	3474D (L)	98	0.107	0.52	4.2	4100
6	82	165	15.6	3474D (L)	98	0.102	0.65	5.3	5000
7	100	70	30.4	3474D (L)	98	0.092	0.30	2.5	3900
8	100	166	12.0	3474D (L)	98	0.092	0.77	6.3	5200
9	100	315	7.0	3474D (L)	98	0.088	1.26	10.3	5900
10	100	330	7.0	3474D (L)	98	0.113	1.61	13.1	...
11	100	172	15.0	NCC ATJ (L)	97	0.093	0.62	5.0	5200
12	100	165	12.0	NCC RT0008 (L)	114	0.065	0.54	5.1	5000
13	100	165	12.0	NCC RT0003 (L)	113	0.064	0.53	5.0	5000
14	100	165	12.0	NCC CS3-12 (L)	104	0.073	0.61	5.3	5200
15	100	170	12.3	NCC ATJ (T)	97	0.085	0.69	5.6	5200

[a]The symbol (L) designates longitudinal grain orientation; i.e., the specimen is machined so that the direction of flow is parallel to the direction of preferred orientation. (T) = transverse. NCC = National Carbon Company.

Table 3 Physical description of graphite test specimens

Run no.	Description
1	Preliminary entrance design. Deep groove in front of specimen. Entire surface deeply pitted and streaked. Cracked longitudinally without breaking.
2	Preliminary entrance design. Deep groove in front of specimen. Entire surface pitted and streaked. No cracks.
3	Final entrance design. Fairly deep groove in front of specimen. Entire surface pitted and streaked. Specimen broke circumferentially 2 in. aft of entrance. No other cracks.
4	Groove over most of the length of specimen with slight pitting. No cracks.
5	Fairly deep groove in front of specimen. Deeply pitted entrance. Slightly pitted aft portion. No cracks.
6	Slight groove in front of specimen. Several areas of local high burning rates in entrance. Smooth over remainder of body. Cracked longitudinally without breaking.
7	No groove. Smooth surface. No cracks.
8	No groove. Smooth surface. Slightly cracked longitudinally without breaking.
9	No groove. Several areas of local high burning rates in entrance. Smooth over remainder of body. Severely cracked longitudinally without breaking.
10	No groove. Several areas of local high burning rates in entrance. Smooth over remainder of body. Broke into 4 pieces longitudinally, Fig. 10.
11	No groove. Smooth surface. Broke diagonally into several pieces.
12	No groove. Smooth surface. Broke diagonally across center of specimen.
13	No groove. Smooth surface. No cracks.
14	No groove. Smooth surface. Cracked diagonally without breaking.
15	No groove. Smooth surface. Cracked and broke diagonally.

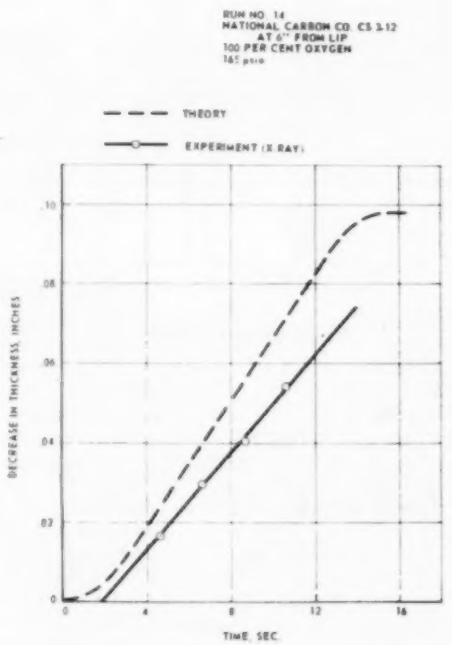

Fig. 7 Decrease in thickness time history in a typical run—Run no. 14

at the beginning and end of the run and the regulation of pressure after the initial transients are overcome.

The decrease in specimen thickness, as indicated by the x-ray instrumentation at a station 6 in. aft of the lip of the specimen, is presented in Fig. 7. The correlation with theory will be discussed later. These data show that the instantaneous burning rate given by the slope of the curve is essentially constant throughout the time for which data were obtained. No meaningful x-ray data could be gained during the initial and final phases of a run due to the pressure transients, Fig. 6, as the change in attenuation of the x-ray beam resulting from the pressure variation completely masked that due to a change in graphite thickness. In that no data were obtained at the beginning or end of a run, the zero reference of the ordinate is not directly determinable. The zero ordinate can be approximated from the following considerations:

1 The pressure-time history is approximated by a constant pressure pulse (165 psia from 1.9 to 13.9 sec) as shown in Fig. 6.

2 The burning rate is assumed to be constant for a constant pressure.

3 From 1 and 2 the resulting curve is a straight line with zero ordinate at 1.9 sec.

4 The line generated in 3 is compared to the data points. Since the two compare favorably approximation 1 and assumption 2 can be assumed to be valid.

The total decrease in specimen thickness is presented in Fig. 8. Each data point is the average of several micrometer readings which were made around the circumference as discussed previously. The material loss is low at the entrance, increases to a maximum at the 3-in. station and is relatively constant aft of 4 in. The significance of these data is discussed in the next section.

The temperature of the burning graphite wall as indicated by the radiamatic pyrometer is shown in Fig. 9. The temperature increases throughout the run until the flow of oxygen is stopped at 12.6 sec. The run duration was not sufficient for the surface equilibrium temperature to be attained. It appears that the equilibrium temperature would be approximately 5200 deg R.

The run conditions and the experimental material losses, ablation rates, and surface equilibrium temperatures for all runs are listed in Table 2. Run conditions were varied systematically to cover the possible range of the primary independent parameters; plenum-chamber pressure, oxygen concentration, and grade of graphite. Various inlet geometries were investigated in Runs nos. 1 through 3 with Run no. 3 using the present design as shown in Fig. 4. All other runs use this latter design as well. The effect of oxygen concentration was investigated in Runs nos. 4, 5, and 6, whereas the effect of pressure was investigated in Runs nos. 7, 8, 9, and 10. In Runs nos. 8 and 11 through 15 the grades of graphite and grain orientations were changed.

The listed pressure is that pressure which existed over the majority of the run. In general, pressure fluctuations were small being on the order of a few psia. The run duration is obtained from the pressure-time history as

$$t = (1/P_1) \int_0^t P(\bar{t})d\bar{t}$$

where P_1 is the pressure listed in Table 2. This procedure is illustrated in Fig. 6 for Run no. 14.

The decrease in thickness at the 6-in. station was obtained from the averaged micrometer readings. The average surface regression rate at this station was obtained by dividing the total decrease in thickness by the run duration. It will be shown that the predicted regression rate is approximately constant for a constant pressure so that the average regression rate listed in Table 2 closely represents the instantaneous regression rate for the majority of the run. In Run no. 4 the number in parentheses is obtained from the slope of the x-ray data over the first half of the run. During the latter part of the run the x-ray data indicated a substantial increase in the surface regression rate, suggesting that the groove which had formed at the front of the specimen due to the low oxygen concentration and hence poor entry ignition had moved back to the x-ray station. For the purpose of correlation this value for surface regression rate is preferred to that obtained from the measurement of total thickness change. The average ablation rate $\dot{m}_w$ is obtained from the surface regression rate and the graphite density. This is more meaningful than surface regression rate for comparison between runs as it eliminates the effect of graphite density.

The graphite surface equilibrium temperatures are those which were reached or approached after considerable time. By varia-

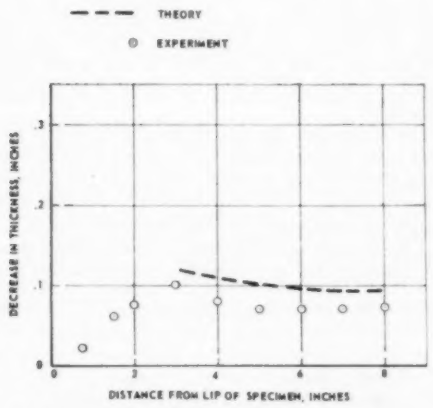

Fig. 8 Decrease in thickness in a typical run—Run no. 14

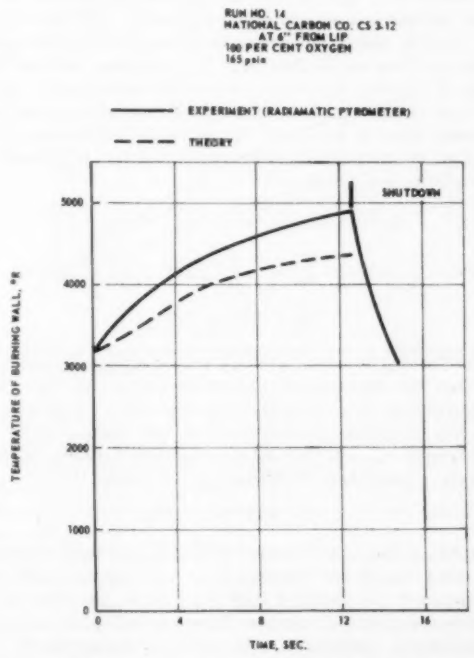

Fig. 9 Temperature-time history in a typical run—Run no. 14

tion of the primary independent parameters, a large temperature range was covered, from 3300 to 5900 deg R.

The following trends in the data are evident:

1 Both ablation rate and surface equilibrium temperature increase with increase in oxygen concentration (Runs nos. 4, 5, 6, and 8).

2 Both ablation rate and surface equilibrium temperature increase with increase in pressure (Runs nos. 7, 8, and 9).

3 Both ablation rate and surface equilibrium temperature are relatively independent of graphite grade and grain orientation.

The final appearance of the graphite test specimens is described in Table 3. As a further illustration, the specimen used in Run no. 10 is shown in Fig. 10. Examination of these data reveals three considerations which would affect the flow adversely and hence the ablation rates and surface temperatures:

1 A groove formed in the entrance region of several specimens with low oxygen concentration.

2 Surface pitting occurred with low oxygen concentration.

3 Cracks and breaks due to thermal stress occurred in cases of rapid heating (combination of high oxygen concentration and high pressure).

With the exception of Run no. 4, in which the groove which formed in the entrance was allowed to extend over most of the length of the specimen, it is the opinion of the authors that these adverse flow conditions did not affect the results appreciably. However, they should be kept in mind during any attempt at correlation of data.

Correlation With Theory

Because the Reynolds number was 1.5×10^7 to 10^8 per ft, depending upon the plenum-chamber pressure, the flow was undoubtedly turbulent. The data were correlated with the turbulent analysis of Denison [6]. To accomplish this the expressions for gas phase heat and mass transfer were solved simultaneously with that of transient heat conduction in the solid. Such calculations were programmed for the IBM 650 computer. An implicit finite-difference method was used to determine the transient heat conduction [8]. The program included the effects of a moving boundary and variable thermal conductivity.

Some results of the turbulent theory are summarized here to indicate what is involved. If the Lewis number and Prandtl number are unity, the heat flux conducted into, or radiated from, the solid surface q_w is given by

$$q_w = (\rho_e u_e c_{fe}/2)[h_{ss} - h_{sw} - B(h_{sw} - h_{cs})] \tag{1}$$

where

$$h_s = \sum_i k_i \left[\int_0^T c_{pi} dT + h_i^0 \right] + u^2/2$$

$$B = \dot{m}_w/(\rho_e u_e c_{fe}/2)$$

When there is no mass transfer from the surface, B becomes zero so that the heat-transfer expression reduces to that of compressible flow with a Prandtl number of unity. It so happens in the case of graphite combustion for a wide range of surface temperature of interest, that diffusion controlled surface combustion occurs. Under these conditions it can be shown that

$$B = B^* = (^3/_4)\Gamma_{ow} \tag{2}$$

where Γ_{ow} is the mass of oxygen atoms per unit mass of mixture at the outer edge of the boundary layer. At extremely high surface temperatures, in excess of 7000 deg F or so, the value of B increases above that of equation (2) corresponding to the condition of gas-phase combustion. At very low temperatures, below 1500 deg F or so, surface kinetics are important and B is less than B^*. It can be seen from equation (1) that not only B but also the mass fractions of all the constituents must be known in order to compute the heat flux. Although nonequilibrium surface kinetics could be included, it was found adequate to assume chemical equilibrium for the purpose of determining the mass fractions.

Fig. 10(a) View of fractured specimen used in Run no. 10

Fig. 10(b) Closeup of fractured specimen used in Run no. 10

In order to estimate the skin friction, the velocity distribution obtained from incompressible data was modified in order to include the effects of density variations across the boundary layer and mass injection. The two empirical constants which occur were chosen in such a manner that the results reduce to the von Karman-Schoenherr relationship for incompressible skin friction with no blowing. The skin-friction law which results is given by

$$\phi/c_{fe}^{1/2} = 1.70 + 4.15 \{\log_{10}[c_{fe}\widetilde{\mathrm{Re}}_{we}(\rho_e/\rho_w)^{1-\beta/2}(1+B)^{\beta/2}]\} \tag{3}$$

where

$$\phi = \int_0^1 \left[\frac{\rho}{\rho_e(1 + Bu/u_e)} \right]^{1/2} d(u/u_e)$$

$$\tilde{\mathrm{Re}}_{w\ell} = \frac{\int_0^x \rho_w u_e r_0^{\epsilon} dx}{\mu_w r_0^{\epsilon}}$$

The quantity β is zero if the von Karman similarity law is used for the mixing length while β is unity if $l = ky$. The former law was used for purposes of correlation. The latter law yields values for c_{f_δ} which are 15 per cent higher. The function ϕ is unity for incompressible flow with no mass injection. In the case of combustion the evaluation of ϕ is complicated due to the influence of variations in the gas mixture across the boundary layer which affect the relationships between density, enthalpy, and velocity ratio. An approximate method for evaluation of ϕ in the case of graphite combustion is presented in [6].

The total decrease in thickness obtained in Run no. 14 is compared to that predicted by the foregoing theory in Fig. 8. The theoretical prediction is 30 per cent high over the rear portion of the specimen. This is typical of all runs. The theory generally predicts 25 to 40 per cent high. Correlation near the front of the specimen is not good. It is theorized that the heat losses by radiation to the surroundings and heat conduction to the supporting structure were such that the surface temperature was not maintained and the combustion was slowed down. This phenomenon of cold entrance would lead to a groove for long-run times, but was not serious in these tests as the entrance curvature was convex to the flow.

The x-ray data for Run no. 14 are compared to theory in Fig. 7. Both theory and experiment indicate essentially a constant burning rate during the time of constant pressure as expressed by a linear decrease in thickness. The theoretical burning rate does decrease very slightly due to the decrease in c_{f_δ} with increase in temperature. The burning rates differ by 30 per cent consistent with the total mass loss.

The temperature of the burning graphite wall is compared to the theory in Fig. 9. The agreement is reasonably good. This is typical of the temperature data. Generally, the theory predicted 200 to 500 deg F low.

As mentioned previously, the predicted mass loss was consistently 25 to 40 per cent high. Therefore, for the purpose of correlation among runs, the theoretical prediction was reduced by a factor of 0.75.

The correlation with chamber pressure in the range 70 to 330 psia at 100 per cent oxygen is presented in Fig. 11. Each data point represents the average rate of surface regression for a single run at a point 6 in. back from the lip of the specimen. The surface regression rate is given by

$$\dot{m}_w/\rho_c = (\rho_e/\rho_c)u_e(c_{f_\delta}/2)B$$

In this series of tests, wall combustion occurred with $B \approx B^* = 0.75$ for 100 per cent oxygen. ρ_e varies directly with the pressure, while c_{f_δ} varies approximately as $P^{-1/5}$ if the effect of blowing is neglected. Therefore the surface regression rate theoretically varies with the $^4/_5$ power of pressure. It can be seen that the predicted variation with pressure is reasonably well verified.

Correlation with oxygen concentration over the range 28 to 100 per cent oxygen at pressure levels of approximately 170 and 310 psia is presented in Fig. 12. The datum point at 28 per cent oxygen was obtained from the x-ray data whereas the other points were obtained from the averaged total mass loss at the 6-in. station. The data points were corrected to the two listed pressures according to the theoretical effect of pressure discussed in the preceding paragraph. B^* is proportional to the oxygen concentration Γ_{0_e}. With increase in Γ_{0_e} the skin-friction coefficient c_{f_δ} is decreased due to the effects of both increased blowing and increased surface temperature. The dashed line in Fig. 12 shows the theoretical surface regression rate neglecting the effect of any change in c_{f_δ}, whereas the solid line includes the theoretical influence of reducing c_{f_δ}. For the former case, c_{f_δ} was computed on the basis of the results of Van Driest for a compressible turbulent boundary layer with no blowing [9] for a surface temperature of 3000 deg R. The experimental data verify well the effect of oxygen concentration on surface regression rate, including the influence of c_{f_δ}.

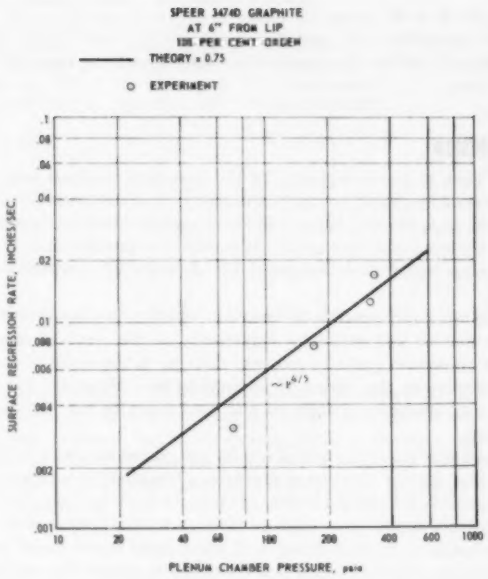

Fig. 11 Effect of pressure upon surface regression rate. Speer 3474D graphite at 6 in. from lip; 100 per cent oxygen.

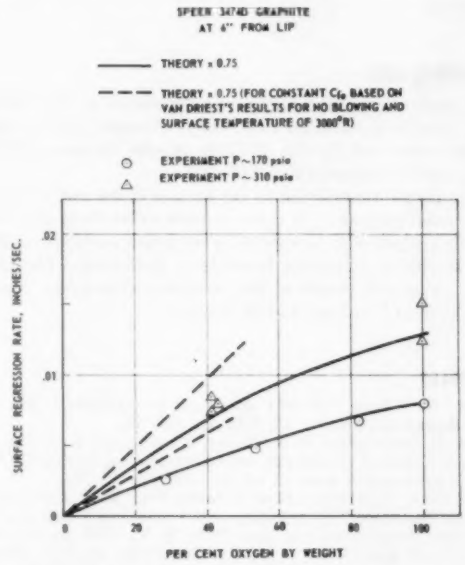
SPEER 3474D GRAPHITE
AT 6" FROM LIP
THEORY x 0.75
THEORY x 0.75 (FOR CONSTANT C_{f_δ} BASED ON VAN DRIEST'S RESULTS FOR NO BLOWING AND SURFACE TEMPERATURE OF 3000°R)
EXPERIMENT P~170 psia
EXPERIMENT P~310 psia
SURFACE REGRESSION RATE, INCHES/SEC.
PER CENT OXYGEN BY WEIGHT

Fig. 12 Effect of oxygen concentration upon surface regression rate. Speer 3474D graphite at 6 in. from lip.

Six runs were conducted with various grades of graphite all at 100 per cent oxygen and approximately 170 psia. These are listed in Table 2 as Runs nos. 8 and 11 through 15. The average ablation rates $\dot{m}_w$ for the different grades differed by approximately ±10 per cent, whereas theoretically they should be the

same for $B = B^*$ except for minor variations in ρ_e and c_{f_e} due to slight variations in P and T_w, respectively. The 10 per cent deviation is within the repeatability which could be expected in such tests.

Conclusion

In view of the complexity of the turbulent analysis and its reliance on empirical constants obtained from incompressible skin-friction experiments, agreement such as was obtained in these tests is considered very good. It is certainly possible that ablation rates could have disagreed by an order of magnitude or more.

It is not really possible to ascertain whether the factor of 0.75 is peculiar to this particular experiment, is the result of uncertainty in certain graphite property data, or is the result of some imperfection in the theory or its application. However, the results are consistent enough to add confidence to the turbulent analysis.

The foregoing experimental results and correlation with theory have been for the ablation of graphite, a combustible sublimator. It is possible, following a similar analysis, to treat the case of other sublimators or ablators which go through a liquid phase prior to vaporization. When melting with subsequent liquid runoff and partial vaporization occurs, it is necessary to match the solution for the gas phase with the conservation equations for the condensed phase. The experimental verification reported herein makes such calibrations reasonable, but further experimentation is desirable.

Acknowledgment

The research reported herein was conducted at the Aeronutronic Aerothermochemical Laboratory, Newport Beach, Calif., and was sponsored by the Ballistic Missile Division, ARDC, USAF, under Contract AF 04(647)-155.

Many people contributed to the success of the analytical and experimental program. It is not possible to list them all. However, the authors wish to express appreciation especially to Prof. F. E. Marble of California Institute of Technology, Dr. D. A. Dooley; and with regard to the experimental program, Messrs. G. P. Carver, C. Hallum, and D. Jefferies.

References

1 M. C. Adams, "Recent Advances in Ablation," *American Rocket Society Journal*, vol. 29, 1959, pp. 625–632.

2 M. R. Denison and D. A. Dooley, "Combustion in the Laminar Boundary Layer of Chemically Active Sublimating Surfaces," *Journal of the Aeronautical Sciences*, vol. 25, 1958, pp. 271–272.

3 L. Lees, "Convective Heat Transfer With Mass Addition and Chemical Reactions," Combustion and Propulsion Third AGARD Colloquium, Pergamon Press, New York, N. Y., 1958, pp. 451–498.

4 T. R. Brogan, "Electric Arc Gas Heaters for Re-Entry Simulation and Space Propulsion," American Rocket Society Preprint No. 724-58, 1958.

5 P. H. Rose, W. E. Powers, and D. Hritzay, "The Large High Pressure Arc Plasma Generator, a Facility for Simulating Missile and Satellite Re-Entry," American Rocket Society Preprint No. 838-59, 1959.

6 M. R. Denison, "The Turbulent Boundary Layer on Chemically Active Ablating Surfaces," *Journal of the Aero/Space Sciences*, vol. 28, 1961, pp. 471–479.

7 R. A. Seban, "Heat Transfer and Flow With Separated and Reattached Boundary Layer as Produced by Surface Irregularities," WADC Technical Report 56-217, Wright-Patterson Air Force Base, Ohio, May 15, 1956.

8 C. F. Dewey, Jr., S. I. Schlesinger, and L. Sashkin, "Temperature Profiles in a Finite Solid With Moving Boundary," *Journal of the Aero/Space Sciences*, vol. 27, 1960, pp. 59–64.

9 E. R. Van Driest, "Turbulent Boundary Layer in Compressible Fluids," *Journal of the Aeronautical Sciences*, vol. 18, 1951, p. 145.

DISCUSSION

Morris W. Rubesin[2]

This paper presents a description of an experiment for obtaining ablation rates in a turbulent boundary layer with a surface material that sublimes and burns. Because a new technique is utilized, that is, the heat of combustion is utilized to cause the ablation rather than a high stream enthalpy, it would be desirable for the authors to compare their results with those of other experiments, if available. It would also be interesting for the authors to comment on how deviations of the Prandtl and Schmidt from unity would affect the basic premises of the experiment. That is, can heat of combustion be made equivalent to free stream enthalpy?

Authors' Closure

A considerable amount of experimental data exists for compressible turbulent boundary layers with heat and mass transfer but without chemical reactions. These have often been compared with the analyses of Rubesin[3] and Dorrance and Dore,[4] for example, by Hartnett, et al.,[5] and Denison.[6] No published experimental data are known to exist for turbulent boundary layers with chemical reactions and at high stream enthalpy. However, Lozier[7] has published data for the stagnation point ablation of graphite at stream enthalpies up to 9000 Btu/lb. For Prandtl and Schmidt numbers of unity, turbulent and laminar analyses differ only in the expression for skin-friction coefficient. Hence a partial check on the physicochemical model, including the equivalence of stream enthalpy with the heat of combustion with excess oxygen, can be obtained from these data.

Lozier tested hemispherically capped graphite cylinders in various air-stabilized arc-jets. Some of the pertinent experimental parameters are repeated in Table 4. Also presented in Table 4 are the ablation rates calculated by the Denison analysis,[6] and the ratio of theoretical to experimental ablation rates. The ablation rates were computed from the data presented by Lozier for the case of diffusion controlled surface combustion in air ($B = 0.173$). The $\rho_e u_e c_{f_e}/2$ were obtained from the approximation $(\rho_e u_e c_{f_{e_0}}/2)(c_{f_e}/c_{f_{e_0}})$ where $c_{f_{e_0}}$ represents the skin-friction coefficient neglecting the effect of blowing. The $\rho_e u_e c_{f_{e_0}}/2$ were computed from the ratio of the net aerodynamic heat flux to a nonablating body but at surface temperature, to the difference in free stream enthalpy and the enthalpy of air at surface conditions. The aerodynamic heat fluxes were computed by Lozier from the relation of Rose and Stark.[8] The ratio $c_{f_e}/c_{f_{e_0}}$ was taken to be 0.90.[9] Correlation is considered to be within the experimental uncertainties in surface temperature, stagnation enthalpies, and calculated heat fluxes. This adds further confidence to

[2] Vidya, Inc., Palo Alto, Calif.

[3] M. W. Rubesin, "An Analytical Estimation of the Effect of Transpiration Cooling on the Heat-Transfer and Skin-Friction Characteristics of a Compressible Turbulent Boundary Layer," NACA TN 3341, December, 1954.

[4] W. H. Dorrance and E. J. Dore, "The Effect of Mass Transfer on the Compressible Turbulent Boundary-Layer Skin Friction and Heat Transfer," *Journal of the Aeronautical Sciences*, vol. 21, 1954, pp. 404–410.

[5] J. P. Hartnett, D. J. Masson, J. F. Gross, and C. Gazley, Jr., "Mass-Transfer Cooling in a Turbulent Boundary Layer," IAS, Paper No. 60–66, 1960.

[6] Reference [6] of paper.

[7] W. W. Lozier, "Development of Graphite and Graphite Base Multicomponent Materials for High Temperature Service," WADC Technical Report 59–789, Wright-Patterson Air Force Base, Ohio, April, 1960.

[8] P. H. Rose and W. I. Stark, "Stagnation Point Heat-Transfer Measurements in Dissociated Air," *Journal of the Aeronautical Sciences*, vol. 25, 1958, pp. 86–97.

[9] References [2 and 3] of paper.

Table 4 Summary of ablation results for graphite stagnation point in air-stabilized arc-jets

Facility	Stagnation enthalpy, Btu/lb	Surface temp, deg K	Experimental stagnation point mass ablation rate, gm/cm² sec*	Theoretical stagnation point mass ablation rate, gm/cm² sec	Ratio of theoretical to experimental ablation rates
National Carbon Co., Parma Lab	1200	2000	0.029	0.037	1.28
Linde, Speedway Lab	2500	3000	0.057	0.052	0.91
Chicago Midway Lab	8500	3500	0.054	0.031	0.57
AVCO, Lawrence Lab	7500	3500	>0.019	0.029	<1.53
AVCO, Everett Lab	9000	~3800	>0.008	0.012	<1.50

* The last two runs are reported to be not steady state.

the idealizations used in the Denison model and indicates that the heat of combustion with excess oxygen is indeed equivalent to stream enthalpy.

The effects of nonunit Prandtl and Schmidt numbers have not been investigated in detail for turbulent flow but it can be said that such effects do not alter the basic premises of the experimental procedure. It would take such refinements to determine the recovery factors in order to predict the precise amount of oxygen required for exact simulation of a re-entry condition. Such an extended analysis might also improve the correlation of experimental ablation rates with theory. Mr. Rubesin's interest is appreciated.

L. N. TAO
Professor of Mechanics,
Illinois Institute of Technology,
Chicago, Ill.
Assoc. Mem. ASME

On Some Laminar Forced-Convection Problems

The forced-convection problems in channels of fully developed laminar flow with heat sources and constant wall-temperature gradient are approached by the method of complex variables. It is shown that the stated problems are reduced to the determination of some analytic functions which satisfy the boundary conditions. Few basic problems, including flows in equilateral triangular ducts and in elliptical tubes, are studied. Also, it is shown that the cases of circular tubes and of parallel plates with a gap are directly deducible from that of elliptical tubes. All these solutions are expressed in closed forms by polynomials.

Introduction

THE HEAT-TRANSFER PROBLEMS of forced convection in channels have been the subject of investigations for many years. Many of these investigations have been associated with the cases of fully developed laminar flow. They are usable in the region of the channel away from the entrance. Based on this assumption we then have the velocity and temperature (or temperature difference) of the flow to be invariant in the axial direction [1].[1] This certainly simplifies the mathematical complexities. However, even in such simplified cases of fully developed laminar liquid, the problems of forced convection in channels are usually limited to cross sections of simple configurations, which can be described by some unblended expressions in Cartesian or polar co-ordinates.

In this paper it will be shown that the complex-variable method can be used to solve some forced-convection problems of fully developed laminar flow in channels with heat sources and linearly varying wall temperature. In essence, the stated problems are governed by a biharmonic equation in two variables. The use of complex variables readily reduces the problems to the determination of some analytic functions which satisfy the boundary conditions. Many techniques of the complex-function theory are then applicable. Hence the approach will greatly enlarge the analyses to channels of various configurations. The complex-variable method has been used successfully by Muskhelishvili and many others in the theory of elasticity [2, 3]. However, it may be mentioned that the boundary conditions in either the first or second fundamental problems of plane elasticity are quite different from our present problems.

In the first part of the paper the formulation of the problem by the use of complex variables will be given. To demonstrate the method, some specific problems will be followed. First, we take a case of flow in an equilateral triangular duct. The problem has been studied by Clark and Kays [4], and by Marco and Han [5]. Clark and Kays attacked the problem by relaxation method and obtained a result of Nu = 3.00. Marco and Han gave the solutions of velocity and temperature fields. Neither of these works include heat sources. This problem with heat sources is re-examined using the complex-variable method. The exact solution for uniformly distributed heat sources is obtained in simple polynomials. When the heat-source intensity vanishes, the solution is reduced to that of [4 and 5].

The second problem to be studied is that of an elliptical tube with uniform heat generation. The solution is expressed in closed form by polynomials. It covers all aspect ratios, i.e., ratios of semiaxes. In addition, the solution of elliptical tubes may also be used to obtain the special cases of circular tubes and of parallel plates by assigning proper values of the parameters. They are again reducible to the known solutions of these special cases when the heat-source intensity vanishes.

Mathematical Formulation

Consider a steady fully developed (both hydrodynamically and thermally) laminar flow with heat sources in a channel of cross section D bounded by a closed curve Γ. Let the axis of the channel be in the Z-direction and axial wall-temperature gradient be constant. The basic momentum and energy equations of a constant-property, nondissipative fluid in Cartesian co-ordinates (x, y, Z) are

$$\nabla^2 u = \frac{1}{\mu}\frac{dp}{dZ} = C_1 \tag{1}$$

$$\nabla^2 t = \left(\frac{\rho c_p}{k}\frac{\partial t}{\partial Z}\right) u - \frac{Q}{k} = C_2 u - C_3 \tag{2}$$

[1] Numbers in brackets designate References at end of paper.

Contributed by the Heat Transfer Division and presented at the Winter Annual Meeting, New York, N. Y., November 27–December 2, 1960, of THE AMERICAN SOCIETY OF MECHANICAL ENGINEERS. Manuscript received at ASME Headquarters, August 9, 1960. Paper No. 60—WA-188.

Nomenclature

a, b = physical dimensions
c_p = specific heat at constant pressure
$f(z)$ = complex function defined in equation (16)
$\bar{f}(\bar{z})$ = complex conjugate of $f(z)$
$g(z)$ = complex function defined in equation (18)
$\bar{g}(\bar{z})$ = complex conjugate of $g(z)$
h = heat-transfer coefficient
k = thermal conductivity
p = pressure
q = heat-transfer rate
r = radius of circular co-ordinates
t = local temperature
t_w = wall temperature
u = local velocity
u_m = average velocity
x, y, Z = Cartesian co-ordinates
z = complex variable, $x + iy$
$\bar{z}$ = conjugate of z, $x - iy$
A = cross-sectional area
A_1, A_2, A_3 = parameters defined in equations (65), (66), and (67)
A_4, A_5, A_6 = parameters defined in equations (69), (70), and (71)
C_1 = parameter, $(dp/dZ)/\mu$
C_2 = parameter, $(\rho c_p/k)(\partial t/\partial Z)$
C_3 = parameter, Q/k

(Continued on next page)

where ∇^2 is the two-dimensional Laplace operator in (x, y). The boundary conditions are

$$u = 0, \quad t = t_w \quad \text{on } \Gamma \tag{3}$$

Using complex variables $z = x + iy$, $\bar{z} = x - iy$, and new temperature variable $T = t - t_w$, the governing equations become

$$\frac{\partial^2 u}{\partial z \partial \bar{z}} = \frac{C_1}{4} \tag{4}$$

$$\frac{\partial^2 T}{\partial z \partial \bar{z}} = \frac{1}{4}(C_2 u - C_3) \tag{5}$$

In equation (5) C_3 is a heat-source function, which is different for different problems. In order to attack the problem in general terms, we introduce

$$T = T_1 + T_2 \tag{6}$$

such that

$$\frac{\partial^2 T_1}{\partial z \partial \bar{z}} = \frac{C_2 u}{4} \tag{7}$$

$$\frac{\partial^2 T_2}{\partial z \partial \bar{z}} = -\frac{C_3}{4} \tag{8}$$

To find the solution of T_1, we first eliminate u between equations (4) and (7),

$$\frac{\partial^4 T_1}{\partial z^2 \partial \bar{z}^2} = \frac{C_1 C_2}{16} = \frac{C_4}{16} \tag{9}$$

Now we write

$$\theta_1 = T_1 - \frac{C_4}{64}(z\bar{z})^2 \tag{10}$$

Equation (9) and conditions (3) are then

$$\frac{\partial^4 \theta_1}{\partial z^2 \partial \bar{z}^2} = 0 \tag{11}$$

$$\left.\begin{aligned} &(a) \quad \theta_1 = -\frac{C_4}{64}(z\bar{z})^2 \\ &(b) \quad \frac{\partial^2 \theta_1}{\partial z \partial \bar{z}} = -\frac{C_4}{16} z\bar{z} \end{aligned}\right\} \quad \text{on } \Gamma \tag{12}$$

And the velocity field is related to θ_1 by

$$u = \frac{1}{C_2}\left[4\frac{\partial^2 \theta_1}{\partial z \partial \bar{z}} + \frac{C_4}{4} z\bar{z}\right] \tag{13}$$

Equation (11) admits a general solution of the form

$$\theta_1 = \bar{z}\phi(z) + z\bar{\phi}(\bar{z}) + \psi(z) + \bar{\chi}(\bar{z}) \tag{14}$$

where the bar denotes the complex conjugate, and $\phi(z)$ and $\psi(z)$, called as Goursat functions in [6], are two complex functions analytic in D. By differentiation, we also have

$$\frac{\partial^2 \theta_1}{\partial z \partial \bar{z}} = \phi'(z) + \bar{\phi}'(\bar{z}) \tag{15}$$

where prime denotes differentiation with respect to the argument.

The foregoing formulation readily indicates that the solution of T_1 is reduced to the determination of two analytic functions $\phi(z)$ and $\psi(z)$ satisfying the boundary conditions (12). Hence many techniques in the complex-function theory can be used. If the equation of the boundary Γ is expressible in the form of

$$z\bar{z} = f(z) + \bar{f}(\bar{z}) \tag{16}$$

then comparing with equation (12*b*) and (15), we must have

$$\phi'(z) = -\frac{C_4}{16} f(z) \tag{17}$$

With known $\phi'(z)$, and hence $\bar{z}\phi(z)$ and $z\bar{\phi}(\bar{z})$, we may find the other analytic function $\psi(z)$, if the boundary equation is also expressible as

$$(z\bar{z})^2 = -\frac{64}{C_4}[\bar{z}\phi(z) + z\bar{\phi}(\bar{z})] + g(z) + \bar{g}(\bar{z}) \tag{18}$$

Comparing with equations (12*a*) and (14), we have

$$\psi(z) = -\frac{C_4}{64} g(z) \tag{19}$$

The other part T_2 is independent of the velocity u. Using

$$\theta_2 = T_2 + G(z, \bar{z}) \tag{20}$$

and

$$G = \iint \frac{C_3}{4}\, dz\, d\bar{z} \tag{21}$$

Equation (8) becomes

$$\frac{\partial^2 \theta_2}{\partial z \partial \bar{z}} = 0 \tag{22}$$

and the boundary condition is

$$\theta_2 = G \quad \text{on } \Gamma \tag{23}$$

This shows that θ_2 is a harmonic function which satisfies condition (23). The general solution is of the form of

$$\theta_2 = \omega(z) + \bar{\omega}(\bar{z}) \tag{24}$$

where $\omega(z)$ is an analytic function in D. Since the heat-source term is arbitrary, the solution cannot be set a priori without

Nomenclature

C_{3m} = average of C_3, $\frac{1}{A}\iint_D C_3 dx\, dy$
C_4 = parameter, C_1C_2
D = domain of cross section
D_e = hydraulic diameter, $4A/S$
$\mathbf{E}(k)$ = complete elliptical integral of second kind
$G(z, \bar{z})$ = function defined in equation (21)
Nu = Nusselt number
Q = heat-source intensity
S = circumference of cross section
T = temperature variable, $t - t_w$
T_1, T_2 = temperature variables defined in equation (6)
α = dimensionless parameter, $C_3/(C_4a^2)$
β = dimensionless parameter, $C_3/(C_4b^2)$
θ_1, θ_2 = temperature variables defined in equations (10) and (20)
λ = aspect ratio of elliptical tube
μ = viscosity
ρ = density
$\phi(z)$ = complex function defined in equation (14)
$\bar{\phi}(\bar{z})$ = complex conjugate for $\phi(z)$
$\psi(z)$ = complex function defined in equation (14)
$\bar{\chi}(\bar{z})$ = complex conjugate of $\psi(z)$
$\omega(z)$ = complex function defined in equation (24)
$\bar{\omega}(\bar{z})$ = complex conjugate of $\omega(z)$
Γ = bounding curve of cross section

specifying the heat-source intensity. However, after we have found θ_2, the solution T_2 is

$$T_2 = \theta_2 - G(z, \bar{z}) \tag{25}$$

In summarizing, the velocity and temperature fields of the problem are

$$u = \frac{C_1}{4}\,[z\bar{z} - f(z) - \bar{f}(\bar{z})] \tag{26}$$

$$T = \frac{C_4}{64}\,(z\bar{z})^2 + \bar{z}\phi(z) + z\bar{\phi}(\bar{z}) + \psi(z) + \bar{\psi}(\bar{z}) + \omega(z) + \bar{\omega}(\bar{z}) - G(z, \bar{z}) \tag{27}$$

The average velocity and temperature are

$$u_m = \frac{1}{A}\iint_D u\,dx\,dy \tag{28}$$

$$T_m = \frac{1}{A}\iint_D T\,dx\,dy \tag{29}$$

Also the mixed mean temperature is

$$T_M = \frac{1}{u_m A}\iint_D u\,T\,dx\,dy \tag{30}$$

The heat-transfer rate is now obtainable from the consideration of heat balance; we then have

$$q = C_2 u_m kA - \iint_D Q\,dx\,dy = (C_2 u_m - C_{3m})kA \tag{31}$$

Also the heat-transfer coefficient h and the Nusselt number Nu based on T_M may then be evaluated,

$$h = -q/ST_M = (C_{3m} - C_2 u_m)kA/ST_M \tag{32}$$

and

$$\mathrm{Nu} = \frac{hD_e}{k} = \frac{D_e}{S}\,\frac{(C_{3m} - C_2 u_m)A}{T_M} = 4\left(\frac{A}{S}\right)^2 \frac{C_{3m} - C_2 u_m}{T_M} \tag{33}$$

where S is the circumference of the section, and D_e is the equivalent hydraulic diameter.

Equilateral Triangular Tubes

Consider a tube of an equilateral triangular cross section. Let the sides be $2\sqrt{3}a$ and the equations of the boundary be

$$\left.\begin{aligned} x - a &= 0 \\ x - \sqrt{3}\,y + 2a &= 0 \\ x + \sqrt{3}\,y + 2a &= 0 \end{aligned}\right\} \tag{34}$$

The product of these equations gives

$$(x - a)(x - \sqrt{3}\,y + 2a)(x + \sqrt{3}\,y + 2a) = 0 \tag{35}$$

or

$$z\bar{z} = \frac{4}{3}\,a^2 - \frac{1}{6a}\,(z^3 + \bar{z}^3) \tag{36}$$

Using equations (16) and (17), we obtain

$$f(z) = \frac{2}{3}\,a^3 - \frac{1}{6a}\,z^3 \tag{37}$$

$$\phi'(z) = \frac{C_4}{96a}\,z^2 - \frac{C_4}{24}\,a^2 \tag{38}$$

and

$$\bar{z}\,\phi(z) = \frac{C_4}{384a}\,z^4\bar{z} - \frac{C_4}{24}\,a^2 z\bar{z} \tag{39}$$

To determine $g(z)$ or $\psi(z)$, we square and rearrange the boundary equation (36) in the following forms:

$$(z\bar{z})^2 = \frac{16}{9}\,a^4 - \frac{2a}{9}\,(z^3 + \bar{z}^3) - \frac{1}{6a}\,z\bar{z}\,(z^3 + \bar{z}^3) \tag{40}$$

and

$$0 = \frac{16}{3}\,a^3\left[z\bar{z} - \frac{4}{3}\,a^2 + \frac{1}{6a}\,(z^3 + \bar{z}^3)\right] \tag{41}$$

Adding these two equations leads to

$$(z\bar{z})^2 = -\frac{1}{6a}\,z\bar{z}(z^3 + \bar{z}^3) + \frac{16a^2}{3}\,z\bar{z} + \frac{2a}{3}\,[(z^3 + \bar{z}^3) - 8a^3] \tag{42}$$

Comparing with equations (18) and (19), we obtain

$$g(z) = \frac{2a}{3}\,(z^3 - 4a^3) \tag{43}$$

$$\psi(z) = \frac{C_4 a}{96}\,(4a^3 - z^3) \tag{44}$$

To determine T_2 we take a simple case of uniform heat generation $C_3 = C_{3m}$. Then equation (21) shows

$$G(z, \bar{z}) = \frac{C_3}{4}\,z\bar{z} \tag{45}$$

Using equations (36) and (25), we have

$$\theta_2 = C_3\left[\frac{a^2}{3} - \frac{1}{24a}\,(z^3 + \bar{z}^3)\right] \tag{46}$$

or

$$T_2 = \frac{C_3}{24a}\,[8a^3 - (z^3 + \bar{z}^3) - 6az\bar{z}] \tag{47}$$

Therefore the velocity and temperature fields are

$$u = \frac{C_1}{4}\left[z\bar{z} - \frac{4}{3}\,a^2 + \frac{1}{6a}\,(z^3 + \bar{z}^3)\right] \tag{48}$$

$$T = \frac{C_4}{64}\left[(z\bar{z})^2 + \frac{1}{6a}\,z\bar{z}(z^3 + \bar{z}^3)\right] + \frac{C_4 a}{12}\left[a^2 - \frac{z^3 + \bar{z}^3}{8} - az\bar{z}\right] - \frac{C_3}{24a}\,[6az\bar{z} + (z^3 + \bar{z}^3) - 8a^3] \tag{49}$$

In terms of physical co-ordinates (x, y), they are

$$u = \frac{C_1}{12a}\,(x - a)[(x + 2a)^2 - 3y^2] \tag{50}$$

$$T = \frac{C_4}{192a}\,(x - a)[(x + 2a)^2 - 3y^2] \times \left[(x^2 + y^2 - 4a^2) - 16\,\frac{C_3}{C_4}\right] \tag{51}$$

When $C_3 = 0$, the result agrees with [5].

The average velocity and temperature are then

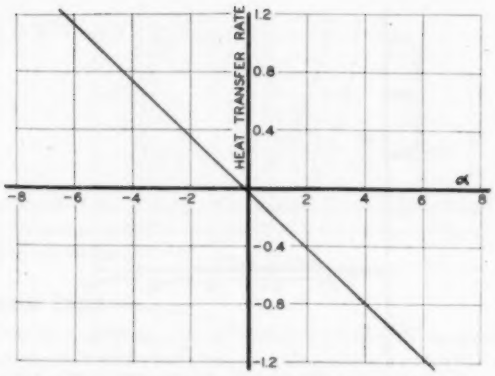

Fig. 1 Equilateral triangular duct—heat-transfer rate (q/C_4kA^2) versus dimensionless parameter α ($= C_3/C_4a^2$)

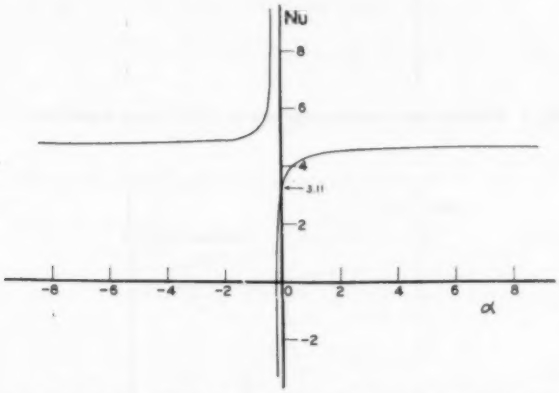

Fig. 2 Equilateral triangular duct—Nusselt number versus dimensionless parameter α ($= C_3/C_4a^2$)

$$u_m = \frac{2}{3\sqrt{3}\,a^2}\int_{-2a}^{a}\int_{0}^{\frac{x+2a}{\sqrt{3}}} u\,dy\,dx = -\frac{3}{20}\,C_1a^2 \tag{52}$$

$$T_m = \frac{2}{3\sqrt{3}\,a^2}\int_{-2a}^{a}\int_{0}^{\frac{x+2a}{\sqrt{3}}} T\,dy\,dx = \frac{9}{280}\,C_4a^4\left(1+\frac{14}{3}\,\frac{C_3}{C_4a^2}\right) \tag{53}$$

And the mixed mean temperature is

$$T_M = \frac{2}{3\sqrt{3}\,u_m a^2}\int_{-2a}^{a}\int_{0}^{\frac{x+2a}{\sqrt{3}}} uT\,dy\,dx = \frac{27}{560}\,C_4a^4\left(1+\frac{40}{9}\,\frac{C_3}{C_4a^2}\right) \tag{54}$$

Hence the heat-transfer rate and the Nusselt number based on T_M are

$$\frac{q}{C_4kA^2} = \frac{u_m}{C_1A} - \frac{C_3}{C_4A} = -\frac{1}{3\sqrt{3}}\left(\frac{3}{20}+\alpha\right) \tag{55}$$

$$\mathrm{Nu} = \frac{(C_3 - C_3u_m)a^2}{T_M} = \frac{28}{9}\left[\frac{1+\frac{20}{3}\,\alpha}{1+\frac{40}{9}\,\alpha}\right] \tag{56}$$

where $\alpha = C_3/C_4a^2$. With vanishing C_3 (or α), we have Nu = 28/9, which is compared to Nu = 3.00 given by relaxation method [4]. The evaluations of heat-transfer rates (in dimensionless form) and Nusselt numbers at various values of α are given in Figs. 1 and 2, respectively.

Elliptical Tubes

Consider the flow in an elliptical tube of semiaxes a and b with uniformly distributed heat sources. Let the equation of the boundary Γ be

$$\frac{x^2}{a^2} + \frac{y^2}{b^2} = 1 \tag{57}$$

or

$$z\bar{z} = \frac{1}{2}\,\frac{a^2-b^2}{a^2+b^2}\,(z^2+\bar{z}^2) + \frac{2a^2b^2}{a^2+b^2} \tag{58}$$

Comparing with equations (16) and (17), we get

$$f(z) = \frac{1}{2}\,\frac{a^2-b^2}{a^2+b^2}\,z^2 + \frac{c^2b^2}{a^2+b^2} \tag{59}$$

$$\phi'(z) = -\frac{C_4}{32}\left[\frac{a^2-b^2}{a^2+b^2}\,z^2 + 2\,\frac{a^2b^2}{a^2+b^2}\right] \tag{60}$$

and

$$\bar{z}\phi(z) = -\frac{C_4}{96}\left[6\,\frac{a^2b^2}{a^2+b^2}\,z\bar{z} + \frac{a^2-b^2}{a^2+b^2}\,z^2\bar{z}\right] \tag{61}$$

To determine $g(z)$ and $\psi(z)$, we rearrange and square the boundary equation (58) in three different forms:

$$(z\bar{z})^2 = \frac{1}{2}\,\frac{a^2-b^2}{a^2+b^2}\,z\bar{z}(z^2+\bar{z}^2) + \frac{a^2b^2(a^2-b^2)}{(a^2+b^2)^2}\,(z^2+\bar{z}^2) + \frac{4a^2b^2}{(a^2+b^2)^2} \tag{62}$$

$$\frac{a^2-b^2}{a^2+b^2}\,(z\bar{z})^2 = z\bar{z}(z^2+\bar{z}^2) - \frac{2a^2b^2}{a^2+b^2}\,(z^2+\bar{z}^2) - \frac{1}{2}\,\frac{a^2-b^2}{a^2+b^2}\,(z^4+\bar{z}^4) \tag{63}$$

$$0 = z\bar{z} - \frac{1}{2}\,\frac{a^2-b^2}{a^2+b^2}\,(z^2+\bar{z}^2) - \frac{2a^2b^2}{a^2+b^2} \tag{64}$$

Introducing

$$A_1 = \frac{2}{3}\,\frac{a^4+b^4+10a^2b^2}{a^4+b^4+6a^2b^2} \tag{65}$$

$$A_2 = \frac{1}{3}\,\frac{a^4-b^4}{a^4+b^4+6a^2b^2} \tag{66}$$

$$A_3 = 8\,\frac{a^2b^2}{a^2+b^2} \tag{67}$$

we multiply equations (62), (63), and (64) by A_1, A_2, and A_3, respectively, and add these three equations,

$$(z\bar{z})^2 = \frac{2}{3}\,\frac{a^2-b^2}{a^2+b^2}\,z\bar{z}(z^2+\bar{z}^2) + \frac{8a^2b^2}{a^2+b^2}\,z\bar{z} + A_4(z^2+\bar{z}^2) + A_5(z^4+\bar{z}^4) + 2A_6 \tag{68}$$

where

$$A_4 = \frac{a^2b^2(a^2 - b^2)}{(a^2 + b^2)^2} A_1 - \frac{2a^2b^2}{a^2 + b^2} A_2 - \frac{1}{2} \frac{a^2 - b^2}{a^2 + b^2} A_3 \quad (69)$$

$$A_5 = -\frac{1}{2} \frac{a^2 - b^2}{a^2 + b^2} A_2 = -\frac{1}{6} \frac{(a^2 - b^2)^2}{a^4 + b^4 + 6a^2b^2} \quad (70)$$

$$A_6 = \frac{2a^4b^4}{(a^2 + b^2)^2} A_1 - \frac{a^2b^2}{a^2 + b^2} A_3 \quad (71)$$

Therefore

$$g(z) = A_4 z^2 + A_5 z^4 + A_6 \quad (72)$$

$$\psi(z) = -\frac{C_4}{64} [A_4 z^2 + A_5 z^4 + A_6] \quad (73)$$

For uniformly distributed heat sources,

$$G(z, \bar{z}) = C_3 z\bar{z}/4 \quad (74)$$

From equations (23) and (58), we have

$$\theta_2 = \frac{C_3}{4} \left[\frac{1}{2} \frac{a^2 - b^2}{a^2 + b^2} (z^2 + \bar{z}^2) + \frac{2a^2b^2}{a^2 + b^2} \right] \quad (75)$$

and

$$T_2 = \frac{C_3}{4} \left[\frac{1}{2} \frac{a^2 - b^2}{a^2 + b^2} (z^2 + \bar{z}^2) + \frac{2a^2b^2}{a^2 + b^2} - z\bar{z} \right] \quad (76)$$

The velocity and temperature fields are

$$u = \frac{C_1}{4} \left[z\bar{z} - \frac{1}{2} \frac{a^2 - b^2}{a^2 + b^2} (z^2 + \bar{z}^2) - \frac{2a^2b^2}{a^2 + b^2} \right] \quad (77)$$

$$T = \frac{C_4}{64} \left[z\bar{z} - \frac{1}{2} \frac{a^2 - b^2}{a^2 + b^2} (z^2 + \bar{z}^2) - \frac{2a^2b^2}{a^2 + b^2} \right] \times \left[A_1 z\bar{z} + A_1 \frac{2a^2b^2}{a^2 + b^2} - A_2 (z^2 + \bar{z}^2) - A_3 - 16 \frac{C_3}{C_4} \right] \quad (78)$$

In terms of physical co-ordinates (x, y), they are

$$u = \frac{C_1}{2(a^2 + b^2)} (b^2x^2 + a^2y^2 - a^2b^2) \quad (79)$$

$$T = \frac{C_4}{32(a^2 + b^2)} (b^2x^2 + a^2y^2 - a^2b^2) \times \left[(A_1 - 2A_2)x^2 + (A_1 + 2A_2)y^2 + \frac{2a^2b^2}{a^2 + b^2} A_1 - A_3 \right] \quad (80)$$

Similarly, we may evaluate the average velocity and temperature, and the mixed mean temperature,

$$u_m = \frac{1}{\pi ab} \iint_D u \, dx \, dy = -\frac{C_1}{4} \left(\frac{a^2b^2}{a^2 + b^2} \right) \quad (81)$$

$$T_m = \frac{1}{\pi ab} \iint_D T \, dx \, dy = \frac{C_4 a^2b^2}{4(a^2 + b^2)} \left[\frac{1}{3} \frac{a^2b^2}{a^2 + b^2} + \frac{C_3}{C_4} \right] \quad (82)$$

$$T_M = \frac{1}{\pi ab u_m} \iint_D u \, T dx \, dy = \frac{C_4 a^2b^2}{144(a^2 + b^2)} \left[\frac{a^2b^2}{a^2 + b^2} \frac{17a^4 + 17b^4 + 98a^2b^2}{a^4 + b^4 + 6a^2b^2} + 48 \frac{C_3}{C_4} \right] \quad (83)$$

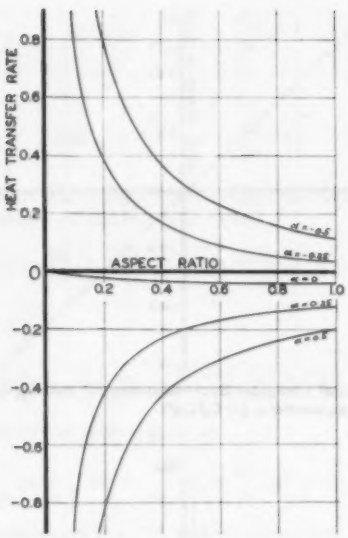

Fig. 3 Elliptical tube—heat-transfer rate (q/C_4kA^2) versus aspect ratio λ

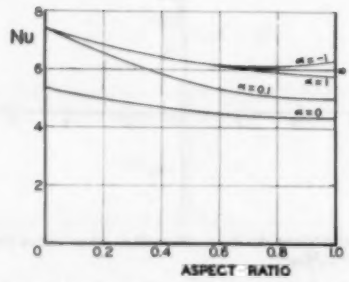

Fig. 4 Elliptical tube—Nusselt number versus aspect ratio λ

The heat-transfer rate and the Nusselt number, according to equations (31) and (33), are

$$\frac{q}{C_4kA^2} = -\frac{1}{\pi ab} \left[\frac{1}{4} \frac{a^2b^2}{a^2 + b^2} + \frac{C_3}{C_4} \right] \quad (84)$$

$$\mathrm{Nu} = 9 \left(\frac{a^2 + b^2}{a^2} \right) \left[\frac{\pi}{\mathbf{E}(c/a)} \right]^2 \times \left[\frac{\frac{a^2b^2}{a^2 + b^2} + 4 \frac{C_3}{C_4}}{\frac{a^2b^2}{a^2 + b^2} \frac{17a^4 + 17b^4 + 98a^2b^2}{a^4 + b^4 + 6a^2b^2} + 48 \frac{C_3}{C_4}} \right] \quad (85)$$

In deriving the foregoing formula we have employed

$$S = 4a\mathbf{E}(c/a)$$

where $c = (a^2 - b^2)^{1/2}$ and $\mathbf{E}(k)$ is the complete elliptical integral of second kind. For numerical evaluation of the Nusselt number and heat-transfer rate, we rewrite equations (84) and (85) in dimensionless forms by introducing the aspect ratio $\lambda = b/a$ and $\alpha = C_3/C_4a^2$,

$$\frac{q}{C_4kA^2} = -\frac{1}{\lambda\pi} \left(\frac{\lambda^2}{4(1 + \lambda^2)} + \alpha \right) \quad (86)$$

$$\mathrm{Nu} = 9(1+\lambda^2)\left[\frac{\pi}{\mathbf{E}(1-\lambda^2)^{1/2}}\right]^2 \times \left[\frac{\dfrac{\lambda^2}{1+\lambda^2}+4\alpha}{\dfrac{\lambda^2}{1+\lambda^2}\dfrac{17(1+\lambda^4)+98\lambda^2}{(1+\lambda^4)+6\lambda^2}+48\alpha}\right] \quad (87)$$

The result of the heat-transfer rates (in dimensionless form) and the Nusselt numbers at various λ and α are plotted in Figs. 3 and 4, respectively.

Special Cases

The analyses of an elliptical tube given in the preceding section may also be used for the cases of a circular tube and between two parallel plates. The solutions for these two cases can be obtained easily by assigning some special values of the parameters.

Circular Tubes. In the case of circular tubes, we let $b = a$ and $x^2 + y^2 = r^2$. Then the velocity and temperature fields are

$$u = \frac{C_1}{4}(r^2 - a^2) \quad (88)$$

$$T = \frac{C_4}{64}(r^2 - a^2)\left(r^2 - 3a^2 - 16\alpha\right) \quad (89)$$

Also u_m, T_m, T_M, q, and Nu are, respectively,

$$u_m = -\frac{C_1 a^2}{8} \quad (90)$$

$$T_m = \frac{C_4 a^2}{8}\left[\frac{a^2}{6} + \frac{C_3}{C_4}\right] \quad (91)$$

$$T_M = \frac{11 C_4 a^2}{384}\left[a^2 + \frac{64}{11}\frac{C_3}{C_4}\right] \quad (92)$$

$$q = -\frac{C_4 k A^2}{\pi}\left(\frac{1}{8} + \frac{\alpha_3}{\alpha_4}\right) \quad (93)$$

$$\mathrm{Nu} = \frac{48}{11}\left[\frac{1+8\alpha}{1+\dfrac{64}{11}\alpha}\right]; \quad \alpha = \frac{C_3}{C_4 a^2} \quad (94)$$

In evaluating the Nusselt number, we have used $\mathbf{E}(0) = \pi/2$. It can be seen that with vanishing C_3 the Nusselt number is reduced to the known result of 48/11 [7].

Parallel Plates. In order to get the solution of flow between parallel plates, we let a approach infinity and b remain finite. Taking the limiting process, we obtain

$$u = \frac{C_1}{2}(y^2 - b^2) \quad (95)$$

$$T = \frac{C_4}{24}(y^2 - b^2)\left(y^2 - 5b^2 - 12\frac{\alpha_3}{\alpha_4}\right) \quad (96)$$

Based on these values of velocity and temperature, we may proceed to find the average velocity, the average temperature, the mixed mean temperature, the heat-transfer rate, and the Nusselt number of flow between parallel plates with a gap,

$$u_m = -\frac{C_1 b^2}{3} \quad (97)$$

$$T_m = \frac{2}{15} C_4 b^4\left[1 + \frac{5}{2}\frac{C_3}{C_4 b^2}\right] \quad (98)$$

$$T_M = \frac{17}{105} C_4 b^4\left[1 + \frac{42}{17}\frac{C_3}{C_4 b^2}\right] \quad (99)$$

$$q \text{ (per unit length)} = -2C_4 k b\left(\frac{b^2}{3} + \frac{C_3}{C_4}\right) \quad (100)$$

$$\mathrm{Nu} = \frac{140}{17}\left[\frac{1+3\beta}{1+\dfrac{42}{17}\beta}\right]; \quad \beta = \frac{C_3}{C_4 b^2} \quad (101)$$

With vanishing C_3 we have Nu = 140/17 which is in agreement with [4].

Discussion and Remarks

The heat-transfer rates (in dimensionless form) and the Nusselt numbers for the cases of equilateral triangular ducts and of elliptical tubes are given in Figs. 1 to 4. Fig. 1 gives the heat-transfer rates of an equilateral triangular duct at various values of α. It shows a linear relationship between q and α. Also there is one point which needs particular attention. This point is when $\alpha = -3/20$, which may be called the critical point. On two sides of this point the heat-flow direction is different. In the case of elliptical tubes we can similarly find this critical point. However, it depends on the aspect ratio and hence is not reported in Fig. 3. From equation (86) we find that the critical point is at $\alpha = -\lambda^2/4(1+\lambda^2)$.

Fig. 2 shows that for $\alpha = -9/40$ the Nusselt number approaches infinity. This does not mean that the heat-transfer rate is infinity. As we examine equation (54), we find that the mixed mean temperature T_M vanishes at $\alpha = -9/40$. The heat-transfer rate is proportional to the product of the heat-transfer coefficient and mixed mean temperature. Therefore the heat-transfer coefficient or the Nusselt number is infinity even though the heat-transfer rate is finite as shown in Fig. 1. The same argument applies to other cases.

In Figs. 3 and 4 the values of the heat-transfer rate and the Nusselt number at $\lambda = 1$ correspond to those of circular tubes. However, those at $\lambda = 0$ do not have any physical meaning. They do not represent the case of flow between parallel plates with a gap. When the aspect ratio λ is zero, we may have either $b = 0$ (parallel plates with no gap) or $a \to \infty$ (parallel plates with a gap). From equations (83) and (84) we see that the values of q and T_M are either zero or infinite. Hence neither of these two conditions represents any physical problem. In problems of flow between parallel plates with a gap they should be determined from equations (100) and (101).

At last, we conclude that the complex-variable method can be adopted to studies of some forced-convection problems. In this paper few basic cases are examined. The solutions can be straightly determined from the boundary conditions. Since the problem is only the determination of some analytic functions satisfying the given boundary conditions, the method of conformal mapping is directly applicable. When conformal mapping is used, the problem is further simplified to the finding of certain mapping function. However, the required mapping functions of the problems given in this paper are usually not simple. For example, the mapping function of the interior of an ellipse onto the interior of a circle is an expression involving Jacobi's elliptical function. Hence they are lengthy and not elementary. In

forced-convection problems of some other configurations where no simple polynomial solution is obtainable, the use of conformal mapping is definitely favorable. A study in this direction is presently in progress.

Acknowledgment

This research was partially supported by the National Science Foundation through grant NSF-G10160.

References

1 S. H. Maslen, "Transverse Velocities in Fully Developed Flows," *Quarterly of Applied Mathematics*, vol. 16, 1958, pp. 173–175.

2 M. I. Muskhelishvili, "Some Basic Problems of the Mathematical Theory of Elasticity" (English translation), P. Noordhoff Limited, Groningen, Holland, 1953.

3 I. S. Sokolnikoff, "Mathematical Theory of Elasticity," McGraw-Hill Book Company, Inc., New York, N. Y., 1956.

4 S. H. Clark and W. M. Kays, "Laminar-Flow Forced Convection in Rectangular Tubes," TRANS. ASME, vol. 75, 1953, pp. 859–866.

5 S. M. Marco and L. S. Han, "A Note on Limiting Laminar Nusselt Number in Ducts With Constant Temperature Gradient by Analogy to Thin-Plate Theory," TRANS. ASME, vol. 77, 1955, pp. 625–630.

6 S. G. Mikhlin, "Integral Equations," Pergamon Press, New York, N. Y., 1957, p. 179.

7 S. Goldstein, "Modern Developments in Fluid Dynamics," Oxford University Press, London, England, vol. 2, 1938, p. 622.

Unsteady Laminar Free Convection

P. M. CHUNG

A. D. ANDERSON

Aeronautical Research Scientists, National Aeronautics and Space Administration, Ames Research Center, Moffett, Field, Calif. Assoc. Mem. ASME

The unsteady, laminar, free-convection boundary layer is analyzed with the Grashof number considered to be time-dependent through either the uniform wall temperature or the acceleration field. Two geometries are considered; the vertical plate and the horizontal circular cylinder. A set of parameters is derived through which it is possible to describe the unsteady behavior of the boundary layer. These parameters allow solutions of the pertinent differential equations to be expressed in series form and an infinite number of sets of perturbation equations result. Numerical integrations of the first few sets are shown graphically. These results enable one to visualize and to calculate, quite readily, the time-dependent deviations from the quasi-steady velocity and temperature profiles as well as the deviation in heat transfer.

Introduction

FREE CONVECTION under unsteady conditions occurs in many engineering problems. In the past, the unsteady situation has been caused by time-dependent variation of the surface or ambient temperatures only. No general solution to this problem has been obtained previously; however, a recent study for an unsteady, laminar, free-convection boundary layer over a vertical plate has been reported.[1] It was found that similarity solutions of the boundary-layer equations could be obtained only when the surface temperature varied with time and position in a few specific ways. With the current interest in space technology, a factor in addition to unsteady temperatures may become important to unsteady free convection; that is, the unsteady force field which prevails in a rocket vehicle during acceleration and deceleration.

In this paper, the behavior of the unsteady, laminar, free-convection, boundary-layer equations are analyzed for a plate located parallel to and for a circular cylinder normal to the acceleration field. The solution obtained applies when either the uniform wall temperature or the acceleration field is arbitrarily time-dependent.

Formulation of Problem

Consider a plate or circular cylinder of unsteady but uniform temperature located in a constant-property fluid of a different temperature, Fig. 1. Now consider that a uniform but time-

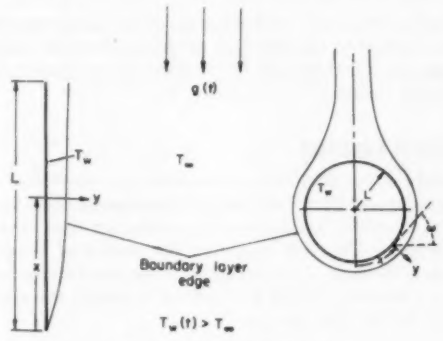

Fig. 1 Models considered

[1] K.-T. Yang, "Possible Similarity Solutions for Laminar Free Convection on Vertical Plates and Cylinders," *Journal of Applied Mechanics*, vol. 27, TRANS. ASME, Series E, vol. 82, June, 1960, pp. 230–236.

Contributed by the Heat Transfer Division and presented at the Winter Annual Meeting, New York, N. Y., November 27–December 2, 1960, of THE AMERICAN SOCIETY OF MECHANICAL ENGINEERS. Manuscript received at ASME Headquarters, August 22, 1960. Paper No. 60—WA-211.

Nomenclature

c_p = specific heat at constant pressure
F = steady-state dimensionless stream function
f = unsteady-state dimensionless stream function defined by equation (8)
f_0, f_{00}, f_1, . . . = perturbed dimensionless stream functions
g = acceleration
g_0 = standard acceleration (32.2 ft/sec²)
Gr = Grashof number, $g\Delta T\beta L^3/\nu^2$
k = thermal conductivity
L = characteristic length (Fig. 1)
Nu = Nusselt number, $q_w L/\Delta T k$
Pr = Prandtl number, $\mu c_p/k$
q_w = heat flux away from wall
T = absolute temperature
$\Delta T = T_w - T_\infty$
t = time
u = x-component of velocity
v = y-component of velocity
$X = x/L$
x = streamwise distance long body surface (Fig. 1)
$Y = y/L$
y = normal distance from body surface
β = thermal expansion coefficient
Γ = function of X in η
η = similarity variable, defined by equation (9)
Θ = steady-state dimensionless temperature
$\theta = T - T_\infty/T_w - T_\infty$
θ_0, θ_{00}, θ_1, . . . = perturbed dimensionless temperatures
μ = dynamic viscosity
ν = kinematic viscosity
$\{\xi_n\}$ = infinite set of dimensionless parameters, defined by equation (20)
Φ = function of X in f
ψ = stream function, defined by equation (5)
ω = angle of inclination of body surface with a normal to acceleration field

Subscripts

n = 0, 1, refers to order of ξ_n 2, . . .
w = wall
∞ = ambient

Superscripts

$'$ = (prime) total differentiation

dependent acceleration field is applied to the system in such a way that the direction of the force field is parallel to the plate or normal to the cylinder. The following conservation equations then describe the behavior of the unsteady, laminar, free-convection boundary layer over the surfaces:

Continuity

$$\frac{\partial u}{\partial x} + \frac{\partial v}{\partial y} = 0 \tag{1}$$

Momentum

$$\frac{\partial u}{\partial t} + u\frac{\partial u}{\partial x} + v\frac{\partial u}{\partial y} = g\Delta T\beta\theta \sin\omega + \nu\frac{\partial^2 u}{\partial y^2} \tag{2}$$

Energy

$$\frac{\partial \theta}{\partial t} + \theta\frac{\Delta T'}{\Delta T} + u\frac{\partial \theta}{\partial x} + v\frac{\partial \theta}{\partial y} = \frac{\nu}{\mathrm{Pr}}\frac{\partial^2\theta}{\partial y^2} \tag{3}$$

The boundary conditions are as follows:

$$\left.\begin{array}{ll} \text{At } y = 0 & \\ & u = v = 0 \\ & \theta = 1 \\ \text{At } y = \infty & \\ & u = 0 \\ & \theta = 0 \end{array}\right\} \tag{4}$$

The angle ω represents the inclination of the surface concerned to a plane normal to the direction of the acceleration field. The function, $\sin\omega$, is then unity for the plate and is equal to $\sin X$ for the circular cylinder.

Solution of Equations

A study of the literature on transient free convection, such as by Sugawara and Itaru,[2] showed that the response of the boundary layer to a sudden variation of the boundary conditions is extremely fast. This fact suggested the seeking of an unsteady solution in the form of perturbations to the quasi-steady solution.

First a stream function ψ is defined to satisfy the continuity equation by the relationships

$$\left.\begin{array}{l} u = \dfrac{\partial \psi}{\partial y} \\ v = -\dfrac{\partial \psi}{\partial x} \end{array}\right\} \tag{5}$$

The momentum and the energy equations (2) and (3) are now rewritten, with the aid of the stream function, as follows:

Momentum

$$\frac{\partial^2\psi}{\partial t\partial y} + \frac{\partial\psi}{\partial y}\frac{\partial^2\psi}{\partial x\partial y} - \frac{\partial\psi}{\partial x}\frac{\partial^2\psi}{\partial y^2} = g\Delta T\theta\beta\sin\omega + \nu\frac{\partial^3\psi}{\partial y^3} \tag{6}$$

Energy

$$\frac{\partial\theta}{\partial t} + \theta\frac{\Delta T'}{\Delta T} + \frac{\partial\psi}{\partial y}\frac{\partial\theta}{\partial x} - \frac{\partial\psi}{\partial x}\frac{\partial\theta}{\partial y} = \frac{\nu}{\mathrm{Pr}}\frac{\partial^2\theta}{\partial y^2} \tag{7}$$

Equations (6) and (7) will now be transformed to a pair of equations which are more suitable to the perturbation type of solution sought. A new nondimensional stream function f is first introduced, and it is, a priori, assumed to be a function of the usual steady-state similarity variable η and an infinite set of nondimensional variables $\{\xi_n(x, t)\}$, which together would express the unsteady characteristics of the boundary layer. The nondimensional temperature θ is also assumed to be a function of the same variables. Now if the transformations

$$\psi(x, y, t) \rightarrow f(\eta, \xi_0, \xi_1, \ldots \xi_n, \ldots)$$

and

$$\theta(x, y, t) \rightarrow \theta(\eta, \xi_0, \xi_1, \ldots \xi_n, \ldots)$$

are carried out in equations (6) and (7), and if the resulting equations could be made to be functions of the variables η and $\{\xi_n\}$ only, then the initial assumptions would have been proved to be self-consistent. Let the function f be related to the original stream function ψ by the equation

$$f(\eta, \xi_0, \xi_1, \ldots \xi_n, \ldots) = \frac{\psi(x, y, t)}{\nu[\mathrm{Gr}(t)]^{1/4}\Phi(X)} \tag{8}$$

Let η be defined by

$$\eta = Y[\mathrm{Gr}(t)]^{1/4}\Gamma(X) \tag{9}$$

The set $\{\xi_n\}$ and the functions Γ and Φ are left undetermined for the moment. The Grashof number

$$\mathrm{Gr}(t) = \frac{g\Delta T\beta L^3}{\nu^2}$$

is a function of time through g or T_∞ which are time-dependent.

The stream function f and the new variables yield expressions for the velocity components as

$$u = \frac{\nu}{L}\mathrm{Gr}^{1/2}\Gamma\,\Phi\frac{\partial f}{\partial\eta} \tag{10}$$

and

$$v = -\frac{\nu}{L}\mathrm{Gr}^{1/4}\left[\Phi' f + \Phi\left(\frac{\Gamma'}{\Gamma}\eta\frac{\partial f}{\partial\eta} + \sum_{n=0}^{\infty}\frac{\partial f}{\partial\xi_n}\frac{\partial\xi_n}{\partial X}\right)\right] \tag{11}$$

The momentum and the energy equations (6) and (7) are transformed to the following equations:

Momentum

$$\begin{aligned}\frac{\Phi\Gamma^3}{\sin\omega}\frac{\partial^3 f}{\partial\eta^3} + \frac{\Phi\Gamma^2\Phi'}{\sin\omega}f\frac{\partial^2 f}{\partial\eta^2} - \left[\frac{\Phi\Gamma(\Phi\Gamma' + \Gamma\Phi')}{\sin\omega}\right]\left(\frac{\partial f}{\partial\eta}\right)^2 \\ + \theta = \frac{\Phi\Gamma}{\sin\omega}\frac{L^2}{\nu}\frac{(\mathrm{Gr}^{1/4})'}{\mathrm{Gr}^{3/4}}\left(2\frac{\partial f}{\partial\eta} + \eta\frac{\partial^2 f}{\partial\eta^2}\right) \\ + \frac{\Phi\Gamma}{\sin\omega}\frac{L^2}{\nu\,\mathrm{Gr}^{1/2}}\sum_{n=0}^{\infty}\frac{\partial^2 f}{\partial\eta\partial\xi_n}\frac{\partial\xi_n}{\partial t} + \frac{\Phi^2\Gamma^2}{\sin\omega}\frac{\partial f}{\partial\eta}\sum_{n=0}^{\infty}\frac{\partial^2 f}{\partial\eta\partial\xi_n}\frac{\partial\xi_n}{\partial X} \\ - \frac{\Phi^2\Gamma^2}{\sin\omega}\frac{\partial^2 f}{\partial\eta^2}\sum_{n=0}^{\infty}\frac{\partial f}{\partial\xi_n}\frac{\partial\xi_n}{\partial X}\end{aligned} \tag{12}$$

Energy

$$\begin{aligned}\frac{1}{\mathrm{Pr}}\frac{\partial^2\theta}{\partial\eta^2} + \frac{\Phi'}{\Gamma}f\frac{\partial\theta}{\partial\eta} = \frac{\Phi\Gamma}{\sin\omega}\frac{L^2}{\nu}\frac{(\mathrm{Gr}^{1/4})'}{\mathrm{Gr}^{3/4}}\eta\frac{\partial\theta}{\partial\eta} \\ + \frac{\Phi\Gamma}{\sin\omega}\frac{L^2}{\nu\mathrm{Gr}^{1/2}}\sum_{n=0}^{\infty}\frac{\partial\theta}{\partial\xi_n}\frac{\partial\xi_n}{\partial t} + \frac{\Phi\Gamma}{\sin\omega}\frac{L^2}{\nu\mathrm{Gr}^{1/2}}\frac{\Delta T'}{\Delta T}\theta \\ + \frac{\Phi^2\Gamma^2}{\sin\omega}\frac{\partial f}{\partial\eta}\sum_{n=0}^{\infty}\frac{\partial\theta}{\partial\xi_n}\frac{\partial\xi_n}{\partial X} - \frac{\Phi^2\Gamma^2}{\sin\omega}\frac{\partial\theta}{\partial\eta}\sum_{n=0}^{\infty}\frac{\partial f}{\partial\xi_n}\frac{\partial\xi_n}{\partial X}\end{aligned} \tag{13}$$

[2] Sugao Sugawara and Michiyoshi Itaru, "The Heat Transfer by Natural Convection in the Unsteady State on a Vertical Flat Wall," *Proceedings of the First Japanese National Congress for Applied Mechanics*, 1951.

The left-hand sides of equations (12) and (13) will be in the same form as the steady-state, free-convection equations for the plate and the cylinder if a unique solution to the following set of equations can be obtained:

$$\frac{\Phi\Gamma^2}{\sin\omega} = 1 \tag{14}$$

$$\frac{\Phi\Gamma^2\Phi'}{\sin\omega} = 3 \tag{15}$$

$$\frac{\Phi^2\Gamma\Gamma'}{\sin\omega} = -1 \tag{16}$$

$$\frac{\Phi'}{\Gamma} = 3 \tag{17}$$

There are four equations for the determination of the functions Γ and Φ. When $\sin\omega$ is set to unity, it can be shown that only two of the four equations are actually independent, and thus the following unique solution of the equations are derived for the plate:

$$\Gamma = \frac{1}{2^{1/2}} X^{-1/4} \tag{18}$$

and

$$\Phi = 2^{3/2} X^{3/4} \tag{19}$$

For the circular cylinder, Hermann[3] found that an approximate but engineeringwise acceptable unique solution could be obtained except for small values of X. However, the boundary-layer assumptions themselves may be questionable for small X. It has been accepted generally that the failure to find a unique solution of equations (14) through (17) in this region will not introduce errors in the heat transfer significantly different from those already present in the boundary-layer analyses. Fig. 2 shows the values of Γ and Φ for the circular cylinder.

Now consider the right-hand side of the momentum and energy equations. A study of these equations reveals that they become functions of η and $\{\xi_n\}$ only when ξ_n is defined as

$$\xi_n = \left(\frac{L^2\Phi\Gamma}{\nu\sin\omega}\right)^{n+1} \frac{\dfrac{d^{n+1}(\mathrm{Gr}^{1/4})}{dt^{n+1}}}{\mathrm{Gr}^{(2n+3)/4}} = \left(\frac{L^2}{\nu\Gamma^2}\right)^{n+1} \frac{\dfrac{d^{n+1}(\mathrm{Gr}^{1/4})}{dt^{n+1}}}{\mathrm{Gr}^{(2n+3)/4}} \tag{20}$$

Here the Grashof number is assumed to be infinitely differentiable. This implies that either ΔT or g is infinitely differentiable with respect to time. When the wall temperature alone is unsteady, the foregoing definition of $\{\xi n\}$ and equations (14) through (17) allow equations (12) and (13) to be transformed to the following equations:

Momentum

$$\frac{\partial^3 f}{\partial\eta^3} + 3f\frac{\partial^2 f}{\partial\eta^2} - 2\left(\frac{\partial f}{\partial\eta}\right)^2 + \theta = \xi_0\left(2\frac{\partial f}{\partial\eta} + \eta\frac{\partial^2 f}{\partial\eta^2}\right) + \sum_{n=0}^{\infty}\frac{\partial^2 f}{\partial\eta\partial\xi_n}\left[\xi_{n+1} - (2n+3)\xi_0\xi_n\right] + 2\sum_{n=0}^{\infty}(n+1)\left(\frac{\partial f}{\partial\eta}\frac{\partial^2 f}{\partial\eta\partial\xi_n} - \frac{\partial^2 f}{\partial\eta^2}\frac{\partial f}{\partial\xi_n}\right)\xi_n \tag{21}$$

Energy

$$\frac{1}{\mathrm{Pr}}\frac{\partial^2\theta}{\partial\eta^2} + 3f\frac{\partial\theta}{\partial\eta} = \xi_0\left(\eta\frac{\partial\theta}{\partial\eta} + 4\theta\right) + \sum_{n=0}^{\infty}\frac{\partial\theta}{\partial\xi_n}\left[\xi_{n+1} - (2n+3)\xi_0\xi_n\right] + 2\frac{\partial f}{\partial\eta}\sum_{n=0}^{\infty}(n+1)\frac{\partial\theta}{\partial\xi_n}\xi_n - 2\frac{\partial\theta}{\partial\eta}\sum_{n=0}^{\infty}(n+1)\frac{\partial f}{\partial\xi_n}\xi_n \tag{22}$$

When the boundary layer is unsteady due to the acceleration alone, the same momentum equation (21) is valid, but the term $\theta(\Delta T'/\Delta T)$ in equation (13) is zero and the following energy equation results.

$$\frac{1}{\mathrm{Pr}}\frac{\partial^2\theta}{\partial\eta^2} + 3f\frac{\partial\theta}{\partial\eta} = \xi_0\,\eta\frac{\partial\theta}{\partial\eta} + \sum_{n=0}^{\infty}\frac{\partial\theta}{\partial\xi_n}\left[\xi_{n+1} - (2n+3)\xi_0\xi_n\right] + 2\frac{\partial f}{\partial\eta}\sum_{n=0}^{\infty}(n+1)\frac{\partial\theta}{\partial\xi_n}\xi_n - 2\frac{\partial\theta}{\partial\eta}\sum_{n=0}^{\infty}(n+1)\frac{\partial f}{\partial\xi_n}\xi_n \tag{23}$$

The boundary conditions (4) become, for both cases:

$$\left.\begin{aligned} &\text{At } \eta = 0 \\ &\qquad f = \frac{\partial f}{\partial\eta} = 0 \\ &\qquad \theta = 1 \\ &\text{At } \eta = \infty \\ &\qquad \frac{\partial f}{\partial\eta} = 0 \\ &\qquad \theta = 0 \end{aligned}\right\} \tag{24}$$

Equations (21), (22), and (23) are functions of η and $\{\xi_n\}$ only, and furthermore, $\{\xi_n\}$ is determined in terms of x and t alone by equation (20). It is now clear that the initial assumptions on f and θ, and the choice of the independent variables are self-consistent.

The transformed equations (21), (22), and (23) are solved here for f and θ by expanding them in power series of ξ_n as

$$f(\eta, \xi_0, \xi_1, \ldots, \xi_n, \ldots) = F(\eta) + \xi_0 f_0(\eta) + \xi_1 f_1(\eta) + \cdot + \xi_0^2 f_{00}(\eta) + \xi_1^2 f_{11}(\eta) + \ldots + \xi_0\xi_1 f_{01}(\eta) + \ldots \tag{25}$$

and

$$\theta(\eta, \xi_0, \xi_1, \ldots, \xi_n, \ldots)$$

[3] R. Hermann, "Heat Transfer by Free Convection From Horizontal Cylinders in Diatomic Gases," NACA TM 1366, November, 1954.

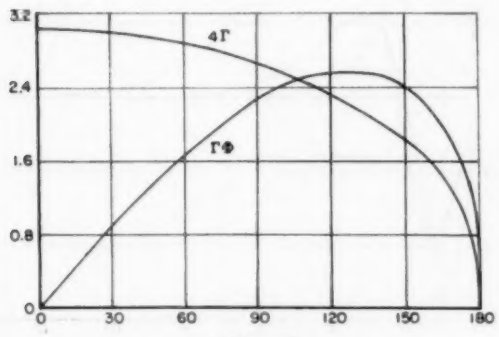

Fig. 2 Functions Γ and Φ for circular cylinders[3]

$$= \Theta(\eta) + \xi_0\theta_0(\eta) + \xi_1\theta_1(\eta) + \ldots + \xi_0^2\theta_{00}(\eta) + \xi_1^2\theta_{11}(\eta) + \ldots + \xi_0\xi_1\theta_{01}(\eta) + \ldots \quad (26)$$

When the foregoing series are substituted into equations (21) and (22) which are for unsteady wall temperature, and terms of equal order of ξ_n are collected, an infinite number of sets of equations result, the first few of which are

$$\left.\begin{aligned} F''' + 3FF'' - 2(F')^2 + \Theta &= 0 \\ \frac{1}{\mathrm{Pr}}\Theta'' + 3F\Theta' &= 0 \end{aligned}\right\} \quad (27a)$$

$$\left.\begin{aligned} f_0''' + 3Ff_0'' - 6F'f_0' + 5F''f_0 + \theta_0 &= 2F' + \eta F'' \\ \frac{1}{\mathrm{Pr}}\theta_0'' + 3F\theta_0' - 2F'\theta_0 &= (\eta - 5f_0)\Theta' + 4\Theta \end{aligned}\right\} \quad (28a)$$

$$\left.\begin{aligned} f_1''' + 3Ff_1'' - 8F'f_1' + 7F''f_1 + \theta_1 &= f_0' \\ \frac{1}{\mathrm{Pr}}\theta_1'' + 3F\theta_1' - 4F'\theta_1 &= \theta_0 - 7f_1\Theta' \end{aligned}\right\} \quad (29a)$$

$$\left.\begin{aligned} f_{00}''' + 3Ff_{00}'' - 8F'f_{00}' + 7F''f_{00} + \theta_{00} &= \eta f_0'' - f_0' + 4(f_0')^2 - 5f_0f_0'' \\ \frac{1}{\mathrm{Pr}}\theta_{00}'' + 3F\theta_{00}' - 4F'\theta_{00} &= (\eta - 5f_0)\theta_0' - 7f_{00}\Theta' + (2f_0' + 1)\theta_0 \end{aligned}\right\} \quad (30a)$$

When the acceleration field is unsteady the following first few sets result, with some of the equations being the same:

$$\left.\begin{aligned} F''' + 3FF'' - 2(F')^2 + \Theta &= 0 \\ \frac{1}{\mathrm{Pr}}\Theta'' + 3F\Theta' &= 0 \end{aligned}\right\} \quad (27b)$$

$$\left.\begin{aligned} f_0''' + 3Ff_0'' - 6F'f_0' + 5F''f_0 + \theta_0 &= 2F' + \eta F'' \\ \frac{1}{\mathrm{Pr}}\theta_0'' + 3F\theta_0' - 2F'\theta_0 &= (\eta - 5f_0)\Theta' \end{aligned}\right\} \quad (28b)$$

$$\left.\begin{aligned} f_1''' + 3Ff_1'' - 8F'f_1' + 7F''f_1 + \theta_1 &= f_0' \\ \frac{1}{\mathrm{Pr}}\theta_1'' + 3F\theta_1' - 4F'\theta_1 &= \theta_0 - 7f_1\Theta' \end{aligned}\right\} \quad (29b)$$

$$\left.\begin{aligned} f_{00}''' + 3Ff_{00}'' - 8F'f_{00}' + 7F''f_{00} + \theta_{00} &= \eta f_0'' - f_0' + 4(f_0')^2 - 5f_0f_0'' \\ \frac{1}{\mathrm{Pr}}\theta_{00}'' + 3F\theta_{00}' - 4F'\theta_{00} &= (\eta - 5f_0)\theta_0' - 7f_{00}\Theta' + (2f_0' - 3)\theta_0 \end{aligned}\right\} \quad (30b)$$

The boundary conditions are, for both cases:

$$\left.\begin{aligned} &\text{At } \eta = 0 \\ &F = F' = 0 \\ &\Theta = 1 \\ &f_0 = f_1 = f_{00} = \ldots = 0 \\ &f_0' = f_1' = f_{00}' = \ldots = 0 \\ &\theta_0 = \theta_1 = \theta_{00} = \ldots = 0 \end{aligned}\right\} \quad (31)$$

$$\left.\begin{aligned} &\text{At } \eta = \infty \\ &F' = 0 \\ &\Theta = 0 \\ &f_0' = f_1' = f_{00}' = \ldots = 0 \\ &\theta_0 = \theta_1 = \theta_{00} = \ldots = 0 \end{aligned}\right\} \quad (32)$$

The first set (27), are the well-known steady-state equations, and their solutions are found elsewhere.[4] The solutions of the sets (28), (29), and (30) are obtained in the present analysis numerically, using an IBM 704 digital computer. Figs. 3 through 6 show the solutions for Pr = 0.72.

Heat Transfer

The heat transfer to the fluid from a particular position x on the surface of the plate or the circular cylinder at a given time t is given by

$$\frac{\mathrm{Nu}(x,t)}{[\mathrm{Gr}(t)]^{1/4}} = \frac{q_w L}{\Delta T k[\mathrm{Gr}(t)]^{1/4}} = -\Gamma(X)[\Theta_w' + \xi_0\theta_{0w}' + \xi_1\theta_{1w}' + \ldots + \xi_0^2\theta_{00w}' + \ldots] \quad (33)$$

[4] E. Schmidt and W. Beckmann, "Das Temperatur- und Geschwindigkeitsfeld vor einer Wärmeabgebenden senkrechten Platte bei naturlicher Konvektion," *Technische Mechanik und Thermodynamik*, vol. 1, 1930. pp. 391–406.

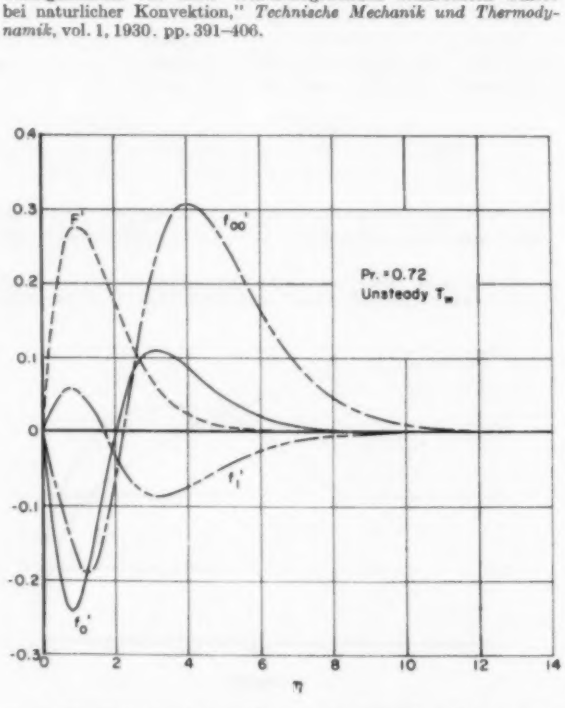

Fig. 3 Nondimensional stream functions for unsteady wall temperature

Equation (33) can be rewritten with the aid of the numerical results shown in Fig. 4 for unsteady wall temperature as

$$\frac{Nu}{Gr^{1/4}} = \Gamma(X)[0.5046 + 1.5522\xi_0 - 0.1893\xi_1 + \ldots - 0.1203\xi_0^2 + \ldots] \quad (34)$$

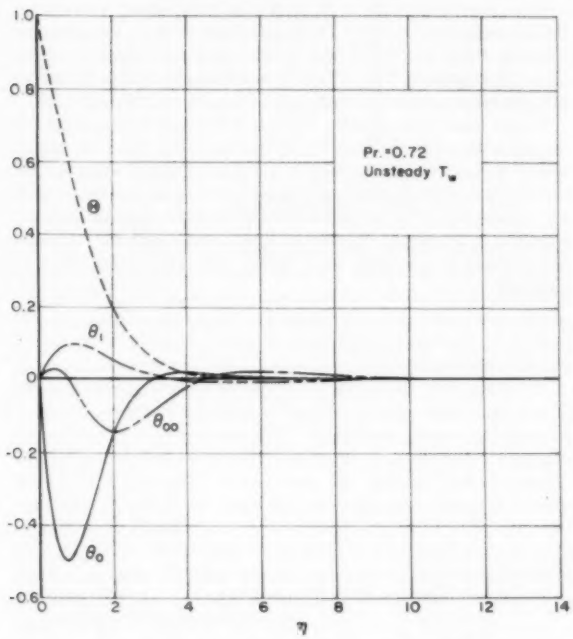

Fig. 4 Nondimensional temperatures for unsteady wall temperature

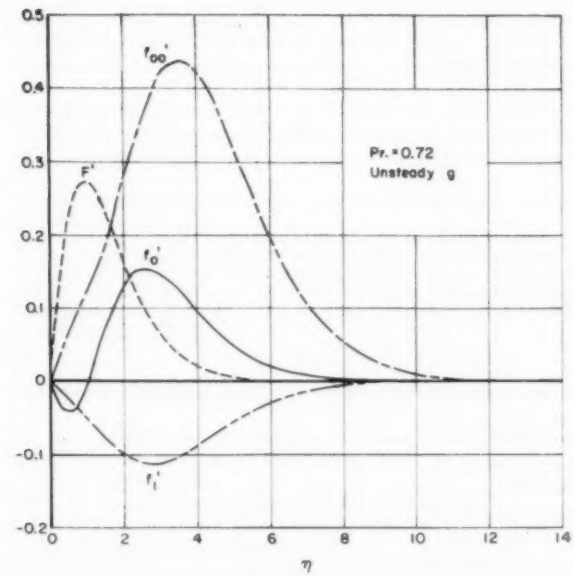

Fig. 5 Nondimensional stream functions for unsteady acceleration field

and in Fig. 6 for unsteady acceleration field as

$$\frac{Nu}{Gr^{1/4}} = \Gamma(X)[0.5046 - 0.3357\xi_0 + 0.1145\xi_1 + \ldots - 0.3671\xi_0^2 + \ldots] \quad (35)$$

The function $\Gamma(X)$ is given by equation (18) for the plate and in Fig. 2 for the circular cylinder. The set $\{\xi_n\}$ is defined by equation (20), from which ξ_0 and ξ_1 are for the unsteady-wall-temperature case

$$\xi_0 = \frac{1}{4\Gamma^2}\left(\frac{L}{\beta g}\right)^{1/2}\frac{\Delta T'}{\Delta T^{5/2}} \quad (36)$$

$$\xi_1 = \frac{1}{4\Gamma^4}\frac{L}{\beta g}\left[\frac{\Delta T''}{\Delta T^2} - \frac{3}{4}\frac{(\Delta T')^2}{\Delta T^3}\right] \quad (37)$$

and for unsteady-acceleration-field case

$$\xi_0 = \frac{1}{4\Gamma^2}\left(\frac{L}{\beta\Delta T}\right)^{1/2}\frac{g'}{g^{3/2}} \quad (38)$$

$$\xi_1 = \frac{1}{4\Gamma^4}\frac{L}{\beta\Delta T}\left[\frac{g''}{g^2} - \frac{3}{4}\frac{(g')^2}{g^3}\right] \quad (39)$$

Discussion

Consider, as an example, a case in which the uniform wall temperature or the acceleration field vary so that $Gr^{1/4}$ varies linearly with time; then $\xi_n(n > 0) = 0$. Now assume that $\xi_0 = 0.2$. From equations (34) and (35) we see that for unsteady wall temperature, the heat transfer is increased about 61 per cent from the quasi-steady value, whereas for an unsteady-acceleration field the heat transfer is decreased by about 17 per cent from the quasi-steady value. Both of these effects are, of course, brought about by the time lag of the boundary layer. In the case of the increasing ΔT (therefore increasing T_w) the average temperature in the boundary layer lags behind the increasing T_w, and the boundary layer during the transition is cooler than the temperature it would reach if the system were to reach a steady state at the increased value of T_w. Therefore the unsteady heat-transfer rate caused by an increasing T_w is greater than the instantaneous steady-state value. In the case of the increasing g, the average velocity of the

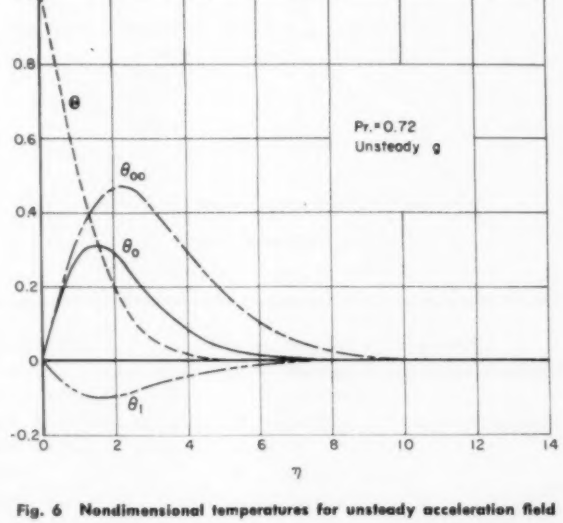

Fig. 6 Nondimensional temperatures for unsteady acceleration field

fluid in the boundary layer lags behind the value it would reach if the system were to reach a steady state at the instantaneous value of g. Thus the unsteady heat-transfer rate due to increasing g is below the instantaneous steady-state value. This shows that the cause of the variation of the Grashof number with time, as well as the magnitude of the variation, is critical in unsteady heat-transfer calculations.

The foregoing value of ξ_0 is quite realistic and occurs, for instance, in the following circumstances: On a circular cylinder of 2 in. diam at $X < 160$ deg or a flat plate at $x = 4$ in., with $\Delta T = 50$ deg R, $g = g_0$ and $\beta = 1/560$ deg R, $\xi_0 \simeq 0.2$ if, for unsteady wall temperature, $\Delta T' = 59$ deg R/sec or, for unsteady acceleration field, if $g' = 1.2\, g_0$/sec. If g were $5g_0$ in the foregoing example, then for an unsteady acceleration field $\xi_0 \simeq 0.2$ when $g' = 13\ g_0$/sec.

If ξ_0 were large, one would not expect the present method to be applicable, however, a transient analysis, for instance one similar to that of an earlier reference,[3] could probably be used.

In addition to the geometries discussed here this method may be used for any geometry for which Γ and Φ can be determined to satisfy equations (14) through (17).

Concluding Remarks

The laminar, free-convection boundary layer over a vertical plate or a horizontal cylinder was analyzed under unsteady conditions. Time variation of either the uniform wall temperature or the acceleration field was considered. The first-order deviations of the velocity and temperature profiles and the heat transfer, from the quasi-steady state, were computed for Pr = 0.72. The associated universal functions were presented graphically.

It was found that the deviations from quasi-steady state could be expressed in terms of a set of parameters $\{\xi_n(x, t)\}$ given by equation (20), of which ξ_0 and ξ_1 are specifically given by equations (36) through (39). When ξ_n is sufficiently small the actual heat transfer can be calculated from equations (34) and (35).

It was found that, for Pr = 0.72, if the wall temperature increases with time, the heat transfer is increased from the quasi-steady value, whereas the heat transfer is decreased when the acceleration field is increased with time. It was further found that for a given value of the parameter ξ_0 the heat transfer deviates from the quasi-steady value much more drastically when the wall temperature is unsteady than when the acceleration field is unsteady.

Buoyancy Effects in Forced Laminar Convection Flow Over a Horizontal Flat Plate

YASUO MORI[1]
Graduate School of Aeronautical Engineering, Cornell University, Ithaca, N. Y.

Effects of buoyancy forces in a forced laminar convection flow over a horizontal flat plate is analyzed. It is shown that the solutions may be expanded into power series in $Gr_x/Re_x^{2.5}$ whose first terms express the solution for the purely forced convection flow. A numerical example is given to show the effects of Grashof number on the velocity profile, the temperature profile, and the Nusselt number.

Introduction

HEAT-TRANSFER PROBLEMS of combined free and forced convection flow have been an attractive and important subject of investigation for several years. Combined convection flows in vertical channels have been studied by many researchers. Buoyancy effects on forced laminar convection flow have been analyzed for a flow around a vertical flat plate by Sparrow and Gregg [1][2] and for a flow in a horizontal tube by Morton [2].

Many practical applications require a very high heat flux in forced laminar convection flow. This leads to the requirement of a large temperature difference between the surface and the main flow. It might also be said that the laminar forced convection flow is one of the most fundamental and important problems in heat transfer.

The purpose of this paper is to analyze the effects of buoyancy, that is, a large Grashof number on forced laminar convective heat transfer and to find when and how the Grashof number must be taken into account in this case.

Analysis

To formulate the problem, a co-ordinate system is taken as shown in Fig. 1. We assume a steady, incompressible laminar flow with constant fluid properties. When the temperature difference between the wall and the basic flow is large, we have to take into account the effects of variations of physical properties, for instance, viscosity and thermal conductivity. However, these effects may be discussed independently of the effects of buoyancy, because as seen from the following fundamental equations, the buoyancy is not explicitly influenced by the variation of viscosity or of thermal conductivity. Therefore the variation of fluid properties is neglected in this report.

In order to formulate the boundary-layer equations, we have to discuss the order of magnitude of the quantities in the momentum equation in the vertical direction. The Navier-Stokes Equation in that direction may be expressed as

$$U\frac{\partial V}{\partial X}+V\frac{\partial V}{\partial Y}=-\frac{1}{\rho}\frac{\partial P}{\partial Y}\pm g\beta(T-T_0)+\nu\left(\frac{\partial^2 V}{\partial X^2}+\frac{\partial^2 V}{\partial Y^2}\right) \quad (1)$$

For the flow above the plate the direction of Y-axis in Fig. 1 is taken opposite to that of gravity and the positive sign in equation (1) must be used, while for the flow below the plate the negative sign is adopted by coinciding the direction of Y-axis with that of gravity. The plate temperature may be either higher or lower than that of the fluid, but we will discuss the case when $T_w > T_0$.

Assuming the Reynolds number to be sufficiently large, we can introduce the following variable according to the boundary-layer theory:

$$u=U/U_0,\quad v=V\mathrm{Re}^{+0.5}/U_0,\quad x=X/L,\quad y=Y\mathrm{Re}^{+0.5}/L,\quad p=P/\rho U_0^2 \quad (2)$$

where L is a reference length and Re and Gr are defined by

$$\mathrm{Re}=\frac{U_0 L}{\nu},\quad \mathrm{Gr}=\frac{g\beta(T_w-T_0)L^3}{\nu^2} \quad (3)$$

The order of magnitude of u, v, x, y, and p are unity.

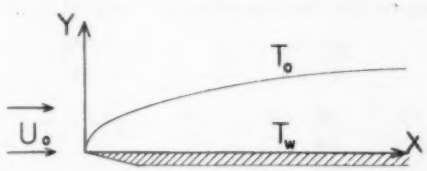

Fig. 1 Co-ordinate system

[1] Visiting Professor from Tokyo Institute of Technology, Meguro-Ku, Tokyo, Japan.

[2] Numbers in brackets designate References at end of paper.

Contributed by the Heat Transfer Division of THE AMERICAN SOCIETY OF MECHANICAL ENGINEERS and presented at the Annual Winter Meeting, New York, N. Y., November 27–December 2, 1960. Manuscript received at ASME Headquarters, August 29, 1960. Paper No. 60—WA-220.

Nomenclature

- g = gravitational acceleration
- L = reference length of the plate
- P = static pressure
- T = temperature in the boundary layer
- T_0 = temperature in the basic flow
- T_w = temperature of the surface
- U = velocity in X-direction
- U_0 = velocity in the basic flow
- V = velocity in Y-direction
- X = distance taken along the surface from the leading edge
- Y = distance taken from the surface perpendicular to it
- Gr = Grashof number
- Gr_x = local Grashof number
- Re = Reynolds number
- Re_x = local Reynolds number
- η = Blasius nondimensional similarity variable
- β = coefficient of thermal expansion
- θ = $(T-T_0)/(T_w-T_0)$
- ψ = stream function
- ρ = density
- ν = kinematic viscosity

Using the relations (2) and (3) we can deduce from equation (1) the following nondimensional equation:

$$\frac{1}{\mathrm{Re}^{0.5}}\left(u\frac{\partial v}{\partial x}+v\frac{\partial v}{\partial y}\right)=-\mathrm{Re}^{0.5}\frac{\partial p}{\partial y}\pm\frac{\mathrm{Gr}}{\mathrm{Re}^2}\theta+\frac{1}{\mathrm{Re}^{0.5}}\left(\frac{1}{\mathrm{Re}}\frac{\partial^2 v}{\partial x^2}+\frac{\partial^2 v}{\partial y^2}\right) \quad (4)$$

where θ is given by

$$\theta=(T-T_0)/(T_w-T_0) \quad (5)$$

If we restrict our discussion to the region of $\mathrm{Gr}/\mathrm{Re}^{1.5}\gg 1$, the left side of equation (4) and the terms in the parentheses on the right side of the same equation can be neglected. Therefore in this case equation (1) may be written as

$$0=-\frac{\partial P}{\partial Y}\pm\rho g\beta(T-T_0) \quad (6)$$

In addition to equation (6) the equations expressing conservation of mass, momentum, and energy for a laminar boundary-layer flow around a horizontal flat plate are

$$\frac{\partial U}{\partial X}+\frac{\partial V}{\partial Y}=0 \quad (7)$$

$$U\frac{\partial U}{\partial X}+V\frac{\partial U}{\partial Y}=-\frac{1}{\rho}\frac{\partial P}{\partial X}+\nu\frac{\partial^2 U}{\partial Y^2} \quad (8)$$

$$U\frac{\partial T}{\partial X}+V\frac{\partial T}{\partial Y}=\frac{\nu}{\mathrm{Pr}}\frac{\partial^2 T}{\partial Y^2} \quad (9)$$

where $\partial P/\partial X=0$ in a basic flow, because we are discussing a flow around a flat plate.

Differentiating equation (8) by Y and equation (6) by X, and eliminating the pressure terms from these equations, we get

$$U\frac{\partial^2 U}{\partial X\partial Y}+V\frac{\partial^2 U}{\partial Y^2}=\nu\frac{\partial^3 U}{\partial Y^3}\mp g\beta(T_w-T_0)\frac{\partial\theta}{\partial X}. \quad (10)$$

Equation (7) may be satisfied by a stream function ψ, defined by

$$U=\frac{\partial\psi}{\partial Y},\quad V=-\frac{\partial\psi}{\partial X} \quad (11)$$

Using equation (11), equations (9) and (10) may be reduced to the following two simultaneous differential equations:

$$\frac{\partial\psi}{\partial Y}\frac{\partial\theta}{\partial X}-\frac{\partial\psi}{\partial X}\frac{\partial\theta}{\partial Y}=\frac{\nu}{\mathrm{Pr}}\frac{\partial^2\theta}{\partial Y^2} \quad (12)$$

$$\frac{\partial\psi}{\partial Y}\frac{\partial^2\psi}{\partial X\partial Y^2}-\frac{\partial\psi}{\partial X}\frac{\partial^2\psi}{\partial Y^2}=\nu\frac{\partial^3\psi}{\partial Y^3}\mp g\beta(T_w-T_0)\frac{\partial\theta}{\partial X}. \quad (13)$$

Except for the last term of equation (13), equation (12) and the integrated form of equation (13) with respect to Y are the same as those for the purely forced laminar convection flow over a flat plate. Therefore as was done in Blasius' boundary-layer solution over a flat plate, we introduce the independent variable as

$$\eta=\frac{Y}{2}\sqrt{\frac{U_0}{\nu X}} \quad (14)$$

In order to find the buoyancy produced deviation from the purely forced laminar convection flow and to satisfy equations (12) and (13), we write ψ and θ as follows by assuming $AX<1$:

$$\psi=\sqrt{U_0\nu X}\,[f_0(\eta)\pm(AX)^m f_1(\eta)+(AX)^{2m}f_2(\eta)+\ldots] \quad (15)$$

$$\theta=\theta_0(\eta)\pm(AX)^m\theta_1(\eta)+(AX)^{2m}\theta_2(\eta)+\ldots \quad (16)$$

where AX is a nondimensional parameter and A is independent of η and X. The positive sign in equations (15) and (16) corresponds to the flow above the plate, while the negative to that below it. Substituting equations (15) and (16) into equations (12) and (13), the parameter AX and the power m are shown to be given by

$$AX=\frac{\mathrm{Gr}^2}{\mathrm{Re}^5}\frac{X}{L}=\frac{\mathrm{Gr}_x{}^2}{\mathrm{Re}_x{}^5},\quad m=\frac{1}{2} \quad (17)$$

In the relation (17), Gr_x and Re_x are, respectively, the local Grashof number and the local Reynolds number and are defined by

$$\mathrm{Gr}_x=\frac{g\beta(T_w-T_0)X^3}{\nu^2},\quad \mathrm{Re}_x=\frac{U_0X}{\nu} \quad (18)$$

while Gr and Re are defined by equation (3).

Substituting equations (15) and (16) into equations (12) and (13) and equating the coefficients of the like powers of AX, the following differential equations are obtained:

$$f_0''''+f_0f_0'''+f_0'f_0''=0 \quad (19)$$

$$\theta_0''+\mathrm{Pr}f_0\theta_0'=0 \quad (20)$$

$$f_1''''+f_0f_1'''+f_0''f_1'+2f_0'''f_1=8\eta\theta_0' \quad (21)$$

$$\theta_1''+\mathrm{Pr}(f_0\theta_1'-f_0'\theta_1)=-2\mathrm{Pr}f_1\theta_0' \quad (22)$$

The boundary conditions are easily obtained from the condition that at the wall surface U and V vanish and T is equal to T_w and that at infinity U tends to U_0 and T to T_0.
This leads to the following boundary conditions:

$$\text{at } \eta=0\quad f_0(0)=f_0'(0)=0,\quad \theta_0(0)=1 \quad (23)$$

$$f_1(0)=f_1'(0)=0,\quad \theta_1(0)=0 \quad (24)$$

$$\text{at } \eta\to\infty\quad f_0'(\infty)=2,\quad \theta_0(\infty)=0 \quad (25)$$

$$f_1'(\infty)=0,\quad \theta_1(\infty)=0 \quad (26)$$

. . . . . .

Integrating equations (19) and (21) to satisfy the boundary conditions, we get

$$f_0'''+f_0f_0''=0 \quad (27)$$

$$f_1'''+f_0f_1''-f_0'f_1'+2f_0''f_1=8\theta_0\eta+8\int_\eta^\infty\theta_0 d\eta. \quad (28)$$

The solution of equation (27) for the boundary conditions (23) and (25) is that obtained by Blasius. The solution of equation (20) is that of E. Pohlhausen. Equations (22) and (28) are linear ordinary equations for θ_1 and f_1 with variable coefficients. Equations (22) and (28) may be numerically integrated by the Runge-Kutta method, but for this purpose f_0, f_0', f_0'', θ_0, and θ_0' must be given to greater accuracy. The more accurate numerical solution of equation (27) than that by Blasius was reported by I. Tani [3]. Using Tani's result with six significant figures, θ_0 and θ_0' are numerically calculated for a given Prandtl number. Using f_0 and θ_0 thus obtained, the integration of equation (28) is begun from $\eta=0$ with the boundary conditions $f_1(0)=f_1'(0)=0$ and an assumed value of $f_1''(0)$. This value of $f_1''(0)$ is reassumed in such a way that the boundary condition at infinity, $f_1'(\infty)=0$, is satisfied. The same procedure is carried out for θ_1. The results for f_1 and θ_1 for Prandtl number $=0.72$ are tabulated in Table 1.

Table 1

η	f_1	f_1'	f_1''	θ_1	θ_1'
0.0	0.0000	0.0000	−6.7888	0.0000	0.7116
0.4	−0.4603	−2.0923	−3.6645	0.2796	0.6644
0.8	−1.5073	−2.9382	−0.6154	0.5025	0.4087
1.2	−2.6624	−2.6818	1.6941	0.5819	−0.0224
1.6	−3.5675	−1.7907	2.4793	0.4947	−0.3753
2.0	−4.0947	−0.8860	1.8901	0.3181	−0.4559
2.4	−4.3240	−0.3254	0.9351	0.1570	−0.3264
2.8	−4.3987	−0.0896	0.5720	0.0605	−0.1639
3.2	−4.4171	−0.0188	0.0802	0.0188	−0.0629
3.6	−4.4206	−0.0031	0.0152	0.0050	−0.0201
4.0	−4.4211	−0.0004	0.0023	0.0013	−0.0061
4.4	−4.4212	−0.0000	0.0003	0.0002	−0.0021
4.8	−4.4212	−0.0000	0.0000	0.0000	−0.0000

Results

The velocity may be calculated from the stream function. It is expressed nondimensionally as follows:

$$\frac{U(\eta)}{U_0} = \frac{f_0'(\eta)}{2} \pm \frac{f_1'(\eta)}{2} \frac{\mathrm{Gr}_x}{\mathrm{Re}_x^{2.5}} + \dots \tag{29}$$

The velocity profiles in the boundary layer above the plate for Pr = 0.72 are shown in Fig. 2 where $AX = 0$ corresponds to a Blasius flow, while those below the plate for the same Prandtl number are shown in Fig. 3.

The local shear stress τ at the plate surface may be computed from the equation (29). Denoting the local shear stress for the purely forced convection flow by τ_0, we obtain

$$\frac{\tau}{\tau_0} = 1 \pm \frac{f_1''(0)}{f_0''(0)} \frac{\mathrm{Gr}_x}{\mathrm{Re}_x^{2.5}} + \dots \tag{30}$$

In the flow above the plate for Pr = 0.72, τ vanishes when $\mathrm{Gr}_x/\mathrm{Re}_x^{2.5}$ is $-f_0''(0)/f_1''(0) = 0.195$, and the velocity profile of this limiting case is shown in Fig. 2.

The nondimensional temperature may be calculated by equation (16) and is given by

$$\theta(\eta) = \frac{T - T_0}{T_w - T_0} = \theta_0(\eta) \pm \theta_1(\eta) \frac{\mathrm{Gr}_x}{\mathrm{Re}_x^{2.5}} + \dots \tag{31}$$

This nondimensional temperature in the flow above the plate for Pr = 0.72 is shown in Fig. 4.

The ratio of the local Nusselt number Nu in the presence of buoyancy to that Nu_0 in the absence of buoyancy is obtained by using the relation (31) and Table 1 for Pr = 0.72 as follows:

$$\frac{\mathrm{Nu}}{\mathrm{Nu}_0} = 1 \pm \frac{\theta_1'(0)}{\theta_0'(0)} \frac{\mathrm{Gr}_x}{\mathrm{Re}_x^{2.5}} + \dots = 1 \mp 1.202 \frac{\mathrm{Gr}_x}{\mathrm{Re}_x^{2.5}} + \dots \tag{32}$$

This ratio is plotted with the solid line for the flow above the plate against $\mathrm{Gr}_x/\mathrm{Re}_x^{2.5}$ in Fig. 5 for Pr = 0.72 and $T_w > T_0$,

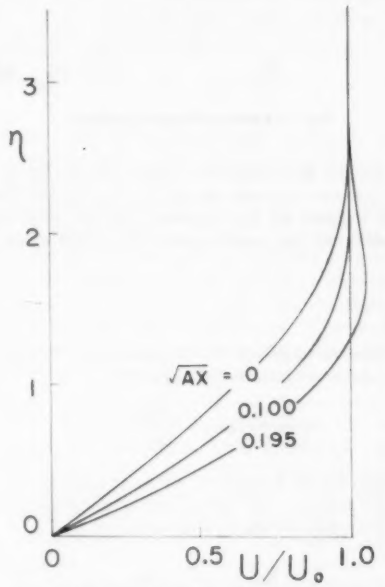

Fig. 3 Velocity profiles of the flow below the plate

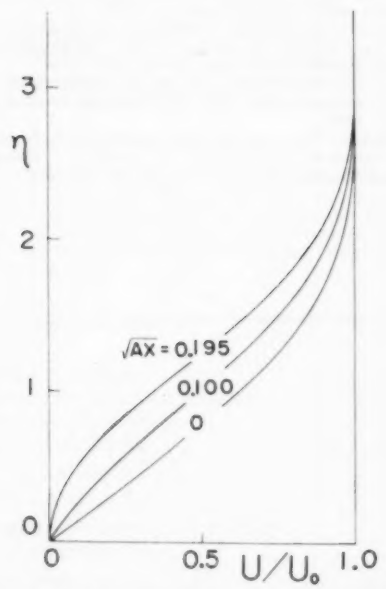

Fig. 2 Velocity profiles of the flow above the plate

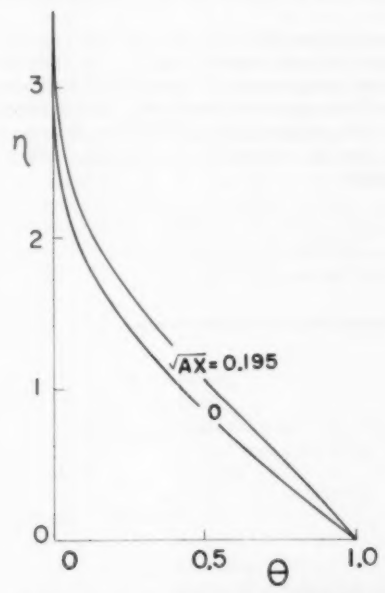

Fig. 4 Nondimensional temperature profiles of the flow above the plate

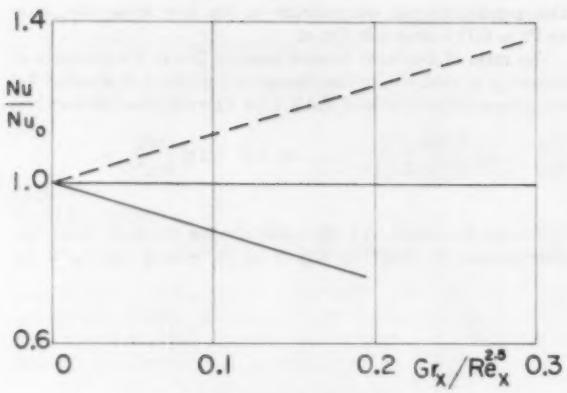

Fig. 5 Ratios of Nusselt numbers

while that for the flow below the plate is shown by the broken line. Fig. 5 shows that the transferred heat in the flow above the plate is reduced by the buoyancy effects until $Gr_x/Re_x^{2.5}$ tends toward 0.195, the point beyond which this theory cannot be applied.

Discussion

The analysis developed in the foregoing can be only applied for the flow above the plate in the region of

$$-\frac{f_0''(0)}{f_1''(0)}\,Re_x > \frac{Gr_x}{Re_x^{1.5}} > 1 \tag{33}$$

where the upper limit is required for no acceptance of a reverse flow along the surface. The lower limit permits the use of equation (6). This region for the flow below the plate is

$$Re_x > \frac{Gr_x}{Re_x^{1.5}} > 1 \tag{34}$$

and its upper limit is required for the convergence of equation (15).

The boundary-layer theory around a flat plate may be applied in the region of Reynolds number from 3×10^5 to the transition. Therefore as far as the buoyancy effect on the forced laminar convection flow is concerned, we need to take into account only the upper limit of the relation (33) or (34) since in the case when the lower limit must be considered, the buoyancy effect is completely negligible.

Other important problems in the study of buoyancy effects in forced laminar convection flow are the effects on transition and the nature of secondary flows. There is no published information concerning the effect of buoyancy upon the transition Reynolds number and Grashof number. Judging from the velocity profile shown in Fig. 2, the transition Reynolds number of the flow above the flat plate would be reduced by buoyancy when the temperature of the wall is higher than that of the fluid. However, for more precise information additional experimental or theoretical investigations are required.

Buoyancy is also considered to bring about a secondary flow as proposed by Görtler [4]; there has been no quantitative treatment about how the secondary flow affects the fundamental flow. However, additional study is also necessary concerning these effects.

Conclusion

In forced laminar boundary-layer flow over a horizontal flat plate buoyancy has been taken into account in the equation of motion in the direction perpendicular to the plate. The magnitude of the effects of buoyancy on the velocity and temperature field are shown to be proportional to $Gr_x/Re_x^{2.5}$, where Gr_x is the local Grashof number and Re_x is the local Reynolds number. When the temperature of the plate is higher than that of the fluid, it is shown that both the shear stress and the heat transfer at the surface are reduced by buoyancy in the flow above the plate, while they are increased in the flow below it.

Acknowledgment

The author is indebted to Prof. W. R. Sears and staffs of Graduate School of Aeronautical Engineering of Cornell University for their encouragement and help and grateful to Prof. B. Gebhart of School of Mechanical Engineering of the same University for his valuable advice. He also wishes to thank Mrs. Chiyoko Asano for carrying out the numerical calculations.

References

1 E. M. Sparrow and J. C. Gregg, "Buoyancy Effects in Forced-Convection Flow and Heat Transfer," *Journal of Applied Mechanics*, vol. 26, TRANS. ASME, Series E, vol. 81, 1959.

2 B. R. Morton, "Laminar Convection in Uniformly Heated Horizontal Pipes at Low Reynolds Numbers," *Quarterly Journal of Mechanics and Applied Mathematics*, vol. 12, pt. 4, 1959.

3 I. Tani, "Revised Numerical Results on Boundary Layer Along a Flat Plate," *Journal of the Aeronautical Research Institute*, University of Tokyo, 1945.

4 H. Görtler, "Über die Analogie zwischen den Instabilitäten Laminaren Grenzschichtströmungen an Konkaven Wänden und die erwärmten Wänden," *Ingenieur-Archiv*, vol. 18, 1959.

H. H. SOGIN[1]
Professor of Mechanical Engineering,
Tulane University,
New Orleans, La.
Mem. ASME

V. S. SUBRAMANIAN
Engineer,
Union Carbide of India, Ltd.,
Calcutta, India

Local Mass Transfer From Circular Cylinders in Cross Flow

This is an investigation of the distribution of the local rate of mass transfer from 4.2-in-diam naphthalene cylinders to air at ordinary temperature and pressure, flowing normal to the axis. The air speeds are near and within the critical zone of the drag. The results in the laminar region are compared with approximate boundary-layer calculations of H. Schuh and of H. J. Merk and with corresponding heat and mass-transfer experimentation in the literature. It is shown that the calculations after Merk are reliable from the point of stagnation to the predicted point of separation.

Introduction

THE CIRCULAR CYLINDER has long been a convenient model for fundamental studies in heat and mass transfer by forced convection. Yet when the literature is combed precious little definitive information remains for evaluating either experimental techniques or boundary-layer solutions. Winding and Cheney [1][2] provide a fair comparative study of experimental investigations up to 1948, notably omitting the classical work by Schmidt and Wenner [2]. A recent review has been provided by Knudsen and Katz [3]. The work of Schmidt and Wenner has been particularly important because only they included both local isothermal heat-transfer and pressure distributions. Indeed, Eckert [4] in 1942, Schuh [5] in 1953, and Merk [6] in 1959, seeking to corroborate their calculations for isothermal surfaces, used only the work of Schmidt and Wenner.

Their tests were made on three cylinders of different diameters for Reynolds numbers in the range from 8290 to 426,000. The "local" heat transfer was measured by using an electrically heated copper bar which formed a narrow segment of the cylinder wall. The procedure required that the remaining portion of the wall be kept at the same temperature as the bar; this was done by condensing steam at practically atmospheric pressure. The cylinder could be turned about its axis to any angular position. The authors' "local" determinations, in fact, amounted to average values measured along a short arc, but not sufficiently short to define the salient features of the distributions. They correlated their data on a constant-property basis, arbitrarily employing integrated mean values of the thermal conductivity and the kinematic viscosity.

Since the details of the heat transfer in the region of separation were unresolved in the experimentation and since the constant-property, boundary-layer calculations were left open to an arbitrary temperature datum, it is not surprising that differences occur between their experimental results and the theoretical results based on their pressure distributions. The present work avoids the lack of resolution and the arbitrariness of temperature datum by using the sublimation of naphthalene.

Froessling [7] introduced the technique of measuring local mass transfer with his work on small naphthalene spheres. Somewhat later [8], he completely formulated the analogical relationships between constant-property incompressible heat transfer and low-concentration incompressible mass transfer. Since that time the technique has been used to estimate mean coefficients of heat transfer in complex configurations such as packed and fluidized beds. Winding and Cheney [1], incidentally to their studies on tube banks, investigated the local mass-transfer rates from single naphthalene circular cylinders to air in normal flow at Re = 32,-800. No pressure distribution was reported, and the blockage ratio was quite high. Christian [9] measured local rates of mass transfer from the outer surfaces of hollow naphthalene cylinders in axisymmetric flow. The local rates of mass transfer were obtained by accurate determination of the changes in radius of the subliming surfaces at points along the elements of the cylinders.

In the present investigation the technique used by Christian was employed to measure the local rates of mass transfer from naphthalene cylinders to air in cross flow. The measurements were made at Reynolds number of 122,000, 218,000, and 342,000; also, at Reynolds number 218,000 a turbulence grid was employed. Pressure distributions were measured at the same values of the Reynolds number, permitting direct comparisons with the

[1] Formerly, Associate Professor of Engineering, Brown University, Providence, R. I.

[2] Numbers in brackets designate References at end of paper.

Contributed by the Heat Transfer Division and presented at the Winter Annual Meeting, New York, N. Y., November 27–December 2, 1960, of THE AMERICAN SOCIETY OF MECHANICAL ENGINEERS. Manuscript received at ASME Headquarters, August 22, 1960. Paper No. 60—WA-193.

Nomenclature

a = radius of cylinder
b = local coefficient of mass transfer
C = dimensionless coefficient
C_p = pressure coefficient
c = concentration of vapor
D = diameter of cylinder
$\mathfrak{D}$ = coefficient of diffusion of naphthalene vapor in air
$\dot{m}''$ = mass flux
Nu = Nusselt number
Pr = Prandtl number
Re = Reynolds number, UD/ν
Sc = Schmidt number, $\nu/\mathfrak{D}$
Sh = Sherwood number, $bD/\mathfrak{D}$
U = undisturbed air speed in tunnel
u, v = x, y-velocity components
x = distance from forward stagnation point along circumference of cylinder
y = distance from surface
ν = kinematic viscosity
ρ = density
τ = time
φ = angle subtended at center of cylinder, measured from stagnation point

Subscripts

i = solid
o = stagnation
s = outer edge of boundary layer
w = wall

approximate boundary-layer solutions formulated by Schuh and by Merk.

Apparatus and Procedure

The wind tunnel [10] test section was rectangular, 32 in. wide and 22 in. high. The test section was closed but the circuit was open. The cylinders were oriented vertically.

The naphthalene was cast in a mold [11] that produced a cylindrical naphthalene shell of 4.2-in. OD, 1/8-in. wall thickness, and 6-in. height. The main surfaces of the mold were lightly coated with silicone grease so that the frozen naphthalene shells could be pressed out and then off the center core. Suitable holes and passages were provided in the several parts of the mold so that they could be heated electrically and water cooled for necessary temperature regulation during the pouring and freezing processes. Three longitudinal keyways milled in the core were fitted with magnesium keys that were inserted into the mold before pouring and that became integral parts of the casting. The keys were used to mount and index the specimens on the profilometer and wind-tunnel mandrels, which had been machined with keyways to match.

In order to control the density of the solid naphthalene, the mold was filled by aspiration. For this purpose the entire mold was sealed so that it could be immersed in a hot-water bath at about 185 deg F and evacuated to a few millimeters mercury.

The density was determined by weighing the casting as soon as it was removed from the mold; it was assumed that the net volume was the volume of the cavity. The repeated measurements yielded $\rho_1 = 1.11$ g per cc, reproducible within ± 1 per cent. The specimens thus prepared appeared to retain their smoothness during exposure to the air stream. One specimen prepared without suction on the mold displayed definite effects of porosity.

The profilometer mandrel was mounted between two centers on a comparator stand. Three calibrated dial gages fixed in a row were used simultaneously to measure profiles in three planes normal to the cylinder axis, one at the center, a second 1/2 in. from one end, and the third 1/2 in. from the other end. The divisions of the gages were 0.0001 in.

The test cylinder was weighed and then measured to establish datum profiles. The cylinder was removed from the mandrel and weighed a second time before being mounted in the wind tunnel. These measurements were repeated in reverse order, at the end of the exposure, so that the local and mean coefficients could be evaluated from the difference between the initial and final determinations.

A single profile survey required about 17 min, during which time the specimen lost about one per cent of the total mass transferred during the main exposure; no correction was made for this loss.

The tunnel mandrel was assembled with the test cylinder and spacers at either end to form a continuous cylinder of 4.2-in. OD and 22-in. height. The center plane of the test cylinder was coincident with the horizontal plane of symmetry in the wind-tunnel test section.

A steel tube served as a windshield while the air was being accelerated or decelerated. The time of exposure was measured from the instant that the shield was raised to its upper position until the instant it was lowered to its protective position. An end run indicated that the transient losses were even less than the free-convection loss during the profile measurements and, therefore, no correction was applied.

During each run the dynamic head was measured by means of a static-pitot tube and the air speed was controlled. The stagnation temperature was measured at frequent intervals by means of four calibrated, shielded thermocouples and an average value was determined for the run.

Pressure Distributions

Pressure distributions are needed for the boundary-layer calculations and for applying small corrections to allow for aerodynamic heating. Also, since the drag depends primarily on the pressure distribution, it provides a means of qualitatively orienting the nature of the flow with respect to the critical Reynolds number.

For this purpose a vertical brass cylinder of the same diameter as the naphthalene model was used. Three pressure taps were located on one element of the tube so that distributions could be measured in three horizontal planes at once as the cylinder was rotated from one angular setting to another. The center tap was approximately at the center plane of the tunnel and the other two were located symmetrically 8 in. above and below.

The center-tap data have been reduced to a pressure coefficient C_p, and the results are plotted in Fig. 1. The distributions at the other two planes were nearly the same as the ones shown, the major differences occurring at the stagnation region.[5] The center-tap readings were employed to be consistent with the mass-transfer distributions determined by the center gage of the profilometer. The distributions of the local velocity u_s at the outer edge of the boundary layer were determined after Bernoulli's theorem:

$$\frac{u_s}{U} = (1 - C_p)^{1/2} \tag{1}$$

The results for the leading portions at the values of the Reynolds number used in this study are plotted in Figs. 2, 3, and 4. The lines through the experimental points are curves of the type

$$\frac{u_s}{U} = A_1 \cdot \left(\frac{x}{a}\right) - A_2 \cdot \left(\frac{x}{a}\right)^2 - A_4 \cdot \left(\frac{x}{a}\right)^4 \tag{2}$$

Table 1 lists the coefficients evaluated in this investigation and includes the ones by Hiemenz, reference [12], and by Schmidt and Wenner.

Drag coefficients are calculated according to

$$C_D = \frac{\text{drag per unit span}}{D \cdot \rho_\infty U^2/2} = \int_0^{\pi} C_p \cdot \cos\varphi \cdot d\varphi \tag{3}$$

Here frictional drag is neglected, and the mean value of C_p at each element is employed [11]. The results are plotted in Fig. 5, where they are compared with the direct measurements of Wieselsberger [13]. From the graph it is concluded that the flow at the lowest Reynolds number is subcritical while the others are in the critical zone. This is corroborated by the general form of the mass-transfer distributions, as will be seen.

The turbulence intensity ϵ is here defined to be the root-mean square of the longitudinal velocity fluctuations expressed as a percentage of the main-stream mean velocity U. It was measured[4] by means of a modified Flow Corporation constant-current

[5] In this tunnel the measured stagnation pressures on blunt models have always been found slightly lower than the main-stream total pressure measured with impact tubes. For convenience, we have referred the individual pressures to the one at the stagnation element on the models. Eckert [4], for apparently a similar reason, had to adjust the pressure distributions measured by Schmidt and Wenner; he chose to move the origin of the angular displacement about 1.5 deg. The reason for these slight differences may possibly be related to the reason why the pressure distributions around the three circumferences are not identical. For example, the differences may arise from a secondary motion due to any nonuniformity in the velocity distribution across the main stream.

[4] The authors are grateful to Prof. John Ward for these measurements.

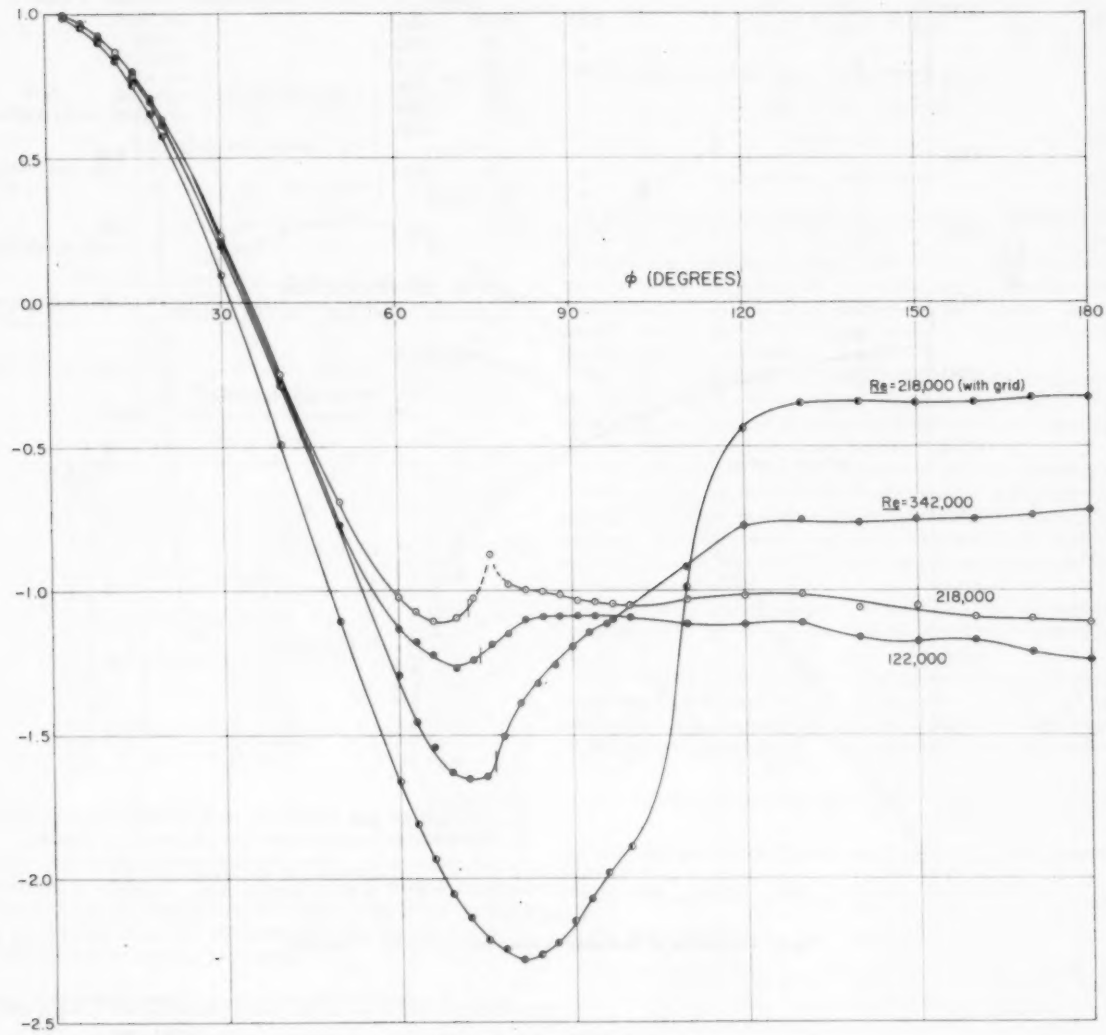

Fig. 1 Pressure distributions

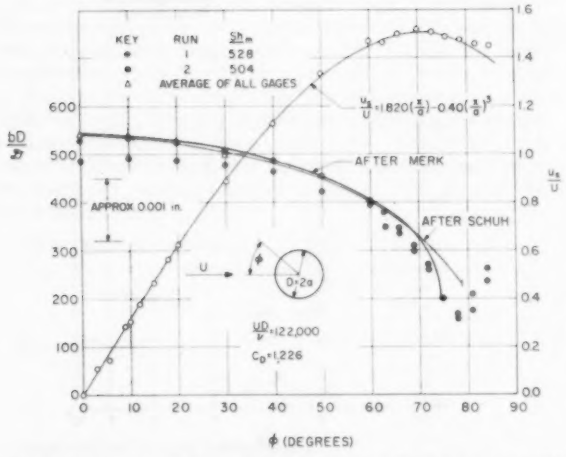

Fig. 2 Distribution of Sherwood number and u_s/U at Re = 122,000

Table 1 Coefficients A_1, A_2, and A_5 in equation (2)

Re	A_1	A_2	A_5	Investigator
18400	1.8157	0.2714	0.047325	Hiemenz [12]
122000	1.820	0.40	0.0	present work
170000	1.8155	0.4094	0.005247	from Eckert [4], after Schmidt-Wenner [2]
218000	1.826	0.43	0.0	present work
342000	1.890	0.39	0.0	present work
218000 with grid	1.9015	0.3227	−0.0062	present work

hot-wire anemometer. The results, presented in Table 2, are certainly accurate within ±10 per cent. Distances in Table 2 are referred to the cylinder axis. The grid used in this investigation is the same as the coarse one used by Kestin and Maeder [10], the one which they designated as "screen 1 at 2 ft." Its mesh was $^3/_4$ in., and the wire size 0.148 in. The distance from the cylinder axis to the screen was 24 in.

Kestin and Maeder measured the turbulence intensity at the plane of the cylinder axis. Their results are shown in Table 2 for comparison. The values for the normal stream at the lower

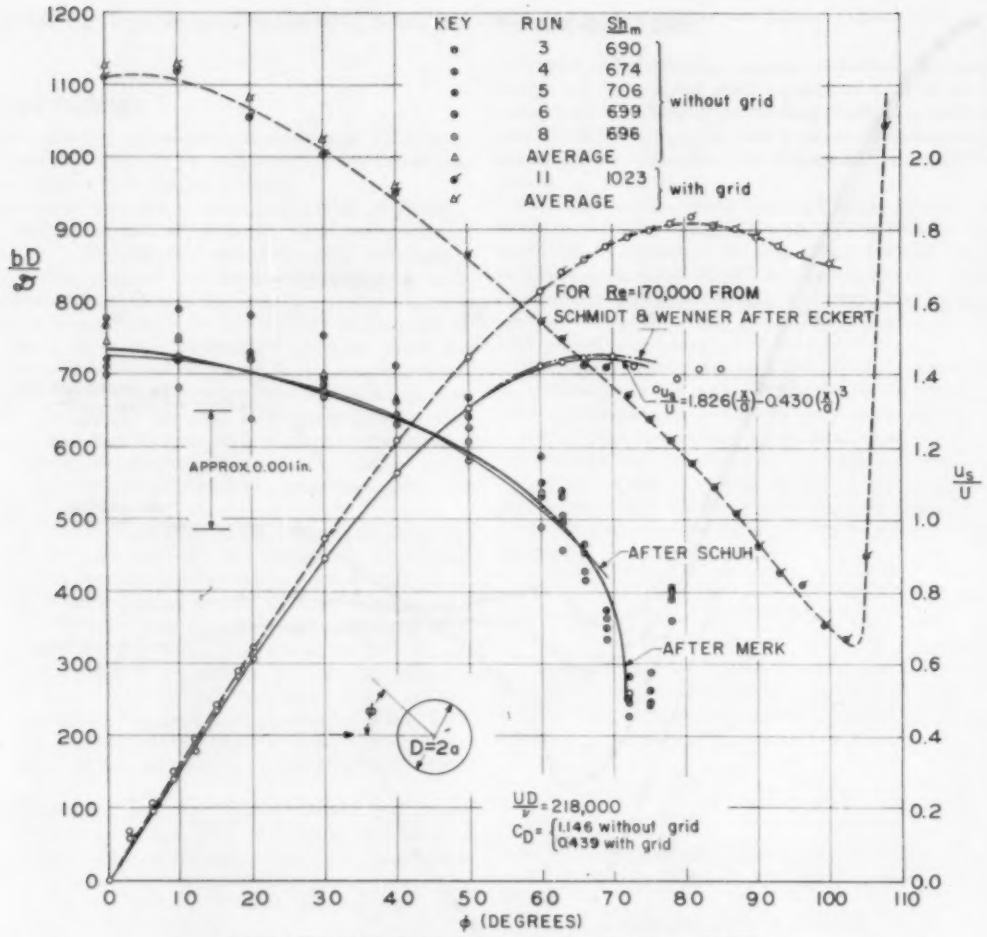

Fig. 3 Distribution of Sherwood number and u_s/U at Re = 218,000

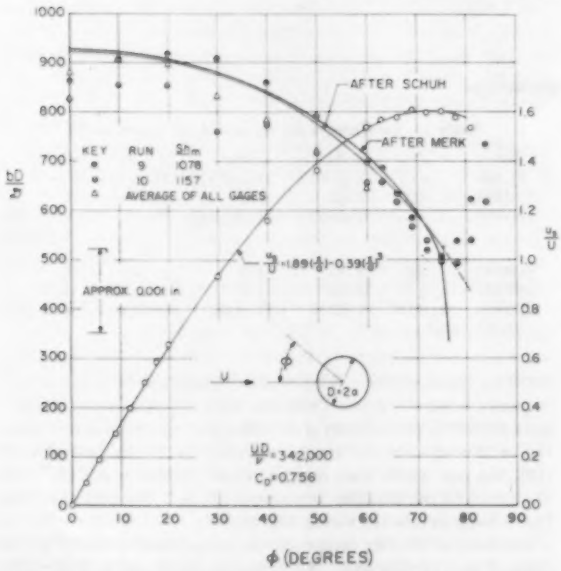

Fig. 4 Distribution of Sherwood number and u_s/U at Re = 342,000

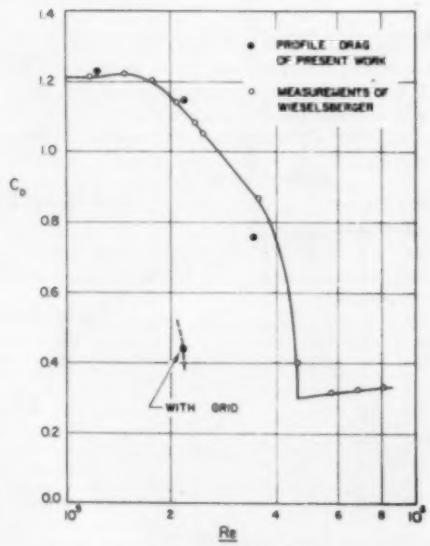

Fig. 5 Drag coefficient

Table 2 Results of measurements of turbulence intensity

Test configuration	Distance from cylinder axis to hot-wire probe, in.	Air speed, U, fps	10^{-3} Re	ϵ, per cent: Present work	ϵ, per cent: Ref. [10]
Normal tunnel (without grid)					
Empty test section	8	58	122	0.8	0.95
		104	218	0.8	0.8
		166	342	0.95	0.45
Cylinder in place	8	166	342	1.05	...
Tunnel with grid 24 in. from cylinder axis					
Empty test section	8	104	218	3.4	...
	0	104	218	2.4	1.3
Cylinder in place	8	104	218	3.7	...

Table 3 Values of E_0 in equation (13)

A	Pr = 0.71	Sc = 2.5
−0.1988	0.2939	0.418
−0.16	....	0.5454
−0.14	0.3761	0.5612
−0.10	0.3875	0.5923
0.00	0.4139	0.6444
0.1	0.4312	0.6784
0.2	0.4441	0.7006
0.3	0.4542	0.7242
0.4	0.4655	0.7428
0.5	0.4762	0.7558
0.6	0.4798	0.7701
0.8	0.4871	0.7901
1.0	0.4964	0.8080
1.2	0.5044	0.8233
1.6	0.5177	0.8480
2.0	0.5284	0.8679
2.4	0.5393	0.8849

speeds are in reasonably good agreement, but the present value at the higher speed and the one for the tunnel with the grid are nearly double the values obtained earlier. The reason for the difference is unknown. The major change of facility since the time of the earlier tests is that the wind tunnel is now enclosed by partitions. Also, the distances between the screens in the settling chamber have been increased.

Theoretical Predictions of Local Rates of Mass Transfer

The present state of knowledge permits us to make predictions only about the region of the cylinder between the points of stagnation and separation, where the flow is laminar. The diffusion of the concentration occurs in a thin region near the wall, and so the usual boundary-layer assumptions are valid. Further, the vapor concentration is less than 0.1 per cent of the air density, so that its effects on the inertia and on the kinematic viscosity of air are negligibly small. Also, the air speeds are sufficiently low so that frictional dissipation plays a minor role. Accordingly, the governing differential equations for two-dimensional, steady-state flow relate the velocity components $u(x, y)$, $v(x, y)$, and the concentration $c(x, y)$ as follows:

Conservation of momentum

$$u\frac{\partial u}{\partial x} + v\frac{\partial v}{\partial y} = u_s\frac{du_s}{dx} + \nu\frac{\partial^2 u}{\partial y^2} \tag{4}$$

Conservation of mixture

$$\frac{\partial u}{\partial x} + \frac{\partial v}{\partial y} = 0 \tag{5}$$

Conservation of naphthalene vapor

$$u\frac{\partial c}{\partial x} + v\frac{\partial c}{\partial y} = \mathfrak{D}\frac{\partial^2 c}{\partial y^2} \tag{6}$$

The boundary conditions are

$$u(x, 0) = 0;\ u(x, \infty) = u_s \tag{7}$$

$$v(x, 0) = 0 \tag{8}$$

$$c(x, 0) = c_w;\ c(x, \infty) = 0 \tag{9}$$

If the symbol c were replaced by a temperature excess and $\mathfrak{D}$ by the thermal diffusivity, the equations would formulate the corresponding problem in steady-state constant-property heat transfer at low air speeds [8]. It is for this reason that the mathematical or experimental solutions of the foregoing mass-transfer problem provide information about the heat transfer on geometrically similar surfaces.

The sublimation induces a finite blowing at the surface so that equation (8) is only approximate. However, the effect of the blowing can be disregarded here because the vapor concentration is very small compared to the air density [14].

In the experiments the concentration at the wall is virtually uniform so that an isothermally heated surface is analogically reproduced, except possibly at the highest air speeds where local frictional effects may become important. The wall concentration c_w in equation (9) is assumed to equal the saturation value at the temperature of the wall.

The function $u_s(x)$ is presumed to be known; in the present investigation it has been measured as explained in the preceding section.

When the distribution of the concentration is known, the engineer can calculate local rates of mass transfer from the wall according to Fick's fundamental equation of diffusion, which is one of the bases of equation (6). Thus the mass flux at the wall is

$$\dot{m}'' = -\mathfrak{D}\left(\frac{\partial c}{\partial y}\right)_{y=0} \tag{10}$$

For convenience, a coefficient of mass transfer b is defined according to

$$\dot{m}'' = bc_w \tag{11}$$

and by eliminating $\dot{m}''$,

$$\frac{bD}{\mathfrak{D}} = -\frac{D}{c_w}\left(\frac{\partial c}{\partial y}\right)_{y=0} \tag{12}$$

The left-hand member of this equation is called the Sherwood number and is denoted by Sh. Its role in this sort of mass transfer is completely analogous to that of the Nusselt number in heat transfer. The sublimation experiments provide values of the left-hand member of equation (12), and the solution of equations (4) to (9) yields the right-hand member.

If $u_s \sim x^m$ (m = const), then equations (4), (5), and (6) can be reduced to two ordinary differential equations, and the so-called similar or wedge solutions are obtained. Solutions of the general problem (e.g., the cylinder) are, however, far less tractable. Approximate methods have been reviewed by Seban and Chan [15], and a relatively new approach has been formulated by Merk [6].

In this investigation two approximate methods have been selected. The first, due to Schuh [5], employs the wedge solutions on the basis of a physical argument of local similarity. The second method, due to Merk [6], uses the wedge solutions of the dynamic problem in a mathematical argument leading to a series expansion in which only the first term is retained. The pertinent result of Merk's solution is briefly presented because of its simplicity and accuracy. The calculated distributions due to Schuh and Merk are then presented in conjunction with the experimental results.

Merk employs wedge solutions after Meksyn (see Merk's bibliography). The local Sherwood number is

$$\mathrm{Sh} = \frac{\left(\frac{u_s}{U}\right)}{\sqrt{2\xi}} \left(E_0 + 2\xi \frac{d\Lambda}{d\xi} E_1 + \ldots\right) \sqrt{\mathrm{Re}} \qquad (13)$$

where

$$\xi = \int_0^x \frac{u_s}{U} \frac{dx}{L} \qquad (14)$$

The quantities E_0 and E_1 are functions of the Schmidt number and the "wedge variable"

$$\Lambda = \frac{2\xi}{(u_s/U)^2} \frac{d(u_s/U)}{d(x/D)} \qquad (15)$$

The function E_0 for Sc = 0.71 and 2.5 is presented in Table 3. The two-dimensional stagnation value corresponds to $\Lambda = 1$, and the separation value to $\Lambda = -0.1988$. Values of E_1 are unavailable. Terms beyond the first in equation (13) are relatively small if ξ and/or $d\Lambda/d\xi$ are small. In neglecting them, Merk calls the approximation "Meksyn's wedge method." Until E_1 is tabulated, experimentation must determine whether the first term suffices. In any case, the solution is in exact agreement with any of the well-known solutions for the stagnation region.

Merk was unable to reach conclusions about the reliability of his solution, particularly in the neighborhood of separation, where there were neither exact solutions of the general problem nor reliable data.

Reduction of Experimental Data

From the initial and final profile measurements, the distributions of the depth sublimed have been calculated. A representative set of data for one test at 104 fps is shown in Fig. 6. Averaging the measurements from the three gages, as was done originally [11], generally distorts the salient features of the distributions and, therefore, all the results have been calculated from the measurements made only with the center gage, except as noted in the figures.

Since the profiles are symmetrical with respect to the plane of symmetry through the cylinder axis, the data are reduced using the averages of the two measurements at $\pm\varphi$, and henceforth the profile measurements are referred to those averages.

The local Sherwood number has been calculated in accordance with its operational definition, i.e., equations (11) and (12), as follows:

$$\mathrm{Sh} = \frac{\Delta y}{\Delta \tau} \cdot \frac{D}{\nu} \cdot \mathrm{Sc} \cdot \frac{\rho_i}{c_w} \qquad (16)$$

The kinematic viscosity is evaluated at the pressure and temperature of the air in the wind-tunnel test section after [16]. The vapor at the wall is assumed to be a thermally perfect gas in equilibrium with the solid at the wall temperature and the concentration c_w is evaluated as in [17]. Local corrections for sublimation cooling and aerodynamic heating, which were usually less than 3 per cent, were evaluated similarly as in [18].

Mean Sherwood numbers, presented in Figs. 2, 3, and 4 are based on averages of the weight measurements and on the concentration of the vapor saturated at the stagnation temperature. But these should be regarded as only approximately equal to the values that would be obtained by integrating the curves depicted in the graphs, for they represent only the center distributions and include the local corrections. The actual differences are about 6 per cent.

Results

Since the laminar region is of particular interest with regard to the boundary-layer predictions, attention is mainly directed toward the upstream distributions. These results are further compared with those of other local measurements in the literature.

The individual distributions of Sherwood number on the forward surface of the cylinder are shown in Figs. 2, 3, and 4 for the Reynolds number 122,000, 218,000, and 342,000, respectively. Shown in each graph are the empirical curve representing u_s/U, and two solid curves representing the results of the mass-transfer calculations, using Sc = 2.5, after the approximate methods of Schuh and of Merk.

At any location, the spread of the data obtained from repeated tests at the same Reynolds number falls within 0.001 in., as can be seen by comparison with the distances marked "Approx. 0.001 in." The systematic displacement of the data indicates that additional controls have to be established to govern the air flow and its temperature and to maintain each specimen in a rigid form. Thus the naphthalene cylinders might best have been cast on a structural sleeve at the expense of the over-all weight measurements. Also, a modification of the profilometer to

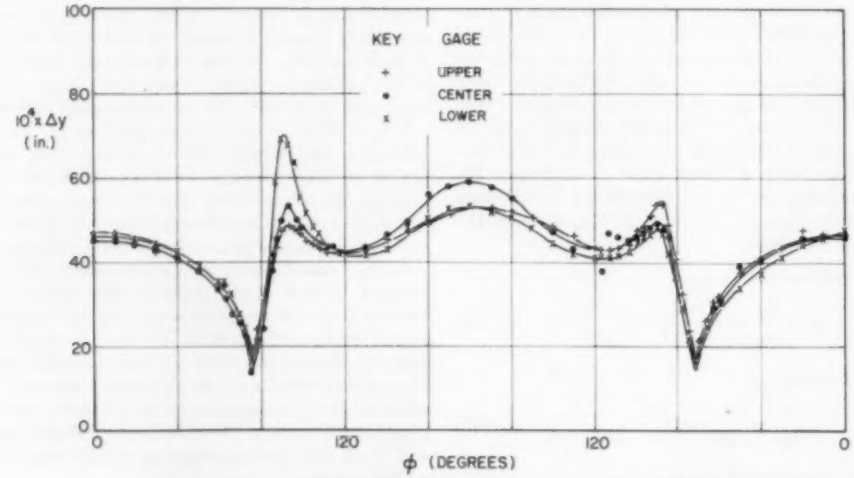

Fig. 6 Representative set of data from the three gages (U = 104 fps)

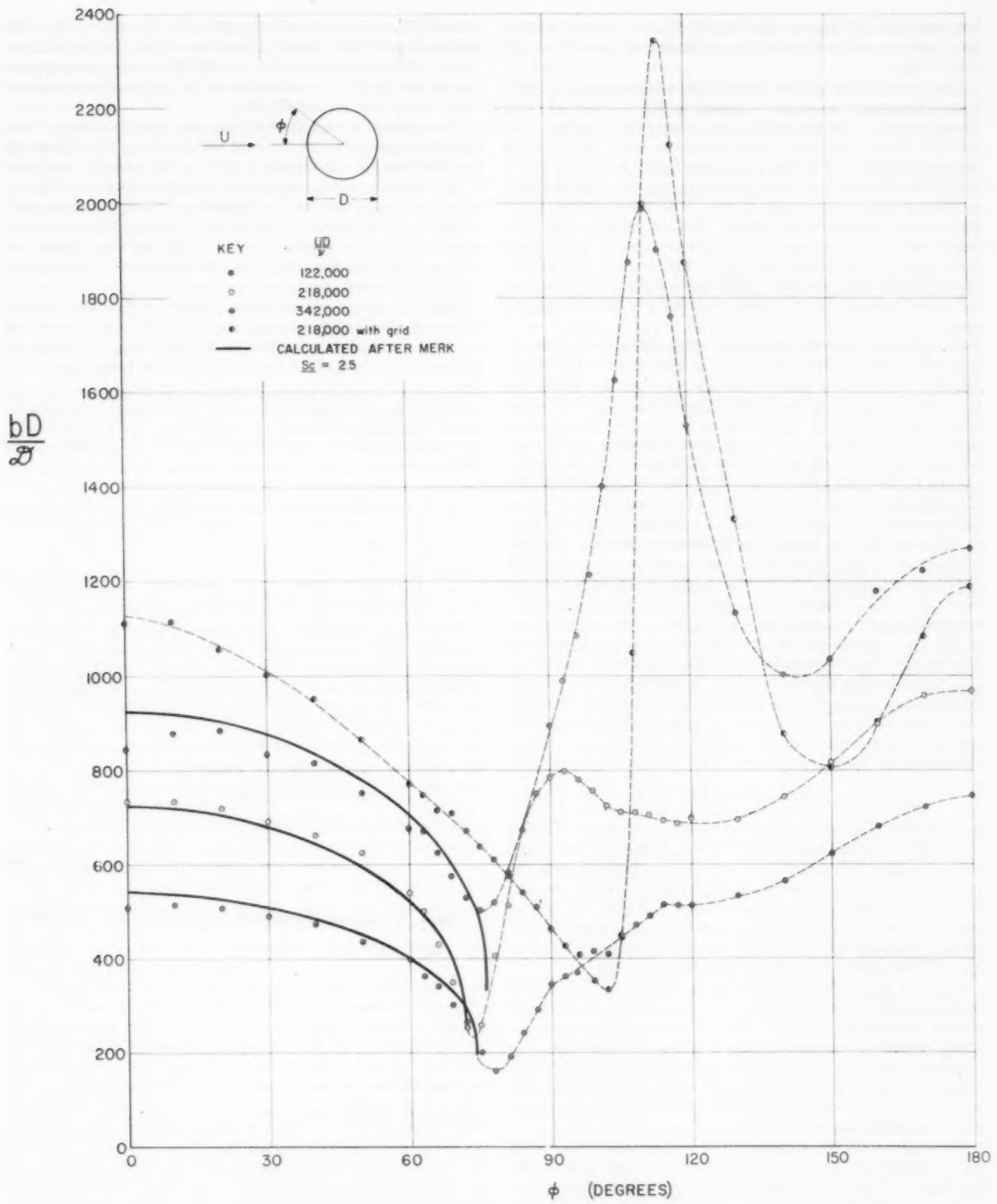

Fig. 7 Average center-gage values of Sherwood number

allow for the hardness (i.e., softness) of the naphthalene and its response to the bearing pressure exerted by the spindle of the dial gage may be needed.

The extremes of the data at any location are systematically about 6 per cent above and below the mean values of the center gage results. Within these margins the results are significant, and conclusions may be drawn from them.

With regard to Figs. 2, 3, and 4, the two calculated distributions of the mass transfer are in excellent agreement with each other, except near separation. In general, Merk's curve falls abruptly,

terminates several degrees upstream of Schuh's point of separation, and agrees favorably with the experimental points over the entire range.

The mean values of the center-gage measurements at each Reynolds number have been plotted in Fig. 7 together with Merk's curves. On the whole, the experimental results corroborate Merk's solution. Two exceptions occur at Reynolds number 342,000: (*a*) At the stagnation region the experimental values consistently rise with increasing angular displacement, reaching a maximum at about 20 deg. This trend remains unexplained and requires further study. (*b*) The values of the Sherwood number at the minimum point are considerably higher than those predicted by Merk's solution. This is further evidence, besides the low drag coefficient, that the boundary layer enters a transition just ahead of the theoretical point of laminar separation.

The effects of the turbulence grid, which changed the intensity from 0.8 to 2.4 per cent, are shown in Figs. 3 and 7 for Re = 218,000. The ratio of the sublimation rate with the grid to the rate without the grid is about 1.5 and nearly uniform in the range of φ from 0 to 60 deg. The ratio of Zapp's [19] heat-transfer data at Re = 110,000 for a change of turbulence intensity from 0.9 to 3.0 per cent follows a similar trend down to φ = 60 deg, but the ratio is only about 1.33. In a more extensive investigation involving the effects of turbulence produced by grids, Seban [20] measured local heat transfer on cylinders of uniform flux. He observed that the stagnation values increased from 25 to 47 per cent at the stagnation region but found no correlation with turbulence intensity for the grids he employed. He observed the ratio 1.47 at Re = 225,000 with a grid of $^1/_8$-in. mesh, which gave a turbulence intensity of 2.6 per cent. There appears to be neither an adequate explanation nor satisfactory correlation of these results to this date. In general, it can be said of Fig. 7 that the solid lines represent regions where our rationale is excellent while the regions subtended by the dashed lines require further study.

In order to bring the results of different investigations in proximity where they can be readily compared, a correlating equation of the form

$$\mathrm{Sh} = C\,\mathrm{Re}^{n}\,\mathrm{Sc}^{m} \qquad (17)$$

is employed. Values of m, usually found empirically, are about $^1/_3$. However, from his analysis of the stagnation point heat transfer Squire [12] found $m \approx 0.4$. In the present work the value 0.4 has been used, and the results at Re = 218,000 (without the grid) have been replotted accordingly, in Fig. 8. The closed points represent the mean values of the center gage, and the vertical bars represent the extremes of the individual distributions in Fig. 3. The solid line is Merk's curve for Sc = 2.5.

The flow characteristics in the experiments of Schmidt and Wenner at Re = 170,000 are quite comparable to those of the present investigation at Re = 218,000, as can be seen by comparing the two distributions of u_s/U in Fig. 3. The difference is undiscernible in the results calculated on the basis of each distribution using Merk's method at Pr = 0.7, and the predicted separation point is identical. These calculated results are represented by the dashed line in Fig. 8.

The original experimental points of Schmidt and Wenner at Re = 170,000 are represented in Fig. 8 by the open points with the flags. In correlating their data Schmidt and Wenner employed the integrated mean values of the kinematic viscosity and the thermal conductivity over the temperature range of their tests. Their experimental points have been recorrelated as suggested by Sogin [21] who compared experimental results on steam-heated plates and naphthalene disks: The density was evaluated at the main-stream temperature, and the dynamic viscosity and the thermal conductivity of the air were evaluated at the mean film temperature $(t_w + t_s)/2$. The modified results of Schmidt and Wenner are represented by the open circles without the flags.[8] They are 10 per cent lower than the original ones.

The modified heat-transfer points, the mean mass-transfer points, and the two theoretical curves are in excellent agreement in the range of φ from 0 to 70 deg.

The region of φ from 70 to 80 deg was unresolved in the heat-transfer experiments on account of the finite circumferential length of the electric heating element. The heat-transfer point at φ = 80 deg may belong to the transition branch of the distribution; it appears too far downstream to be associated with separation predicted from the velocity distribution of Schmidt and Wenner. The experimental value of the mass transfer at separation is quite remarkable by comparison and illustrates the resolution that can be achieved.

Distributions for rather extreme values of Reynolds number in the subcritical range are compared in Fig. 9. The curve is the result of calculations after Merk's solution using Sc = 2.5 and the distribution of u_s/U at Re = 122,000 of the present investiga-

[8] The new value of the Reynolds number is 194,000; but the nominal value of 170,000 is retained in the discussion to avoid confusion. Henceforth, the nominal Reynolds number from the literature is used in referring to all the heat-transfer results discussed in this paper.

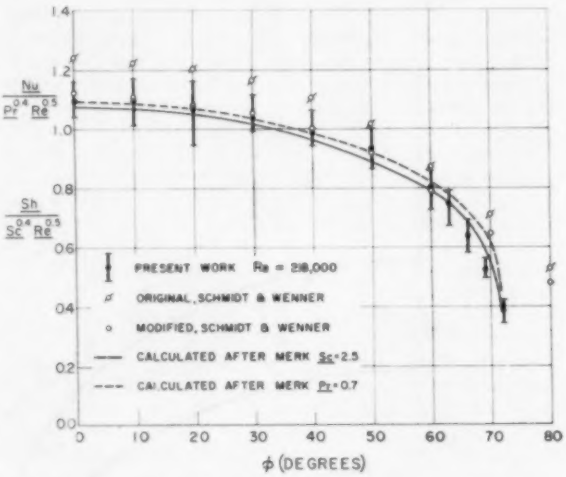

Fig. 8 Comparison of mass and heat transfer at Re = 218,000

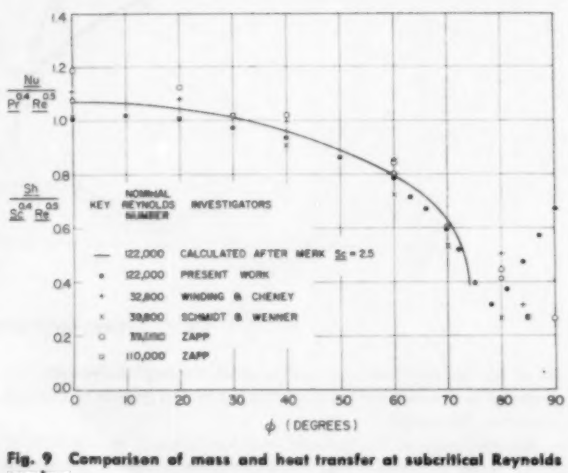

Fig. 9 Comparison of mass and heat transfer at subcritical Reynolds numbers

tion. By comparison with Fig. 8, Merk's curve for Pr = 0.7 would be slightly higher. The mean values of the sublimation experiments at Re = 122,000 are mapped from Fig. 7. Also, the mass-transfer distribution of Winding and Cheney at Re = 32,800 is shown. The heat-transfer distributions in Fig. 9 have been modified for property values as explained with reference to the work of Schmidt and Wenner in Fig. 8. The turbulence intensity in Zapp's experiments was 0.9 per cent; also, that of Schmidt and Wenner has been estimated at 0.9 per cent [10].

In summary, Figs. 8 and 9 are evidence that Merk's solution represents the experimental results almost within the accuracy with which they have been obtained. At separation the results of the present work follow the trend of Merk's predictions while the results of the other investigations lack resolution.

There is still no adequate analysis for the distribution beyond the separation point. P. D. Richardson [22] examined data in the literature and correlated heat and mass transfer at the rear stagnation region by means of equation (17) with $n = 2/3$ and $m = 1/3$. The value of C, however, was found to depend on the blockage ratio, and therefore, in this region it becomes rather difficult to compare results from different investigations on an absolute basis. This difficulty probably will remain until the nature of the flow at the rear interface is better understood.

The general features of the mass-transfer distributions between separation and the rear stagnation region are the same as those found by Schmidt and Wenner for heat transfer.

Conclusions

The present status of the art of the experimental technique using naphthalene to measure local coefficients yields distributions that are smooth but systematically and slightly displaced from each other in repeated tests. The exact reasons for the departures are still unknown, but some additional controls that may improve the reproducibility have been suggested. Since the measurements provide details that are rarely achieved by other techniques used in comparable problems and since the averages are in excellent agreement with the boundary-layer theory, the authors are of the opinion that the present results and the technique itself serve a useful purpose.

The effect of a turbulence grid which changed the intensity from 0.8 to 2.4 per cent was to increase the mass transfer in the laminar region nearly 50 per cent.

The theoretical and experimental results for heat and mass transfer in the laminar range can be put in proximity for practical purposes if it is assumed that the Sherwood and Nusselt numbers vary with the 0.4 power of the Schmidt and Prandtl numbers, respectively.

Laminar heat-transfer results in the literature can be well correlated with constant property theory if the mass velocity of the main stream is used in the Reynolds number, and if the dynamic viscosity in the Reynolds number and the thermal conductivity in the Nusselt number are evaluated at the mean film temperature. This scheme has yet to be checked against a solution based on variable property theory.

The results of the approximate methods of Schuh and of Merk for Sc = 2.5 are in satisfactory agreement down to $\varphi = 60$ deg, but Schuh's curve predicts values that are too high in the apparent region of separation. The results of Merk's solution and of the present experimentation agree satisfactorily in the entire region from stagnation to predicted separation. In general, Merk's solution is highly recommended for both its rapidity and its accuracy.

Acknowledgment

This research was supported by the United States Air Force under Contract No. AF 49(638)-46, and monitored by the Air Force Office of Scientific Research of the Air Research and Development Command.

The authors are grateful to Messrs. Vernon Goff, George Pierce, and Mrs. Ruth J. Sogin, for their various contributions in constructing the apparatus, making the specimens, and reducing the data.

The present paper is based on AFOSR Technical Report 60-78/I, which contains most of the details.

References

1 C. C. Winding and A. J. Cheney, Jr., "Mass and Heat Transfer in Tube Banks," *Industrial and Engineering Chemistry*, vol. 40, 1948, p. 1087.

2 E. Schmidt and K. Wenner, "Wärmeabgabe über den Umfang eines angeblasenen geheizten Zylinders," *Forschung auf dem Gebiete des Ingenieurwesens*, vol. 12, 1941, p. 65. Translation: NACA TM 1050, 1943.

3 J. G. Knudsen and D. L. Katz, "Fluid Dynamics and Heat Transfer," McGraw-Hill Book Company, Inc., New York, N. Y., 1958.

4 E. R. G. Eckert, "Die Berechnung des Wärmeübergangs in der laminaren Grenzschicht umströmter Körper," *Forschung auf dem Gebiete des Ingenieurwesens*, vol. 13, 1942, Fh. 416B.

5 H. Schuh, "A New Method for Calculating Laminar Heat Transfer on Cylinders of Arbitrary Cross Section and on Bodies of Revolution at Constant and Variable Wall Temperature," Stockholm Tekniska Hogskolan Flygtekniska Institutionen, Technical Note 33, 1953.

6 H. J. Merk, "Rapid Calculations for Boundary-Layer Transfer Using Wedge Solutions and Asymptotic Expansions," *Journal of Fluid Mechanics*, vol. 5, 1959, p. 460.

7 N. Froessling, "Über die Verdunstung fallender Tropfen," *Gerlands Beiträge zur Geophysik*, vol. 52, 1938, p. 170.

8 N. Froessling, "Verdunstung, Wärmeübergang, und Geschwindigkeitsverteilung bei zweidimensionaler und rotationssymmetrischer laminarer Grenzschichtströmung," Lunds Universitets Arskrift, N. F. Avd. 2, Band 36, Nr. 4 Kungl. Fysiografiska Sallskapets Handlingar, N. F. Band 51, Nr. 4, 1940.

9 W. J. Christian, "Mass Transfer From Sharp-Edged Cylinders in Axisymmetric Flow," PhD thesis, Illinois Institute of Technology, 1957.

10 J. Kestin and P. F. Maeder, "Influence of Turbulence on Transfer of Heat From Cylinders," NACA TN 4018, 1957.

11 V. S. Subramanian, "Mass Transfer From a Circular Cylinder to Air in Normal Flow," MS thesis, Brown University, 1959.

12 S. Goldstein, "Modern Developments in Fluid Mechanics," vol. I and II, Oxford University Press, London, England, 1938.

13 C. Wieselsberger and A. Betz, "Ergebnisse der Aerodynamischen Versuchsanstalt zu Göttingen," II Lieferung, published by Oldenbourg, Muenchen, Germany, 1923, p. 23.

14 H. H. Sogin and R. J. Goldstein, "Turbulent Transfer From Isothermal Spanwise Strips on a Flat Plate," AFOSR Technical Note, prepared under Contract No. AF 49(638)-46.

15 R. A. Seban and H. W. Chan, "Heat Transfer to Boundary Layers With Pressure Gradients," WADC Technical Report 57-111, 1957, (ASTIA AD 118075).

16 J. Hilsenrath, et al., "Tables of Thermal Properties of Gases," NBS Circular 564, 1955.

17 H. H. Sogin, "Laminar Transfer From Isothermal Spanwise Strips on a Flat Plate," JOURNAL OF HEAT TRANSFER, TRANS. ASME, Series C, vol. 82, 1960, p. 53.

18 S-Y. Ko and H. H. Sogin, "Laminar Mass and Heat Transfer From Ellipsoidal Surfaces of Fineness Ratio 4 in Axisymmetrical Flow," TRANS. ASME, vol. 80, 1958, p. 387.

19 G. M. Zapp, "The Effect of Turbulence on Local Heat Transfer Coefficients Around a Cylinder to an Air Stream," MS thesis, Oregon State College, 1950.

20 R. A. Seban, "The Effect of Free Stream Turbulence on the Heat Transfer From Cylinders," WADC Technical Report 57-480 (ASTIA AD 155766).

21 H. H. Sogin, "Sublimation From Disks to Air Streams Flowing Normal to Their Surfaces," TRANS. ASME, vol. 80, 1958, p. 61.

22 P. D. Richardson, "Estimation of the Heat Transfer From the Rear of an Immersed Body to the Region of Separated Flow," WADD Technical Note 59-1, 1960.

DISCUSSION

James G. Knudsen[6]

The authors are to be commended for the research described in this paper. Their work adds considerably to our knowledge of mass transfer from cylinders as well as substantiating previous heat and mass-transfer studies on this system. The technique of using a volatile material such as naphthalene is a good one, and as the authors indicate, has the advantage of permitting determination of true local coefficients. It was used very successfully by Schnautz,[7] who determined local mass-transfer coefficients on flat plates, cylinders, and spheres at various turbulence levels.

The authors have also shown the effect of main-stream turbulence, but as yet no correlation is proposed to account for this variable in a quantitative manner. It is to be hoped that efforts will continue in this direction.

The authors correlate their data with the equation

$$Sh = CRe^{n}Sc^{m}$$

The exponents n and m are open to question. At a constant Reynolds number, taking $m = 1/3$ rather than 0.4, results in a somewhat better agreement between heat and mass-transfer data. It also appears that the exponent on the Reynolds number ($n = 0.5$) does not adequately correlate the data. Fig. 10 shows some mass-transfer data obtained by Schnautz at a turbulence level of 1 per cent at Reynolds numbers between 97,000 and 44,000. A definite variation with Reynolds number is still evident since Schmidt number is constant. The same trend appears in the authors' data when Figs. 8 and 9 are compared.

The writer questions if the authors' data in Fig. 8 at a Reynolds number of 218,000 might not be affected by the fact that transition appears to be occurring on the cylinder. Fig. 7 shows a rapid rise in the mass-transfer coefficient at about $\phi = 80$ deg. This is typical of what occurs with laminar to turbulent transition in the boundary layer on the cylinder. The authors' Fig. 5 definitely shows the Reynolds number to be in the initial part of the critical region even without the grid in the air stream.

A problem of interest to the writer is one of the analogy between mass, heat, and momentum transfer. Have the authors compared average j-factors for their cylinder with average values of the local friction coefficient normally reported in the literature?

[6] Assistant Dean of Engineering, Oregon State College, Corvallis, Ore.

[7] J. A. Schnautz, "Effect of Turbulence Intensity on Mass Transfer From Plates, Cylinders, and Spheres in Air Streams," PhD thesis, Oregon State College, June, 1958. Available on microfilm from University Microfilms, Ann Arbor, Mich.

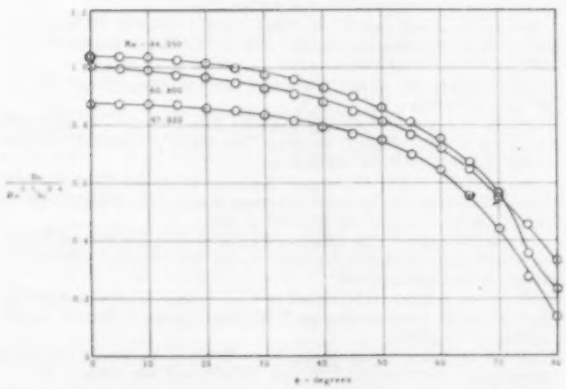

Fig. 10 Schnautz's data for transfer of naphthalene from a cylinder to air in cross flow

R. A. Seban[8]

These results show, for the region in which laminar flow occurs on the cylinders, the expected correlation of the mass-transfer coefficients with heat-transfer coefficients, provided, of course, that the distributions of the free stream velocity are the same for the systems for which the comparison is made. The possibility of predicting the mass transfer is therefore also anticipated, for there exist numerous examples in which various methods of prediction have been shown to forecast successfully the heat transfer on the front of a circular cylinder, and the rather general success is due to the relative simplicity of the velocity distribution, which departs significantly from the stagnation-flow situation only for $\phi > 40$ deg. Two of these methods are illustrated in the paper and demonstrate real success in giving even fine detail about the local variation of the heat-transfer coefficient near the separation point.

Those of the present results obtained downstream of the screen have been indicated to be of the same order as similar heat-transfer results given in the authors' reference [20], and indeed the correspondence is remarkably close to that shown in greater detail by Seban.[9] There, as in the present results, is shown the reduced effect of the increased turbulence level as the acceleration of the free stream diminishes, and the apparent retardation of separation to a rearward position characteristic of super critical flow. Near the end of the region there is evidence of a transition to turbulent flow in the rapid increase in the heat-transfer coefficient.

A rapid increase in the local heat-transfer coefficient is shown also in the results for a Reynolds number of 3.42×10^5, without the screen, but the form of the pressure coefficient is so altered in this case as to perhaps make plausible the assumption of a separation bubble between about 80 and 110 deg. Viewed in this way, the less rapid rise in the heat-transfer coefficient in this region is of the nature of coefficients which have been found to be typical of separated regions. Thus the maxima in the heat-transfer coefficients, occurring near 110 deg in Fig. 7, might be due to different hydrodynamic conditions.

Authors' Closure

We are grateful to Dr. Knudsen for his contribution and questions and to Dr. Seban for his elucidation of the results in the regions of transition and separation.

No comparisons of the sort that Dr. Knudsen mentions in his last question were made. We respond to his remarks on exponents m and n.

In correlating the experimental data we were guided by the theory. The recommended $m = 0.4$ focuses on the stagnation point and interpolates E_0 in the range $0.7 < Pr < 2.5$ more satisfactorily than $m = 1/3$. Compare the last three columns in the following tabulation for $A = 1$.

Pr	$E_0(Pr)$	$E_0(Pr)/E_0(1)$	$Pr^{0.4}$	$Pr^{1/3}$
0.71	0.4964	0.873	0.872	0.892
1.00	0.5689	1.000	1.000	1.000
2.50	0.8080	1.420	1.443	1.358

Figs. 8 and 9 indicate that Merk's solution adequately describes the heat and mass transfer in the idealized conditions of flow for which it is intended. The deviations must be ascribed to the effects of second order variables which the current theory ignores. In regarding deviations of the exponent n from the theoretical value, 0.5, it is best to compare results within in-

[8] University of California, Berkeley, Calif. Mem. ASME.

[9] R. A. Seban, "The Influence of Free Stream Turbulence on the Local Heat Transfer From Cylinders," JOURNAL OF HEAT TRANSFER, TRANS. ASME, Series C, vol. 82, 1960, pp. 101–107.

dividual investigations; for second order variables are usually under better control in a single investigation than they are in several. From this viewpoint, Schnautz's data, which we see here for the first time, compound the mystery surrounding exponent n. For while they indicate $n < 0.5$ and the data herein reported fairly show $n = 0.5$, other evidence gathered by the senior author shows $n > 0.5$:

First,[10] on a heated 4.2-in-diam cylinder in the Brown tunnel, the stagnation-point value of $\mathrm{Nu}/\sqrt{\mathrm{Re}}$ increased 10 per cent as Re was changed from 130,000 to 260,000, even though the distribution of the pressure coefficient in this region changed hardly at all and the mainstream turbulence intensity reportedly diminished. And second,[11] on a heated 6.73-in-wide flat-plate strip facing the stream, distributions shown in Fig. 11 were obtained. The distribution of the pressure coefficient on the forward surface, virtually independent of Re and of the grid, could be well represented by

$$\frac{u_e}{U} = \frac{1.2(x/L)}{\sqrt{1 - 3(x/L)^2}} \quad (0 \leq |x/L| \leq 0.4) \tag{18}$$

Hence, after Merk,

$$\frac{\mathrm{Nu}}{\sqrt{\mathrm{Re}}} = \frac{0.134(x/L)[4.96 + (x/L)^2]}{\sqrt{\{[1 - 3(x/L)^2]\,[1 - \sqrt{1 - 3(x/L)^2}]\}}} \tag{19}$$

Clearly, the measured stagnation-point heat transfer increases from 15 to 40 per cent above the theory as Re increases from 122,000 to 331,000; the grid adds another 50 per cent. The second order effects are relatively large in this harsh, very blunt, configuration.

Thus we agree with Dr. Knudsen that equation (17) is not entirely satisfactory. The theory needs refinement, possibly to account for the time-dependent disturbances in regions of accelerating flow as outlined, for example, in [10]. In this connection, Dr. Seban's observation of "the reduced effect of the increased turbulence level as the acceleration of the free stream diminishes" should not be regarded as a broad generalization since there is a reduced effect on the flat-plate strip, also, as the acceleration of the free stream *increases*. These observations indicate that we ought to further examine the causes and effects of disturbances upstream, in the retarded, unstable, and unsteady flow that surrounds the idealized stagnation-point streamline whence the boundary layer and the free stream draw their sustenance.

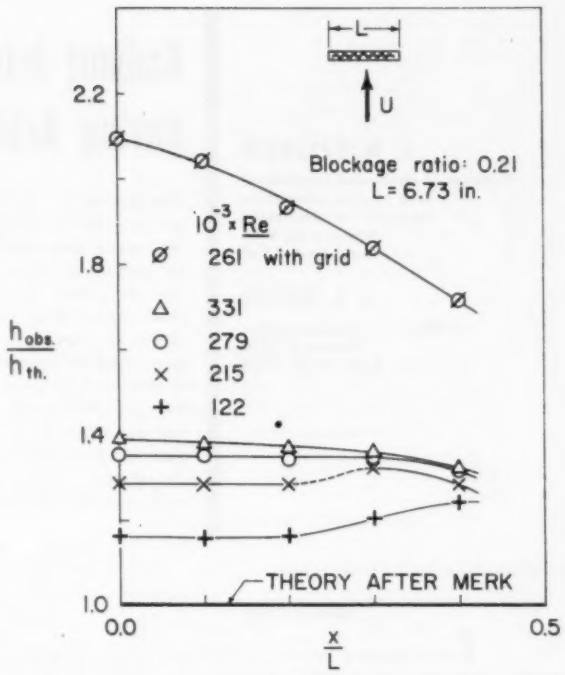

Fig. 11

[10] J. Kestin, P. F. Maeder, and H. H. Sogin, "The Influence of Turbulence on the Transfer of Heat to Cylinders Near the Stagnation Point," submitted for publication.

[11] H. H. Sogin, Kurt Burkhard, and P. D. Richardson, "Heat Transfer in Separated Flows," ARL Tech. Rept. No. 4, Contract No. AF 33(616)-5756, July, 1960.

Radiant Interchange Between Circular Disks Having Arbitrarily Different Temperatures[1]

E. M. SPARROW
Professor of Mechanical Engineering, Heat Transfer Laboratory, University of Minnesota, Minneapolis, Minn.
Assoc. Mem. ASME

J. L. GREGG
NASA Lewis Research Center, Cleveland, Ohio.
Assoc. Mem. ASME

The problem of radiant heat transfer between parallel disks has been analyzed by generalizing the standard gray-body enclosure theory. In particular, the assumption that the radiant flux leaving a surface and the local heat flux are uniformly distributed over the surface has been lifted by an integral equation formulation. It has been shown that the general problem of disks at arbitrarily different temperatures can be conveniently broken down into two subproblems, each of which can be solved independently of the temperature level. Numerical solutions of the governing integral equations have been carried out for spacing ratios h/R (h = spacing, R = disk radius) ranging from 5.0 to 0.05 and for emissivities ranging from 0.1 to 0.9. Local heat-transfer results have been presented which, depending on spacing and emissivity, display marked variations over the disk surface. Over-all heat-transfer results have been calculated and compared with the predictions of the standard simplified enclosure theory. These predictions of the simplified theory were found to be unexpectedly good, especially in view of the large surface variations of the local heat transfer.

Introduction

Considerable practical interest in radiation heat transfer has been stimulated by space vehicle applications, both in connection with the disposal of waste heat and with the collection of solar energy. Along with these new applications, there has arisen a motivation to re-evaluate and refine the calculation procedures which are commonly used to determine the radiant interchange between surfaces. In addition, there is a need for radiant heat-transfer information on a number of basic geometrical configurations.

In calculating the heat radiation between surfaces, the first thought is to use the standard gray-body enclosure theory as set forth by Eckert and Drake [1],[2] pp. 408–412, or by Hottel [2], pp. 72–76. The recommending feature of this procedure is that the desired results may be obtained by dealing with nothing more complicated than a set of linear algebraic equations. One of the assumptions implicit in this treatment[3] is that for any given surface in the enclosure, the radiant energy leaving the surface and the heat flux are uniform over that surface. Except for very open geometrical configurations, it is expected that this assumption would be violated since the radiant incidence can vary substantially over the surface, with corresponding surface variations in the reflected energy. There thus arise questions as to the accuracy of the results thus obtained. In addition, such a calculation cannot provide the sometimes-needed information on the local heat transfer at various positions on a surface. To generalize the formulation by including the details of variations over the surface involves the use of integral equations rather than algebraic equations.

In a previous study [3], the radiant interchange in some simple gray-body systems was analyzed using the integral equation formulation. Consideration was directed to systems made up of pairs of rectangular surfaces, with each rectangle having *one* dimension of *infinite* extent. For the situation where both surfaces are maintained at the same uniform temperature, it was found that large nonuniformities in incident radiation and local heat flux could occur as the spacing between the surfaces diminished. The over-all heat loss obtained from these solutions was compared with the predictions of the simple analysis based on uniform

[1] The research reported here was supported in part by National Science Foundation grant G10177.

[2] Numbers in brackets designate References at end of paper.

Contributed by the Heat Transfer Division and presented at the Winter Annual Meeting, New York, N. Y., November 27–December 2, 1960, of The American Society of Mechanical Engineers. Manuscript received at ASME Headquarters, July 11, 1960. Paper No. 60—WA-75.

[3] For a fuller discussion of the other simplifying assumptions, see reference [3].

Nomenclature

- A = surface area
- B = combined radiant flux (emitted plus reflected) leaving a position per unit time and area; radiosity
- F = angle factor
- H = radiant energy incident on a position per unit time and area
- h = spacing between disks
- Q = over-all net heat loss rate from a disk surface
- q = local net heat loss rate per unit area
- r = radial co-ordinate
- R = disk radius
- T = absolute temperature
- T^* = reduced temperature, $[T_2^4 - T_1^4]^{1/4}$
- x = dimensionless radial co-ordinate, r/R
- α = gray-body absorptivity
- β = dimensionless radiosity, $B/\epsilon\sigma T^4$
- γ = spacing ratio, h/R
- ϵ = gray-body emissivity
- ρ = gray-body reflectivity
- σ = Boltzmann's constant

Subscripts

- 1 = disk 1
- 2 = disk 2

Superscripts

- a = subproblem (a): both disks at temperature T_1
- b = subproblem (b): disk 1 at zero temp, disk 2 at temp T^*

radiation conditions. It was found that in spite of the large local variations, the over-all heat transfer predicted by the simple theory was surprisingly accurate. Only for low emissivity surfaces and close spacings were there substantial deviations. These findings have practical implications. Reference [3] also provided heat-transfer data which can be applied to specific situations (e.g., the upper limit of the heat transfer for longitudinal radiating fins).

In the present study, consideration is given to a somewhat more general situation than that analyzed in reference [3]. Attention will be directed to *finite* surfaces rather than semi-infinite surfaces, and the temperatures of the radiating surfaces are allowed to be arbitrarily different. The specific system chosen for study is a pair of parallel circular disks as shown in Fig. 1. The surfaces are diffuse gray-body emitters and reflectors which may have different temperatures T_1 and T_2. Both surfaces have the same emissivity value ϵ. Radiant energy is exchanged between the disks, and in addition, radiation may escape to the environment. In the main body of the analysis, radiation inward from the environment will not be considered; but as shown at the end, this can always be added into the solution since the problem is linear. The problem is formulated in terms of integral equations taking into account the variation of the radiation over the surface. The governing equations are solved for a range of spacing to radius ratios h/R extending from 5.0 to 0.05 for emissivities of 0.1, 0.5, and 0.9. The solutions yield the net local heat transfer as a function of position on the disk surface. Over-all heat loss values are computed and compared with those of the simple theory in order to determine if the findings of reference [3] also apply to finite geometries. The specific heat-transfer results have application in space vehicle radiators and sun shields, etc., as well as to other branches of technology. For instance, for a set of circumferential fins whose tip radius is much larger than that of the base surface cylinder, the present results provide an upper bound for the heat loss.

Analysis

The Radiation Balance Equation. The equations governing the radiant interchange between the surfaces may be derived using the same general approach which was employed in reference [1] (pp. 416–418) and in reference [3]. Attention is directed to an elementary annular ring at r_1 on disk 1 (see Fig. 1). The radiant energy leaving such an elementary area is composed of two parts: A direct emission; and a reflection of the incident radiation. The energy emitted per unit area is given by $\epsilon\sigma T^4$. Next, denoting the incident energy per unit area by H, the reflected energy is simply ρH. With these, the combined radiant flux B—often called the radiosity—leaving the elementary ring per unit area is

$$B_1(r_1) = \epsilon\sigma T_1^4 + \rho H_1(r_1) \tag{1}$$

In writing this expression, we attach subscripts 1 to B and H in order to indicate that reference is being made to disk 1. Further cognizance is taken of the fact that B_1 and H_1 are functions of radial position r_1. The temperature T_1 is taken to be independent of position; but in general, prescribed variations of the surface temperature can also be included.

As it stands, equation (1) contains two unknowns, B_1 and H_1. So, additional relationships are required. It is easy to see that the energy H_1 which is incident on the ring at r_1 is related to the energy which leaves the surface of the other disk. Following the same line of reasoning as in reference [3], equations (2)–(3), an expression for H_1 in terms of the radiosity distribution on disk 2 is found to be

$$H_1(r_1) = \int_{r_2=0}^{r_2=R} B_2(r_2) F_{dr_1-dr_2} \tag{2}$$

where $F_{dr_1-dr_2}$ is the angle factor appropriate to a system of two

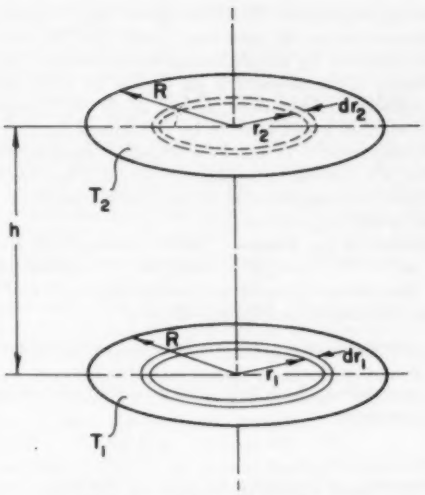

Fig. 1 Parallel disk configuration

elementary rings. Finally, introducing this into the radiation balance (1) leads to

$$B_1(r_1) = \epsilon\sigma T_1^4 + \rho \int_{r_2=0}^{r_2=R} B_2(r_2) F_{dr_1-dr_2} \tag{3}$$

Equation (3) remains incomplete until the angle factor $F_{dr_1-dr_2}$ has been evaluated. The most direct way of determining the angle factor is to start with the basic definition (e.g., equation (14-6), reference [1]) and *integrate* over the appropriate angles. However, such an integration can prove to be quite difficult. It is equally satisfactory and much easier to find $F_{dr_1-dr_2}$ by *differentiating* the angle factor which appears in the literature for finite disks, reference [4], equation (31–45). The detailed manipulations are given in the Appendix and only the end results are used here. However, it may be pointed out that this type of short-cut can be used in other problems and is worth remembering.

Taking the angle factor $F_{dr_1-dr_2}$ from equation (36) and substituting in equation (3) provides the following relationship between the radiosities $B_1(r_1)$ and $B_2(r_2)$:

$$B_1(r_1) = \epsilon\sigma T_1^4 + (1-\epsilon) \int_0^R B_2(r_2) \frac{2h^4 + 2h^2r_1^2 + 2h^2r_2^2}{[(h^2 + r_1^2 + r_1^2)^2 - 4r_1^2r_2^2]^{3/2}} r_2 dr_2 \tag{4}$$

where the reflectivity ρ has been replaced by $1 - \epsilon$. The spacing between the disks is denoted by h. Equation (4) has been derived by starting with an elementary area on disk 1 and writing a radiation balance equation. A second equation can be derived by starting with an element on disk 2, and by following the same steps, there is obtained

$$B_2(r_2) = \epsilon\sigma T_2^4 + (1-\epsilon) \int_0^R B_1(r_1) \frac{2h^4 + 2h^2r_1^2 + 2h^2r_2^2}{[(h^2 + r_1^2 + r_2^2)^2 - 4r_1^2r_2^2]^{3/2}} r_1 dr_1 \tag{5}$$

Taken together, equations (4) and (5) constitute a simultaneous system for determining the unknown radiosities B_1 and B_2 as a function of the co-ordinates r_1 and r_2. Since the unknowns appear under the integral signs as well as in other parts of the equations, (4) and (5) are called integral equations.

Although the radiosity B is of interest from the viewpoint of pyrometry, it is the *heat transfer* which is the quantity of greatest

engineering importance. It will be shown later that once the distributions of B_1 and B_2 have been found, then the heat transfer can be computed by simple arithmetic operations. So, the determination of the radiosity is the key to the entire problem.

By inspection of equations (4) and (5), it might appear that a specific solution would have to be determined for every specific pair of temperatures T_1 and T_2 which might be of interest. Fortunately, it is possible to rephrase the problem in a manner which eliminates the dependence on the specific temperatures. It is to this task which we now turn.

Subdivision of the Problem. Since equations (4) and (5) are linear in T^4, it is possible to subdivide the general problem in which the surfaces have different temperatures T_1 and T_2 ($T_2 > T_1$) into two simpler problems as follows:

(a) A situation where the two disks have the same temperature T_1.

(b) A situation where disk 1 has zero temperature and disk 2 has temperature

$$T^* = [T_2^4 - T_1^4]^{1/4}. \tag{6}$$

The summing of problems (a) and (b) precisely describes the general problem.

We can now specialize equations (4) and (5) to apply to the subproblems. For problem (a), there is no distinction between surface 1 and surface 2, and so

$$B_1(r_1) = B_2(r_2) = B^a(r), \qquad \text{when } r_1 = r_2 \tag{7}$$

where we use the superscript a to denote problem (a). There is thus only one unknown, and either of equations (4) or (5) can be reduced to

$$\beta^a(x_1) = 1 + 2(1-\epsilon)\gamma^2 \int_0^1 \beta^a(x_2) \frac{\gamma^2 + x_1^2 + x_2^2}{[(\gamma^2 + x_1^2 + x_2^2)^2 - 4x_1^2x_2^2]^{3/2}} x_2 dx_2 \tag{8}$$

where

$$\beta^a = B^a/\epsilon\sigma T_1^4, \qquad x = r/R, \qquad \gamma = h/R \tag{9}$$

It is interesting to note that the use of dimensionless variables has completely removed the temperature from the problem and has consolidated the effects of spacing and disk size into a single parameter γ.

Turning next to problem (b), it is clear that because of the inequality in disk temperatures, the radiosities B_1 and B_2 will not be equal. Replacing T_1 by zero, T_2 by T^*, and introducing the superscript b, the governing equation as specialized from (4) and (5) is

$$\left.\begin{aligned} \beta_1^b(x_1) &= 2(1-\epsilon)\gamma^2 \int_0^1 \beta_2^b(x_2) \frac{\gamma^2 + x_1^2 + x_2^2}{[(\gamma^2 + x_1^2 + x_2^2)^2 - 4x_1^2x_2^2]^{3/2}} x_2 dx_2 \\ \beta_2^b(x_2) &= 1 + 2(1-\epsilon)\gamma^2 \int_0^1 \beta_1^b(x_1) \frac{\gamma^2 + x_1^2 + x_2^2}{[(\gamma^2 + x_1^2 + x_2^2)^2 - 4x_1^2x_2^2]^{3/2}} x_1 dx_1 \end{aligned}\right\} \tag{10}$$

where

$$\beta^b = B^b/\epsilon\sigma T^{*4} \tag{11}$$

Once again, the explicit temperatures have been eliminated by the introduction of dimensionless radiosities β_1^b and β_2^b.

To recapitulate, the solution of equation (8) gives the radiosity distribution for the problem of two disks at the same temperature; while equations (10) provide the radiosities for the situation where disk 1 is at zero temperature and disk 2 is at some temperature different from zero. Once the solutions for the subproblems have been found, the radiosities for the general problem of two disks at different temperatures T_1 and T_2 may be found by simple addition as follows

$$B_1(r_1) = B^a(r_1) + B_1^b(r_1) = \epsilon\sigma[T_1^4\beta^a(x_1) + T^{*4}\beta_1^b(x_1)] \tag{12}$$

$$B_2(r_2) = B^a(r_2) + B_2^b(r_2) = \epsilon\sigma[T_1^4\beta^a(x_2) + T^{*4}\beta_2^b(x_2)] \tag{13}$$

where

$$T^* = [T_2^4 - T_1^4]^{1/4}$$

Next, we want to relate the radiosities to the heat transfer.

Heat Flux Formulas. The *net* local heat loss per unit area from any location on the disk surface is found as the difference between the leaving radiant flux (radiosity) B and the incident flux H, i.e.,

$$q = B - H \tag{14}$$

or equivalently, as the difference between the emitted and the absorbed energy, i.e.,

$$q = \epsilon\sigma T^4 - \alpha H \tag{15}$$

The heat transfer arises both from radiant interchange between the disks and from energy which escapes from the enclosure into the environment. The incident flux H may be eliminated from either of these expressions by utilizing equation (1), giving

$$q = \frac{\epsilon}{1-\epsilon}[\sigma T^4 - B] \tag{16}$$

For typical positions r_1 and r_2 on surfaces 1 and 2, equation (16) may be written as

$$q_1(r_1) = \frac{\epsilon}{1-\epsilon}[\sigma T_1^4 - B_1(r_1)]$$

$$q_2(r_2) = \frac{\epsilon}{1-\epsilon}[\sigma T_2^4 - B_2(r_2)] \tag{17}$$

So, from equations (17), it is clear that the local heat flux is immediately determined once radiosities B_1 and B_2 have been found.

It is useful to rephrase the local heat-flux expressions in terms of the results of the subproblems (a) and (b). For problem (a), where both disks are at the same uniform temperature T_1, it follows that $q_1^a(r_1) = q_2^a(r_2) = q^a(r)$ when $r_1 = r_2$, and so

$$\frac{q^a(r)}{\epsilon\sigma T_1^4} = \frac{1 - \epsilon\beta^a(r)}{1-\epsilon} \tag{18}$$

Equation (18) compares the net local heat loss with the energy emitted per unit area. If only a single disk were present, then the ratio represented by equation (18) would be unity. So, the departure from the unity gives the effect of the second disk in reducing the heat transfer. Since the problem of two disks at the same temperature is of itself of considerable interest, the heat-transfer results furnished by equation (18) have their own utility apart from any use we will make of them in connection with the general problem of disks at different temperature.

Next, turning to problem (b), the expressions for the local heat flux appropriate to typical positions on disks 1 and 2 are found by specializing equations (17) as follows:

$$q_1^b(r_1) = -\frac{\epsilon}{1-\epsilon}B_1^b(r_1), \qquad \text{or} \qquad \frac{q_1^b(r_1)}{\epsilon\sigma T^{*4}} = -\frac{\epsilon}{1-\epsilon}\beta_1^b(r_1) \tag{19a}$$

$$q_2^b(r_2) = \frac{\epsilon}{1-\epsilon}\,[\sigma T^{*4} - B_2^b(r_2)], \quad \text{or} \quad \frac{q_2^b(r_2)}{\epsilon\sigma T^{*4}} = \frac{1-\epsilon\beta_2^b(r_2)}{1-\epsilon} \tag{19b}$$

Since the temperature of disk 1 in problem (*b*) is zero, there will be absorption of energy without emission and, consequently, $q_1^b < 0$.

With the heat flux expressions for the subproblems at hand, we may return to the general problem of disks at different temperatures. Utilizing equations (12), (13), (18), and (19) successively, the heat flux expressions (17) for the general problem become

$$q_1(r_1) = q^a(r_1) + q_1^b(r_1), \qquad q_2(r_2) = q^a(r_2) + q_2^b(r_2) \tag{20a}$$

or

$$\left.\begin{aligned} q_1(r_1) &= \left[\frac{q^a(r_1)}{\epsilon\sigma T_1^4}\right]\epsilon\sigma T_1^4 + \left[\frac{q_1^b(r_1)}{\epsilon\sigma T^{*4}}\right]\epsilon\sigma T^{*4} \\ q_2(r_2) &= \left[\frac{q^a(r_2)}{\epsilon\sigma T_1^4}\right]\epsilon\sigma T_1^4 + \left[\frac{q_2^b(r_2)}{\epsilon\sigma T^{*4}}\right]\epsilon\sigma T^{*4} \end{aligned}\right\} \tag{20b}$$

So, the heat fluxes are additive. It will later be found that the form of equation (20*b*) is extremely convenient for numerical computations.

Once the local heat fluxes have been determined, the over-all heat fluxes can be computed by direct integration as follows:

$$Q = \int_0^R q 2\pi r dr \tag{21}$$

From the findings of the previous paragraph, we can write that

$$Q_1 = Q_1^a + Q_1^b, \qquad Q_2 = Q_2^a + Q_2^b \tag{22}$$

where

$$Q_1^a = Q_2^a = \int_0^R q^a 2\pi r dr \tag{22a}$$

$$Q_1^b = \int_0^R q_1^b 2\pi r dr, \qquad Q_2^b = \int_0^R q_2^b 2\pi r dr \tag{22b}$$

In summary, it has been shown that the heat-flux results are known once the radiosities have been determined.[4] Further, it has been demonstrated that the heat-transfer results for the general problem of two disks at different temperatures are additive combinations of those for the simpler subproblems (*a*) and (*b*).

Solutions. It has not been possible to obtain exact analytical solutions for the governing integral equations (8) and (10). Instead, numerical means were used in conjunction with an electronic digital computer. The procedure was essentially one of iteration. For instance, for equation (8), trial values of β covering the range $0 \leq x_2 \leq 1$ were selected. Then, for a fixed x_1, the integral on the right side of the equation was carried out numerically; and this yielded on the left side a new β-value corresponding to that x_1. This was repeated for each x_1 in the range $0 \leq x_1 \leq 1$. In this way, an entire new set of β-values was generated which then served as input data to the right side of the equation. The entire process was repeated until convergence was achieved. For equations (10), the situation was somewhat more complicated since two equations are involved in the iteration. In this instance, the β_1^b output of the first equation was used as input for the right side of the second equation. Similarly, the β_2^b values computed from the second equation were used as input for the first equation.

It was generally found that the variation of β as a function of position x became greater as the spacing ratio $\gamma = h/R$ and the emissivity ϵ decreased. For the larger γ,ϵ combinations, a step size Δx of 0.01 over the interval $0 \leq x \leq 1$ was found to give excellent results. For the smaller γ, ϵ combinations, the step size was decreased to 0.005. Thus for the former cases, each iteration required that an integration over 101 points be carried out 101 times; while for the latter, 201 points were integrated 201 times for each iteration. It was generally found that the number of iterations required to achieve convergence increased as γ and ϵ decreased.

The numerical solutions were carried out for spacing ratios $\gamma = h/R$ of 5.0, 1.0, 0.5, 0.1, and 0.05 for emissivities of 0.1, 0.5, and 0.9. Inasmuch as the heat transfer is generally of greater importance than the radiosity, the solutions will be reported here in terms of the local and average heat transfer. The radiosities can be derived from the local heat transfer by use of equations (18) and (19).

Simplified Theory. For the purpose of making comparisons with the present analysis, the predictions of the simplified theory which assumes uniform radiation conditions will be derived. The formulation parallels that which has been presented in the previous sections, but now, B and H are assumed constant over the surface. We start with the radiant flux balance equation (1), and note that

$$H_1 = F_{R-R}B_2 \tag{23}$$

where F_{R-R}, the angle factor for two finite parallel disks of radius R, is given in terms of the spacing ratio γ as follows [reference [4], equation (31–47)]

$$F_{R-R} = \frac{\gamma^2 + 2 - \gamma\sqrt{\gamma^2+4}}{2} \tag{24}$$

Introducing equation (23) into (1), there results

$$B_1 = \epsilon\sigma T_1^4 + (1-\epsilon)F_{R-R}B_2 \tag{25}$$

In an analogous way, a radiant flux balance on disk 2 yields

$$B_2 = \epsilon\sigma T_2^4 + (1-\epsilon)F_{R-R}B_1 \tag{26}$$

Simultaneous solution of these linear algebraic equations can be carried out to find B_1 and B_2.

However, since we are interested in comparisons, it is useful to solve equations (25) and (26) separately for the two subproblems (*a*) and (*b*) which were considered in the preceding sections of the paper.

For problem (*a*)—both disks at the same temperature T_1—it is found that

$$B_1^a = B_2^a = \frac{\epsilon\sigma T_1^4}{1-(1-\epsilon)F_{R-R}} \tag{27}$$

With this, the local and over-all heat transfer may be evaluated by applying equations (16) and (22*a*), giving

$$\frac{q^a}{\epsilon\sigma T_1^4} = \frac{Q^a/\epsilon\sigma T_1^4}{\pi R^2} = \frac{1-F_{R-R}}{1-(1-\epsilon)F_{R-R}} \tag{28}$$

For problem (*b*)—disk 1 at zero temperature, disk 2 at $T^* = [T_2^4 - T_1^4]^{1/4}$—simultaneous solution of equations (25) and (26) leads to:

$$\frac{B_1^b}{\epsilon\sigma T^{*4}} = \frac{(1-\epsilon)F_{R-R}}{1-(1-\epsilon)^2F_{R-R}^2}, \qquad \frac{B_2^b}{\epsilon\sigma T^{*4}} = \frac{1}{1-(1-\epsilon)^2F_{R-R}^2} \tag{29}$$

[4] As pointed out in reference [3], it is possible to solve for β^a, β_1^b, and β_2^b in terms of the corresponding q's from equations (18) and (19). The β may then be eliminated from the governing equations (8) and (10), leaving instead a set of integral equations for the heat fluxes q^a, q_1^b, and q_2^b.

Then, substituting these findings into equations (19) and (22*b*), the local and over-all heat fluxes are found to be

$$\frac{q_1^b}{\epsilon\sigma T^{*4}} = \frac{Q_1^b/\epsilon\sigma T^{*4}}{\pi R^2} = -\frac{\epsilon F_{R-R}}{1-(1-\epsilon)^2 F_{R-R}^2} \tag{30a}$$

$$\frac{q_2^b}{\epsilon\sigma T^{*4}} = \frac{Q_2^b/\epsilon\sigma T^{*4}}{\pi R^2} = \frac{1-(1-\epsilon)F_{R-R}^2}{1-(1-\epsilon)^2 F_{R-R}^2} \tag{30b}$$

For the general problem where disks 1 and 2 have arbitrarily different temperatures T_1 and T_2, the local and over-all heat fluxes are found as before by adding together the results for the subproblems (*a*) and (*b*) in accordance with equations (20*b*) and (22). The simplified theory predicts that the local heat transfer is constant over the disk surface.

The heat fluxes embodied in equations (28) and (30) have been evaluated for the same γ,ϵ combinations as were considered in connection with the integral equation formulation, and the results will be presented later when comparisons are made.

Heat-Flux Results

Local Heat Flux: Both Disks at Temperature T_1. The situation where both disks have the same temperature—subproblem (*a*)—is itself of considerable interest. The local heat-transfer results for this case have been evaluated from the solutions of the governing equation (8) in conjunction with (18). The local heat fluxes thus obtained have been plotted in Figs. 2, 3, and 4 as a function of position on the disk surface. The figures correspond, respectively, to emissivity values of 0.9, 0.5, and 0.1. In each figure, there are five curves depicting spacing ratios h/R from 5.0 to 0.05. The ordinate in all figures is the ratio of the net local heat flux to the energy emitted by the surface per unit area. By inspecting the figures, it is seen that there are certain general trends which are common to surfaces of any emissivity ϵ and, in addition, there are systematic differences from figure-to-figure as a function of ϵ.

First, let us consider the general trends. For very large spacings, $h/R \geq 5.0$, the local heat flux is seen to be essentially uniform over the disk surface and very nearly equal to the emission $\epsilon\sigma T^4$. So, the presence of the second disk plays a very minor role. As the spacing decreases, the heat flux becomes increasingly nonuniform and its level decreases. The heat flux at locations near the edge of the disk (large radii) may become much larger than that in the centeral region of the disk. For example, for $\gamma = 0.05$ and $\epsilon = 0.5$, the value of $q/\epsilon\sigma T^4$ ranges from .005 at $r = 0$ to 0.6 at $r = R$ (Fig. 3). This implies that in order to maintain a uniform wall temperature, significantly different heat inputs will have to be supplied as a function of position. From this, we can draw some interesting inferences about other thermal boundary conditions; for example, if a uniform heat flux were supplied to the surface, then there could be a significant hot-spot area in the central region of the disk.

The effect of decreasing spacing in creating nonuniformities and in diminishing the heat flux is easy to understand. The net heat transfer from the surface is equal to the emission minus the absorbed incidence. The greater the incidence, the smaller the heat transfer. Now, the amount of radiant energy incident on any location depends upon the field of view from that location. The field of vision from any place on the disk surface consists of two general regions: 1 The external environment, from which no energy is received; 2 the opposite disk, from which radiant energy is received. As the spacing is decreased, more and more of the field of view is occupied by the opposite disk, and hence the heat transfer decreases. Furthermore, for any given spacing, locations in the central region of the disk see more of the opposite disk in their field of view than do points near the edge. So, the energy incident on the central region is greater and consequently the heat transfer is lower.

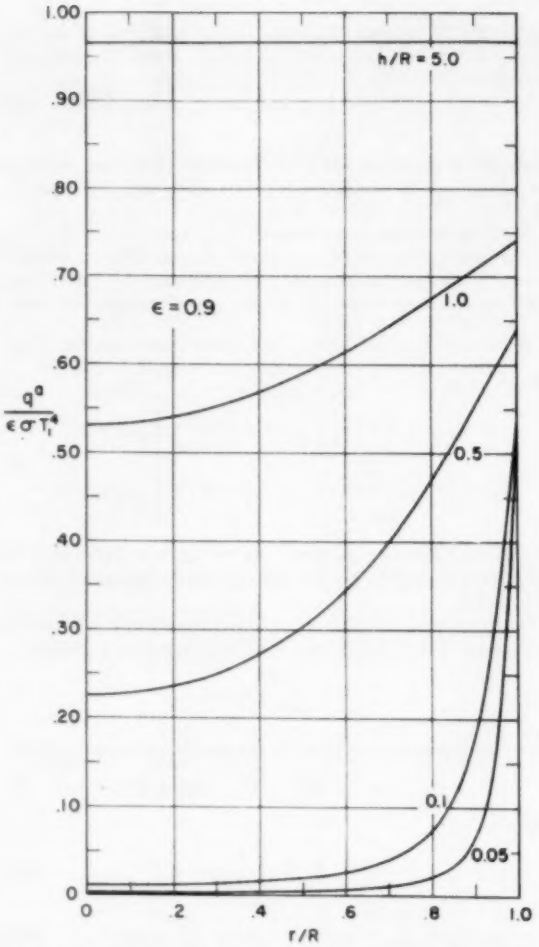

Fig. 2 Local heat-flux variation for situation where both disks have same temperature T_1, $\epsilon = 0.9$

Next, we want to consider the influence of the emissivity on the heat-transfer results. From the figures, it is seen that *relative to the emission* $\epsilon\sigma T^4$, the heat flux is lower for the surfaces of higher emissivity. This can be understood by remembering that for gray-body conditions, a highly emitting surface is also a highly absorbing surface. So, for a given spacing, a surface with high ϵ absorbs more of the incident energy than does a surface with low ϵ. Consequently, the heat transfer relative to the emission is diminished. It is seen from Fig. 2 ($\epsilon = 0.9$) that there is a large central region from which there is very little heat transfer when the disks are closely spaced. For such highly absorbing, closely spaced surfaces, the central region begins to approximate an isothermal enclosure. So, the incident radiation H is nearly black; and since $\alpha = \epsilon$, it follows that $q = \epsilon\sigma T^4 - \alpha\sigma T^4 = 0$. For lesser absorbing surfaces (e.g., Fig. 4), closer spacings are needed to achieve this condition.

The qualitative findings of Figs. 2, 3, and 4 with respect to spacing and emissivity are in agreement with those of reference [3]. There, consideration was given to a system composed of two identical parallel rectangular plates, with each rectangle having one dimension of infinite extent. It is interesting to know that the qualitative trends are not altered as we pass from a semi-infinite to a finite geometry.

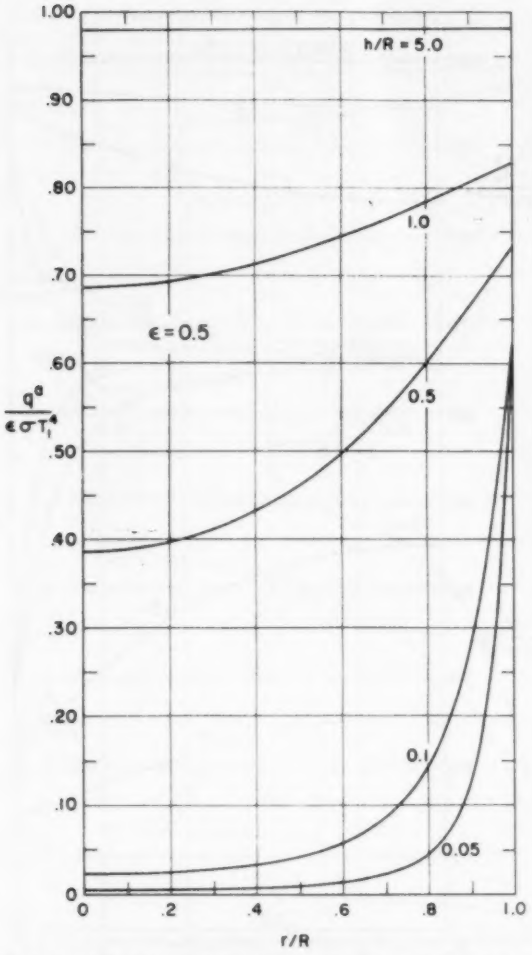

Fig. 3 Local heat-flux variation for situation where both disks have same temperature T_1, $\epsilon = 0.5$

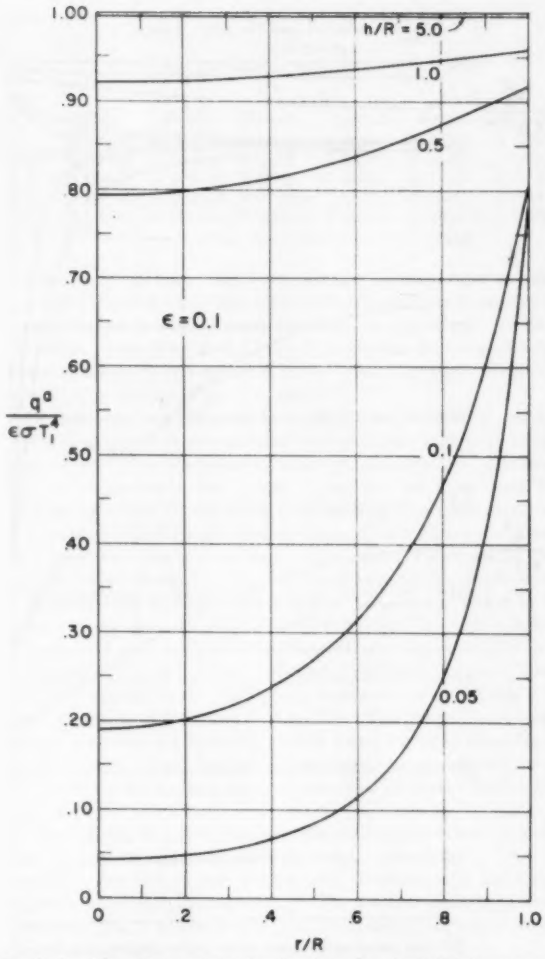

Fig. 4 Local heat-flux variation for situation where both disks have same temperature T_1, $\epsilon = 0.1$

The simplified enclosure theory as applied in equation (28) cannot predict local heat flux variations as a function of radial position.[5] So, as far as the local heat flux is concerned, the simplified theory has utility only for widely spaced surfaces. The predictions of the simplified theory in the form $q/\sigma T_1^4$ are listed in Table 1 under the heading *simpl*.

Local Heat Flux: Disk 1 at Zero Temperature, Disk 2 at T^*. The local heat transfer for subproblem (*b*) has been evaluated from the solutions of equations (10) in conjunction with (19*a*) and (19*b*). The results thus obtained have been plotted in Figs. 5, 6, and 7 as a function of position, respectively, for $\epsilon = 0.9$, 0.5, and 0.1. Each figure contains two sets of curves. The upper set corresponds to the disk 2 (temperature T^*), while the lower set corresponds to disk 1 (zero temperature). Within each set, there are curves for spacing ratios of 5.0, 1.0, 0.5, 0.1, and 0.05. The ordinate variable for disk 2 is the ratio of the actual heat transfer *from* the disk to its emission $\epsilon\sigma T^{*4}$ per unit area. For disk 1, the ordinate gives the heat transfer $(-q)$ *to* the surface relative to the emission of disk 2.

[5] The simplified theory could be generalized to provide an approximation to the local heat-flux variation by applying it to several subregions on the disk surface. The limit of this subdividing process would yield the integral equations used here.

Let us begin by considering the general trends which are evident from the figures. For the largest spacing ratio, $h/R = 5.0$, the heat transfer from disk 2 is essentially identical to its emission $\epsilon\sigma T^{*4}$, while the energy transferred to disk 1 is a small fraction of $\epsilon\sigma T^{*4}$. As the spacing between the disks decreases, the heat transferred from disk 2 decreases, while the heat transfer to disk 1 increases. Also, the variation of the heat transfer over both surfaces becomes more marked as the spacing becomes smaller.

Again, we want to illuminate the mechanism by which changes in spacing effect the heat transfer. First of all, it should be noted that since the temperature of disk 1 is zero (no emission), the net heat transfer will always be *to* this surface and will depend upon the amount of energy incident on it. Since the environment is assumed nonradiating, the incidence at any location on disk 1 will be determined by the extent to which disk 2 occupies the field of view. Clearly, as the spacing decreases, the incidence will be greater and so will the heat transfer to disk 1. Also, for a given spacing, locations in the central regions of disk 1 get a better view of the opposite disk than do locations near the edge. Hence there is greater incidence near the central regions and consequently the heat transfer to disk 1 is a maximum at $r = 0$ and decreases monotonically with increasing radius.

In explaining the effect of spacing on the heat-transfer per-

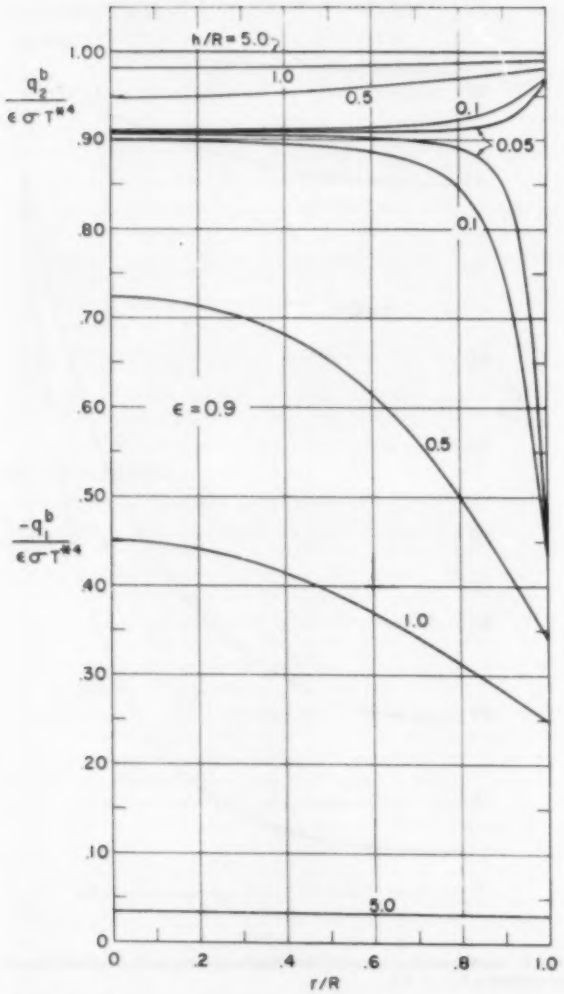

Fig. 5 Local heat-flux variation for situation where disk 1 is at zero temperature and disk 2 is at T^*, $\epsilon = 0.9$

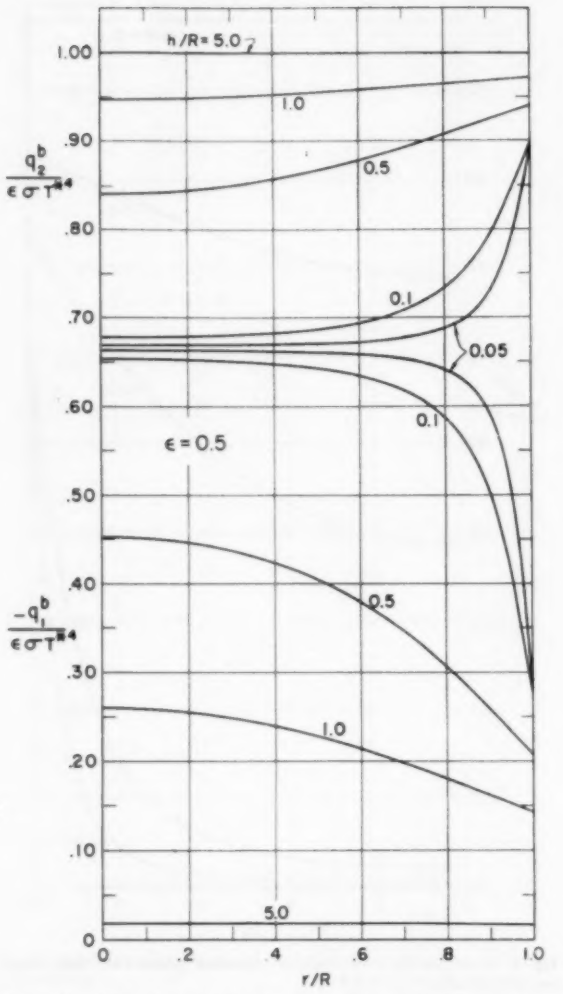

Fig. 6 Local heat-flux variation for situation where disk 1 is at zero temperature and disk 2 is at T^*, $\epsilon = 0.5$

formance of disk 2, a discussion similar to that given for problem (*a*) applies. But now, the energy incident on disk 2 is merely due to reflection of its own output by the opposite disk. Consequently, the incidence on disk 2 will now be smaller than it was in problem (*a*). Since the heat transfer is found by subtracting the absorbed incidence from the emitted energy, the role of the incidence is smaller and, consequently, the effect of decreasing spacing will be less.

The surface emissivity ϵ also plays an important part in determining the heat-transfer results. From the figures, it is seen that as ϵ increases, the heat absorbed by disk 1 (the cold surface) increases relative to the emission $\epsilon\sigma T^{*4}$. However, for disk 2, the trends are not so simply stated. For closely spaced surfaces ($h/R = 0.05$ and 0.1), the curves of $\frac{q_2}{\epsilon\sigma T^{*4}}$ increase their level with increasing ϵ. But, for wider spacings ($h/R = 0.5$ and 1.0) it is seen that the curves for $\epsilon = 0.1$ and 0.9 both lie above the curve for $\epsilon = 0.5$. So, the trends in the behavior of $q_2/\epsilon\sigma T^{*4}$ with ϵ depend upon the spacing. This finding is very likely connected with the opposite effects of a decrease in the relative incidence on disk 2 and an increase in the absorptivity($\alpha = \epsilon$). However, for all cases, the absolute level of q_2 increases with ϵ.

For highly absorbing, closely spaced surfaces, it is seen from Fig. 5 that over a large portion of the surface, the heat transferred from disk 2 is almost entirely absorbed by disk 1, and little escapes to the surroundings.

The local heat-transfer predictions of the simplified enclosure theory are of utility only for situations where the variation of q over the surface is small. Such situations are usually encountered when the spacing between the radiating surfaces is large. However, Fig. 5 shows that for highly absorbing surfaces under the conditions of subproblem (*b*), q is relatively constant over disk 2 (the hot surface) even for close spacings. So, for these conditions, the results of the simplified theory should also apply quite well to disk 2 for a wide range of spacings. The local heat-transfer predictions of the simplified theory are listed in the form $q/\sigma T^{*4}$ in Tables 2(*i*) and (2*ii*) for disks 1 and 2, respectively.

Over-All Heat Transfer Both Disks at Temperature T_1. The over-all heat transfer from the disk surface has been evaluated by integrating the local heat transfer in accordance with equation (22*a*).

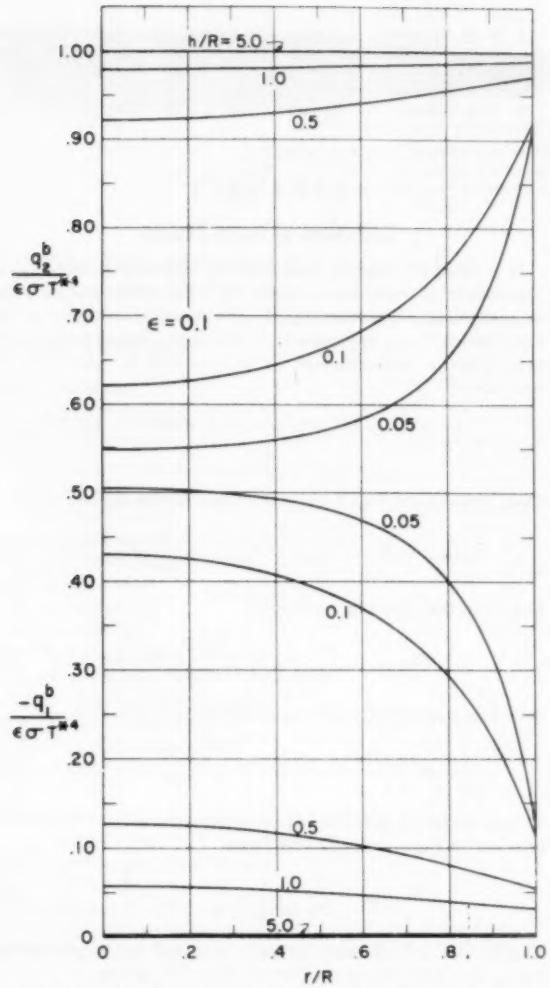

Fig. 7 Local heat-flux variation for situation where disk 1 is at zero temperature and disk 2 is at T^*, $\epsilon = 0.1$

The results thus obtained are listed in Table 1 under the heading *exact*. The over-all heat transfer from either disk corresponds to half of the radiant energy which escapes from the enclosure into the environment. As expected on physical grounds, the over-all heat transfer decreases as the spacing decreases. Further, it is seen that the over-all heat transfer decreases as the emissivity decreases, a result which is also physically reasonable.

It is of considerable interest to compare the over-all heat-transfer results of the integral equation formulation with those from the simplified theory. The latter have been evaluated from equation (28) and are listed in Table 1 under the heading *simpl*. Inspection of the table reveals that, as expected, the over-all heat transfer is predicted very accurately for the larger spacings. But, it is quite surprising that for close spacing and high emissivity, these predictions continue to be very good. For example, for $h/R = 0.05$ and $\epsilon = 0.9$, the over-all heat transfer as given by the simplified theory is only about 2 per cent high. This is remarkable agreement in view of the variations in local heat transfer as shown in Fig. 2. As the emissivity decreases, the predictions of the simplified theory becomes markedly poorer at the small spacings. For $\epsilon = 0.1$ and a spacing ratio of 0.05, the deviation is 40 per cent. But even this may be considered as quite good in view of the extreme surface variations in incident energy which occurs in such a situation. So, on the whole, the performance of the simplified theory in predicting the over-all heat-transfer results is considerably better than might have been expected after viewing Figs. 2, 3, and 4.

Table 1 Over-all heat transfer, $\frac{Q^a/\sigma T_1^4}{\pi R^2}$

For both disks at temperature T_1

	$\epsilon = 0.1$		$\epsilon = 0.5$		$\epsilon = 0.9$	
h/R	Exact	Simpl	Exact	Simpl	Exact	Simpl
5	0.09962	0.09962	0.4906	0.4906	0.8698	0.8698
1	0.09408	0.09418	0.3811	0.3820	0.5780	0.5783
0.5	0.08558	0.08649	0.2761	0.2808	0.3726	0.3742
0.1	0.04196	0.05125	0.07840	0.08686	0.09261	0.09413
0.05	0.02398	0.03389	0.04090	0.04650	0.04756	0.04850

It may also be of interest to compare the performance of the simplified theory in the parallel disk problem with that in the (semi-infinite) parallel plate problem of reference [3]. The comparison is probably best made under the condition that the spacing ratio h/L for the plates (h = spacing, L = plate length) is the equal to $h/2R$ for the disk system. Under such a condition, it is seen from Table 1 and from Table 2(a) of reference [3] that the simplified theory is more accurate for the double disk system.

Over-All Heat Transfer: Disk 1 at Zero Temperature, Disk 2 at T^*. The over-all heat-transfer results from the integral equation formulation have been evaluated according to equation (22b) and are listed in Tables 2(i) and 2 (ii) under the heading *exact*. Table 2(i) corresponds to the disk 1 (zero temperature) and Table 2(ii) corresponds to disk 2 (temperature T^*). The over-all heat transferred from disk 2 goes partly to disk 1 and partly to the external environment. The extent of the heat loss to the environment may be found by subtracting the heat absorbed by disk 1 (i.e., $-Q_1^b$) from Q_2^b.

From Table 2(i), it can be seen that the heat absorbed by disk 1 increases as the spacing decreases and the absorptivity ($=\epsilon$) increases. For disk 2, the heat transfer decreases with decreasing spacing and decreasing emissivity. The fraction of the heat transfer from disk 2 which goes to the environment decreases as the spacing decreases and as the emissivity increases.

Again, it is of interest to compare the predictions of the simple enclosure theory with the results based on the solutions of the integral equations. The over-all heat transfer as given by the simplified theory has been evaluated from equations (30) and appears in Tables 2(i) and 2(ii) under the heading *simpl*. For disk 1 (the zero temperature surface) the agreement is surprisingly good for all conditions. The greatest deviations again occur for small spacings and small emissivities, but these are no more than 15 per cent. For disk 2, the predictions of the simple theory are even more accurate, with the largest errors only about 7 per cent. Once again, we are surprised by the performance of a theory which ignores the large variations of local heat transfer and provides accurate results for the over-all heat transfer. It is interesting to note that the predictions of the simple theory are more accurate in a system having surfaces at different temperatures, subproblem (b), than in a system having surfaces at the same temperature, subproblem (a).

Results for Two Disks at Different Temperatures. To find the local heat-transfer results for two disks at different temperatures T_1 and $T_2 (T_2 > T_1)$, it is only necessary to combine the results of Figs. 2 through 7 in an additive manner. For instance, if we are interested in disk 1, then the first of equations (20b) is used. The first square bracket is read directly from the appropriate curve in Figs. 2, 3, or 4; while the second square bracket is found among the lower set of curves in Figs. 5, 6, or 7. The temperature T^* equals $[T_2^4 - T_1^4]^{1/4}$. The local heat transfer for locations on

Table 2 Over-all heat transfer
Disk 1 at zero temp, Disk 2 at T^*

(i) Disk 1, $\dfrac{-Q_1{}^b/T^{*4}}{\pi R^2}$

	$\epsilon = 0.1$		$\epsilon = 0.5$		$\epsilon = 0.9$	
h/R	Exact	Simpl	Exact	Simpl	Exact	Simpl
5	0.0003713	0.0003712	0.009275	0.009274	0.03004	0.03004
1	0.004370	0.004332	0.09930	0.09911	0.3100	0.3099
0.5	0.009150	0.008721	0.1698	0.1680	0.4959	0.4956
0.1	0.03151	0.02687	0.2883	0.2845	0.7393	0.7391
0.05	0.04055	0.03562	0.3099	0.3073	0.7778	0.7775

(ii) Disk 2, $\dfrac{Q_2{}^b/\sigma T^{*4}}{\pi R^2}$

	$\epsilon = 0.1$		$\epsilon = 0.5$		$\epsilon = 0.9$	
h/R	Exact	Simpl	Exact	Simpl	Exact	Simpl
5	0.09998	0.09999	0.4998	0.4998	0.8998	0.8999
1	0.09846	0.09851	0.4805	0.4811	0.8878	0.8882
0.5	0.09474	0.09522	0.4459	0.4488	0.8685	0.8698
0.1	0.07346	0.07812	0.3667	0.3713	0.8318	0.8331
0.05	0.06454	0.06951	0.3508	0.3538	0.8253	0.8260

disk 2 is obtained in a similar fashion by evaluating the second of equations (20*b*), but now, the upper curves of Figs. 5, 6, and 7 are used.

To compute the over-all heat transfer, equation (22) is evaluated using the information in Tables 1 and 2.

Extension to a Radiating Environment

In the anaylsis which has been given here, it has been assumed that there is no radiation passing inward from the external environment. The extension of the formulation to include a radiating environment can be carried out without difficulty. In fact, all that has been done here remains unchanged. It is only necessary to consider an additional subproblem (*c*) defined as follows: Both disks are maintained at zero temperature, and external radiation enters the enclosure in some prescribed manner. Subproblem (*c*) may be solved completely independently of the others. In fact, if the external radiation were from a high temperature source, then the appropriate short-wave-length absorptivity values can be used without any regard for what has been done in treating the low temperature radiation due to T_1 and T_2. Once the radiosities and heat-transfer results for subproblem (*c*) are available, they may be added to those which have been presented here to give the complete solution.

References

1 E. R. G. Eckert and R. Drake, "Heat and Mass Transfer," McGraw-Hill Book Company, Inc., New York, N. Y., 1959.

2 W. H. McAdams, "Heat Transmission," third edition, McGraw-Hill Book Company, Inc., New York, N. Y., 1954, chapter 4.

3 E. M. Sparrow, J. L. Gregg, J. V. Szel, and P. Manos, "Analysis, Results, and Interpretation for Radiation Between Some Simply Arranged Gray Surfaces," JOURNAL OF HEAT TRANSFER, TRANS. ASME, Series C, vol. 83, 1961, p. 207.

4 Max Jakob, "Heat Transfer," vol. 2, John Wiley & Sons, Inc., New York, N. Y., 1957.

APPENDIX

Derivation of Angle Factors

It is desired to find an expression for the angle factor $F_{dr_2-dr_2}$ appropriate to radiation between the elementary annular rings dr_1 and dr_2 as pictured in Fig. 1. We start by noting that the angle factor $F_{r_2-r_1}$ appropriate to two finite circular disks with radii r_2 and r_1 and separated by a distance h is reference [4], equation (31–45)

$$F_{r_2-r_1} = \frac{r_1^2 + r_2^2 + h^2 - \sqrt{(r_1^2 + r_2^2 + h^2)^2 - 4r_1^2r_2^2}}{2r_2^2} \tag{31}$$

Then, referring to Fig. 1 and using angle factor algebra

$$F_{dr_1-dr_2} = F_{dr_1-(r_2+dr_2)} - F_{dr_1-r_2} = \frac{\partial}{\partial r_2}(F_{dr_1-r_2})dr_2 \tag{32}$$

But, from the reciprocity theorem

$$F_{dr_1-r_2} = \frac{A_2}{dA_1} F_{r_2-dr_1} = \frac{r_2^2}{2r_1dr_1} F_{r_2-dr_1} \tag{33}$$

Once again, applying angle factor algebra it follows that

$$F_{r_2-dr_1} = F_{r_2-(r_1+dr_1)} - F_{r_2-r_1} = \frac{\partial}{\partial r_1}(F_{r_2-r_1})dr_1 \tag{34}$$

Then introducing (34) into (33) and substituting the resulting expression for $F_{dr_1-r_2}$ into (32), we have

$$F_{dr_1-dr_2} = \frac{1}{2r_1}\frac{\partial}{\partial r_2}\left[r_2^2\frac{\partial}{\partial r_1}(F_{r_2-r_1})\right] \tag{35}$$

Finally, the desired angle factor is obtained by differentiating $F_{r_2-r_1}$, equation (31), in accordance with (35), giving

$$F_{dr_1-dr_2}/r_2dr_2 = \frac{2h^4 + 2h^2r_1^2 + 2h^2r_2^2}{[(h^2 + r_1^2 + r_2^2)^2 - 4r_1^2r_2^2]^{3/2}} \tag{36}$$

Further, the reciprocal angle factor $F_{dr_2-dr_1}$ immediately follows from

$$F_{dr_2-dr_1} = \frac{r_1dr_1}{r_2dr_2} F_{dr_1-dr_2}$$

Journal of HEAT TRANSFER — Technical Briefs

This section consists of contributions of 750 words or less (about 2½ double-spaced typewritten pages, including figures). Technical Briefs will be reviewed and approved by the specific division's reviewing committee prior to publication. After approval such contributions will be published as soon as possible, normally in the next issue of the Journal

Two-Phase Frictional Pressure Drop Prediction From Levy's Momentum Model

J. F. MARCHATERRE[1]

Nomenclature

A = cross-sectional area
a = a constant
D_e = pipe diameter or equivalent diameter
f = friction factor
G = mass velocity
g = local acceleration due to gravity
g_c = gravitational constant
k, k' = constants
P = pressure
V = velocity
w = mass flow rate
x = gas weight fraction or quality
y = distance along flow path
α = gas volume fraction
θ = angle of inclination
ρ = density

Subscripts

g refers to gas
GTP refers to gas-phase friction
l refers to liquid
LTP refers to liquid-phase friction
0 refers to liquid flow alone
TPF refers to two-phase friction

LEVY [1][2] HAS POINTED OUT that in a two-phase system each fluid phase should satisfy a momentum equation of the Bernoulli type. Using these equations, he obtained a theoretical prediction of vapor volume fractions in a flowing system. An examination of the same momentum model can lead to some important deductions about frictional pressure losses in vertical two-phase flow. If the momentum equations for each phase are written, then for the liquid,

$$dP + \rho_l \frac{V_l dV}{g} = \left(\frac{dP}{dy}\right)_{LTP} dy - \frac{g}{g_c} \rho_l \sin\theta \, dy \qquad (1)$$

and for the gas

$$dP + \frac{1}{gA_g} d\left(A_g \rho_g V_g^2\right) + \frac{V_l}{gA_g} d(A_l \rho_l w_l) = \left(\frac{dP}{dy}\right)_{GTP} dy - \frac{g}{g_c} \rho_g \sin\theta \, dy \qquad (2)$$

Equating the expressions for dP (static pressure constant across a tube cross section) and substituting for V_g and V_l gives:[2]

$$\frac{1}{\alpha}\frac{G^2}{g\rho_l} d \frac{\left[\frac{(1-x)^2}{(1-\alpha)}\frac{x^2}{\alpha}\frac{\rho_l}{\rho_g} - \frac{1}{2}\frac{(1-x)^2}{(1-\alpha)^2}\right]}{dy} = \left(\frac{dP}{dy}\right)_{GTP} - \left(\frac{dP}{dy}\right)_{LTP} + \frac{g}{g_c}(\rho_l - \rho_g)\sin\theta \qquad (3)$$

The assumption of Levy [1] was that the left-hand side of equation (3) is equal to zero for steady-state conditions. This assumption, while it does not explain the experimental data completely, was borne out by comparison with the data of Cook [2] and Marachaterre [3]. Making this assumption, multiplying by α, and adding and subtracting $(dP/dy)_{LTP}$ gives

$$\alpha\left(\frac{dP}{dy}\right)_{GTP} - \alpha\left(\frac{dP}{dy}\right)_{LTP} + \left(\frac{dP}{dy}\right)_{LTP} - \left(\frac{dP}{dy}\right)_{LTP} + \alpha\frac{g}{g_c}(\rho_l - \rho_g)\sin\theta = 0 \qquad (4)$$

Since[2]

$$\left(\frac{dP}{dy}\right)_{TPF} = \alpha\left(\frac{dP}{dy}\right)_{GTP} + (1-\alpha)\left(\frac{dP}{dy}\right)_{LTP} \qquad (5)$$

and

$$\left(\frac{dP}{dy}\right)_0 = -\frac{f_0 G^2}{2g_c D_e \rho_l} \qquad (6)$$

$$\frac{\left(\frac{dP}{dy}\right)_{TPF}}{\left(\frac{dP}{dy}\right)_0} = \frac{\left(\frac{dP}{dy}\right)_{LTP}}{\left(\frac{dP}{dy}\right)_0} + \frac{g(\rho_l - \rho_l)\alpha(\sin\theta)\,2\rho_l D_e}{f_0 G^2} \qquad (7)$$

If the assumption is made that $\left(\frac{dP}{dy}\right)_{LTP}$ can be obtained in terms of the liquid flow conditions and some apparent friction factor f^*, then

$$\left(\frac{dP}{dy}\right)_{LTP} = -\frac{f^* G^2 (1-x)^2}{2g_c D_{e(l)} \rho_l (1-\alpha)^2} \qquad (8)$$

and

$$\frac{\left(\frac{dP}{dy}\right)_{LTP}}{\left(\frac{dP}{dy}\right)_0} = \left[\frac{f^* D_e}{f_0 D_e(l)}\right]\frac{(1-x)^2}{(1-\alpha)^2} \qquad (9)$$

The ratio $\frac{f^* D_e}{f_0 D_e(l)}$ is difficult to evaluate since the liquid phase frictional pressure losses are made up of losses at both the wall and interface. For liquid over the entire pipe perimeter,

$$D_{e(l)} = (1-\alpha) D_e$$

and the assumption is made that this can be generalized to $D_{e(l)} = (1-\alpha)^k D_e$ for the case where there are interfacial losses or some gas contacting the wall. For the case of large interfacial losses,

[1] Argonne National Laboratory, Argonne, Ill.
Contributed by the Heat Transfer Division of THE AMERICAN SOCIETY OF MECHANICAL ENGINEERS. Manuscript received at ASME Headquarters, April 6, 1961.

[2] Numbers in brackets designate References at end of paper.
[2] The derivation of these equations is given in detail by Levy [1].

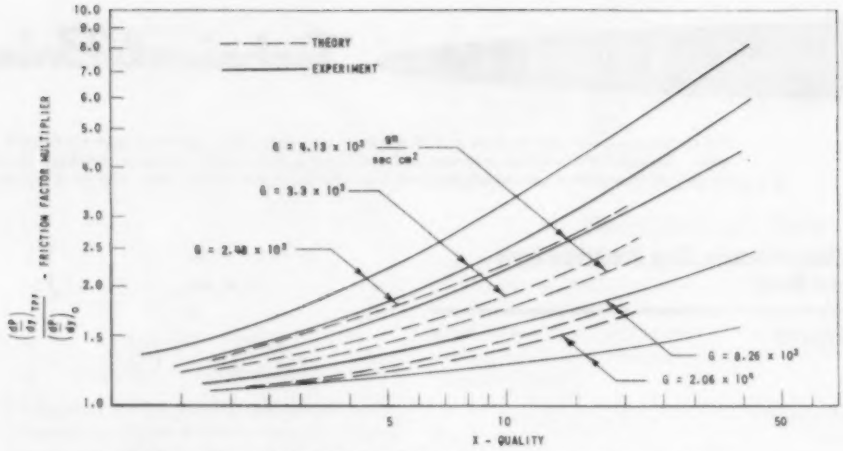
THEORY
EXPERIMENT
G = 4.13 x 10³ gm/sec cm²
G = 3.3 x 10³
G = 2.48 x 10³
G = 8.26 x 10³
G = 2.06 x 10³
(dP/dy)TPF / (dP/dy)0 - FRICTION FACTOR MULTIPLIER
X - QUALITY

Fig. 1 Comparison of theory with data of Sher and Green, 136 atm, steam water

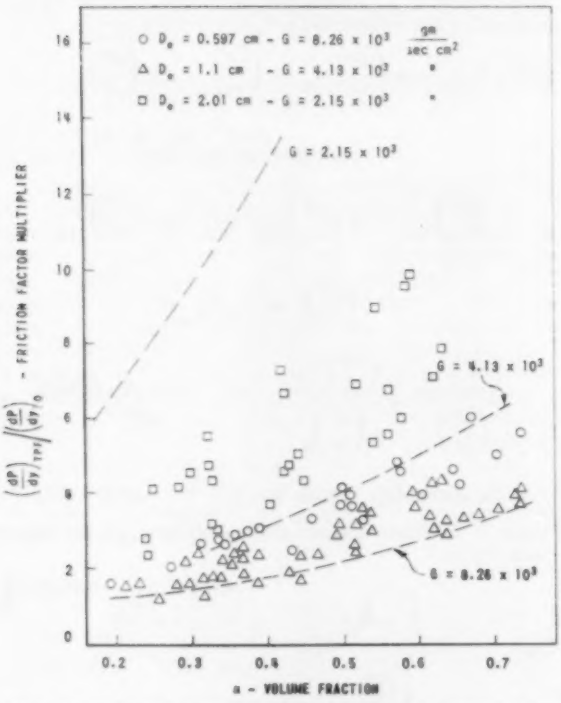
De = 0.597 cm - G = 8.26 x 10³ gm/sec cm²
De = 1.1 cm - G = 4.13 x 10³
De = 2.01 cm - G = 2.15 x 10³
G = 2.15 x 10³
G = 4.13 x 10³
G = 8.26 x 10³
(dP/dy)TPF / (dP/dy)0 - FRICTION FACTOR MULTIPLIER
α - VOLUME FRACTION

Fig. 2 Comparison of theory with data of Petrick at 3 diam and three flow rates in an air-water system at atmospheric pressure

the apparent friction factor f^* will be less than would be predicted from a Reynolds number based on the average fluid conditions, since the force at the interface will be in the opposite direction from the force at the wall. The assumption is made that f^* will vary as the liquid flow area since it must reduce to f_0 at $\alpha = 0$. Making this assumption

$$f^* = (1 - \alpha)^{b'} f_0$$

and

$$\left[\frac{f^* D_e}{f_0 D_e(l)}\right] = (1 - \alpha)^a \tag{10}$$

where a can be either positive or negative. A comparison with the data of Petrick [4] indicated that a should be ≈ 1. For this case equation (9) becomes

$$\frac{\left(\frac{dP}{dy}\right)_{LTP}}{\left(\frac{dP}{dy}\right)_0} = \frac{(1 - x)^2}{1 - \alpha} \tag{11}$$

Equation (7) becomes

$$\frac{\left(\frac{dP}{dy}\right)_{TPF}}{\left(\frac{dP}{dy}\right)_0} = \frac{(1 - x)^2}{1 - \alpha} + \frac{2g(\rho_l - \rho_g)\rho_l \alpha (\sin \theta) D_e}{f_0 G^2} \tag{12}$$

It is important to note at this point that a variety of assumptions can be made for the form of the liquid friction. The formulation chosen in this paper was chosen because of its simplicity. Better formulations or measurements should enable closer prediction of experimental data. In any case, an equation of the form of equation (12) will be obtained and the second term will remain unchanged.

Equation (12) has been compared with the data of Sher and Green [5] and Petrick [4], Figs. 1 and 2, for the vertical upward flow of two-phase mixtures. These data are indicative of the type of mass velocity effect noted by these investigators. The data of Petrick compare well with the theory of high mass velocities and/or small channels but deviate considerably in other ranges.

The theory presented for friction factor multipliers represents the experimental data at least qualitatively and predicts the mass velocity effect noted by Petrick [4] and by Sher and Green [5]. Considering the nature of the assumptions made in formulating the expression for $\left(\frac{dP}{dy}\right)_{LTP}$ the agreement is very good. It also might be expected that the theory would deviate considerably if the flow pattern varies considerably from annular flow. Also, this formulation does not preclude the existence of a mass flow rate effect in horizontal flow, since it is expected that changes in flow pattern could also cause changes in frictional pressure drop. It would appear that further advances in this area will be made only if flow patterns are carefully described and data and theoretical formulations restricted to each type of flow pattern.

References

1 S. Levy, "Steam Slip—Theoretical Prediction From Momentum Model," JOURNAL OF HEAT TRANSFER, TRANS. ASME, Series C, vol. 82, 1960, pp. 113–124.

2 W. H. Cook, "Boiling Density in Vertical Rectangular Multi-Channel Sections With Natural Circulation," Argonne National Laboratory Report No. 5621 (November, 1956).

3 J. F. Marchaterre, "The Effect of Pressure on Boiling Density in Multiple Rectangular Channels," Argonne National Laboratory Report No. 5522 (February, 1956).

4 M. Petrick, "Two-Phase Air-Water Flow Phenomena," Argonne National Laboratory Report No. 5787 (March, 1958).

5 N. C. Sher and S. J. Green, "Boiling Pressure Drop in This Rectangular Channels," presented at the Nuclear Engineering and Science Conference, Preprint No. 146 (March, 1958).

Transient Temperature Measurement Errors in Heated Slabs for Thermocouples Located at the Insulated Surface

D. R. BURNETT[1]

A method is developed for estimating the error in "cold side" transient temperature measurements of slabs heated at one surface which is due to conduction of heat away from the junction through a thermocouple wire. Results are presented for a range of slab thickness/wire diameter ratios.

Nomenclature

a = wire radius
b = slab thickness
c = specific heat
k = thermal conductivity
q = heat rate per unit area
t = time
α = thermal diffusivity
ρ = density
γ = $\alpha t/b^2$, Fourier number (dimensionless)

Subscripts

s = slab
w = wire

Introduction

THE MEASUREMENT of transient temperatures by the use of thermocouples attached to the unheated surface of slabs in order to estimate temperatures and heating rates at the heated surface is common in heat-transfer work. There is an error in these measurements due to the conduction of heat along the thermocouple wire away from the junction. A method is described for estimating this error for the configuration shown in Fig. 1, and results calculated by this method for a wire and slab of the same material are shown in Fig. 2.

[1] Thermodynamics Department, Lockheed Aircraft Corporation, Missiles and Space Division, Sunnyvale, Calif. Assoc. Mem. ASME.

Contributed by the Heat Transfer Division of THE AMERICAN SOCIETY OF MECHANICAL ENGINEERS. Manuscript received at ASME Headquarters, January 31, 1961.

Physical Model

The configuration analyzed is that of a slab of infinite extent and finite thickness with a constant heat flux incident upon one surface and no heat flux across the other except in one circular area where a wire is attached. This wire is infinitely long and has heat flowing across its surface only at the area of attachment to the slab.

Mathematical Analysis

The method of Masters and Stein [1][2] has been adapted to a new physical situation by utilizing information available in Carslaw and Jaeger [2]. The linearity of the heat-conduction equation enables the temperature in the slab to be expressed by equation (1).

$$W(x, r, t) = T(x, t) + U(x, r, t) \tag{1}$$

$T(x, t)$ is the temperature rise due to surface heating at a constant rate at one surface, and $U(x, r, t)$ is the temperature change due to the presence of a disk-shaped sink at the opposite surface. This sink simulates the effect of the wire. The expression for $T(x, t)$ given by reference [2] with co-ordinates transformed to those of Fig. 1 is:

$$T(x, t) = [qb/k_s]\left[\alpha_s t/b^2 + (3x^2 - 6bx + 2b^2)/6b^2 - (2/\pi^2)\sum_{n=1}^{\infty}(-1)^n/n^2 \exp(-\alpha_s t n^2\pi^2/b^2)\cos(n(b-x)/b)\right] \tag{2}$$

In this analysis the series is neglected as it is insignificant for the values of the Fourier number considered ($\alpha_s t/b^2 = 1$). Reference [1] gives the general expression for the temperature field in a slab of finite thickness due to a disk-shaped sink in the form of a convolution integral. This expression contains the sink strength in general form. In the case at hand the flux into a semi-infinite solid which has a surface temperature equal to $T(b, t)$ has been used for the sink strength. $T(b, t)$ was taken from equation (2) with the series omitted. The convolution integral was then converted into closed form by the use of Laplace

[2] Numbers in brackets designate References at end of paper.

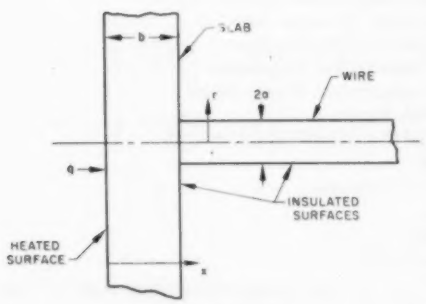

Fig. 1 Problem geometry

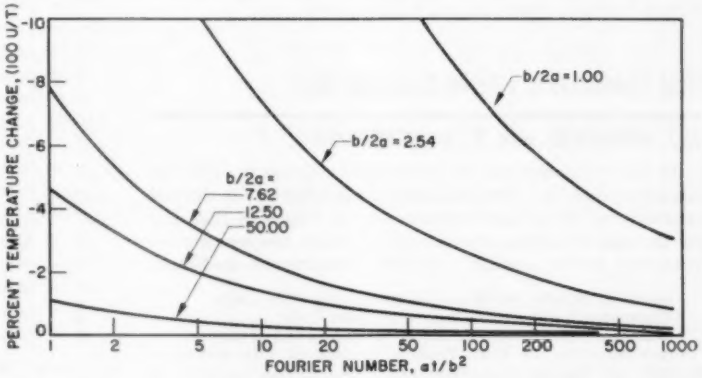

Fig. 2 Estimated per cent thermocouple error

transforms. With $\alpha_s t/b^2$ set equal to γ this expression is:

$$U(b, 0, t) = -(qb/k_s)(k_w\rho_w c_w/k_s\rho_s c_s)^{1/2} \sum_{n=0}^{\infty} [\gamma\{4i^2 \operatorname{erfc}(n/(\gamma)^{1/2}) + 4i^2 \operatorname{erfc}([n+1]/(\gamma)^{1/2}) - 4i^2 \operatorname{erfc}([4n^2 + (a/b)^2]^{1/2}/2(\gamma)^{1/2}) - 4i^2 \operatorname{erfc}([(2n+2)^2 + (a/b)^2]^{1/2}/2(\gamma)^{1/2})\} - (1/6)\{\operatorname{erfc}(n/(\gamma)^{1/2}) + \operatorname{erfc}([n+1]/(\gamma)^{1/2}) - \operatorname{erfc}([4n^2 + (a/b)^2]^{1/2}/2(\gamma)^{1/2}) - \operatorname{erfc}([(2n+2)^2 + (a/b)^2]^{1/2}/2(\gamma)^{1/2})\}] \quad (3)$$

This series is made up of the algebraic sum of eight terms each of which can be shown to form a convergent series. The complete series is therefore convergent. Since these series can be considered as finite difference integrations of the appropriate functions, a means is available for estimating the error due to omitting terms. This is because the actual values of the integrals are available. The values shown are calculated to have an error no greater than ±0.05 per cent on the scale used in Fig. 2. The required functions are tabulated in reference [2].

The conduction error is then approximated by the ratio of $U(b, 0, t)$ to $T(b, t)$ which is a function of (a/b), $(\alpha_s t/b^2)$, and $(k_w\rho_w c_w/k_s\rho_s c_s)^{1/2}$ only. This is shown in Fig. 2 for the case of the wire and slab of the same material. The case of a slab and wire of different materials is obtained from these values by multiplying values from the figure by the ratio $(k_w\rho_w c_w/k_s\rho_s c_s)^{1/2}$. If needed the value of $U(b, 0, t)$ can be found by multiplying the figure obtained from the graph by $T(b, t)$ and dividing by one hundred.

Discussion

The solution is conservative in that the flux into the wire (sink strength) is based on the temperature at the rear of the slab in the absence of the sink. This temperature is higher than that at the actual slab-wire junction. It is nonconservative in assuming no heat loss from the wire. In addition, the constant heat flux boundary condition of this solution is often not the case in practical problems. It would be expected that rapidly fluctuating rates would lead to larger errors than those indicated herein. Although in many cases the sum of these effects would be small, it is felt that these results are suitable primarily for use as guidance in designing instrumentation rather than for attempting to predict errors for correction purposes.

References

1 J. I. Masters and S. Stein, "Effect of an Axial Cavity on the Temperature History of a Surface Heated Slab," *Review of Scientific Instruments*, vol. 27, no. 12, December, 1956.

2 H. S. Carslaw and J. C. Jaeger, "Conduction of Heat in Solids," Oxford University Press, London, England, 1948.

Heat Conduction in a Series Composite Wall

J. J. BROGAN[1] **and P. J. SCHNEIDER**[2]

An exact solution for the temperature response of two-layer series composite wall, both materials of which have finite thermal conductivity, was originally obtained by E. Mayer in 1952 [1][3] for the case of sudden exposure to a uniform temperature environment with a constant convective heat-transfer coefficient. However, in that paper eigenvalues were calculated only for the case where the conductivity of the layer exposed to heating is lower than the conductivity of the backup layer whose rear face is considered adiabatic. This is the case of an insulated structure in which the load-carrying skin is insulated against unattenuated heat gain by interposing a low conductivity material.

An exact solution for the same system was discussed recently by R. Harris and J. Davidson [2]. This latter paper presents eigenvalues over a much more complete range of parameters than the former and, in addition, calculated temperature results are graphed. Once again, however, only the case of low conductivity material over a high conductor is treated.

We have worked with a number of thermal systems in which the inverse disposition of materials is present, namely, a good conductor over an insulator. One example of such a material combination is graphite over plastic. There is, accordingly, a need for the eigenvalues in this inverse case.

Denoting the material exposed to heating as 1, and the backup material as 2, and letting x_1 and x_2 be the normal co-ordinate with origins at the rear face of each material, then the Harris and Davidson solution for the temperature response of each layer is

$$\frac{t_1 - t_i}{t_g - t_i} = 1 + \beta\xi \sum_{n=1}^{\infty} \frac{e^{-\gamma_n^2 Fo_2}}{K_n} \sin\gamma_n \left(\sin\frac{\gamma_n}{\beta}\frac{x^1}{\delta_1}\right) - \sum_{n=1}^{\infty} \frac{e^{-\gamma_n^2 Fo_2}}{K_n} \cos\gamma_n \left(\cos\frac{\gamma_n}{\beta}\frac{x^1}{\delta_1}\right) \quad (1)$$

and

$$\frac{t_2 - t_i}{t_g - t_i} = 1 - \sum_{n=1}^{\infty} \frac{e^{-\gamma_n^2 Fo_2}}{K_n} \left(\cos\gamma_n \frac{x^2}{\delta_2}\right)$$

where

$$K_n = \frac{\gamma_n}{2}\left\{\left[\frac{\xi}{Bi_1}\gamma_n \cos\frac{\gamma_n}{\beta} + \beta\xi \sin\frac{\gamma_n}{\beta} + \frac{1}{\beta^2 Bi_1} \times \left(\beta \sin\frac{\gamma_n}{\beta} + \gamma_n \cos\frac{\gamma_n}{\beta}\right) + \frac{1}{\beta}\sin\frac{\gamma_n}{\beta}\right]\cos\gamma_n + \left[\cos\frac{\gamma_n}{\beta} - \frac{\gamma_n}{\beta Bi_1}\sin\frac{\gamma_n}{\beta} + \frac{\xi}{\beta Bi_1} \times \left(\beta\cos\frac{\gamma_n}{\beta} - \gamma_n \sin\frac{\gamma_n}{\beta}\right) + \xi\cos\frac{\gamma_n}{\beta}\right]\sin\gamma_n\right\} \quad (2)$$

in which

Bi_1 = Biot number based on exposed material = $h\delta_1/k_1 = 1/\zeta$
C = material specific heat
Fo_2 = Fourier number based on backup material = $\alpha_2\theta/\delta_2^2$
h = unit convective surface conductance
k = material thermal conductivity
t_1 = temperature of exposed layer
t_2 = temperature of backup layer
t_g = environmental gas temperature
t_i = initial temperature of both layers
w = material density
α = material thermal diffusivity = k/wC
$\beta = \sqrt{\rho/\xi}$
δ = material thickness
θ = time
$\xi = k_2\delta_1/k_1\delta_2$
$\rho = C_2w_2\delta_2/C_1w_1\delta_1$

and where the γ_n are eigenvalues representing roots of the transcendental equation

---

[1] Lockheed Missiles and Space Company, Palo Alto, Calif.
[2] Thermatest Laboratories, Inc., Sunnyvale, Calif.
[3] Numbers in brackets designate References at end of paper.

Contributed by the Heat Transfer Division of The American Society of Mechanical Engineers. Manuscript received at ASME Headquarters, May 19, 1961.

Table 1 Eigenvalues

$\xi = 0.0001$

ρ	n	γ_n for ζ = 0.0001	0.001	0.01	0.1	1.0	10.0	100.0	1000.0
0.01	1	1.5706	1.5706	1.5706	1.5706	1.5705	1.5685	0.9907	0.3146
	2	4.7119	4.7119	4.7119	4.7118	4.7111	3.1107	1.5813	1.5774
	3	7.8530	7.8530	7.8530	7.8528	7.8456	4.7161	4.7145	4.7144
	4	10.9936	10.9936	10.9936	10.9929	8.0101	7.8583	7.8560	7.8560
	5	14.1309	14.1309	14.1303	14.0911	10.9982	10.9962	10.9961	10.9961
0.1	1	1.5706	1.5706	1.5706	1.5706	1.5705	1.5690	1.5502	0.9344
	2	4.7119	4.7119	4.7119	4.7119	4.7114	4.7087	3.1863	1.6645
	3	7.8532	7.8532	7.8532	7.8531	7.8523	7.8309	4.7900	4.7343
	4	10.9944	10.9944	10.9944	10.9943	10.9930	9.8181	7.9589	7.8666
	5	14.1357	14.1356	14.1356	14.1355	14.1334	11.0406	11.0081	11.0044
1.0	1	1.5706	1.5706	1.5706	1.5706	1.5705	1.5691	1.5547	1.3985
	2	4.7119	4.7119	4.7119	4.7119	4.7114	4.7071	4.6525	3.1560
	3	7.8532	7.8532	7.8532	7.8531	7.8524	7.8448	7.6877	5.0299
	4	10.9945	10.9945	10.9945	10.9944	10.9933	10.9818	9.7921	8.0008
	5	14.1367	14.1357	14.1357	14.1356	14.1343	14.1177	11.3643	11.0930
10.0	1	1.5706	1.5706	1.5706	1.5706	1.5705	1.5691	1.5551	1.4261
	2	4.7119	4.7119	4.7119	4.7119	4.7114	4.7072	4.6643	4.2385
	3	7.8532	7.8532	7.8532	7.8531	7.8524	7.8453	7.7706	6.9268
	4	10.9945	10.9945	10.9945	10.9944	10.9934	10.9833	10.8717	9.5221
	5	14.1358	14.1358	14.1357	14.1356	14.1343	14.1213	13.9637	12.1872
100.0	1	1.5706	1.5706	1.5706	1.5706	1.5705	1.5691	1.5551	1.4285
	2	4.7119	4.7119	4.7119	4.7119	4.7114	4.7072	4.6652	4.2992
	3	7.8532	7.8532	7.8532	7.8531	7.8524	7.8453	7.7751	7.2038
	4	10.9945	10.9945	10.9945	10.9944	10.9834	10.9835	10.8945	10.1481
	5	14.1358	14.1358	14.1357	14.1356	14.1343	14.1216	13.9940	13.1284

$\xi = 0.001$

ρ	n	γ_n for ζ = 0.0001	0.001	0.01	0.1	1.0	10.0	100.0	1000.0
0.01	1	1.5691	1.5691	1.5691	1.5689	1.5663	0.9760	0.3141	0.09949
	2	4.6779	4.6774	4.6722	4.6800	2.7234	1.5809	1.5768	1.5764
	3	5.0006	4.9965	4.9877	4.7914	4.7149	4.7139	4.7127	4.7126
	4	7.8564	7.8564	7.8563	7.8554	7.8521	7.8502	7.8499	7.8499
	5	10.9946	10.9945	10.9943	10.9931	10.7886	10.0274	9.9390	9.9301
0.1	1	1.5692	1.5692	1.5692	1.5691	1.5676	1.5483	0.9529	0.3010
	2	4.7073	4.7073	4.7072	4.7067	4.6995	3.1121	1.6642	1.6336
	3	7.8440	7.8440	7.8438	7.8423	7.7987	4.7489	4.7330	4.7320
	4	10.9760	10.9760	10.9756	10.9694	8.8639	7.8669	7.8642	7.8640
	5	14.0764	14.0760	14.0758	13.9048	11.0219	11.0019	11.0008	11.0007
1.0	1	1.5692	1.5692	1.5692	1.5691	1.5677	1.5533	1.3978	0.6761
	2	4.7076	4.7076	4.7076	4.7072	4.7027	4.6471	3.1519	2.1148
	3	7.8460	7.8460	7.8459	7.8451	7.8371	7.8480	5.0390	4.9190
	4	10.9841	10.9841	10.9840	10.9829	10.9700	9.6948	7.9989	7.9781
	5	14.1220	14.1220	14.1219	14.1203	14.1001	11.3439	11.0910	11.0838
10.0	1	1.5692	1.5692	1.5692	1.5691	1.5677	1.5537	1.4249	0.8373
	2	4.7077	4.7077	4.7076	4.7072	4.7030	4.6600	4.2323	3.1450
	3	7.8461	7.8461	7.8460	7.8453	7.8382	7.7633	6.9236	5.8864
	4	10.9845	10.9845	10.9844	10.9834	10.9733	10.8601	9.5192	8.7719
	5	14.1229	14.1229	14.1228	14.1215	14.1083	13.9485	12.1889	11.7367
100.0	1	1.5692	1.5692	1.5692	1.5691	1.5677	1.5537	1.4273	0.8577
	2	4.7077	4.7077	4.7076	4.7072	4.7030	4.6611	4.2961	3.2962
	3	7.8461	7.8461	7.8461	7.8453	7.8383	7.7682	7.1897	6.3759
	4	10.9846	10.9846	10.9845	10.9836	10.9736	10.8751	10.1439	9.4363
	5	14.1230	14.1230	14.1229	14.1216	14.1089	13.9916	13.1245	12.5310

$\xi = 0.01$

ρ	n	γ_n for ζ = 0.0001	0.001	0.01	0.1	1.0	10.0	100.0	1000.0
0.01	1	1.4711	1.4704	1.4635	1.3814	0.8531	0.3094	0.09933	0.03146
	2	1.5704	1.5696	1.5625	1.5182	1.5770	1.5714	1.5709	1.5708
	3	4.6125	4.6104	4.5872	4.6255	3.4229	3.1726	3.1447	3.1419
	4	4.8118	4.8097	4.7909	4.7326	4.7145	4.7126	4.7124	4.7124
	5	7.7529	7.7504	7.7088	7.2155	6.4358	6.2989	6.2848	6.2833
0.1	1	1.5539	1.5539	1.5537	1.5519	1.5281	0.9182	0.3005	0.09932
	2	4.5020	4.5007	4.4877	4.3968	2.7471	1.6608	1.6292	1.6269
	3	5.1697	5.1666	5.1368	4.9292	4.7370	4.7170	4.7151	4.7149
	4	7.8780	7.8779	7.8768	7.8677	7.8457	7.8172	7.8145	7.8142
	5	10.9847	10.9845	10.9834	10.9710	10.6070	9.9737	9.8940	9.8859
1.0	1	1.5551	1.5551	1.5550	1.5535	1.5391	1.3842	0.6744	0.2226
	2	4.6621	4.6621	4.6615	4.6562	4.5897	3.1211	2.1140	2.0328
	3	7.7962	7.7961	7.7947	7.7803	7.5871	5.0196	4.9066	4.8987
	4	10.8101	10.8097	10.8055	10.7557	8.9297	7.9787	7.9542	7.9520
	5	13.6835	13.6815	13.6601	13.3632	11.2306	11.0575	11.0470	11.0460
10.0	1	1.5552	1.5552	1.5551	1.5537	1.5399	1.4134	0.8346	0.2973
	2	4.6654	4.6654	4.6650	4.6607	4.6179	4.2704	3.1442	2.8918
	3	7.7748	7.7747	7.7740	7.7666	7.6901	6.8831	5.8348	5.7585
	4	10.8827	10.8826	10.8815	10.8706	10.7812	9.4924	8.7639	8.7028
	5	13.9885	13.9883	13.9868	13.9717	13.7932	12.1723	11.7193	11.6843
100.0	1	1.5552	1.5552	1.5551	1.5537	1.5400	1.4160	0.8548	0.3095
	2	4.6657	4.6657	4.6653	4.6611	4.6200	4.2665	3.3942	3.1420
	3	7.7762	7.7761	7.7754	7.7685	7.7001	7.1609	6.3750	6.2368
	4	10.8857	10.8856	10.8856	10.8759	10.7804	10.1040	9.4360	9.3421
	5	13.9972	13.9971	13.9958	13.9834	13.8608	13.0479	12.5209	12.4500

$\xi = 0.1$

ρ	n	γ_n for ζ = 0.0001	0.001	0.01	0.1	1.0	10.0	100.0	1000.0
0.01	1	0.4913	0.4909	0.4866	0.4475	0.2703	0.09796	0.03141	0.009949
	2	1.4236	1.4227	1.4137	1.3251	1.0665	0.9884	0.9796	0.9787
	3	1.6349	1.6344	1.6297	1.6006	1.5692	1.5640	1.5634	1.5634
	4	2.4910	2.4888	2.4670	2.2963	2.0542	2.0130	2.0087	2.0083
	5	3.4733	3.4702	3.4398	3.2846	3.0147	2.9853	2.9823	2.9820
0.1	1	1.2645	1.2639	1.2582	1.1998	0.7964	0.2957	0.09816	0.03014
	2	1.8770	1.8761	1.8679	1.7991	1.6280	1.5766	1.5714	1.5709
	3	4.0289	4.0239	4.0835	4.1561	3.4010	3.1703	3.1445	3.1419
	4	5.0184	5.0162	4.9958	4.8581	4.7315	4.7143	4.7126	4.7124
	5	7.5473	7.5439	7.5082	7.1238	6.4235	6.2976	6.2846	6.2833
1.0	1	1.4196	1.4195	1.4181	1.4043	1.2867	0.6581	0.2220	0.07066
	2	3.9520	3.9507	3.9384	3.8116	2.8870	2.0861	1.9823	1.9834
	3	5.6855	5.6834	5.6627	5.4620	4.9195	4.7549	4.7375	4.7358
	4	8.0653	8.0634	8.0537	7.9768	7.6938	7.5531	7.5347	7.5328
	5	10.8965	10.8955	10.8869	10.7958	10.1037	9.7268	9.6823	9.6777
10.0	1	1.4280	1.4279	1.4267	1.4151	1.3096	0.8094	0.2961	0.09517
	2	4.2840	4.2836	4.2801	4.2454	3.9426	3.1366	2.8875	2.8582
	3	7.1399	7.1393	7.1335	7.0758	6.6091	5.8655	5.7279	5.7136
	4	9.9359	9.9351	9.9869	9.9062	9.3142	8.6723	8.5796	8.5690
	5	12.8519	12.8508	12.8408	12.7368	12.0536	11.5029	11.4319	11.4248
100.0	1	1.4288	1.4287	1.4275	1.4161	1.3134	0.8284	0.2981	0.09529
	2	4.3037	4.3034	4.3003	4.2704	4.0252	3.3786	3.1419	3.1136
	3	7.2302	7.2198	7.2156	7.1756	6.8843	6.3670	6.2565	6.2219
	4	10.1633	10.1529	10.1783	10.1348	9.8471	9.4327	9.3403	9.3301
	5	13.1863	13.1858	13.1813	13.1379	12.8681	12.5191	12.4450	12.4368

$$\beta\xi\left(\frac{\gamma_n}{\beta Bi_1}\cos\frac{\gamma_n}{\beta}+\sin\frac{\gamma_n}{\beta}\right)\tan\gamma_n = \left(\cos\frac{\gamma_n}{\beta}-\frac{\gamma_n}{\beta Bi_1}\sin\frac{\gamma_n}{\beta}\right) \quad (3)$$

Roots of equation (3) are tabulated in reference [2] for $\xi \geq 1$, and in Table 1 we give the first five corresponding roots for the inverse case of $\xi < 1$.

References

1 E. Mayer, "Heat Flow in Composite Slabs," *ARS Journal*, May–June, 1952, pp. 150–158.

2 R. S. Harris, Jr., and J. R. Davidson, "An Analysis of Exact and Approximate Equations for the Temperature Distribution in an Insulated Thick Skin Subjected to Aerodynamic Heating," NASA TN D-519, January, 1961.

Heat Conduction Through Walls During Fire

LIE TIAM TJOAN[1]

An expression is given for the temperature rise of a wall exposed on one side to a standard fire. It appears that calculated and experimental results agree with each other when a theoretical thermal conductivity is assumed which is a power of the thermal conductivity at room temperature.

Introduction

During a few years a series of tests has been performed on walls to examine the behavior of the walls when one side is exposed to a fire. Especially the temperature rise on the unexposed surface of the wall was of interest. This temperature determines the fire resistance of the wall, which may be defined as the time taken for the temperature of the unexposed surface of the wall to increase by 130 deg C when the wall is exposed on one side to a standard fire [1].[2]

To predict the fire resistance of walls, calculations have been made by using a solution of the equation of conduction of heat in which prescribed conditions for the temperature at the exposed surface are satisfied by adjusting step by step the heat supplied to the wall. The calculations have been made for a semi-infinite wall because it was not possible to satisfy the boundary condition at the unexposed surface of a finite wall which loses heat by Newtonian cooling.

The Temperature in the Wall as a Function of Time

The heat transfer by conduction through a wall is given by the equation

$$\frac{\partial\theta}{\partial t} = a\frac{\partial^2\theta}{\partial x^2}, \quad (1)$$

where θ = the temperature at distance x from exposed surface, a = the thermal diffusivity, and t = the duration of the exposure. When the wall is heated on one side ($x = 0$) according to the conditions of a standard fire,[3] the temperatures are as given in Table 1.

[1] Institute for Fire Prevention T.N.O., Rijswijk, the Netherlands.

[2] Numbers in brackets designate References at end of paper.

[3] The temperatures are those according to Dutch Standard NEN 1076, and are almost identical with the temperatures of the specifications used in other countries.

Contributed by the Heat Transfer Division of The American Society of Mechanical Engineers. Manuscript received at ASME Headquarters, December 27, 1960.

Table 1

$x = 0$	
t in seconds	θ in deg C
$t_0 = 0$	θ_0
$t_1 = 300$	500
$t_2 = 600$	700
$t_3 = 1200$	800
$t_4 = 1800$	850
$t_5 = 3600$	925
$t_6 = 7200$	1000
$t_7 = 10800$	1050
$t_8 = 14400$	1100
$t_9 = 21600$	1200

$x = \infty\theta = \theta_0$ = ambient temperature.

A solution of (1) which satisfies the foregoing conditions, valid in the time interval $0 \leqslant t \leqslant 600\ s$, is (2)

$$\theta_1 = C_1(t)^{1/2}\,\text{ierfc}\,\frac{x}{2(at)^{1/2}} + \theta_0, \quad (2)$$

where

$$C_1 = 2\frac{q_1}{(\lambda\rho c)^{1/2}}$$

q_1 = amount of heat absorbed by the wall per unit time and unit area
λ = thermal conductivity of the material
ρ = density of the material
c = specific heat of the material

In general, the solution valid in the time interval

$t_{n-1} \leqslant t \leqslant t_n$ is

$$\theta_n = \sum_{m=1}^{n}(C_{m-1} - C_m)(t_{m-1})^{1/2}\,\text{ierfc}\,\frac{x}{2(a\ t_{m-1})^{1/2}} + C_n (t)^{1/2}\,\text{ierfc}\,\frac{x}{2(at)^{1/2}} + \theta_0 \quad (3)$$

From (2) and (3) it follows that the conditions for the temperature on the exposed surface are satisfied if, assuming an ambient temperature of 20 deg C, $C_1 = 49.12$; $C_2 = 49.41$; $C_3 = 17.47$; $C_4 = 11.38$; $C_5 = 7.56$; $C_6 = 5.35$; $C_7 = 4.65$; $C_8 = 5.51$; $C_9 = 6.57$.

Comparison of Calculated and Experimental Results

Fire tests have been performed on walls of different kinds of concrete and clay brick with densities in the range 0.6×10^{-3} kg/cm^3 to 2.4×10^{-3} kg/cm^3. The thicknesses of the walls varied from 5 cm to 17 cm.

On comparison of the results it appears that experimentally found fire resistances are lower than those calculated. If, however, a thermal conductivity is employed $\lambda' = (\lambda/\lambda_0)^{1.6}\lambda$ where λ_0 is a constant and λ the thermal conductivity at room temperature, the calculated fire resistances are in agreement with experimental results. It is likely that the differences between experimental and calculated results are mainly due to the increase of the thermal conductivity with temperature.

In Fig. 1 calculated and experimental fire resistances of walls of several densities are given as function of the thickness of the wall. For simplicity the following approximations have been made:

(a) The thermal conductivity at room temperature is proportional to the density and roughly given by the relation $\lambda = 1.3\cdot\rho$.

(b) The specific heat is about 250 cal/kg deg C.

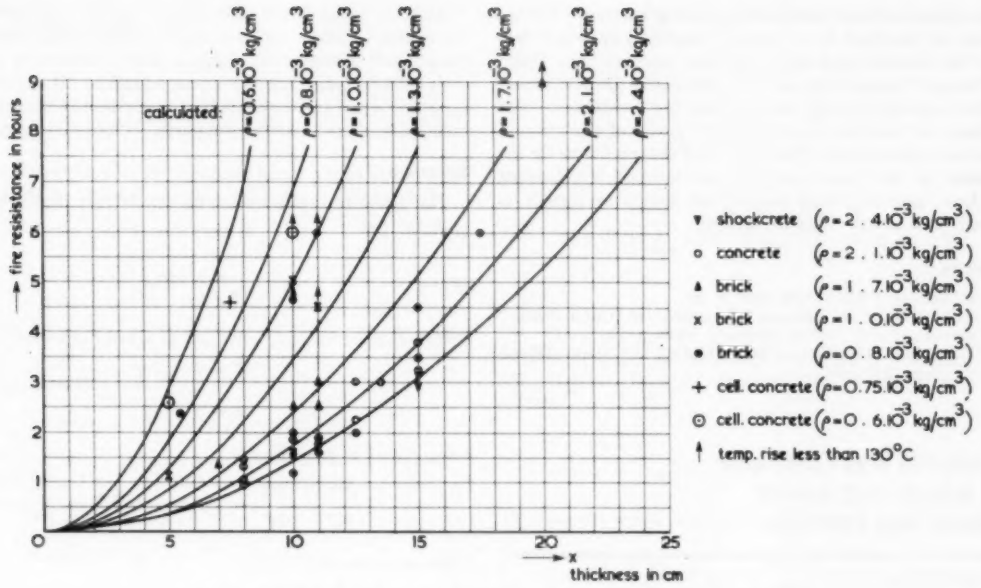

Fig. 1 Calculated and experimental fire resistances as function of thickness

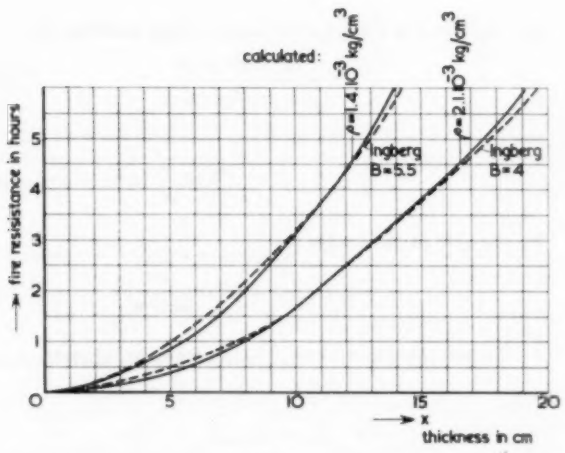

Fig. 2 Comparison of calculated fire resistances with experimental results of Ingberg

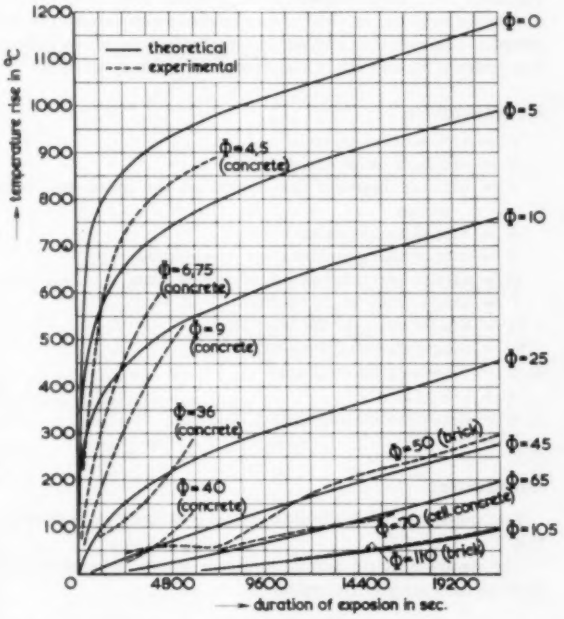

Fig. 3 Temperature rise as a function of the duration of exposure for several values of $\Phi = \frac{1/2x}{\sqrt{a'}}$

In Fig. 2 a comparison is made with the empirical relation of Ingberg [3] $t = (Bx)^{1.7}$ between the fire resistance t and the thickness x. The dotted lines are plotted for the values of the constant B of $B = 4$ and $B = 5.5$ corresponding with expanded slag and with concrete. It can be seen that the line for expanded slag agrees with our calculated line for $\rho = 1.4 \times 10^{-3}$kg/cm³ and the line for concrete agrees with our line for concrete with a density of 2.1×10^{-3}kg/cm³.

In Fig. 3 a comparison is made between measured and calculated temperature rises. The temperature rises are given as a function of time and $\Phi = {}^1/_2 x/(a')^{1/2}$, where x is the distance from the exposed surface and a' is the adjusted thermal diffusivity. As can be seen, there are considerable differences between measured and calculated temperature rises for small values of Φ, especially for $\Phi \leqslant 9$, which latter value applies to concrete with thicknesses of $\leqslant 2$ cm. Thus for very thin walls the solution for a semi-infinite solid with adjusted thermal conductivity as given before is not sufficiently accurate. However, for larger values of Φ, corresponding with wall-thicknesses of about 10 cm there is fair agreement between measured and calculated temperature rises.

Conclusions

Fire tests on walls of clay brick and different kinds of concrete

show an increase of heat transmission during heating. The increase can be described by a thermal conductivity which is a power of the thermal conductivity at room temperature. When such a thermal conductivity is used, calculated fire resistances are in close agreement with experimental fire resistances. The fire resistance of walls can be predicted by means of a solution of the equation of conduction of heat, in which the conditions for the temperature on the exposed surface are satisfied by choosing suitable heat supplies during each of the nine time periods in which the course of a fire may be divided.

References

1 Dutch Standard NEN 1076, 1957, p. 20.
2 H. S. Carslaw and J. C. Jaeger, "Conduction of Heat in Solids," Oxford University Press, Oxford, England, 1959, p. 75.
3 S. H. Ingberg, "Fire Tests of Brick Walls," U.S. Dept. of Commerce NBS, Rep. 143, 1954.

Heat Conduction in an Eccentrically Hollow, Infinitely Long Cylinder With Internal Heat Generation

M. R. EL-SADEN[1]

This paper discusses the steady temperature distribution in an infinitely long, eccentrically hollow cylinder with uniform rate of internal heat generation. An exact theoretical solution is presented. The result is applied to the special case of no internal heat generation, and the rate of heat conduction is obtained.

Nomenclature

a = radius of inner circle
b = radius of outer circle
c = distance between the centers of the inner and outer circles
k = unit thermal conductivity
q = rate of heat generation per unit volume
Q = rate of heat conduction per unit of time
T = temperature at any point
T_1 = temperature on the inner circle
T_2 = temperature on the outer circle
α, β = dimensionless constants
ϵ = $e/b - a$
ξ, η = dimensionless variables
λ = b/a

Introduction

THE GEOMETRY of the problem under consideration is shown in Fig. 1.

The steady heat conduction equation in two dimensions with uniform internal heat generation is

$$\frac{\partial^2 T}{\partial x^2} + \frac{\partial^2 T}{\partial y^2} + \frac{q}{k} = 0 \tag{1}$$

The boundary conditions for the present problem are

$$T = T_1 \text{ on the inner circle} \tag{2}$$

$$T = T_2 \text{ on the outer circle} \tag{3}$$

Also, the temperature distribution must be symmetrical about the x-axis. Cylindrical co-ordinates are not used here because the method of separation yields a solution that does not satisfy the nonlinear boundary conditions, equations (2) and (3). What is needed is a transformation that linearises the boundary conditions without complicating the partial differential equation (1).

Solution

The use of bipolar co-ordinates [1][2] is very convenient in this problem. Let

$$z = ic \operatorname{ctn} \frac{\zeta}{2} \tag{4}$$

where

$$\zeta = \xi + i\eta \tag{5}$$

$$z = x + iy \tag{6}$$

Substituting in equation (1),

$$\frac{\partial^2 T}{\partial \xi^2} + \frac{\partial^2 T}{\partial \eta^2} = -\frac{q}{k(\cosh \eta - \cos \xi)^2} \tag{7}$$

From equation (4),

$$e^{-i\zeta} = e^{\eta - i\xi} = \frac{z + c}{z - c} = \frac{(x + c) + iy}{(x - c) + iy} \tag{8}$$

The constant c is not yet determined. From equation (8),

$$e^{2\eta} = \frac{(x + c)^2 + y^2}{(x - c)^2 + y^2} \tag{9}$$

and

$$\xi = \tan^{-1} \frac{2cy}{x^2 + y^2 - c^2} \tag{10}$$

Equation (9) can be written as

$$(x - c \operatorname{ctnh} \eta)^2 + y^2 = \frac{c^2}{\sinh^2 \eta} \tag{11}$$

[1] Associate Professor of Mechanical Engineering, North Carolina State College, Raleigh, N. C.

Contributed by the Heat Transfer Division of THE AMERICAN SOCIETY OF MECHANICAL ENGINEERS. Manuscript received at ASME Headquarters, June 22, 1961.

[2] Numbers in brackets designate References at end of paper.

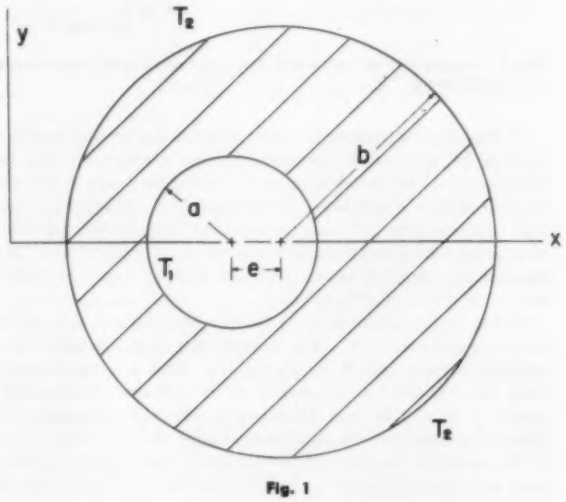

Fig. 1

Equation (11) is that of a circle with the center off the origin. Hence, on the inner circle,

$$l = c \operatorname{ctnh} \alpha \tag{12}$$

$$a = \frac{c}{\sinh \alpha} \tag{13}$$

where α is the value of η on the inner circle, and l is the x-co-ordinate of the center of the inner circle. On the outer circle,

$$m = c \operatorname{ctnh} \beta \tag{14}$$

$$b = \frac{c}{\sinh \beta} \tag{15}$$

where m is the x-co-ordinate of the outer circle and β is the value of η on it.

From equations (12) and (14),

$$e = m - l = c \operatorname{ctnh} \beta - c \operatorname{ctnh} \alpha \tag{16}$$

where e is the distance between the centers of the two circles.

Equations (13), (15), and (16) constitute three equations in three unknowns: α, β, and c, which give

$$\cosh \alpha = \frac{1}{\lambda} \frac{(\lambda + 1) + \epsilon^2(\lambda - 1)}{2\epsilon} \tag{17}$$

$$\cosh \beta = \frac{(\lambda + 1) - \epsilon^2(\lambda - 1)}{2\epsilon} \tag{18}$$

$$c = a \sinh \alpha = b \sinh \beta \tag{19}$$

where

$$\lambda = b/a, \qquad \epsilon = e/b - a \tag{20}$$

This gives the boundary conditions on η. The boundary conditions on ξ can be obtained from equation (10), which shows that due to the symmetry, when

$$y = 0, \quad \xi = 0, \text{ or } \pi \tag{21}$$

Therefore the transformed problem is

$$\frac{\partial^2 T}{\partial \xi^2} + \frac{\partial^2 T}{\partial \eta^2} = -\frac{\dot{q}}{k(\cosh \eta - \cos \xi)^2} \tag{22}$$

Subject to the boundary conditions

$$T(\xi, \alpha) = T_1 \tag{23}$$

$$T(\xi, \beta) = T_2 \tag{24}$$

$$\left.\frac{\partial T}{\partial \xi}\right)_{\xi = 0} = 0 \tag{25}$$

$$\left.\frac{\partial T}{\partial \xi}\right)_{\xi = \pi} = 0 \tag{26}$$

The complementary solution to equation (22) is

$$T_c = A\eta + B + (G'e^{n\eta} + D'e^{-n\eta})(E \cos n\xi + F \sin n\xi)$$

while the particular solution is

$$T_p = \frac{\dot{q}c^2}{2k} \frac{\cosh \eta}{\cosh \eta - \cos \xi}$$

Hence the total solution is

$$T = A\eta + B + (G'e^{n\eta} + D'e^{-n\eta})(E \cos n\xi + F \sin n\xi) + \frac{\dot{q}c^2}{2k} \frac{\cosh \eta}{\cosh \eta - \cos \xi} \tag{27}$$

Applying the boundary condition, equations (25) and (26), gives

$$F = 0$$

and

$$n = 0, 1, 2, \ldots\ldots$$

Therefore,

$$T = A\eta + B + \sum_1^\infty (Ge^{n\eta} + De^{-n\eta}) \cos n\xi + \frac{\dot{q}c^2}{2k} \frac{\cosh \eta}{\cosh \eta - \cos \xi} \tag{28}$$

In order to apply the boundary conditions of equations (23) and (24), the last term in equation (28) should be expressed as follows

$$\frac{\cosh \eta}{\cosh \eta - \cos \xi} = \operatorname{ctnh} \eta \left(1 + 2 \sum_1^\infty e^{-n\eta} \cos n\xi\right) \tag{29}$$

Therefore equation (28) can be written as

$$T = A\eta + B + \frac{\dot{q}c^2}{2k} \operatorname{ctnh} \eta + \sum_1^\infty (Ge^{n\eta} + De^{-n\eta}) \cos n\xi + \frac{\dot{q}c^2}{k} \operatorname{ctnh} \eta \sum_1^\infty e^{-n\eta} \cos n\xi \tag{30}$$

Applying equations (23) and (24),

$$T_1 = A\alpha + B + \frac{\dot{q}c^2}{2k} \operatorname{ctnh} \alpha + \sum_1^\infty (Ge^{n\alpha} + De^{-n\alpha}) \cos n\xi + \frac{\dot{q}c^2}{k} \operatorname{ctnh} \alpha \sum_1^\infty e^{-n\alpha} \cos n\xi \tag{31}$$

and

$$T_2 = A\beta + B + \frac{\dot{q}c^2}{2k} \operatorname{ctnh} \beta + \sum_1^\infty (Ge^{n\beta} + De^{-n\beta}) \cos n\xi + \frac{\dot{q}c^2}{k} \operatorname{ctnh} \beta \sum_1^\infty e^{-n\beta} \cos n\xi \tag{32}$$

Equations (31) and (32) yield

$$A = \frac{\dot{q}c^2}{k} \frac{\operatorname{ctnh} \alpha - \operatorname{ctnh} \beta}{2(\beta - \alpha)} - \frac{T_1 - T_2}{(\beta - \alpha)} \tag{33}$$

$$B = \frac{\dot{q}c^2}{k} \frac{\alpha \operatorname{ctnh} \beta - \beta \operatorname{ctnh} \alpha}{2(\beta - \alpha)} + \frac{\beta T_1 - \alpha T_2}{\beta - \alpha} \tag{34}$$

$$G = \frac{\dot{q}c^2}{k} \frac{\operatorname{ctnh} \alpha - \operatorname{ctnh} \beta}{e^{2n\beta} - e^{2n\alpha}} \tag{35}$$

$$D = \frac{\dot{q}c^2}{k} \frac{e^{2n\alpha} \operatorname{ctnh} \beta - e^{2n\beta} \operatorname{ctnh} \alpha}{e^{2n\beta} - e^{2n\alpha}} \tag{36}$$

Equation (28) or equation (30), along with equations (33), (34), (35), and (36) gives the complete temperature distribution.

The values of η and ξ at any point (x, y) can be obtained from equations (9) and (10).

Special Case ($\dot{q} = 0$)

If there is no heat generation, then

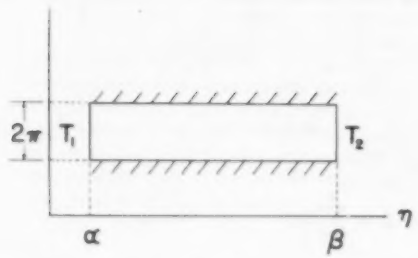

Fig. 2

$$A = -\frac{T_1 - T_2}{\beta - \alpha}$$

$$B = \frac{\beta T_1 - \alpha T_2}{\beta - \alpha}$$

and

$$G = D = 0$$

Hence,

$$T = -\frac{T_1 - T_2}{\beta - \alpha}\eta + \frac{\beta T_1 - \alpha T_2}{\beta - \alpha} \qquad (37)$$

The transformed problem is that of one-dimensional, steady-heat conduction through a slab of length $(\beta - \alpha)$ and width equal to the limits on ξ, that is 2π, as shown in Fig. 2.

The rate of heat conduction per unit thickness is

$$Q = -k(2\pi)\frac{dT}{d\eta} = -2\pi kA = \frac{2\pi k(T_1 - T_2)}{\beta - \alpha} \qquad (38)$$

where α and β are given by equations (17) and (18).

References

1 H. Bateman, "Partial Differential Equations of Mathematical Physics," Dover Publications, New York, N. Y., chapter III, 1944.

2 K. S. Miller, "Partial Differential Equations in Engineering Problems," Prentice-Hall, Inc., New York, N. Y., chapter VI, 1953.

On Some Analytic Solutions of Steady Heat Conduction in Composite Slabs of Various Cross Sections

PAU-CHANG LU[1]

It is well known that the elementary problem of steady heat conduction in a composite slab with infinite lateral extent becomes rather complicated once the restriction of time independence is removed. A similar situation arises when the slab is no longer of unlimited extent.

Referring to Fig. 1, we consider in this note the following problem:

$$\nabla^2\theta_1 + \theta_{1zz} = 0 \qquad (1)$$

$$\nabla^2\theta_2 + \theta_{2zz} = 0 \qquad (2)$$

$$z = -l_1: \quad \theta_1 = 0 \qquad (3)$$

$$z = l_2: \quad \theta_2 = e_0 \qquad (4)$$

$$z = 0: \quad k_1\theta_{1z} = k_2\theta_{2z} = H(\theta_2 - \theta_1) \qquad (5)$$

$$\text{On } \Gamma: \quad \theta_1 = \theta_2 = e_\Gamma \text{ mixed with } \frac{\partial\theta_1}{\partial n} = \frac{\partial\theta_2}{\partial n} = 0 \qquad (6)$$

where θ is the temperature difference referred to the temperature on $z = -l_1$, and H is the contact heat-transfer coefficient at the interface. Other symbols are all self-evident.

To solve the equations (1) and (2) with boundary conditions (3) to (6), we apply suitable integral transforms with respect to x_1 and x_2 as follows:

$$\theta^*(\xi, \eta, z) = \int_\alpha^\beta\int_\gamma^\delta \theta(x_1, x_2, z)K_1(\xi, x_1)K_2(\eta, x_2)dx_1dx_2 \qquad (7)$$

With proper choice of the kernels K_1 and K_2 and the upper and lower limits α, β, γ, and δ, the original system can be reduced to the subsidiary system

$$\theta_{1zz}^* - (\xi^2 + \eta^2)\theta_1^* + f = 0 \qquad (8)$$

$$\theta_{2zz}^* - (\xi^2 + \eta^2)\theta_2^* + f = 0 \qquad (9)$$

$$z = -l_1: \quad \theta_1^* = 0 \qquad (10)$$

$$z = l_2: \quad \theta_2^* = e_0^* \qquad (11)$$

$$z = 0: \quad k_1\theta_{1z}^* = k_2\theta_{2z}^* = H(\theta_2^* - \theta_1^*) \qquad (12)$$

where f is a group of terms independent of z.

The solution of this subsidiary system is

$$\theta_1^* = \frac{1}{\Delta}[\alpha_{11}\sinh(\zeta z) + \alpha_{12}\cosh(\zeta z)] + f/\zeta^2 \qquad (13)$$

$$\theta_2^* = \frac{1}{\Delta}[\alpha_{21}\sinh(\zeta z) + \alpha_{22}\cosh(\zeta z)] + f/\zeta^2 \qquad (14)$$

where

$$\zeta = (\xi^2 + \eta^2)^{1/2} \qquad (15)$$

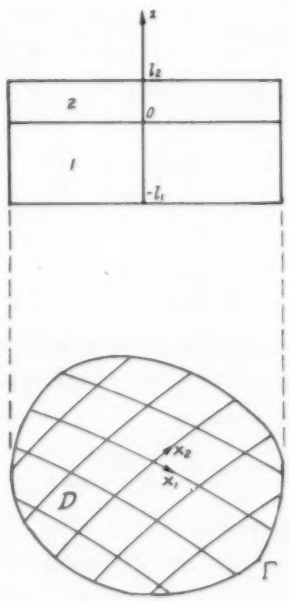

Fig. 1

[1] Graduate Assistant, Department of Mechanical Engineering Case Institute of Technology, Cleveland, Ohio.

Contributed by the Heat Transfer Division of The American Society of Mechanical Engineers. Manuscript received at ASME Headquarters, June 1, 1961.

$$\Delta = H\zeta[k_1 \sinh(\zeta l_2)\cosh(\zeta l_1) + k_2 \sinh(\zeta l_1)\cosh(\zeta l_2)] + k_1k_2\zeta^2 \cosh(\zeta l_1)\cosh(\zeta l_2) \quad (16)$$

$$\alpha_{11} = k_2H\zeta\{e_0^* \cosh(\zeta l_1) + (f/\zeta^2)[\cosh(\zeta l_2) - \cosh(\zeta l_1)]\} \quad (17)$$

$$\alpha_{12} = k_2H\zeta e_0^* \sinh(\zeta l_1) - (f/\zeta^2)[k_1H\zeta \sinh(\zeta l_2) + k_2H\zeta \sinh(\zeta l_1) + k_1k_2\zeta^2 \cosh(\zeta l_2)] \quad (18)$$

$$\alpha_{21} = k_1H\zeta\{e_0^* \cosh(\zeta l_1) + (f/\zeta^2)[\cosh(\zeta l_2) - \cosh(\zeta l_1)]\} \quad (19)$$

$$\alpha_{22} = k_2\zeta e_0^*[H \sinh(\zeta l_1) + k_1\zeta \cosh(\zeta l_1)] - (f/\zeta^2)[k_2H\zeta \sinh(\zeta l_1) + k_1H\zeta \sinh(\zeta l_2) + k_1k_2\zeta^2 \cosh(\zeta l_1)] \quad (20)$$

θ_1 and θ_2 are then obtained from θ_1^* and θ_2^* by the inversion formulas of the transforms used. All these inversion formulas are in the form of an infinite series or a real integral, hence the results can be directly employed for numerical calculations of temperature distributions or heat-transfer parameters.

Results obtained in this way are listed in the following for six cases. In each case, to save space, items listed are of the following order: (*a*) Shape of D and boundary conditions on Γ. (*b*) Transform used. (*c*) The expressions for ζ, f, e_0^*. (*d*) The expressions for θ_1 or θ_2 (represented by $\theta_{1,2}$) in terms of θ_1^* and θ_2^* which are to be regarded simply as quantities defined by equations (13) to (20).

Case I. Rectangle $0 \leqslant x \leqslant a$, $0 \leqslant y \leqslant b$, with $\theta = e_1, e_2, e_3, e_4$ on $x = 0, a, y = 0, b$, respectively.

Double finite Fourier sine transform:[2]

$$\theta^* = \int_0^b\int_0^a \theta \sin\frac{n\pi x}{a} \sin\frac{m\pi y}{b}\, dxdy$$

$$\zeta = \left(\frac{m^2\pi^2}{b^2} + \frac{n^2\pi^2}{a^2}\right)^{1/2}$$

$$f = \frac{m\pi}{b}[e_3 - (-1)^n e_4] + [1 - (-1)^m]\frac{bn}{ma}[e_1 - (-1)^n e_2]$$

$$e_0^* = \frac{abe_0}{mn\pi^2}[1 - (-1)^m][1 - (-1)^n]$$

$$\theta_{1,2} = \frac{4}{ab}\sum_{m=1}^{\infty}\sum_{n=1}^{\infty}\theta_{1,2}^* \sin\frac{n\pi x}{a} \sin\frac{m\pi y}{b}$$

Case II. Circle $r \leq a$ with $\theta = e_3$ on $r = a$. Finite Hankel transform[2]:

$$\theta^* = \int_0^a \theta J_0(\lambda_i r) r dr$$

$\zeta = \lambda_i$

$f = a\lambda_i e_3 J_1(\lambda_i a)$

$e_0^* = (e_0 a/\lambda_i)\, J_1(\lambda_i a)$

$\theta_{1,2} = (2/a^2)\sum_i \theta_{1,2}^* \dfrac{J_0(\lambda_i r)}{J_1^2(\lambda_i a)}$, summed over all the positive roots of $J_0(\lambda_i a) = 0$

Case III. Circular ring $a \leq r \leq b$ with $\theta = e_3, e_4$ on $r = a, b$, respectively.

Finite Hankel transform:[2]

$$\theta^* = \int_a^b \theta B_0(\lambda_i r) r dr$$

where

$$B_0(\lambda_i r) = Y_0(\lambda_i a)J_0(\lambda_i r) - J_0(\lambda_i a)Y_0(\lambda_i r)$$

$\zeta = \lambda_i$

$$f = \frac{2}{\pi}\left\{\frac{J_0(\lambda_i a)}{J_0(\lambda_i b)} e_4 - e_3\right\}$$

$$e_0^* = \frac{2e_0}{\pi\lambda_i^2}\left\{\frac{J_0(\lambda_i a)}{J_0(\lambda_i b)} - 1\right\}$$

$\theta_{1,2} = \dfrac{\pi^2}{2}\sum_i \dfrac{\lambda_i^2 J_0^2(\lambda_i b)\theta_{1,2}^* B_0(\lambda_i r)}{J_0^2(\lambda_i a) - J_0^2(\lambda_i b)}$, summed over-all positive roots of $B_0(\lambda_i b) = 0$.

Case IV. Same as III, but insulated on $r = a$. Generalized finite Hankel transform:[3]

$$\theta^* = \int_a^b \theta C_0(\lambda_i r) r dr$$

where

$$C_0(\lambda_i r) = J_1(\lambda_i a)Y_0(\lambda_i r) - Y_1(\lambda_i a)J_0(\lambda_i r)$$

$\zeta = \lambda_i$

$$f = -\frac{2}{\pi}\cdot\frac{J_1(\lambda_i a)}{J_0(\lambda_i b)} e_3$$

$$e_0^* = -\frac{2}{\pi\lambda_i^2}\cdot\frac{J_1(\lambda_i a)}{J_0(\lambda_i b)}$$

$\theta_{1,2} = \dfrac{\pi^2}{2}\sum_i \dfrac{\lambda_i^2 J_0^2(\lambda_i b)}{J_1^2(\lambda_i a)}\theta_{1,2}^* C_0(\lambda_i r)$, summed over-all the positive roots of $C_0(\lambda_i b) = 0$.

Case V. Same as III, but insulated on $r = b$.

Generalized finite Hankel transform:[3]

$$\theta^* = \int_a^b \theta B_0(\lambda_i r) r dr$$

$\zeta = \lambda_i$

$$f = -\frac{2e_3}{\pi}$$

$$e_0^* = -\frac{2e_0}{\pi\lambda_i^2}$$

$\theta_{1,2} = -\dfrac{\pi^2}{2}\sum_i \lambda_i^2\theta_{1,2}^* B_0(\lambda_i r)$, summed over $B_0'(\lambda_i b) = 0$.

Case VI. Region outside the circle $r = a$ with $\theta = e_3$ on the circle. e_0 vanishes when $r > b$.

Weber transform:[4]

$$\theta^* = \int_a^{\infty} \theta B_0(\lambda r) r dr$$

$\zeta = \lambda$

[2] See, e.g., I. N. Sneddon, "Functional Analysis," *Handbuch der Physik*, vol. 2, Springer Verlag, Berlin, Germany, 1955.

[3] This transform can be established from the general theory of Sturm-Liouville transforms as explained in R. V. Churchill, "Extensions of Operational Mathematics," Proceedings of the Conference on Differential Equations, University of Maryland, College Park, Md., 1955

[4] This transform can be deduced from Weber's integral theorem as proved by Titchmarsh; see E. C. Titchmarsh, "Weber's Integral Theorem," *Proceedings London Mathematical Society*, vol. 22, 1924, pp. 15–28. Hence it seems proper to name it after Weber.

$$f = -\frac{2e_0}{\pi}$$

$$e_0^* = -\frac{e_0}{\lambda^2}\left[\lambda b B_0'(\lambda b) + \frac{2}{\pi}\right]$$

$$\theta_{1,2} = \int_0^\infty \frac{\theta_{1,2}^* B_0(\lambda r)}{J_0^2(\lambda a) + Y_0^2(\lambda a)}\,\lambda d\lambda$$

The method of integral transforms is basically limited by the same restrictions on the classical method of separation of variables. Thus with the available transforms in mind (i.e., generalized Fourier, generalized finite Fourier, generalized finite Hankel, and Weber), the co-ordinate system x_1 and x_2 must be either rectangular Cartesian or polar. Furthermore, Γ must be composed of co-ordinate lines; and the boundary condition must not be mixed along each one of these lines. This then requires that D be a half plane, an infinite strip, a semi-infinite strip, a rectangle, a circle, a circular ring, a full circular sector, a circular ring sector, and an infinite plane with a circular hole. As to the boundary condition on Γ, the general "radiation" or heat-flux condition must be excluded because of the difference between k_1 and k_2. However, e_Γ is not necessarily constant as in all the cases quoted. If Γ is entirely insulated, the problem becomes trivial.

The temperatures on $z = -l_1$, l_2 need not be constant (in case VI, we have already introduced a step change in θ_2). As a matter of fact, even radiation condition is admissible on these two faces. Finally, the problem of a composite slab with more than two layers can be solved in a similar manner, only the solution of the subsidiary system is more complicated.

Tables of Cosh $(1 + i)X$, $\dfrac{\text{Sinh}\,(1 + i)X}{(1 + i)X}$, and $(1 + i)X$ Sinh $(1 + i)X$ for Periodic Heat Conduction Calculations

D. G. STEPHENSON[1] **and C. J. SHIRTLIFFE**[1]

THE CALCULATION of periodic heat conduction in one dimension is greatly simplified by using the matrix formulation [1].[2] For a homogeneous slab of finite thickness with periodic boundary conditions, the harmonic components of the surface temperatures and heat flows are related by

$$\begin{bmatrix}\theta_1\\ q_1\end{bmatrix} = \begin{bmatrix}A, & RB\\ C/R, & A\end{bmatrix}\cdot\begin{bmatrix}\theta_2\\ q_2\end{bmatrix}$$

where

θ = harmonic component with period P of periodic temperature
q = harmonic component with period P of periodic heat flow (subscripts 1 and 2 refer to the two surfaces of the slab)
A = Cosh$(1 + i)X$
B = $\dfrac{\text{Sinh}\,(1 + i)X}{(1 + i)X}$
C = $(1 + i)X$ Sinh$(1 + i)X$

$$X = L\sqrt{\frac{\pi}{\alpha P}}$$

$R = L/k$
L = slab thickness
k = thermal conductivity
α = thermal diffusivity

For multilayer slabs the square matrix relating input and output is just the product of the matrices of the individual layers multiplied in the same order as they occur in the composite slab.

To simplify the computation of the matrix elements, tables have been prepared [2] for A, B, and C in both Cartesian and polar co-ordinate form for $X = 0\,(0.01)\,3.00$ and $3.00\,(0.10)\,6.00$. The arguments of the numbers in polar form are given in degrees to 3 decimal places, while the modulus and both the real and imaginary values are given to 6 decimal places. The second differences of the tabulated values are included to indicate where linear interpolation is adequate, and to facilitate accurate interpolation with Everett's formula. The tables were prepared on a Bendix G-15D digital computer which carried out the arithmetic to 12 significant figures and then rounded the results to the specified number of decimal places. The tables occupy 70 pages and are not thought to be of sufficient general interest to justify extensive distribution. A limited number of photostatic copies have been published by the Division of Building Research of the National Research Council of Canada and can be obtained for a nominal charge.

These tables have been found to be very useful in calculating the thermal conductivity and diffusivity of materials from the results of periodic heat flow tests. This note is intended to inform others of the existence of these tables.

References

1 H. S. Carslaw and J. C. Jaeger, "Conduction of Heat in Solids," Clarendon Press, Oxford, England, second edition, 1959, p. 110.

2 C. J. Shirtliffe and D. G. Stephenson, "Tabulated Values of Special Hyperbolic Functions, Cosh$(1 + i)X$, $\dfrac{\text{Sinh}(1 + i)X}{(1 + i)X}$, $(1 + i)X$ Sinh$(1 + i)X$," National Research Council, Division of Building Research, NRC 6159, January, 1961, 70 pp.

[1] National Research Council, Division of Building Research, Ottawa, Canada.

[2] Numbers in brackets designate References at end of paper.

Contributed by the Heat Transfer Division of THE AMERICAN SOCIETY OF MECHANICAL ENGINEERS. Manuscript received at ASME Headquarters, April 10, 1961.

Mass Transfer in Laminar Flow About a Rotating Cone

C. L. TIEN[1]

THE PRESENT NOTE is to indicate the applicability of the mass-transfer results in laminar flow about a rotating disk [1][3] to the case of a rotating cone. When the cone angle is not too small [2] and the blowing velocity from the cone surface is not too large [1], the boundary-layer character exists in the region adjacent to the cone surface. Under the boundary-layer approximations, except for the pressure distribution [3], the same governing equations and boundary conditions on the velocity, temperature, and diffusion fields as (1a) through (6a) and (12b) in reference [1] may be obtained by use of the following transformations [2]:

$$V_r = (\omega r \sin\alpha)F(\eta) \qquad V_\varphi = (\omega r \sin\alpha)G(\eta)$$

$$V_z = (\omega\nu \sin\alpha)^{1/2}H(\eta)$$

$$\frac{T - T_\infty}{T_w - T_\infty} = \theta(\eta) \qquad \frac{W_1 - W_{1\infty}}{W_{1w} - W_{1\infty}} = \Phi(\eta)$$

[1] Assistant Professor of Mechanical Engineering, University of California, Berkeley, Calif.

[3] Numbers in brackets designate References at end of paper.

Contributed by the Heat Transfer Division of THE AMERICAN SOCIETY OF MECHANICAL ENGINEERS. Manuscript received at ASME Headquarters, May 26, 1961.

$$\eta = z\left(\frac{\omega \sin \alpha}{\nu}\right)^{1/2}$$

where α is half of the cone angle, r is radial co-ordinate along the cone surface, φ is the angular co-ordinate around the cone axis, z is the co-ordinate normal to the cone surface, and the rest of the symbols have the same meaning as defined in reference [1]. All the results presented in reference [1] can therefore be extended for the case of mass transfer about a rotating cone.

References

1 E. M. Sparrow and J. L. Gregg, "Mass Transfer, Flow, and Heat Transfer About a Rotating Disk," JOURNAL OF HEAT TRANSFER, TRANS. ASME, Series C, vol. 82, 1960, p. 294.

2 C. L. Tien, "Heat Transfer by Laminar Flow From a Rotating Cone," JOURNAL OF HEAT TRANSFER, TRANS. ASME, Series C, vol. 82, 1960, p. 252.

3 C. S. Wu, "The Three-Dimensional Incompressible Laminar Boundary Layer on a Spinning Cone," Applied Scientific Research, sec. A, vol. 8, 1959, p. 140.

Improved Computer Oriented Methods for Calculation of Steam Properties

T. W. MARTIN[1]

NEW METHODS, designed for implementation on digital computers, to approximate certain thermodynamic properties of steam and water are presented. These methods have been incorporated into published subroutines which arrive at results equivalent to those obtained by routines using previously published methods, doing so with a considerable savings of elapsed computer time.

Introduction

With the advent of the IBM 704 digital computer in 1956, an effort was undertaken to approximate the steam properties tabulated in Keenan and Keyes Steam Tables.[2] The results of this project were published by Steltz and Silvestri.[3] Four years of extensive use proved the reliability and utility of these routines. With the order of the IBM 7090 digital computer, it was decided to reprogram these steam table subroutines, not only to take advantage of some of the capabilities of the new computer, but also to include some revisions of the algorithms which had been developed but never fully put into use. A primary requisite of any modification was that it not in any way increase the deviation of computed results from the values tabulated in Keenan and Keyes.[2] This project was completed in August, 1960; and after a period of checkout, the routines, in the form of subroutines for use in the FORTRAN[4] system, were distributed to SHARE[5] for publication and distribution to any interested parties in February, 1961.

The new algorithms are reformulations of those used by Steltz and Silvestri[3] and arrive at essentially the same end results. The reader is referred to that paper for a complete discussion of the original programs and the remarkably small deviations from the tabulated values of Keenan and Keyes.[2]

Methods

The two primary methods of calculation used in the steam table subroutines are functional approximation and interpolation; further, certain routines make iterated use of other subroutines, using the foregoing two methods, to arrive at desired results by relaxation methods. Studies indicated that the two most often used (both by direct and by iterated use) sets of calculations were those contained in the routines called HSS and HCL. HSS calculates the enthalpy, entropy, and specific volume in the superheated steam region as functions of pressure and temperature; and HCL calculates enthalpy and entropy in the compressed liquid region, again as functions of pressure and temperature. The HSS routine is an example of the use of functional approximation, while the HCL routine arrives at results by an interpolation process. With these facts in mind, it was decided that the most fruitful approach to the problem of acceleration of the steam table calculations would be to optimize the interpolation processes and to investigate and reformulate, if possible, the algorithms used for the superheated steam calculations.

Investigations indicated that the desired accuracy (absolute deviations from values tabulated by Keenan and Keyes less than 0.10 Btu/lb for enthalpy and 0.0001 Btu/lb deg F for entropy) could be maintained in the compressed liquid routine by using interpolation tables based on equal increments of independent variables. To take advantage of this situation a special purpose fourth order Lagrangian interpolation subroutine was coded. The average execution time for the HCL routine on the 704 computer was 184 millisec; with the new interpolation subroutine on the 7090, this calculation now requires only 6.3 millisec. The usual ratio used to compare the internal processing speeds of the 704 and the 7090 is 6.3:1, so the foregoing figures represent an actual acceleration of 4.65 times.

A casual investigation of the algorithms used in the HSS routine as published by Steltz and Silvestri[3] did not immediately reveal an easy solution to the acceleration problem. However, after many reformulations, the formulas which appear in the Appendix were derived. It can be verified that these new formulas are mathematically equivalent to the previously published methods.

A special situation arose in connection with this routine. It will be noted that several high order terms appear in these formulations. For many admissible values of pressure and temperature these terms were of such small significance that they could be dropped from consideration; indeed, Schnackel[6] has published a method which omits these terms from computation. An investigation was undertaken to determine, if possible, exactly which values of pressure and temperature lead to insignificance of the high order terms, and to develop an analytic expression to allow a test to be made economically before undertaking the rather time consuming calculations necessary to evaluate these terms. An expression involving only pressure and temperature was derived to express this test and is presented in the Appendix.

The execution time for the original 704 HSS subroutines was 50.15 millisec, while the average time for the new 7090 routine is 2.28 milliseconds. Again applying the 6.3:1 ratio for machine speeds, it can be seen that this represents an actual acceleration of 3.5 times.

Similar investigations were undertaken for several of the

---

[1] Engineer, Advanced Systems Engineering and Analytical Department, Westinghouse Electric Corporation, East Pittsburgh, Pa.

[2] Joseph H. Keenan and Frederick G. Keyes, "Thermodynamic Properties of Steam," John Wiley & Sons, Inc., New York, N. Y., 1951.

[3] William G. Steltz and George J. Silvestri, "The Formulation of Steam Properties for Digital Computer Application," TRANS. ASME, vol. 80, 1958, p. 967.

[4] FORTRAN, an abbreviation for Formula Translator, is a coding system for digital computers which translates from a pseudoalgebraic format into machine instructions.

[5] SHARE, a co-operative organization of IBM 704, 709, and 7090 computer users.

Contributed by the Heat Transfer Division of THE AMERICAN SOCIETY OF MECHANICAL ENGINEERS. Manuscript received at ASME Headquarters, July 18, 1961.

[6] H. C. Schnackel, "Formulations for the Thermodynamic Properties of Steam and Water," TRANS ASME, vol. 80, 1958, p. 959.

routines used to evaluate properties along the saturation line. Since these formulations were a good bit more simple than those found in the HSS calculation procedures, it was found that the original routines were already fairly well optimized except where they required interpolation procedures. In these cases, advantage could again be taken of tables using equal increments of independent variable. The accelerations realized by the 7090 routines over the old 704 routines ranged from 1.3 to 1.9 times. Formulations for evaluating pressure and entropy as functions of temperature along the saturation line are presented since they differ from those presented by Steltz and Silvestri[3] due to a different internal scaling process.

Results

To test the effect of this programming, the revision of only the HSS subroutine was introduced into the Generalized Heat Balance program on the 704. With only this change, a rerun of an already completed series of calculations was made with a resulting savings of 15 per cent elapsed computer time over the original run using the old version of the superheated steam routine.

Acknowledgment

The author wishes to express his appreciation to William G. Steltz of the South Philadelphia Works for his help in suggesting modification possibilities and his diligent checking of the new methods derived from his and George J. Silvestri's original work.

APPENDIX

In what follows below the following units are used:

Pressure	psia	p
Temperature	deg F	t
Enthalpy	Btu/lb	h
Entropy	Btu/lb deg F	s
Specific volume	ft³/lb	v

1 The computations contained in the HSS routine are (given p such that $0.2 \leq p \leq 5501$ and t such that $50 \leq t \leq 1601$):

$$E_1 = (t + 459.688)/2.84378159$$
$$E_2 = 0.0862139787\ E_1$$
$$E_3 = \ln(E_2)$$
$$E_4 = -E_3/0.048615207$$
$$E_5 = 0.73726439 - 0.0170952671\ E_4$$
$$E_6 = 0.1286073p$$
$$E_7 = \ln(E_6)$$
$$E_8 = E_7/9.07243502$$
$$E_9 = 14.3582702 + 45.4653859\ E_8$$
$$E_{10} = (E_9)^2/0.79836127$$
$$E_{11} = 37.2999654 \times 10^{-4}/E_{10}$$
$$E_{12} = 186210.0562\ E_{11}$$
$$E_{13} = \exp(E_{12} + E_7 - E_5 + 4.3342998)$$
$$E_{14} = E_{13} - E_6$$
$$E_{15} = E_{11}(E_{14})^2$$
$$E_{16} = (E_{15})^2$$
$$E_{17} = 3464.3764/E_5$$
$$E_{18} = -1.279514846\ E_{17}$$
$$E_{19} = E_{13}(E_{18} + 41.273)$$
$$E_{20} = E_{16}(E_5 + 0.5\ E_{17})$$
$$E_{21} = 2(E_{19} + 2\ E_{20})$$
$$E_{22} = E_{15}(E_{17}\ E_{15} - E_{18})$$

If $E_2 > 18.8131323 + E_9\ E_5$, bypass the following steps, skipping down to the evaluation of v. Otherwise,

$$E_{23} = (E_{14})^2\ E_{14}$$
$$E_{24} = ((E_{11})^2/0.141431346 \times 10^{-10})^6$$
$$E_{25} = -\frac{E_{22}}{24}(E_{24} - 6.71076923 \times 10^{-4})$$
$$E_{26} = E_{23} + E_{25}$$
$$E_{27} = E_{22} + E_{23}\ E_{24}$$
$$E_{28} = E_{21} + 13E_{25}$$
$$v = 0.0302749643\ (E_{21} - E_{14} + 83.47150448\ E_5)/E_6$$

It should be noted that v must be greater or equal 0.1603 ft³/lb for the foregoing calculations to be valid.

$$E_{29} = E_{13} + 2(E_{13}\ E_{12})$$
$$E_{27} = \frac{E_{26}E_{21}}{E_{14}} + E_{21} - E_{22} - E_{26}$$
$$h = 835.417534 - E_4 + E_1 + 0.04355685(E_{19} + E_{10} - E_{14} + E_{27})$$
$$s = E_5 - E_8 - 0.00132049845\ (472.24937 + E_{29} - E_{27} - 2E_{10})/E_2$$

2 To evaluate pressure p as a function of temperature t along the saturated liquid line, $50 \leq t \leq 705.4$:

$$p = \exp\left(8.0728362 + \frac{x(A + Bx + Cx^3 + Ex^4)}{(1 + Dx)(t + 459.688)}\right)$$

where $x = t - 705.398$ and

	$50 \leq t < 200$	$200 \leq t \leq 705.4$
A	7.46908269	7.70517043
B	$-7.50675994 \times 10^{-3}$	$-5.29739118 \times 10^{-2}$
C	$-0.46203229 \times 10^{-6}$	$-2.96725673 \times 10^{-6}$
D	$-0.1215470111 \times 10^{-2}$	$-0.766360055 \times 10^{-2}$
E	0	$1.439870206 \times 10^{-11}$

3 To evaluate entropy s as a function of temperature t along the saturated liquid line, $50 \leq t \leq 670$:

$$s = \sum_{i=0}^{7} A_i t^i \text{ where}$$

	$50 \leq t < 450$	$450 \leq t \leq 670$
A_0	-0.0696290356	-228.79652
A_1	$2.27832672 \times 10^{-3}$	3.00212553
A_2	$-3.91489491 \times 10^{-6}$	$-1.6822179 \times 10^{-2}$
A_3	$1.41615577 \times 10^{-8}$	5.2260294×10^{-6}
A_4	$-4.52669227 \times 10^{-11}$	$-9.71693885 \times 10^{-8}$
A_5	$9.15595102 \times 10^{-14}$	$1.08131391 \times 10^{-10}$
A_6	$-9.95259058 \times 10^{-17}$	$-6.66855103 \times 10^{-14}$
A_7	$4.48759603 \times 10^{-20}$	$1.75836714 \times 10^{-17}$

Comparison of the Implicit and Explicit Methods for Finite Difference Heat-Transfer Calculations

J. T. ANDERSON,[1] J. M. BOTJE,[2] and W. K. KOFFEL[3]

In a recent publication,[4] Prof. G. M. Dusinberre has challenged the advantage of applying the implicit method of solving finite difference equations in heat-transfer problems. Specifically, doubts were expressed on (*a*) the accuracy and (*b*) the possibility of saving computer time.

[1] Department of Mechanical Engineering, West Virginia University, Morgantown, W. Va.

[2] Aircraft Nuclear Propulsion Department, General Electric Company, Cincinnati, Ohio. Assoc. Mem. ASME.

[3] Jet Engine Department, General Electric Company, Cincinnati, Ohio. Mem ASME.

[4] G. M. Dusinberre. "A Note on the 'Implicit' Method for Finite Difference Heat-Transfer Calculations," Journal of Heat Transfer, Trans. ASME, Series C, vol. 83, 1961, p. 94.

Contributed by the Heat Transfer Division of The American Society of Mechanical Engineers. Manuscript received at ASME Headquarters, August 18, 1961.

From the standpoint of accuracy it should be remembered that in the application of finite difference methods to heat-transfer problems, reasonable care must always be taken to choose distance and time increments such that the truncation errors in distance and time are kept within the acceptable limits. Noting that both spatial and time truncation errors are a function of the second derivative of temperature with respect to distance and time, respectively, it is consequently immaterial whether the implicit or explicit form of finite difference calculation is used; that is, for the same distance increment, location, and the same time increment, both methods will give essentially the same truncation error.

The example given by Professor Dusinberre shows a considerable amount of error associated with the implicit method; it should be noted, however, that the explicit method would have resulted in essentially the same truncation errors if the same abnormally long time steps had been employed. In addition, the explicit method would have an additional problem due to the possibility of instability of the solution, when such abnormally long time steps are used.

The implicit method has the fundamental advantage that no restriction is placed on the length of time step from the standpoint of stability of the solution. The length of the time step can, by judicious application, be employed to effect a savings of computer time, without sacrificing accuracy of the solution; for example, Liebmann[5] using the implicit method set up an example problem using a graded set of time steps covering a transient in 36 time increments with a maximum error less than 2 per cent. The same problem using the explicit method would require 10,000 time steps.

[5] G. Liebmann, "The Solution of Transient Heat Flow and Heat-Transfer Problems by Relaxation," *British Journal of Applied Physics*, April, 1955.

A more direct comparison of digital computer time may be obtained in the application of the implicit method to the solution of a practical transient heat-transfer problem in the aircraft gas turbine. The presence of small nodes in the model network having dimensions of the order of 0.06 in. was unavoidable, and it was calculated that some three hours of IBM 704 time would be required using the explicit method to solve a standard 200-node, three-minute transient problem. Using the implicit method to solve the same problem resulted in 12 min of computer time.[6]

A further example of comparative computation time may be seen if, in the example given by Dusinberre, it was necessary to include a thin node of thickness equal to one sixteenth of the radius, having a specific heat the same as the rest of the nodes and a thermal conductivity ten times as great as the rest of the nodes. The limiting time step for the system now becomes $^1/_{160}$th of the original time step which would result in the explicit method taking 160 times as many time steps to solve the problem as the implicit method would take.

It is concluded that the implicit method is just as accurate as the explicit method and is further capable of solving problems involving small nodes in considerably less time than the explicit method. In addition, the implicit method has additional flexibility by permitting:

1 Variation of node size where needed for accuracy without the accompanying penalty of a limiting time step.

2 Variation of time step length to permit the use of computer time saving techniques such as the geometrical progression demonstrated by Liebmann.

3 Direct calculation of the steady-state temperature distribution.

[6] J. T. Anderson, J. M. Botje, W. K. Koffel, "Digital Computer Solution of Complex Transient Heat Transfer Problems," Engineering Experiment Station Bulletin, West Virginia University, 1961.

CONTENTS

(*Continued*)

512 **On Some Analytic Solutions of Steady Heat Conduction in Composite Slabs of Various Cross Sections**
Pau-Chang Lu

514 **Tables of Cosh $(1 + i)X$, $\frac{\text{Sinh } (1 + i)X}{(1+i)X}$, and $(1 + i)X$ Sinh $(1 + i)X$ for Periodic Heat Conduction Calculations**
D. G. Stephenson and C. J. Shirtliffe

514 **Mass Transfer in Laminar Flow About a Rotating Cone**
C. L. Tien

515 **Improved Computer Oriented Methods for Calculation of Steam Properties**
T. W. Martin

516 **Comparison of the Implicit and Explicit Methods for Finite Difference Heat-Transfer Calculations**
J. T. Anderson, J. M. Botje, and W. K. Koffel

Journal of HEAT TRANSFER

Information for Authors

• Manuscripts should be submitted in final form to the Editor. Each manuscript must be accompanied by a statement that it has not been published elsewhere nor has it been submitted for publication elsewhere. A paper which would occupy more than 8 pages of the Journal may be returned to the author for abridgment.

• The author should state his business connection, the title of his position, and his mailing address. A short abstract (50 to 100 words) should be included on the first page immediately preceding the introductory paragraph of the paper.

Three copies of the manuscript are required. One of these must be a carefully prepared printer's copy, typed in double spacing, on one side of the page only, with wide margins, on $8^1/_2$ by 11-in. opaque white paper. Mimeographed manuscripts, if prepared with exceptional care, can be accepted provided they are completely edited.

• As far as possible, all mathematical expressions should be typewritten. Greek letters and other symbols not available on the typewriter should be carefully inserted in ink. Care should be taken to distinguish between capital and lowercase letter, between zero (0) and the letter (*O*), between the numeral (1) and the letter (*l*), etc. A letter representing a vector cannot be printed with an arrow above or below it. The letter should be underscored with a single wavy line, wherever it appears in the text, to designate boldface type.

• A list of symbols carefully marked for the use of the editor (thus: κ, Greek l.c. kappa), if it has not been included in the body of the paper, should accompany the manuscript on a separate page.

• Before preparing a manuscript the author should study printed articles in the Journal, with special attention to the form and style of mathematical expressions, tables, footnotes, references, and abstract. Numbers that identify mathematical expressions should be enclosed in parentheses. Numbers that identify references at the end of the paper should be enclosed in brackets. Care should be taken to arrange all tables and mathematical expressions in such a way that they will fit into a single column when set in type. Equations that might extend beyond the width of one column (fractions that should not be broken or long expressions enclosed in parentheses) should be rephrased to go on two or more lines within column width. Fractional powers are preferred to root signs and should always be used in more elaborate formulas. The solidus should be used instead of the horizontal line for fractions wherever possible.

• A normal paper should not exceed 8 pages in the Journal. It is about 8000 words or 20 double-spaced typewritten pages exclusive of drawings. A Technical Brief should not exceed 750 words or about one page in the Journal inclusive of drawings.

• Originals and two copies of figures must accompany the manuscript. Line drawings should not be larger than $8^1/_2 \times 11$ in. and should be planned for reduction to column width. Lettering should be large enough to be clearly legible when the illustration is reduced. The originals of line drawings must be in India ink on white or pale blue tracing paper or tracing cloth. Photographs of equipment or test specimens must be glossy prints and should be used sparingly. Captions for figures should be typed double-spaced and included as the last page of the manuscript. The figure number and author's name should be written in the margin or on the back of each illustration.

• Titles of papers should be brief.

• Authors can obtain copies of the ASME Manual MS-4, "An ASME Paper," from the Editor and are urged to do so before drafting their papers in final form.

• Papers published in Journals of the Transactions of the ASME must be presented at a Meeting, either in person or by title.

• An author is entitled to 25 preprints free of charge (in the case of two authors 15 each; three or more authors, 10 each). Larger quantities of preprints or reprints can be ordered from Editorial Department, The American Society of Mechanical Engineers, 345 East 47th Street, New York 17, N. Y. Quotations will be sent on request.

Please address all communications to:

Editor, ASME,

United Engineering Center

345 East 47th Street,

New York 17, N. Y.

ASME Publications Committee